Enhancement of Natural and Forced Convection Condensation Using Three-dimensional Extended Structures

HO JIN YAO

SCHOOL OF MECHANICAL AND AEROSPACE ENGINEERING
NANYANG TECHNOLOGICAL UNIVERSITY

September 2019

Enhancement of Natural and Forced Convection Condensation Using Three-dimensional Extended Structures

HO JIN YAO

SCHOOL OF MECHANICAL AND AEROSPACE ENGINEERING

A thesis submitted to the
Nanyang Technological University
in partial fulfilment of the requirements for the degree of
Doctor of Philosophy

September 2019

Statement of Originality

I hereby certify that the work embodied in this thesis is the result of original research, is free of plagiarised materials, and has not been submitted for a higher degree to any other University or Institution.

6 Sep 2019
Date

Ho Jin Yao

Supervisor Declaration Statement

I have reviewed the content and presentation style of this thesis and declare that it is free of plagiarism and of sufficient grammatical clarity to be examined. To the best of my knowledge, the research and writing are those of the candidate except as acknowledged in the Author Attribution Statement. I confirm that the investigations were conducted in accord with the ethics policies and integrity standards of Nanyang Technological University and that the research data are presented honestly and without prejudice.

Leong

6 Sep 2019
Date

Prof. Leong Kai Choong

Authorship Attribution Statement

This thesis contains material from eight papers published in the following peer-reviewed journals and from papers accepted at conferences in which I am listed as an author.

Chapters 3, 4 and 5 are published as

1. **Ho, J.Y.**, Leong, K.C., Wong, T.N., Filmwise condensation of steam on sinusoidal pin fin arrays: Effects of fin height and fin pitch, *International Journal of Heat and Mass Transfer*, Vol. 130, pp. 1004-1015 (2019).
2. **Ho, J.Y.**, Wang, X.W., Leong, K.C., Filmwise condensation of steam on vertical plates with novel pin fin arrays produced by selective laser melting, *International Journal of Heat and Mass Transfer*, Vol. 126, pp. 652-666 (2018).
3. **Ho, J.Y.**, Leong, K.C, Filmwise condensation of steam on pin fin arrays fabricated by selective laser melting, *Defect and Diffusion Forum,* Vol. 390, pp. 71-82 (2019).
4. **Ho, J.Y.**, Leong, K.C., Filmwise Condensation of Steam on Pin Fin Arrays Fabricated by Selective Laser Melting, 14th *International Conference on Diffusion in Solids and Liquids (DSL*2018*)*, 25-29 June, Amsterdam, The Netherlands.
5. **Ho, J.Y.**, Leong, K.C., Filmwise condensation on micro-fin surfaces produced by selective laser melting, *Proceedings of the* 13*th International Conference on Heat Transfer, Fluid Mechanics and Thermodynamics* (*HEFAT*2017), pp. 85-90, 17-19 July, Portorož, Slovenia (2017).

The contributions of the co-authors are as follows:

- Prof. Leong Kai Choong provided the project direction and guidance related to the research. He also edited and suggested improvements to the manuscript drafts.
- Prof. Wong Teck Neng provided guidance related to the research and suggested improvements to the manuscript drafts.

- Dr. Wang Xuwen suggested ideas on the development of the enhanced structures.
- I designed and installed the experimental setup, designed and fabricated the enhanced structures, conduct the experiments, analysed the data and developed the models. I also prepared the manuscript drafts.

Chapters 3, 4 and 7 are published as

1. **Ho, J.Y.**, Leong, K.C., Wong, T.N., Forced convection condensation of R134a in three-dimensional conical pin fin tubes, *International Journal of Heat and Mass Transfer*, Vol. 144, Article 118599 (2019) .
2. Wang, X.W., **Ho, J.Y.**, Leong, K.C., Wong, T.N., Condensation heat transfer and pressure drop characteristics of R-134a in horizontal smooth tubes and enhanced tubes fabricated by selective laser melting, *International Journal of Heat and Mass Transfer*, Vol. 126, pp. 949-962 (2018).
3. Wang, X.W., **Ho, J.Y.**, Leong, K.C., Condensation heat transfer and pressure drop characteristics of R134a in horizontal smooth tubes and enhanced tubes fabricated by selective laser melting, *Proceedings of the* 16*th International Heat Transfer Conference, IHTC*-16, pp. 2496-2484, August 10-15, Beijing, China (2018).

The contributions of the co-authors are as follows:

- Prof. Leong Kai Choong provided the project direction and guidance related to the research. He also edited and suggested improvements to the manuscript drafts.
- Prof. Wong Teck Neng provided guidance related to the research and suggested improvements to the manuscript drafts.
- Dr. Wang Xuwen designed the enhanced structures and assisted in the fabrication of the condenser tubes. In addition, he also designed and developed the experimental setup and drafted one part of the manuscript.

- I assisted in the design of the enhanced structures. In addition, I designed and developed the experimental setup and fabricated the condenser tubes. I also assisted in the preparation of the manuscript.

6 Sep 2019
Date

Ho Jin Yao

Abstract

Condensation heat transfer is widely used in many engineering applications such as in air-conditioning systems, power generators and desalination plants. Due to its extensive applications, enhanced condensation heat transfer is essential for improving system efficiency and reducing energy consumption. The use of fin structures has the potential for condensation applications due to their increased heat transfer area. In addition, the fin geometry is also essential to promote condensate thinning by surface tension forces. However, existing extended surfaces are largely two-dimensional fins which have the disadvantage of large condensate retention. Three-dimensional pin fins, on the other hand, have the potential of reducing condensate retention. However, existing three-dimensional fin designs have poor geometrical variations. To overcome these issues, three-dimensional pin fins of new geometries which take advantage of surface tension effects and reduced condensate retention can be fabricated by selective laser melting (SLM).

The objectives of this thesis are to investigate natural and forced convection condensation using three-dimensional pin fin structures of new geometries and fin parameters. The test specimens are fabricated by SLM as it provides the design freedom to produce structures with complex geometries and good dimensional accuracy. A condensation chamber is developed to study the natural convection condensation on fin arrays whereas forced convection condensation in enhanced tubes is investigated using a two-phase flow facility. Steam and R134a are used as the working fluids.

For natural convection condensation, three-dimensional conical, sinusoidal and cylindrical pin fins of different fin heights and fin pitches are investigated and comparisons are made against the equivalent two-dimensional fins. Visualisation studies are also performed to determine the liquid retention height on the fin structures. The results show that three-dimensional pin fin structures exhibit better heat transfer performance than the equivalent two-dimensional fins. This is mainly due to the lower condensate retention height and the significant surface tension effects. In addition, the conical pin fin surfaces also show the highest heat transfer performance as compared to other three-dimensional pin fins.

A theoretical model which accounts for the effects of surface tension and gravitational forces on the liquid film is developed to evaluate the condensation performance of a conical pin fin. The modelling results validated the existence of a thin liquid film region near the fin tip. In addition, due to the concave trough of the liquid pool, another thin liquid film region is produced near the fin base. The surface tension force also reduces the film thickness in the circumferential direction. These mechanisms have resulted in the significant heat transfer enhancements of the conical pin fin structure.

For forced convection condensation, the condenser tubes with conical and domed-shape pin fins were fabricated by SLM. These condenser tubes show good integrity and are able to sustain high pressure operation. This is also the first time the SLM technique is used to produce enhanced tubes for improving forced convection condensation with high pressure refrigerant. The experiments are conducted using R134a as the working fluid and the effects of refrigerant mass flux, vapour quality, circumferential fin pitch and longitudinal fin pitch on the heat transfer coefficient and

pressure drop are investigated. It is found that the heat transfer coefficients of the conical pin fin tubes increase with increasing vapour quality and mass flux and these values are also significantly higher than those of the plain tubes. Both circumferential and longitudinal fin pitch were found to significantly affect the heat transfer coefficient of the conical pin fin tubes whereas the pressure drop values are affected only by the change in the circumferential fin pitch. Based on the boundary layer approach, a semi-empirical model is developed to predict the Nusselt numbers of the conical pin fin tubes. Relatively reasonable predictions are achieved with an overall mean absolute error of 10.5%.

Preface

The motivation to pursue the PhD degree in NTU stemmed from my personal desire to obtain an in-depth understanding of two-phase flow and heat transfer. Undeniably, this has been my favourite engineering topic since I first completed an undergraduate final year project in this field, which was also supervised by Prof. Leong, more than nine years ago. Having worked in the defence and HVAC industries for several years, I have realised the importance of efficient condenser design on the overall performance of a refrigeration system. This is especially relevant to a tropical country like Singapore, where her relatively high ambient temperature limits the condenser's heat rejection capacity. These reasons have led me to embark on this PhD research.

The years of my PhD studies have been fruitful and rewarding. I have benefited substantially in terms of the knowledge I have gained not only in the field of heat transfer but also in the areas of additive manufacturing and numerical modelling, which were new to me prior to this work. Having to pursue this PhD on a part-time basis while taking on a full-time position as a researcher in NTU has also widened my research horizon and honed my organisational and time management skills. Nonetheless, this work would not be completed without those who have helped and taught me along the way. To these people, this thesis is humbly dedicated.

Acknowledgements

I would like to express my heartfelt gratitude towards my supervisor, Prof. Leong Kai Choong, for providing me the opportunity to pursue a research appointment in NTU and for carrying out this PhD research work. This research work would not have been possible without his dedicated guidance and encouragement throughout the course of my PhD. I would also like to thank my co-supervisor, Prof. Wong Teck Neng, for his advice and insightful suggestions during the various discussions. In addition, I would also like to thank him for the providing me the opportunity to continue my research appointment in NTU.

I would also like to thank my fellow colleagues, Dr. Wang Xuwen (former Research Fellow in NTU), Dr. Wong Kin Keong (former PhD student of Prof. Leong), Messrs. Ranjith Kandasamy (Research Associate) and See Yao Song (PhD student of Prof Leong) for their support during my research work.

Special thanks also go to Mr. Chia Yak Khoong, Assistant Manager and Technician-in-Charge of the Heat Transfer Laboratory for his technical support and continuous help on issues related to the test facilities. I would also like to express my appreciation to Mr. Yuan Kee Hock of the Heat Transfer Laboratory and Mr. Foo Jong Hin of the Thermal and Fluids Laboratory for their help in handling the purchases related to this research. Mr. Daniel Yeo Yin Ping from the Future of Manufacturing Lab 1 had also provided much support on issues related to 3D printing.

I would like to express my appreciation to the School of Mechanical and Aerospace Engineering of Nanyang Technological University, Singapore for providing a conducive environment to conduct my research work. I would also like to acknowledge the National Research Foundation, Prime Minister's Office, Singapore for the financial support of the SLM 250 selective laser melting equipment housed in the Singapore Centre for 3D Printing which I have used extensively in this research. Last but not least, I would also like to show my deepest appreciation to my family and friends for their support and encouragement throughout the course of my PhD studies.

Contents

List of Figures

List of Tables

Nomenclature

A	area (m^2)
A_t	total heat transfer area (mm^2)
Bo	Bond number
D_h	hydraulic diameter (m)
d_b	fin base diameter (mm)
d_i	inner tube diameter (mm)
d_o	outer tube diameter (mm)
f	Fanning friction factor
Fr	Froude number
g	gravitational acceleration (m/s^2)
h	heat transfer coefficient ($W/m^2{\cdot}K$)
h_{ave}	average heat transfer coefficient ($W/m^2{\cdot}K$)
h_{fg}	latent heat of vaporization (J/kg)
H	enthalpy of refrigerant (J/kg)
H_{ave}	condensate retention height (mm)
J_G	dimensionless vapour velocity
k	thermal conductivity ($W/m{\cdot}K$)
l	fin height (mm)
m	mass flow rate (kg/s)
m_{ref}	refrigerant mass flux ($kg/m^2{\cdot}s$)
$\dot{m}_{ref}$	refrigerant mass flow rate (kg/s)
Nu	Nusselt number
p	fin pitch (mm)

p_c	circumferential fin pitch (rad)
p_l	longitudinal fin pitch (mm)
P	pressure (bar)
ΔP	pressure drop (bar)
ΔP_{ave}	average pressure drop (bar)
Pr	Prandtl number
q''	heat flux (W/m^2)
Q	heat rate (W)
Re	Reynolds number
Re_c	critical Reynolds number
Re_{eq}	equivalent Reynolds number
T	temperature (ºC)
u	velocity (m/s)
$u*$	friction velocity (m/s)
v	specific volume (m^3/kg)
x	vapour quality
We	Weber number
X_{tt}	Martinelli parameter
y^+	dimensionless distance

Greek Symbols

β	circumferential-to-longitudinal fin pitch ratio
ε	surface area enhancement factor
ρ	density (kg/m^3)
μ	dynamic viscosity (kg/m·s)

η	thermal enhancement factor
η_1	efficiency index
σ	surface tension (N/m)
τ	shear stress (Pa)
ψ	dimensionless parameter defined in Eq. (2-8)
φ	condensate retention angle (rad)
θ	angle (rad)
ϕ	two-phase multiplier
δ	liquid film thickness (mm)
ν	kinematic viscosity (m^2/s)

Subscripts

ave	average
c	cold
h	hot
i	internal
in	in
out	out
sat	saturation
f	fluid
g	vapour
evp	evaporator
ref	refrigerant
s	specimen
w	wall

List of Publications

A. Journal papers

A.1 Journal papers arising from this thesis

1. **Ho, J.Y.**, Leong, K.C., Wong, T.N., Forced convection condensation of R134a in three-dimensional conical pin fin tubes, *International Journal of Heat and Mass Transfer*, Vol. 144, Article 118599, (2019).

2. **Ho, J.Y.**, Leong, K.C, Filmwise condensation of steam on pin fin arrays fabricated by selective laser melting, *Defect and Diffusion Forum,* Vol. 390, pp. 71-82 (2019).

3. **Ho, J.Y.**, Leong, K.C., Wong, T.N., Filmwise condensation of steam on sinusoidal pin fin arrays: Effects of fin height and fin pitch, *International Journal of Heat and Mass Transfer*, Vol. 130, pp. 1004-1015 (2019).

4. **Ho, J.Y.**, Wang, X.W., Leong, K.C., Filmwise condensation of steam on vertical plates with novel pin fin arrays produced by selective laser melting, *International Journal of Heat and Mass Transfer*, Vol. 126, pp. 652-666 (2018).

5. Wang, X.W., **Ho, J.Y.**, Leong, K.C., Wong, T.N., Condensation heat transfer and pressure drop characteristics of R-134a in horizontal smooth tubes and enhanced tubes fabricated by selective laser melting, *International Journal of Heat and Mass Transfer*, Vol. 126, pp. 949-962 (2018).

A.2 Journal papers related to this thesis

6. **Ho, J.Y.**, Leong, K.C., Wong, T.N., Experimental and numerical investigation of forced convection heat transfer in porous lattice structures produced by selective laser melting, *International Journal of Thermal Sciences*, Vol. 137, pp. 276-287 (2019).

7. Wang, X.W., **Ho, J.Y.**, Leong, K.C., An experimental investigation of single droplet impact cooling on hot enhanced surfaces fabricated by selective laser melting, *International Journal of Heat and Mass Transfer*, Vol. 120, pp. 652-670 (2018).

8. **Ho, J.Y.**, Leong, K.C., Cylindrical porous inserts for enhancing the thermal and hydraulic performance of water-cooled cold plates, *Applied Thermal Engineering*, Vol. 121, pp. 863-878 (2017).

9. Leong, K.C., **Ho, J.Y.**, Wong, K.K., A critical review of pool and flow boiling heat transfer of dielectric fluids on enhanced surfaces, *Applied Thermal Engineering*, Vol. 112, pp. 999-1019 (2017).

10. **Ho, J.Y.**, Wong, K.K., Leong, K.C., Wong, T.N., Convective heat transfer performance of airfoil heat sinks fabricated by selective laser melting, *International Journal of Thermal Sciences*, Vol. 114, pp. 213-228 (2017).

11. Wong, K.K., **Ho, J.Y.,** Leong, K.C. and Wong, T.N., Fabrication of heat sinks by Selective Laser Melting for convective heat transfer applications, *Virtual and Physical Prototyping*, Vol. 11, pp. 159-165 (2016).

12. **Ho, J.Y.**, Wong, K.K., Leong, K.C., Saturated pool boiling of FC-72 from enhanced surfaces produced by selective laser melting. *International Journal of Heat and Mass Transfer*, Vol. 99, pp. 107-121 (2016).

13. **Ho, J.Y.**, Leong, K.C., Yang, C., Saturated pool boiling from carbon nanotube coated surfaces at different orientations, *International Journal of Heat and Mass Transfer*, Vol. 79, pp. 893-904 (2014).

B. Conference papers

B.1 Conference papers arising from this thesis

1. Wang, X.W., **Ho, J.Y.**, Leong, K.C., Wong, T.N., Condensation heat transfer and pressure drop characteristics of R134a in horizontal smooth tubes and enhanced tubes fabricated by selective laser melting, *Proceedings of the* 16*th International Heat Transfer Conference, IHTC*-16, pp. 2496-2484, August 10-15, Beijing, China (2018).

2. **Ho, J.Y.**, Leong, K.C., Filmwise condensation of steam on pin fin arrays fabricated by Selective Laser Melting, 14*th* *International Conference on Diffusion in Solids and Liquids (DSL*2018*)*, 25-29 June, Amsterdam, The Netherlands.

3. **Ho, J.Y.**, Leong, K.C., Filmwise condensation on micro-fin surfaces produced by selective laser melting, *Proceedings of the* 13*th International Conference on Heat Transfer, Fluid Mechanics and Thermodynamics* (*HEFAT*2017), pp. 85-90, 17-19 July, Portorož, Slovenia (2017).

B.2 Conference papers related to this thesis

4. **Ho, J.Y.**, Leong, K.C. and X.W. Wang, Heat transfer characteristics of a topology optimized structure for PCM-based thermal management devices, *Proceedings of the* 14*th International Conference on Heat Transfer, Fluid Mechanics and Thermodynamics* (*HEFAT*2019), 22-24 July 2019, Wicklow, Ireland.

5. **Ho, J.Y.**, Wong, K.K., Leong, K.C., Wong, T.N., Tor, S.B., Customised design of a water-cooled cold plate fabricated by selective laser melting, 3*rd* *International Conference on Progress in Additive Manufacturing (Pro-AM* 2018*)*, 14-17 May, Singapore (2018).

6. **Ho, J.Y.**, Leong, K.C., Enhanced thermal performance of a water-cooled cold plate with porous inserts fabricated by selective laser melting, *Proceedings of the* 13*th International Conference on Heat Transfer, Fluid Mechanics and Thermodynamics* (*HEFAT*2017), pp. 860-865, 17-19 July, Portorož, Slovenia, (2017).

7. Wong, K.K., **Ho, J.Y.**, Leong, K.C., Wong, T.N., Convective heat transfer performance of staggered heat sink arrays fabricated by selective laser melting, 2*nd International Conference on Progress in Additive Manufacturing (Pro-AM* 2016*)*, 16-19 May, pp. 67-72, Singapore (2016).

8. **Ho, J.Y.**, Wong, K.K., Leong, K.C., Yang, C., Enhanced nucleate pool boiling from microstructured surfaces fabricated by selective laser melting, *Proceedings of the ASME* 2016 5*th Micro/Nano Heat and Mass Transfer International Conference, MNHMT*2016, p. MNHMT2016-6616, January 3-6, Biopolis, Singapore (2016).

9. **Ho, J.Y.**, Wong, K.K., Leong, K.C., Yang, C., Nucleate pool boiling from selective laser melted microgrooves/microcavities surfaces with HFE-7000, *Proceedings of the* 1*st Thermal and Fluid Engineering Summer Conference, TFESC*, pp. 1917-1928, August 9-12, New York, USA (2015).

10. **Ho, J.Y.**, Leong, K.C., Yang, C., Pranoto, I., An experimental study of carbon nanotube coatings for pool boiling heat transfer enhancement, *Proceedings of the* 15*th International Heat Transfer Conference, IHTC*-15, pp. 6409-6417, August 10-15, Kyoto, Japan (2014).

Chapter 1 - Introduction

1.1 Overview

Heterogeneous condensation is a phase change process which occurs when saturated or superheated vapour comes into contact with a surface that is maintained at a subcooled temperature. Filmwise condensation and dropwise condensation are the two modes of heterogeneous condensation. In filmwise condensation, a continuous liquid film wets the surface whereas in dropwise condensation, the surface is covered by discrete liquid droplets. Even though dropwise condensation exhibits higher heat transfer rates, it has not been widely implemented at the industrial level as it is challenging to sustain long-term dropwise condensation [1, 2]. Therefore, filmwise condensation remains the dominant mode of condensation heat transfer in many industrial systems such as in power generation plants, desalination plants, automotive air-conditioning and electronic cooling systems [3].

Natural convection condensation on external surfaces and forced convection condensation in tube channels are commonly used in engineering systems. In natural convection condensation, the cooling surface is surrounding by quiescent vapour and the liquid film flow is driven by gravity and surface tension forces. Examples of its applications are in the shell-side of shell-and-tube heat exchangers [4] and in the condensers of two-phase thermosyphons [5]. On the other hand, forced convection condensation is also widely used in the tube-side of the refrigerant condensers [6]. In this application, refrigerant vapour is directed through and condensed within the tube channels. As the velocity of the vapour is large, it assists in the removal of the condensate.

In a recent market research, it was reported that the global value of the heat exchangers market was US$13.5 billion in 2017 and was projected to reach US$22.59 billion by 2023 [7]. For condensers used in the automotive industry alone, it was also forecasted that its global market value could reach more than US$12 billion by 2025 [8]. Due to the widespread application of condensers, there is a continuous demand to produce higher performance condensers to improve system efficiency. From the manufacturing perspective, it is also important to reduce production costs and increase production output of the condensers so as to meet the global demands. There is a need, therefore, for more research to further improve condensation heat transfer rates, to achieve a better understanding of the thermal transport mechanisms and to develop new manufacturing techniques to produce new structures for enhancing condensation.

1.1.1 Natural convection condensation heat transfer on extended surfaces

The use of finned structures is an efficient method in enhancing natural convection condensation. Increases in heat transfer area and surface tension force induced by the fins are the dominant factors that affect the condensation performances. In addition, condensate film characteristics are also significantly influenced by the fin parameters such as fin geometry, dimensions and arrangements. Condensation on two-dimensional fin structures such as integral [9] and longitudinal [10] fins, as shown in Fig. 1-1 (a), has been extensively researched in the past few decades. The effects of fin pitch and height on the condensate retention [11, 12] of these fin structures are well-established and several heat transfer models [13, 14] which account for the surface tension and gravitational forces on integral-fin tubes have been developed. In comparison, relatively fewer investigations on three-dimensional fin structures such as pin fins [15] and enhanced fin tubes (EFTs) [16] have been reported. The use of pin fins, as shown in Fig. 1-1 (b), was first reported by Briggs [17] for condensing R-113 and steam. More recently, Ali and Briggs [18] showed that the condensation heat fluxes on pin fin tubes are higher than those on the equivalent integral-fin tubes. These investigations suggest the promising use of three-dimensional fin structures as compared to conventional two-dimensional fins for enhancing condensation.

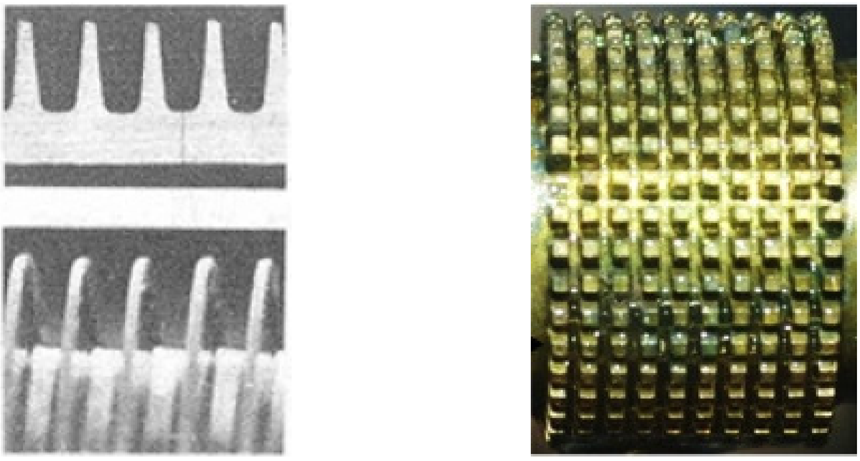
(a) (b)

Fig. 1-1 (a) Conventional two-dimensional integral-fin tube [6] and (b) three-dimensional pin fin tube [19].

1.1.2 Forced convection condensation heat transfer in enhanced tubes

Forced convection condensation heat transfer in confined channels such as plain circular tubes is closely related to the two-phase flow structures. An example of the two-phase flow patterns during condensation in a horizontal plain tube at high mass velocity is shown in Fig. 1-2. As the flow pattern changes from annular flow at high vapour quality to slug and plug flows at low vapour quality, the heat transfer mechanism correspondingly varied from vapour-shear dominated to gravity dominated. In the vapour-shear dominated regime, the condensate drainage is driven by the local shear stress at the liquid-vapour interface whereas in the gravity dominated regime, gravitational force is mainly responsible for the condensate drainage.

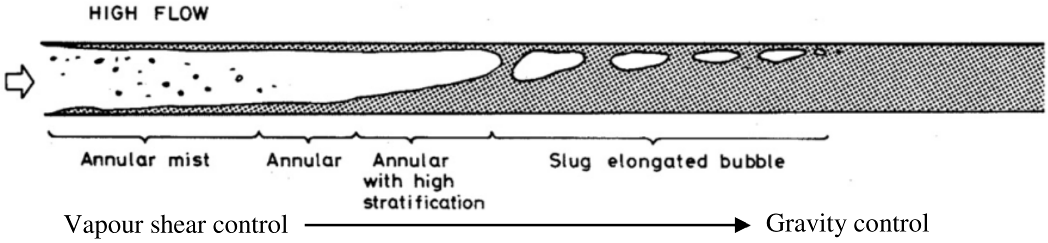

Fig. 1-2 Two-phase flow patterns in a horizontal plain tube during forced convection condensation [20].

Similar to natural convection condensation, enhancements of forced convection condensation heat transfer can be achieved with geometrically enhanced features on the internal tube walls. The enhanced features which were extensively investigated include helical micro-fins [21], herringbone structures [22], and enhanced heat transfer (EHT) tubes [23], as shown in Fig. 1-3 and their thermal-hydraulic performances had been characterised. For instance, the helical micro-fins were characterised by moderately high heat transfer enhancements and low penalty in pressure drop whereas the herringbone structures exhibited higher heat transfer coefficients than the helical micro-fins at high vapour velocities. The increase in the effective heat transfer area, turbulence induced in the liquid film and redistribution of the condensate film are some mechanisms suggested for their heat transfer enhancements [24].

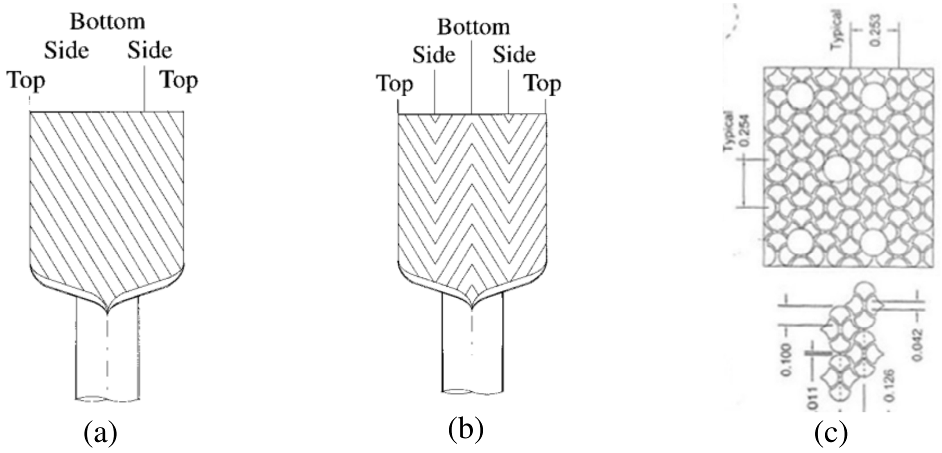

(a) (b) (c)

Fig. 1-3 Schematic diagrams of (a) helical micro-fins [22], (b) herringbone structures [22] and (c) EHT tubes [25].

1.1.3 Selective laser melting technique

Selective laser melting (SLM) is a branch of additive manufacturing which enables functional metallic components to be fabricated. In SLM, a layer of metallic powder material is first deposited onto a substrate of similar material composition to ensure good bonding onto the substrate surface. As shown in Fig. 1-4, the laser selectively scans a cross section predefined by the computer-aided design (CAD) software which in turn melts and fuses the powder. A three-dimensional structure can be produced by melting consecutive layers of powder over each other. Due to its capability to customise parts without the need of making new casting moulds, production lead-time can be reduced and manufacturing efficiency can be improved. In addition, SLM also enables the design freedom to produce complex structures which are difficult to achieve by conventional manufacturing techniques. However, components fabricated by SLM usually have high surface roughness. In addition, due to the laser melting process and the powder distribution sizes, surface features with dimensions smaller than 100 µm are also difficult to achieve.

Materials such as stainless steel, titanium and aluminium alloy can be used in the SLM process. Among these materials, using aluminium alloy as the base powder for producing heat transfer devices is preferred due to its high thermal conductivity, light weight and resistance to corrosion.

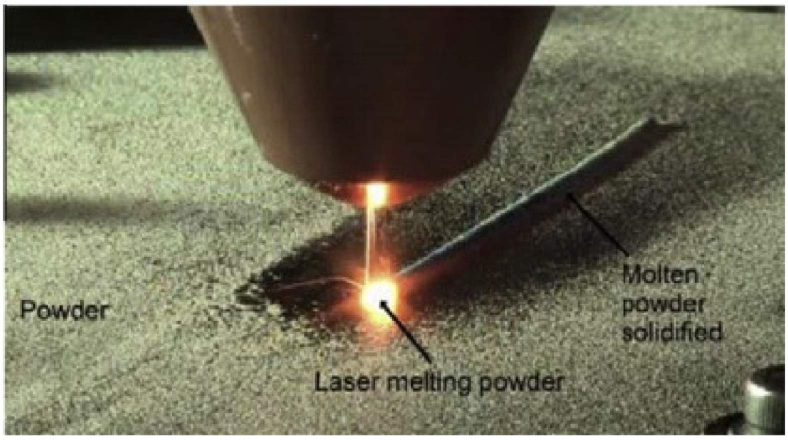

Fig. 1-4 Laser melting process in SLM [26].

1.2 Motivation of research

The preceding sections provide an overview of the current developments in natural and forced convection condensation whereas a comprehensive literature survey on this topic is presented in Chapter 2. These reviews show that fin structures have been explored by many researchers and there has been an increasing interest on the use three-dimensional pin fins to promote condensation heat transfer. However, likely due to the limitation in conventional manufacturing techniques, existing three-dimensional fin structures [shown in Fig. 1-1 (b)] are mainly square or rectangular pin fins and there are few geometrical variations. On the other hand, despite the potential of three-dimensional fin structures in enhancing natural convection condensation, the use of these millimetre size structures for improving forced convection condensation in tube channels has not been reported. Three-dimensional pin fin structures can induce significantly large surface tension force and promote condensate drainage. Furthermore, the use of millimetre size pin fins may also allow the fin structure to protrude out of the thick condensate film near the tube wall and contact the vapour core to further promote condensation.

These potential advantages of three-dimensional pin fins thus provide the motivation of this thesis to develop new 3D fins with enhanced thermal performances by exploring the use of the selective laser melting technique.

1.3 Objectives and Scope

The objectives of this research are to investigate the possible enhancements of natural and forced convection condensation using three-dimensional pin fin structures of new geometries and fin parameters. The selective laser melting (SLM) technique shall be used to fabricate the test specimens as it provides the design freedom to produce structures with complex geometries. Through experimental and theoretical investigations, this research also aims to achieve fundamental understanding of the condensation heat transfer mechanisms of the various enhanced structures.

The scope of this thesis includes the following:

1. Design and fabrication of two-dimensional and three-dimensional fin arrays by SLM. These fin geometries will take advantage of mechanisms such as surface tension effects and improved condensate drainage for enhanced condensation heat transfer.
2. Performing natural convection condensation experiments using steam as the working fluid to characterise the heat transfer performances of three-

dimensional fins. Comparisons shall also be made against the equivalent two-dimensional fins. The effects of fin geometry, fin height and fin pitch will be investigated. The condensate retention height on these fin structures will be measured and analysed.

3. Development of a theoretical model which takes into account the effects of surface tension and gravitational forces on the liquid film on the three-dimensional fins. As the liquid film characteristics are directly related to the thermal performances of the three-dimensional fins, this model aims to shed light into the dominant thermal transport mechanisms involved.
4. Performing forced convection condensation experiments using circular tubes with three-dimensional pin fin structures. The R134a refrigerant, which is commonly used in refrigeration and air-conditioning systems, will be employed as the working fluid. The effects of fin geometries, circumferential and longitudinal fin pitch will be investigated under different refrigerant mass fluxes and vapour qualities.
5. Development of a semi-empirical model for forced convection condensation of three-dimensional pin fin tubes. This model will also account for the effects of fin pitch, vapour quality and mass flux.

1.4 Outline of thesis

This thesis consists of eight chapters. A brief introduction and motivation of this thesis is outlined in Chapter 1. Chapter 2 provides the theoretical background and literature review on the developments of natural and forced convection condensation with plain and enhanced surfaces. Recent progress on enhanced heat transfer surfaces fabricated using the SLM technique is also surveyed. Chapter 3 presents the test specimen designs and illustrates the fabrication techniques employed to produce these specimens. The geometrical parameters of the test specimens are also characterised. In Chapter 4, details of the test facilities developed for the investigation of natural and forced convection condensate are provided and the experimental methodology are discussed. Chapter 5 reports the natural convection condensation experimental results. The heat transfer performances of the two- and three-dimensional fins of equivalent geometries are compared and the effects of fin geometry, fin pitch and fin height are examined. The visualisation studies on the condensate retention height on the different fin structures are also presented. Chapter 6 focuses on the development of the theoretical model of the liquid film thickness on a three-dimensional pin fin structure and the theoretical predictions are compared against the experimental results. In Chapter 7, the forced convection condensation heat transfer and pressure drop performances of three-dimensional pin fin tubes are discussed and analysed. In addition, a semi-empirical model for the condensation heat transfer inside conical pin fin tube is also developed and validated. Finally, the various findings arising from this thesis are summarised in Chapter 8 and the recommendations for future research work are discussed.

Chapter 2 – Theoretical Background and Literature Review

2.1 Natural convection condensation

2.1.1 A theoretical background on filmwise condensation on plain surfaces

The theoretical model for laminar filmwise condensation on a plain vertical plate was first presented in the pioneering work of Nusselt [27]. In his model, the momentum transport of the condensate film was assumed to be driven only by molecular diffusion and gravitational force. On this basis, the momentum equation for the condensate film was reduced to Eq. (2-1), where the z-axis is in the direction of gravitational acceleration, y-axis is the direction perpendicular to the surface and u_z is the velocity vector parallel to the surface. Following the one-dimensional heat conduction assumption across the condensate film and assuming that the heat transfer rate by conduction is equal to the latent heat removed from the vapour, the condensation heat flux (q'') was obtained by Eq. (2-2). Solving Eqs. (2-1) and (2-2) and taking an arithmetic mean over the plate length gives the average Nusselt number (Nu) for condensation on vertical plate as shown in Eq. (2-3). With a similar approach, Nu_d for condensation on a horizontal tube can be derived as Eq. (2-4), where d denotes the diameter of the tube.

$$\frac{d^2u_z}{dy^2} = -\frac{(\rho_f-\rho_g)g}{\mu_f} \tag{2-1}$$

$$q'' = h_{fg}\rho_f \frac{d}{dz}\left[\int_0^{\delta} u_z\, dy\right] = \frac{k_f}{\delta}(T_{sat} - T_w) \tag{2-2}$$

$$\mathrm{Nu} = 0.943\left[\frac{\rho_f(\rho_f-\rho_g)gh_{fg}L^3}{\mu_f k_f(T_{sat}-T_w)}\right]^{1/4} \tag{2-3}$$

$$\mathrm{Nu}_d = 0.725\left[\frac{\rho_f(\rho_f-\rho_g)gh_{fg}d^3}{\mu_f k_f(T_{sat}-T_w)}\right]^{1/4} \tag{2-4}$$

In the derivation of Eqs. (2-3) and (2-4), the condensate film was assumed to be at saturation temperature. In reality, as the liquid film is in contact with the wall, subcooling of the liquid film occurs. In addition, when the vapour is at superheated temperature, the condensation surface is required to cool the vapour down to saturation temperature before the phase change process begins. By considering these effects of liquid film subcooling and superheated vapour, Rohsenow [28] modified Eq. (2-3) by replacing h_{fg} of Eq. (2-5) with h_{fg}^*. In this equation, the second term on the right-hand side of the equation accounts for the liquid film subcooling and the last term incorporates the effects of vapour superheat. However, since the h_{fg} values are often several orders of magnitude larger than $c_{p,f}$ and $c_{p,g}$, it can be deduced from Eq. (2-5) that the effects of liquid subcooling and vapour superheat are small.

$$h_{fg}^* = h_{fg} + 0.68c_{p,f}(T_{sat} - T_w) + c_{p,g}(T_g - T_{sat}) \tag{2-5}$$

For a smooth surface under laminar flow condition, the condensate film was sometimes observed to be wavy. The formation of waves on the liquid film may result in 10 – 25 % improvements in the heat transfer coefficients as compared to the values predicted by Nusselt [29]. Grimley [30] suggested that these waves were formed above the critical Reynolds number (Re_c) defined in Eq. (2-6). However, as the mechanisms of enhancement due to wave formation were difficult to quantify, a mean factor of 1.15 was typically multiplied to Eq. (2-3) to account for this effect.

$$\mathrm{Re}_c = 0.392\left[\left(\frac{\sigma_f}{\rho_f g}\right)^{1/2}\left(\frac{g}{\nu_f}\right)^{1/3}\right]^{3/4} \tag{2-6}$$

The effects of liquid film inertia were first examined by Sparrow and Gregg [31, 32]. Using the boundary layer theory treatment and employing similarity transformation, they obtained the modified Nusselt number (Nu) which includes the effect of the liquid film inertia and can be expressed as a function of the dimensionless parameters shown in Eq. (2-7). It should be noted that, in this equation, $\mathrm{Nu}_{\mathrm{Nu}}$ denotes the original Nusselt number proposed in Ref. [27]. On the other hand, as the liquid film flows downwards, it experienced an interfacial shear force by the surrounding vapour which retards its downward motion. Chen [33, 34] analysed this effect by approximating the interfacial shear stress and solving only the liquid-side momentum and energy equations. They arrived at a Nu relationship which is similar to that of Eq. (2-7). Subsequently, Koh [35] and Koh et al. [36] included the effects of interfacial shear more accurately by simultaneously solving both the liquid-side and vapour-side governing equations and by employing the continuity of shear stress along the liquid-vapour interface. From their investigation, it was concluded that the effects of liquid film inertia and interfacial shear (when the surrounding vapour was stagnant) on Nu were only significant when the Prandtl numbers were much smaller than 1 such as those of liquid metals or when $\frac{c_{p,f}(T_{sat}-T_w)}{h_{fg}}$ is much larger than 0.1. For common working fluids such as steam, these effects were negligible and the Nusselt film theory can adequately predict the condensation phenomenon.

$$\frac{\mathrm{Nu}}{\mathrm{Nu}_{\mathrm{Nu}}} = f\left(\frac{c_{p,f}(T_{sat}-T_w)}{h_{fg}}, \mathrm{Pr}\right) \tag{2-7}$$

As the condensate flows downstream of a vertical plate or circumferentially around a horizontal tube, the increase in condensate thickness in the streamwise direction will result in varying curvature of the condensate surface. This change in curvature will induce surface tension force which may in turn affects the liquid film and heat transfer. Krupiczka [37] examined the effects of surface tension on natural convection condensation on a horizontal tube and showed that the local heat transfer coefficient (h_l) depends on the surface tension force (σ) and tube radius (r) which can be expressed as a dimensionless parameter (ψ) as shown in Eq. (2-8). For a constant σ, ψ increases with decreasing r which resulted in the increase in h_l on the lower part of the tube. However, the effect of surface tension is only significant when ψ is sufficiently large, *viz.*, more than 1.

$$\psi = \frac{9}{4}\left(\frac{\sigma}{\rho_f g r^2}\right)\left(\frac{\nu^2}{r^3 g h_{fg} c_{p,f} \mathrm{Pr}(T_{sat}-T_w)}\right)^{1/4} \qquad (2\text{-}8)$$

2.1.2 Filmwise condensation on extended surfaces I: Liquid film and heat transfer models

Similar to natural convection condensation on plain surfaces, natural convection condensation on extended surfaces can be modelled by solving the liquid film equation. However, unlike plain surfaces, the presence of fin structures may vary the curvature of the liquid film significantly and induce surface tension force on the liquid film. As the surface tension effect influences the condensate flow and heat transfer rate from the fins, this factor has to be considered. Gregorig [38] first recognised the existence of surface tension forces which pulled the liquid film from the fin tip to the concave trough of a vertical fluted tube. Subsequently, models of laminar film condensation on fin structures which consider both surface tension and gravitational forces were reported by Hirasawa et al. [39]. Fig. 2-1 shows a schematic diagram of a vertical plate with longitudinal half-triangular fins which was modelled by Hirasawa et al. [39]. In this figure, the *x*-axis is in the direction of gravity, *y*-axis is the direction along the fin surface and *z*-axis is in the direction perpendicular to the fin surface. In the *x*-direction, the liquid flow is driven only by gravity and therefore, by neglecting the inertia term, the momentum equation is written as Eq. (2-9). On the other hand, due to the change in liquid film curvature along the surface of the fin in the *y*-direction, surface tension was viewed as the main driving force which gives the *y*-direction momentum equation as Eq. (2-10), where p is induced by the change in curvature of the liquid film and can be obtain from Eq. (2-11). As the liquid film is thin, the changes in the velocity and temperature in the *x*- and *y*-directions are small and therefore, it can be assumed that these quantities only vary in the *z*-direction. By neglecting the convection term, and taking into consideration the above, the energy equation of Eq. (2-12) is obtained. Furthermore, in assuming that the additional liquid mass flux generated is due to conduction heat transfer across the liquid film, the continuity equation is written as Eq. (2-13). Finally, Eqs. (2-9), (2-10) and (2-12) are integrated and substituted into Eq. (2-13) to obtain the equation for the liquid film thickness (δ) as shown in Eq. (2-14). The first term on the left-hand side of Eq. (2-14) denotes the effect of gravity whereas the second term is the influence of surface tension on the condensate. The local heat flux (q_l'') and local heat transfer coefficient (h_l) are related to the liquid film thickness and can be computed by Eqs. (2-15) and (2-16).

$$\mu_f \frac{\partial^2 u_x}{\partial z^2} + \rho_f g = 0 \tag{2-9}$$

$$\mu_f \frac{\partial^2 u_y}{\partial z^2} - \frac{\partial p}{\partial y} = 0 \tag{2-10}$$

$$p = p_s - \sigma\kappa_y = p_s - \frac{\sigma\left(\partial^2\delta/\partial y^2\right)}{\left[1+\left(\partial\delta/\partial y\right)^2\right]^{3/2}} \tag{2-11}$$

$$k_f\frac{\partial^2 T}{\partial z^2} = 0 \tag{2-12}$$

$$\frac{\partial}{\partial x}\int_0^{\delta} u_x\, dz + \frac{\partial}{\partial y}\int_0^{\delta} u_y\, dz = \frac{k_f\Delta T}{h_{fg}\rho_f\delta} \tag{2-13}$$

$$\frac{\rho_f g}{3\mu_f}\frac{\partial\delta^3}{\partial x} + \frac{\sigma}{3\mu_f}\frac{\partial}{\partial y}\left[\delta^3\frac{\partial}{\partial y}\left\{\frac{\partial^2\delta/\partial y^2}{\left[1+\left(\partial\delta/\partial y\right)^2\right]^{3/2}}\right\}\right] = \frac{k_f\Delta T}{\rho_f h_{fg}}\frac{1}{\delta} \tag{2-14}$$

$$q_l'' = k_f\frac{\Delta T}{\delta} \tag{2-15}$$

$$h_l = \frac{k_f}{\delta} \tag{2-16}$$

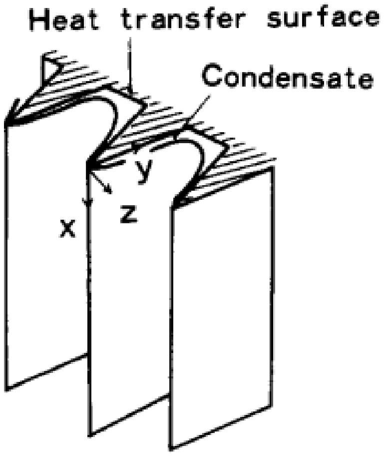

Fig. 2-1 Schematic of vertical plate with longitudinal half-triangular fins [39].

As can be seen from Fig. 2-1, the fin geometry varies along the *y*- and *z*-directions. For the ease of solving the liquid film equation, Eq. (2-14) was transformed to other curvilinear orthogonal coordinate systems which take the geometry of the fin structure into consideration. For instance, Hirasawa et al. [39] set up a parabolic cylindrical coordinate system to investigate the half-triangular fins and Mori et al. [40] adopted a similar coordinate system to model the heat transfer performance of a triangular fin, a wavy fin and flat-bottomed groove fins. An example of the triangular fin is shown in

Fig. 2-2 (a) where the fin is divided into three regions. In Regions I and II where the liquid film curvatures vary, Eq. (2-14) was employed. On the other hand, in Region III the liquid film has a constant curvature and the surface tension term was neglected. Qi et al. [41] proposed a model for involute grooves which is depicted in Fig. 2-2 (b). For Regions I and II where surface tension effects are dominant, Eq. (2-14) was employed in the orthogonal curvilinear system to obtain the liquid film thickness. However, as the influence of surface tension was assumed to be more significant than gravity in these regions, the first term of Eq. (2-14) was neglected. Their results suggested that the involute groove had 50% higher heat transfer rate as compared to the conventional trapezoidal groove and their model shows up to 15% deviation from the experimental results. Honda and Nozu [42], on the other hand, proposed a model for integral finned tubes where Eq. (2-14) was adopted and corrected for the effects of fin geometry, fin spacing and condensate flooding point. More recently, new fin structures of sinuous profiles which consist of convex tip and concave stem were developed by Wang et al. [43] and are shown in Fig. 2-2 (c). By numerically solving the non-dimensional liquid film equation, they determined that the continuous change in curvature of the fin produced a large thin film region near the fin tip. It was deduced that the sinuous fins have higher heat transfer rates as compared to conventional triangular and rectangular fins.

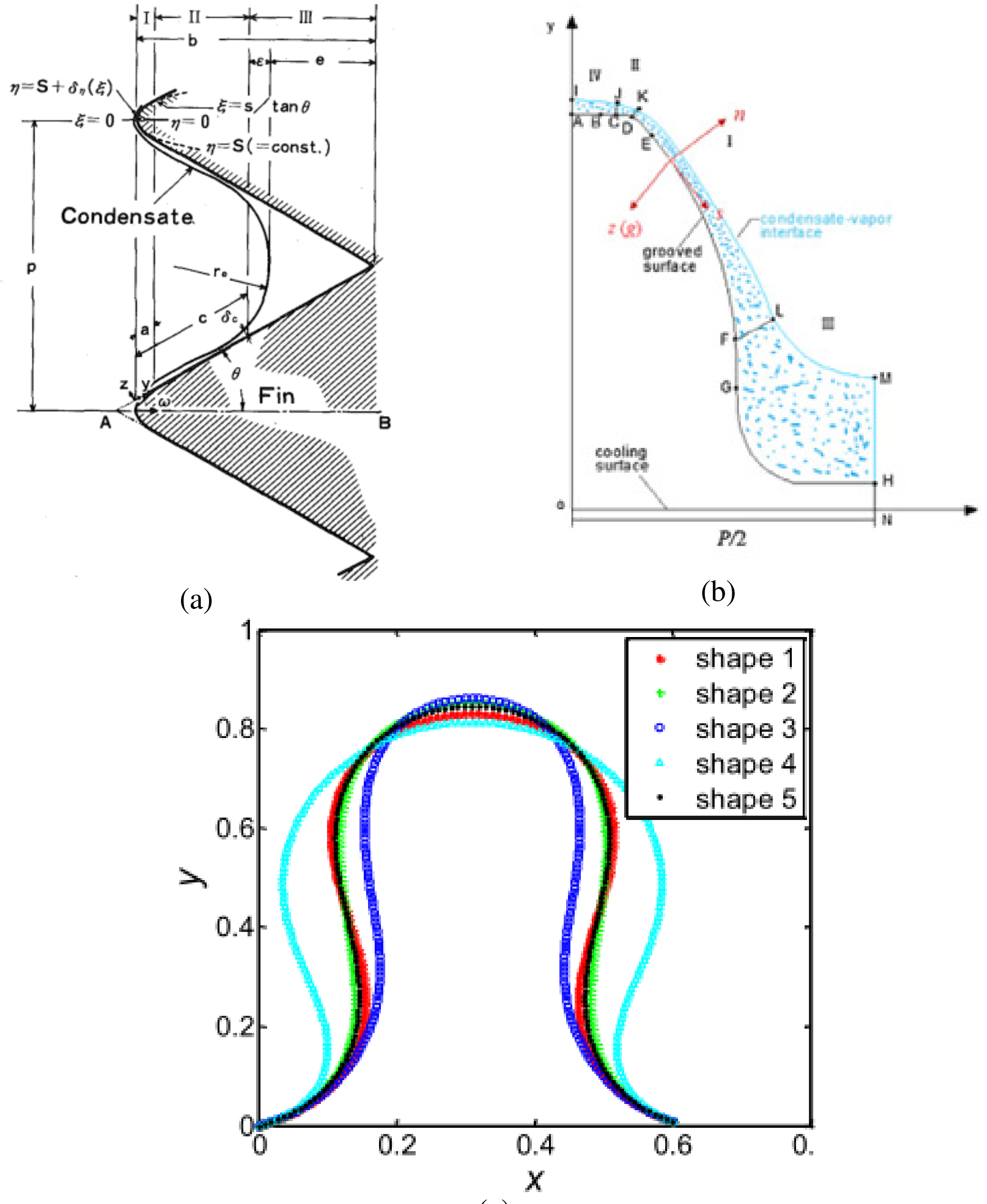

(a)

(b)

(c)

Fig. 2-2 Physical models of (a) triangular fin [40], (b) involute groove [41] and (c) sinusoidal fin [43].

Due to the complexity involved in solving the liquid film equation of Eq. (2-14), several simplified models were proposed. For instance, Adamek and Webb [44] divided the integral-fin structures into surface tension and gravity dominated regions, as shown in Fig. 2-3. In the gravity-dominated region, the Nusselt laminar film theory

[27] was applied. On the other hand, in the surface tension-dominated region, a linear pressure gradient across the condensate film was assumed and the liquid film equation between points i and k was reduced to that of Eq. (2-17), where l_{ik} is the length between the two points, and r_i and r_k are the curvatures at points i and k, respectively. Their model was found to predict the condensation rate of various integral-fin tubes with an accuracy of ±15%.

$$\delta_{ik} = \left[\frac{4k_f \mu_f \Delta T l_{ik}^2}{\rho_f h_{fg} \sigma (1/r_i - 1/r_k)}\right]^{1/4} \qquad (2\text{-}17)$$

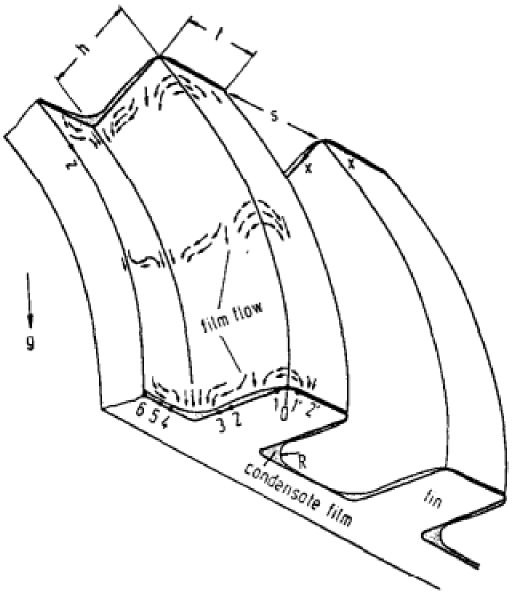

Fig. 2-3 Condensate flow pattern on integral-fin tube [44].

Another simplified model that was developed to predict the condensation heat transfer performances on integral-fin tubes was reported by Rose [45]. He performed a dimensional analysis to establish the relationships between the liquid film thickness and the relevant dimensionless parameters for gravity and surface tension driven flow. The integral-fin tube was divided into fin tip, fin flanks and interfin space regions for the analysis and in each region, the effects of gravity and surface tension effects were considered. Following these procedures, Eqs. (2-18) – (2-20), which give the average heat fluxes at the fin tip, fin flanks and interfin space, respectively, were derived. In these equations, d_o and d_r denote the fin tip and fin root diameters, h_v and h are the mean vertical and radial fin heights and s is the fin spacing. On the other hand, B_t, B_f and B_s are empirical constants that were determined by curve fitting Eqs. (2-18) – (2-20) with the experimental data. Comparison with experimental results showed relatively good accuracy of the model with not more 20% deviation. Subsequently, Briggs and Rose [46] extended Rose's model [45] to account for the change in temperature along the fins. More recently, Ali and Briggs [47] improved the model to predict the condensation heat transfer on pin finned tubes.

$$q_t'' = \left[\frac{\rho_f h_{fg} k_f^3 \Delta T^3}{\mu_f}\left(\frac{0.728^4(\rho_f - \rho_g)g}{d_o} + \frac{B_t \sigma}{t^3}\right)\right]^{1/4} \tag{2-18}$$

$$q_f'' = \left[\frac{\rho_f h_{fg} k_f^3 \Delta T^3}{\mu_f}\left(\frac{0.943^4(\rho_f - \rho_g)g}{h_v} + \frac{B_f \sigma}{h^3}\right)\right]^{1/4} \tag{2-19}$$

$$q_s'' = \left[\frac{\rho_f h_{fg} k_f^3 \Delta T^3}{\mu_f}\left(\frac{(\xi(\phi))^3(\rho_f - \rho_g)g}{d_r} + \frac{B_s \sigma}{s^3}\right)\right]^{1/4} \tag{2-20}$$

2.1.3 Filmwise condensation on extended surfaces II: Condensate flooding

Condensate flooding is a phenomenon in which a thick layer of condensate is retained on the finned structures due to capillary forces. This thick condensate layer completely fills the inter-fin spacing and blankets the whole fin structure. As a result of the large thermal resistance, the heat transfer rate in this region is significantly reduced. An illustration of condensate flooding on an integral-fin tube is shown in Fig. 2-4. The angle from the top of the tube to the point where the fin is fully covered by the condensate is known as the retention angle (φ). In general, higher φ increases heat transfer rate as a smaller area of the surface is flooded.

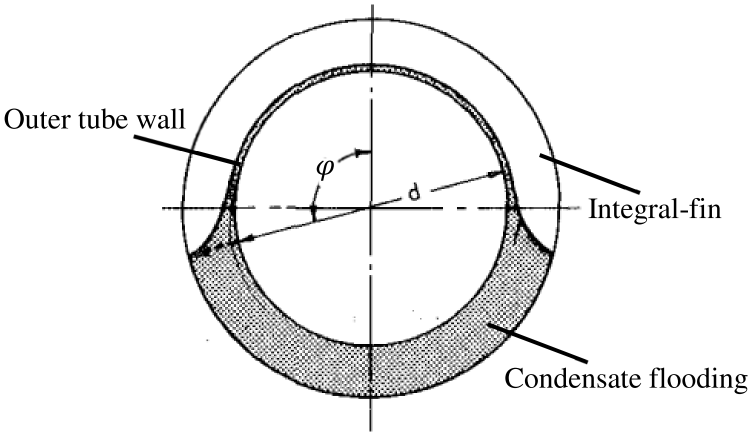

Fig. 2-4 Illustration of condensate flooding and retention angle on an integral-fin tube [48].

Rudy and Webb [11] and Honda et al. [49] conducted experimental investigations using various working fluids which include steam, R-113, methanol and ethylene glycol on integral-fin tubes of different horizontal fin spacings (*b*). By performing a force balance on the retained liquid, they developed theoretical models to predict the condensate flooding angles. For the integral-fin of trapezoidal cross-section, the expression for φ was obtained as Eq. (2-21). Apart from the fin spacing (*b*), φ also depends on the half-angle of the fin tip (θ). For a fin of rectangular cross-section (θ = 0), Eq. (2-21) is reduced to Eq. (2-22). However, it should be noted that Eqs. (2-21) and (2-22) are only valid for $b \leq 2h$, where *h* is the fin height. Yau et al. [48] investigated the condensate flooding angle of integral-fin tubes with drainage strip. It was determined that the drainage strip was efficient in increasing the retention angles. They modified Eq. (2-21) by introducing an empirical constant to account for the effect of drainage strip and obtained Eq. (2-23).

$$\varphi = \cos^{-1}\left(\frac{2\sigma cos\theta}{\rho_f gbr} - 1\right) \tag{2-21}$$

$$\varphi = \cos^{-1}\left(\frac{2\sigma}{\rho_f gbr} - 1\right) \tag{2-22}$$

$$\varphi = \cos^{-1}\left(\frac{0.83\sigma\cos\theta}{\rho_f gbr} - 1\right) \tag{2-23}$$

More recently, the retention angle on condenser tubes with three-dimensional pin fin structures was investigated by Ali and Briggs [50]. It was reported that the better heat transfer performances of the pin fin tubes as compared to the equivalent integral-fin tubes were primarily due to the reduced condensate flooding. Based on his experimental data, Eq. (2-21) was modified to include the effects of circumferential pin fin spacing (S_c) and thickness (t_c) and the model which predicts the condensate flooding angle is presented in Eq. (2-24). In this equation, C is an empirical constant which assumes different values for different fluids. The values of C for water, ethylene glycol and R-113 are 0.25, 0.35 and 0.45, respectively.

$$\varphi = \cos^{-1}\left[\left(1 - C\frac{S_c}{t_c}\right)\left(\frac{2\sigma cos\theta}{\rho_f gbr}\right) - 1\right] \tag{2-24}$$

Finally, it should be noted that for circular tubes and flat plates with the same integral-fin geometries and arrangements, Rudy and Webb [11] determined that their liquid retention heights were also the same. This phenomenon was similarly reported by Ali [51] for circular tubes and flat plates with three-dimensional pin fin structures.

2.1.4 Review on natural convection condensation with enhanced surfaces

The use of fin structures to improve natural convection condensation has been extensively investigated and significant improvements in the condensation heat transfer coefficient were achieved. The magnitude of enhancement was found to depend on the fin geometry, fin type (i.e., two-dimensional or three-dimensional fins), fin pitch, fin height and fin thickness. This is because these fin parameters directly influence the heat transfer mechanisms such as surface tension, gravity driven condensate flow and condensate flooding height. In this section, the progress on the investigations of natural convection condensation with fin structures in the last three decades are reviewed and summarised.

Sukhatme et al. [52] compared the heat transfer coefficients of two-dimensional integral-fin tubes against those of three-dimensional fin tubes using R-11 as the working fluid. The two three-dimensional fin tubes, as shown in Fig. 2-5, are termed Thermoexcel-C and Everfin·Δ and they were fabricated by cutting grooves on the integral-fins. Effects of fin pitch, height, thickness and semi-vertex angle were investigated. Their results indicated that the heat transfer performances of the three-dimensional fin tubes were better than the conventional integral-fin tubes and heat transfer coefficients of up to 19.8 kW/m^2·K was achieved.

Honda et al. [4] experimentally investigated a series of two and three-dimensional tubes of different fin geometries as shown in Fig. 2-6. The two-dimensional fins are flat-sided integral-fins (Tubes A and B of Fig. 2-6) whereas the three-dimensional fins (Tubes C to F of Fig. 2-6) consist of jagged edges of irregular fin height and fin shape. Experiments were performed to determine the condensation performances of R-113 on the tube bundles. It was found that the flat-sided integral-fin (Tube B) exhibited the highest heat transfer coefficient.

Cheng and Tao [53] and Kumar et al. [54] investigated the performance of the sawtooth-fin and spine integral-fin as shown in Fig. 2-7 (a) and (b), respectively. The sawtooth-fin was tested in R-152a vapour whereas steam and R134a were used as the working fluids for the spine integral-fin experiments. It was determined that these two fin geometries resulted in higher heat transfer coefficients as compared to the conventional integral-fin. While no explanation was provided by Cheng and Tao [53] on the mechanism of enhancement for the sawtooth-fin, Kumar et al. [54] suggested that the spine integral-fin geometry caused the thinning of the condensate film due to the surface tension force and also facilitated better condensate drainage from the lower portion of the tube.

Condenser tubes with novel three-dimensional petal-shaped fins as shown in Fig. 2-8 were investigated by Zhang et al. [55]. These condenser tubes were fabricated in-house and the condensation experiments were conducted with R407C refrigerant. It was deduced that due to the fin design which interrupted the vapour flow circumferentially and induced vorticity, enhancement factors of up to 5.25 as compared to a smooth tube were achieved.

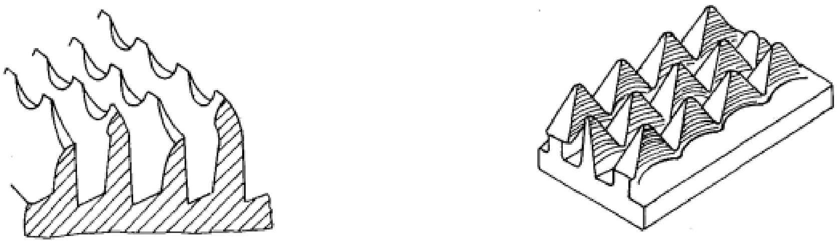

(a) (b)

Fig. 2-5 Schematics of three-dimensional fins (a) Thermoexcel-C [52] and (b) Everlin·Δ [52].

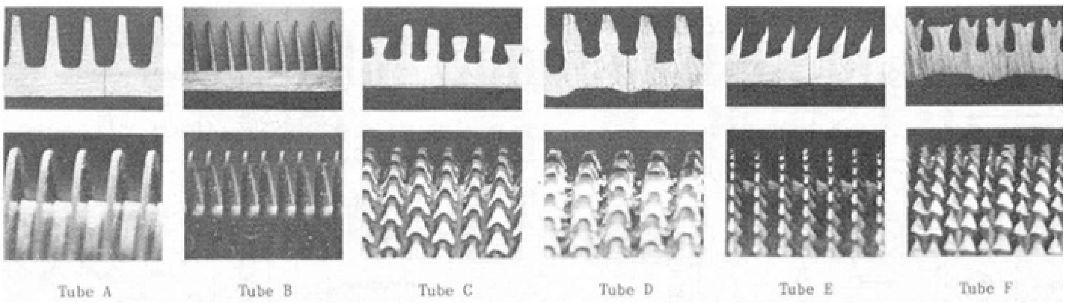

Fig. 2-6 Flat-sided integral fins and complex three-dimensional fins investigated by Honda et al. [4].

(a) (b)

Fig. 2-7 Schematics of (a) sawtooth-fin [53] and (b) spine integral-fin [54].

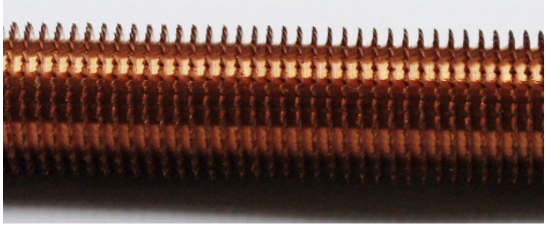

Fig. 2-8 Images of three-dimensional petal-shaped fins [55].

Wrapping wires around the condenser tubes is another method used to enhance external condensation. Murase et al. [56] deduced that the wrapping wires also induced surface tension forces which led to the thinning of the condensate film. In addition, retention of condensate was observed. The retention of condensate was determined as the dominant factor affecting their heat transfer performances. Ali and Qasim [57] concluded that the wire winding pitch of 4 mm exhibited the highest condensation heat flux for circular wrapping wires made of copper, brass and aluminium. In addition, Ali et al. [58] also showed that enhancements of up to 13.4% were achieved by using wrapping wires of 1 mm square cross-section, as compared to those of circular cross-section.

The thermal conductivity of the tube material also plays a significant role on an enhanced tube's condensation performance. Low thermal conductivity materials will result in significant reduction in the temperatures along the fin and thus reduce the average condensation heat transfer coefficient of the surface. The effects of the condenser tube's thermal conductivity were investigated by Ali and Briggs [15]. They determined that the reduction of fin efficiency was more evident in the low thermal conductivity brass and bronze tubes as compared to copper tubes. Ji et al. [59] compared the heat transfer coefficients of tubes with the same fin structures but with different thermal conductivity materials in R134a refrigerant. They concluded that the enhanced copper tubes have better heat transfer performances than the enhanced tubes made from titanium, cupronickel and stainless steel that are of lower thermal conductivities. Similar conclusions on the effects of material thermal conductivity on the condensation heat transfer coefficients were also reported by Zhang et al. [60] and Zhao et al. [61].

In most of the above studies, the three-dimensional fin structures investigated do not have regular geometries. For example, the fins of Tubes C and F in Fig. 2-6 do not have uniform height and the grooves of Tube D are also uneven. As these three-dimensional fins are usually produced by cutting slots on the two-dimensional integral fins, this machining process may result in large dimensional inaccuracy and also damaging of the fin structures. Therefore, it was difficult to perform a systematic study on the effects of fin pitch, fin height and fin thickness of these three-dimensional fin structures.

The only known systematic studies on the effects of fin parameters (fin spacing, fin height and fin thickness) of three-dimensional fin structures were conducted by Ali and Briggs [15, 18] and Ali [62]. The fin structures were rectangular pin fins. They determined that at a constant fin thickness and spacing, the highest enhancement ratio was achieved with the fin height of 1.6 mm [15]. On the other hand, for fins of equal thickness and height, the fin spacing of 0.5 mm showed the highest heat transfer enhancement ratio of 4.9 times as compared to that of a plain surface [18]. In addition, it was also deduced that the heat transfer performances of the pin fin tubes were strongly influenced by the circumferential fin spacing but were independent of the circumferential fin thickness.

2.2 Forced convection condensation

2.2.1 Background on two-phase flow in plain horizontal tubes

Based on the conservation of momentum and assuming one-dimensional two-phase (liquid and vapour) flow, the total pressure gradient (dP/dz) across a plain horizontal tube consists of the frictional pressure gradient $(dP/dz)_F$ and acceleration pressure gradient $(dP/dz)_A$. The expression is given in Eq. (2-25), where z denotes the tube axial direction. The frictional pressure gradient represents the shear forces between the two-phase mixture and the tube wall and the acceleration pressure gradient accounts for the change in pressure when the vapour condenses to liquid. In order to obtain expressions for $(dP/dz)_F$ and $(dP/dz)_A$, two limiting conditions are considered.

$$\frac{dP}{dz} = \left(\frac{dP}{dz}\right)_F + \left(\frac{dP}{dz}\right)_A \quad (2\text{-}25)$$

Homogeneous flow model

In the first condition, the liquid and vapour velocities are assumed to be equal and the two phases are in thermodynamic equilibrium. This model is commonly known as the homogeneous model and is employed in the modelling of the bubbly and wispy-annular flow regimes. In these regimes, the liquid and vapour velocities are high and the velocity difference between the two phases is negligible. With the above assumptions and by further assuming that the compressibilities of the liquid and vapour phases are negligible, the expression for $(dP/dz)_A$ can be reduced to that of Eq. (2-26) where G is the mass velocity, x is the vapour quality and v_{fg} is the difference in the specific volumes of the saturated liquid and vapour. On the other hand, $(dP/dz)_F$ is approximated by the Fanning equation as shown in Eq. (2-27), where $\bar{v}$ is the average specific volume of the homogenous fluid of Eq. (2-28) and f_{TP} is the two-phase friction factor. Using the Blasius equation [63], the relationship between f_{TP} and G can be established and is shown in Eq. (2-29). In this equation, D is the inner tube diameter and $\bar{\mu}$ is the average dynamic viscosity of the two-phase mixture which depends on the vapour quality. Several models such as those of McAdams et al. [64] and Cicchitti et al. [65] as shown in Eqs. (2-30) and (2-31), respectively can be used to determine $\bar{\mu}$.

$$-\left(\frac{dP}{dz}\right)_A = G^2 v_{fg} \frac{dx}{dz} \quad (2\text{-}26)$$

$$-\left(\frac{dP}{dz}\right)_F = \frac{2 f_{TP} G^2 \bar{v}}{D_h} \quad (2\text{-}27)$$

$$\bar{v} = v_f + x v_{fg} \quad (2\text{-}28)$$

$$f_{TP} = \frac{0.079}{(G D_h/\bar{\mu})^{1/4}} \quad (2\text{-}29)$$

$$\frac{1}{\bar{\mu}} = \frac{x}{\mu_g} + \frac{1-x}{\mu_f} \tag{2-30}$$

$$\bar{\mu} = x\mu_g + (1-x)\mu_f \tag{2-31}$$

<u>Separated flow model</u>

In the second condition, the vapour and fluid phases are viewed as two segregated streams where the velocities of the two phases may not be equal. Such a flow pattern is observed in the annular flow regime where a thin layer of liquid film surrounds the tube wall and a higher speed vapour core in the centre. The model that is used to predict the pressure drop in this flow regime is known as the separated flow model. Following the assumptions that the compressibilities of the liquid and vapour phases are negligible and the vapour quality varies linearly over the tube length, the acceleration pressure drop can be derived as Eq. (2-32). In this equation, α denotes the void fraction, which is the ratio of the cross-sectional area occupied by the vapour phase (A_g) to the tube cross-sectional area (A). By applying the principle of minimum entropy production on the kinetic energy flux of the two-phase flow, Zivi [66] derived an expression which relates α to the vapour quality for the annular flow region as Eq. (2-33). With α known, the acceleration pressure drop across a horizontal plain tube can be computed by substituting Eq. (2-33) and the vapour qualities at the tube inlet and outlet into Eq. (2-32).

$$-\Delta P_A = G^2\left\{\left[\frac{x_{out}^2}{\rho_g\alpha_{out}} + \frac{(1-x_{out})^2}{\rho_f(1-\alpha_{out})}\right] - \left[\frac{x_{in}^2}{\rho_g\alpha_{in}} + \frac{(1-x_{in})^2}{\rho_f(1-\alpha_{in})}\right]\right\} \tag{2-32}$$

$$\alpha = \left[1 + (\frac{1-x}{x})\left(\frac{\rho_g}{\rho_f}\right)^{2/3}\right]^{-1} \tag{2-33}$$

On the other hand, the two-phase multiplier method is widely used to obtain the frictional pressure drop across a tube. In this approach, the two-phase frictional pressure drop $\left(\frac{dP}{dz}\right)_F$ is assumed to be equal to the frictional pressure drop of each phase multiplied by the corresponding two-phase multiplier (ϕ) as shown in Eq. (2-34). In this equation, $\left(\frac{dP}{dz}\right)_f$ and $\left(\frac{dP}{dz}\right)_g$ represent the liquid and vapour frictional pressure drops which can be expressed as Eqs. (2-35) and (2-36). Lockhart and Martinelli [67] suggested that ϕ should depend on the ratio of the pressure gradients of the liquid and vapour phases. They proposed a dimensionless parameter (X) for this relationship which is now known as the Lockhart-Martinelli parameter and is given in Eq. (2-37). For the case where the liquid and vapour are both in the turbulent flow regimes, the expression for the turbulent-turbulent Lockhart-Martinelli parameter (X_{tt}), which is related only to the liquid and vapour properties and the vapour quality, can be derived as Eq. (2-38). It should be noted that the flow regime (laminar or turbulent) of each phase can be determined from the Reynolds number of the corresponding phases given in Eqs. (2-39) and (2-40). By performing curve fitting on the experimental data, the relationship between ϕ and X was established by Chisholm [68] as shown in Eq. (2-41). When both the liquid and vapour are in the turbulent flow regime, *C* takes the value of 20.

$$\left(\frac{dP}{dz}\right)_F = \Phi_f^2\left(\frac{dP}{dz}\right)_f = \Phi_g^2\left(\frac{dP}{dz}\right)_g \tag{2-34}$$

$$-\left(\frac{dP}{dz}\right)_f = \frac{2f_f v_f G^2(1-x)^2}{D_h} \tag{2-35}$$

$$-\left(\frac{dP}{dz}\right)_g = \frac{2f_g v_g G^2 x^2}{D_h} \tag{2-36}$$

$$\mathrm{X} = \left(\frac{dP}{dz}\right)_f / \left(\frac{dP}{dz}\right)_g \tag{2-37}$$

$$X_{tt} = \left(\frac{\rho_g}{\rho_f}\right)^{0.5} \left(\frac{\mu_f}{\mu_g}\right)^{0.1} \left(\frac{1-x}{x}\right)^{0.9} \quad (2\text{-}38)$$

$$\mathrm{Re}_f = \frac{G(1-x)D_h}{\mu_f} \quad (2\text{-}39)$$

$$\mathrm{Re}_g = \frac{GxD_h}{\mu_g} \quad (2\text{-}40)$$

$$\phi_f^2 = 1 + \frac{C}{X} + \frac{1}{X^2} \quad (2\text{-}41)$$

Even though Lockhart and Martinelli [67] only correlated their models with experimental results of air-water and air-oil mixtures, their two-phase multiplier approach provided the basis upon which many subsequent models for other fluids were developed. For example, Friedel [69] proposed that $\left(\frac{dP}{dz}\right)_F$ is equal to the product of the two-phase multiplier (ϕ_{fo}) and the frictional pressure drop $\left(\frac{dP}{dz}\right)_{fo}$ when the total flow (liquid and vapour) is assumed to be liquid only. By correlating his model with 25,000 data points, the expression for ϕ_{fo} was developed for air-water mixture, air-oil mixture and R12 refrigerant. Subsequently, using the two-phase multiplier approach, an adiabatic two-phase frictional pressure drop correlation for R22, R134a and R407C refrigerants was proposed by Wang et al. [70]. A summary of the various two-phase frictional pressure gradient correlations developed for different fluids, tube diameter and flow regimes can be found in Refs. [71 – 73].

2.2.2 Background on condensation heat transfer in plain horizontal tubes

Analysis of condensation heat transfer in horizontal tubes can be divided into gravity-dominated condensation and vapour shear-dominated condensation. Gravity-dominated condensation occurs at low vapour velocities when the gravitational force which pulls the condensate down the tube wall is significantly higher than the vapour shear force which drives the condensate in the direction of flow. This resulted in an increase in liquid film thickness circumferentially from the top side of the tube to the bottom. On the other hand, vapour shear-dominated condensation represents the other limiting condition where the shear stress at the liquid-vapour interface has more significant influence on the heat transfer rate as compared to gravitational force. This resulted in a near-symmetrical thin liquid film surrounding the tube wall and a high-speed vapour core in the centre. Heat transfer in gravity-dominated condensation is dependent on the temperature difference between the tube wall and the surrounding fluid but is insensitive to mass flux. For vapour shear-dominated condensation, the heat transfer coefficient depends largely on mass flux and vapour quality and is independent of the temperature difference. In this section, the literature on condensation heat transfer in horizontal plain tubes is reviewed.

Gravity-dominated condensation

Gravity-dominated condensation is commonly observed in the stratified and wavy flow regimes. Due to the similarity in their heat transfer mechanisms to filmwise condensation on external surfaces, analyses of gravity-dominated condensation in tubes are also similar. Chato [74] assumes that the heat transfer is predominant only on the upper portion of the tube where laminar filmwise condensation prevailed. On the other hand, due to the thick liquid pool accumulated at the lower portion of the tube, heat transfer in this region is negligible. Based on these assumptions, he modified the Nusselt model for external condensation on horizontal tube [Eq. (2-4)] by introducing a new constant and obtained the correlation of Eq. (2-42), where h_i is the internal condensation heat transfer coefficient. From this equation, it can be seen that the constant of 0.555 is smaller than 0.725 of Eq. (2-4) for external condensation. This reduction in heat transfer is due to the accumulation of liquid pool in the tube for internal condensation. During condensation, the depth of the liquid pool changes with vapour quality along the fluid mean flow direction. To account for this effect, Jaster and Kosky [75] replaced the constant of Eq. (2-42) with a void fraction (α) function and obtained the heat transfer model of Eq. (2-43) for the stratified flow regime. With the void fraction model of Eq. (2-33) proposed by Zivi [66], Jaster and Kosky [75] showed their model was within a standard deviation of 37% when compared to the experimental data.

$$\mathrm{Nu_{tp}} = \frac{h_i D_h}{k_f} = 0.555\left[\frac{\rho_f(\rho_f-\rho_g)g h_{fg} D_h^3}{\mu_f k_f (T_{sat}-T_w)}\right]^{1/4} \tag{2-42}$$

$$\mathrm{Nu_{tp}} = \frac{h_i D_h}{k_f} = 0.725\alpha^{3/4}\left[\frac{\rho_f(\rho_f-\rho_g)g h_{fg} D_h^3}{\mu_f k_f (T_{sat}-T_w)}\right]^{1/4} \tag{2-43}$$

The models of Chato [74] and Jaster and Kosky [75] neglect the heat transferred from the liquid pool at the bottom section of the tube. This assumption might not be valid at higher mass flux range of the stratified flow regime as convection heat transfer in the liquid pool can be significant. Rosson and Meyers [76] determined from their experimental measurements that the condensation heat transfer coefficient reduced circumferentially from the top to the bottom portion of the tube. From these experimental observations, they developed a model for the average Nusselt number (Nu_{tp}) based on Eq. (2-44). In this equation, Nu_{tp} is the summation of the heat transferred from the top section of the tube where filmwise condensation occurs (Nu_{top}) and the bottom section where forced convection dominates (Nu_{bot}). On the other hand, the β term denotes the fraction of the tube perimeter on which filmwise condensation takes place and is related to the superficial liquid and vapour Reynolds numbers. Using a similar approach, Dobson [77] and Dobson et al. [78] subsequently developed a correlation for heat transfer in the wavy flow regime. In their model, the thick liquid pool at the lower tube section varies with vapour quality and is geometrically related to Zivi's void fraction equation [66].

$$\mathrm{Nu}_{tp} = \beta \mathrm{Nu}_{top} + (1-\beta)\mathrm{Nu}_{bot} \tag{2-44}$$

Vapour shear-dominated condensation

As the vapour velocity increases, the vapour pushes the liquid pool at the lower tube section towards the upper tube section and circumferentially around the tube wall. This results in the formation of a uniform thin liquid film around the tube wall and gives rise to the annular flow regime. As vapour shear is mainly responsible for the liquid film characteristics, the heat transfer mechanisms in this regime are also different from those in the gravity-dominated regime. Several models have been proposed over the last few decades to predict the heat transfer coefficients in the vapour shear-dominated regime and some of the widely referenced models can be broadly categorised into the (1) two-phase multiplier approach and (2) boundary layer approach.

The two-phase multiplier approach assumes that the heat transfer in the two-phase annular flow is equal to that of single-phase forced convection multiplied by a two-phase multiplier. This approach is analogous to that proposed by Lockhart and Martinelli [67] for the modelling of two-phase frictional pressure drop. For example, Shah [79] hypothesised that since the tube walls are wetted by a layer of liquid film during condensation and evaporation (in the absence of bubble nucleation), their heat transfer mechanisms are similar. He then modified the correlation previously derived for convective boiling [80] and developed the correlation for condensation as shown in Eq. (2-45). It can be seen from this equation that the Dittus-Boelter correlation for single-phase internal forced convection heat transfer [81] is adopted and the two-phase multiplier, represented in the last bracketed term, depends only on the vapour quality (x) and reduced pressure (P_r). It should be noted that $\mathrm{Re}_{f,o}$ denotes the Reynolds number assuming the liquid-vapour mixture flowing only as liquid and is given as Eq. (2-46). The correlation shows a mean deviation of 15% - 17% when compared to 474 data points of different fluids. Another semi-empirical correlation which relates Nu_{tp} to a two-phase multiplier was derived by Cavallini and Zecchin [82]. Following a theoretical analysis on the annular flow and multiple linear regression analysis, they obtained an expression as shown in Eq. (2-47) where the two-phase multiplier is represented in the bracketed term on the right-hand side of the equation. In this equation, Re_f denotes the Reynolds number based on the superficial liquid velocity and can be computed by Eq. (2-39). Other widely-used correlations which were derived based on a similar approach are those of Dobson and Chato [83] and Akers and Rosson [84] and they are expressed as Eqs. (2-48) and (2-49), respectively. These correlations are compared against the experimental results of some common refrigerants such as R12, R22, R134a and R32-R125 mixtures and have shown relatively accurate predictions.

$$\mathrm{Nu}_{tp}=\frac{h_i D_h}{k_f}=0.023\mathrm{Re}_{fo}^{0.8}\mathrm{Pr}_{fo}^{0.4}\left[(1-x)^{0.8}+\frac{3.8x^{0.76}(1-x)^{0.04}}{P_r^{0.38}}\right] \quad (2\text{-}45)$$

$$\mathrm{Re}_{fo}=\frac{GD_h}{\mu_f} \quad (2\text{-}46)$$

$$\mathrm{Nu}_{tp}=\frac{h_i D_h}{k_f}=0.05\mathrm{Re}_{f}^{0.8}\mathrm{Pr}_{f}^{0.33}\left[1+\left(\frac{\rho_f}{\rho_g}\right)^{0.5}\left(\frac{x}{1-x}\right)\right]^{0.8} \quad (2\text{-}47)$$

$$\mathrm{Nu}_{tp} = \frac{h_i D_h}{k_f} = 0.023\mathrm{Re}_f^{0.8}\mathrm{Pr}_f^{0.4}\left(1 + \frac{2.22}{\mathrm{X}_{tt}^{0.89}}\right) \tag{2-48}$$

$$\mathrm{Nu}_{tp} = \frac{h_i D_h}{k_f} = 0.026\mathrm{Pr}_f^{0.33}\left\{G\left[(1-x) + x\left(\frac{\rho_f}{\rho_g}\right)^{0.5}\right]\right\}^{0.8} \tag{2-49}$$

On the other hand, the boundary layer approach that was used to develop the condensation heat transfer model for the annular flow regime was proposed by Azer et al. [85] and later modified by Traviss et al. [86]. In general, this approach analyses the turbulent liquid film which surrounds the tube wall and assumes that the heat transferred by diffusion across the liquid film is more significant than convection. On this basis, the energy equation of the liquid film is given by Eq. (2-50), where ε_H is the turbulent eddy conductivity. This equation also implies that the heat flux through the liquid film is only in the y-direction and is a constant. Using separation of variables and integrating both sides of the equation, the condensation heat transfer coefficient (h_i) can be defined as Eq. (2-51). With the introduction of the friction velocity (u^*) and dimensionless distance (y^+) as shown in Eqs. (2-52) and (2-53) and further assuming a turbulent Prandtl number (Pr_t) of unity such that the turbulent eddy conductivity (ε_H) is equal to the turbulent eddy viscosity (ε_M), h_i can be rewritten as Eq. (2-54), where T^+ is the dimensionless temperature of Eq. (2-55). From Eqs. (2-52) – (2-55) it can be seen that as long as τ_w and the relationship between $\frac{\varepsilon_M}{\upsilon_l}$ and y^+ are known, h_i can be determined. As the wall shear stress (τ_w) is related to the frictional pressure gradient $\left(\frac{dP}{dz}\right)_f$, the Lockhart-Martillini type correlations and the two-phase frictional multiplier can be used to approximate τ_w. On the other hand, by employing the universal velocity profile [87], the relationship between $\frac{\varepsilon_M}{\upsilon_l}$ and y^+ was established by Traviss et al. [86].

By substituting this relationship into Eq. (2-55), it was determined that T^+ is a piecewise function of the liquid phase Reynolds number (Re_f).

More recently, Chamra et al. [88], Wang et al. [89] and Kim and Mudawar [90] also adopted the boundary layer approach to predict the condensation heat transfer in micro-fin, multi-channel tubes and micro-channels, respectively. They proposed new functions for τ_w using the two-phase frictional multipliers and new relationships between T^+ and Re_f for these enhanced structures. Their correlations agreed reasonably well the experimental data with the mean absolute errors (*MAE*) of less than 20%.

$$\frac{\partial}{\partial y}\left\{\rho_f C_{pf}(\alpha_f + \varepsilon_H)\frac{\partial T}{\partial y}\right\} = 0 \tag{2-50}$$

$$\frac{1}{h_i} = \int_{T_w}^{T_\delta}\frac{dT}{q''} = \int_0^{\delta}\frac{dy}{\rho_f C_{pf}(\alpha_f+\varepsilon_H)} \tag{2-51}$$

$$u^* = \sqrt{\tau_w/\rho_f} \tag{2-52}$$

$$y^+ = \frac{yu^*}{\upsilon_f} \tag{2-53}$$

$$h_i = \frac{\rho_f C_{pf} u^*}{T^+} \tag{2-54}$$

$$T^+ = \int_0^{\delta^+}\frac{dy^+}{(\mathrm{Pr}_f + \frac{\varepsilon_M}{\upsilon_f})} \tag{2-55}$$

2.2.3 Review on two-phase flow and condensation heat transfer in enhanced tubes

Several surface structures have been introduced on the inner walls of the condenser tubes to improve their condensation heat transfer performances. Their heat transfer enhancement mechanisms include the increase in heat transfer surface area, improved condensate drainage due to surface tension effects and induced turbulence and swirling motion on the condensate film. As enhanced tubes of circular geometry are widely used in air-conditioning systems and in the automotive and process industries, they have been extensively investigated in the last few decades. These enhanced tubes include (1) microfin tubes, (2) herringbone tubes, (3) enhanced heat transfer (EHT) tubes, (4) corrugated tubes, and (5) dimpled tubes. In this section, the various heat transfer and pressure drop characteristics of these enhanced tubes are reviewed and analysed.

Microfin tubes

A schematic diagram of the microfin structure is shown in Fig. 2-9. It consists of trapezoidal shaped fins which spiral along the internal tube walls at a constant helix angle (β). The fins are hundreds of micrometres in height and thickness and are evenly spaced. As compared to other types of enhanced tubes, microfin tubes are the most widely investigated. Reviews on the two-phase flow patterns and heat transfer characteristics during condensation in these tubes were provided by Doretti et al. [24] and Cavallini et al. [91]. They reported that, for R-22 refrigerant at mass flux of 200 $kg/m^2 \cdot s$, the microfin tube exhibited a heat transfer enhancement factor of up to 3 as compared to a plain tube. In addition, it was also determined through visualisation that at the R134a refrigerant mass flux of 200 $kg/m^2 \cdot s$, saturation temperature of 40°C and vapour quality of 0.5, an annular flow pattern was observed in the microfin tube whereas the flow pattern in the plain tube was still in the stratified-wavy regime. These results suggested that in addition to the increased heat transfer area, the helical angle of the microfins could have also induced a centrifugal effect on the liquid film and altered its flow pattern thus, enhancing the heat transfer. Subsequently, Han and Lee [92] experimentally investigated the condensation heat transfer performances of

R134a, R22 and R410A in microfin tubes of different inner tube diameters (8.92 mm – 4 mm). They determined that, under the same operating conditions, the microfin tubes were able to achieve relatively high heat transfer enhancements (80 - 180%) while maintaining moderate increase in pressure drop (20 - 80%) as compared to a plain tube. Sapali and Patil [93] examined the effects of the saturation temperature on the heat transfer performance of the microfin tubes. Their experiments were conducted using R134a and R410A refrigerants and saturation temperatures ranging from 35 to 60°C. With the refrigerant mass fluxes of 90 to 800 $kg/m^2{\cdot}s$, they determined that the average heat transfer coefficient decreased with increasing saturation temperature for both microfin and plain tubes. Wu et al. [94] performed condensation experiments of R410A in six different microfin tubes. These tubes were of different inner tube diameters, fin heights and fin densities but had the same helical angle. The experiments were performed at the fixed inlet and outlet vapour qualities of 0.8 and 0.1, respectively and the refrigerant mass flux was varied from 99 $kg/m^2{\cdot}s$ to 603 $kg/m^2{\cdot}s$. It was determined that the heat transfer coefficient of the microfin tubes did not increase monotonically with mass flux. For instance, when the mass flux was between 99 to 400 $kg/m^2{\cdot}s$, the heat transfer coefficient first decreases with increasing mass flux and then increases gradually with the further increase in mass flux. They suggested that the condensate drainage due to surface tension force and interfacial turbulence due to centrifugal force are the main contributors to the heat transfer enhancements of the microtube tubes. On the other hand, the non-monotonic behaviour of the heat transfer coefficient was likely due to the complex interactions of these mechanisms which vary as mass flux changes. More recently, the thermal performances of condenser tubes with inner diameter smaller than 5 mm were investigated by Li et al. [95] and Zhang et al. [96]. At the same mass flux and operating conditions, it was determined that the reduction in tube diameter increases the heat transfer coefficient of the microfin tube and they suggested that the enhancements were due to the increased surface tension force and interfacial shear stress.

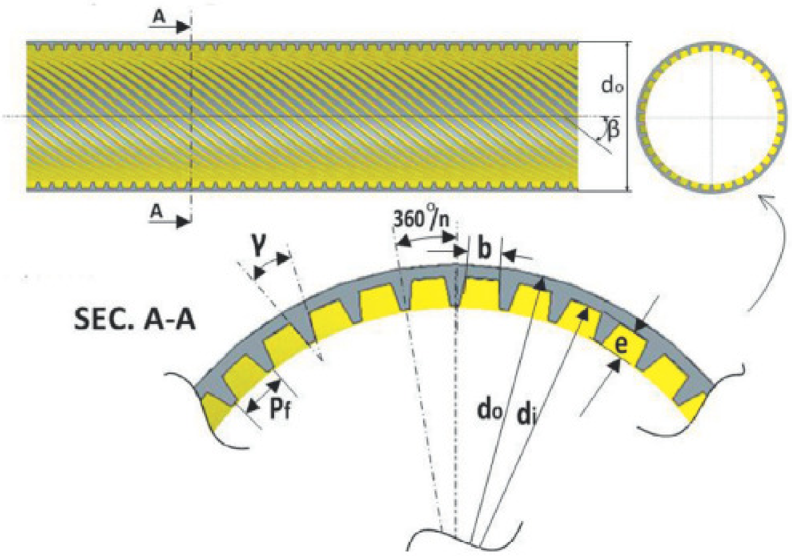

Fig. 2-9 Schematic of a microfin tube [95].

One of the earliest correlations for condensation heat transfer in microfin tubes was proposed by Cavallini et al. [97]. They extended the original correlation of Cavallini and Zecchin [82], as shown in Eq. (2-47), for condensation in a smooth tube by introducing three dimensionless parameters (Rx, Fr and Bo) and the resulting correlation for microfin tube is shown in Eq. (2-56). In this equation, l, n_g, γ, β are the fin height, groove quantity, fin apex angle and helical angle, respectively. In addition, the dimensionless parameter, Rx, accounts for the microfin geometry and the increased heat transfer area and is defined by Eq. (2-57). On the other hand, Fr and Bo are defined by Eqs. (2-58) and (2-59), respectively. It should be noted that the product of Fr and Bo considers the relative effects of surface tension and vapour shear.

$$\mathrm{Nu}_{tp} = \frac{h_i D_h}{k_f} = 0.05\mathrm{Re}_f^{0.8}\mathrm{Pr}_f^{0.33}\left[1 + \left(\frac{\rho_f}{\rho_g}\right)^{0.5}\left(\frac{x}{1-x}\right)\right]^{0.8}\mathrm{Rx}^2(\mathrm{Fr}\cdot\mathrm{Bo})^{-0.26} \tag{2-56}$$

where

$$\mathrm{Rx} = \frac{[2n_g l(1-\sin(\gamma/2))]/[\pi D_h\cos(\gamma/2)]+1}{cos\beta} \tag{2-57}$$

$$\mathrm{Fr} = \frac{u_{go}^2}{gD_h} \tag{2-58}$$

$$\mathrm{Bo} = \frac{g\rho_f\pi D_h l}{8\sigma n_g} \tag{2-59}$$

It can be seen that Eq. (2-56) is independent of wall temperature and therefore is only suitable for predicting condensation at high mass flux. Cavallini et al. [98], subsequently, improved this model to predict the condensation heat transfer coefficient for both wall temperature dependent and independent zones.

Herringbone tubes

The herringbone tubes consist of arrays of V-shape fins arranged at a helix angle (β) of approximately 16° on its internal tube walls. A schematic diagram of the fin arrangement is shown in Fig. 2-10 (a) and a photograph of the internal fins is shown in Fig. 2-10 (b). Ebisu and Torikoshi [99] fabricated the herringbone tube by embossing a flat strip of copper to obtain the herringbone structure. The embossed strip of copper was then rolled and welded to form a tube. Ebisu and Torikoshi [99], subsequently, tested the condensation heat transfer performances of the herringbone tube using R407C refrigerant and it was found that the herringbone tube showed up to 200% higher heat transfer coefficient as compared to a microfin tube. They suggested that the heat transfer enhancement was due to the larger heat transfer area of the herringbone tube and the redistribution of the condensate by the V-shape fins which produced two thin-film regions on the side walls. Miyara et al. [22] conducted a separate investigation on a herringbone tube using R410A and R22 refrigerants. They reported that the herringbone tubes demonstrated higher heat transfer coefficients than the microfin tube only in the high mass flux regions, where $G \geq 300$ kg/m^2·s. On the other hand, at low mass flux ($G = 100$ kg/m^2·s), the herringbone tube had slightly lower or similar heat transfer coefficient as the microfin tube. They suggested that the redistribution of condensate is only effective at high mass flux while at low mass flux the condensate accumulates mainly at the bottom of the tube. Subsequently, Oliver et al. [100] extended the investigation on herringbone tubes to higher mass fluxes of 400 – 800 kg/m^2·s. Using R22, R134a and R407C as the working fluids, their results show that the heat transfer enhancement factor of the herringbone tube was about 1.4 as compared to the microfin while the pressure drops were about 27% higher. Similar comparative studies between herringbone and microfin tubes were also reported by Goto et al. [101] and Lambrechts et al. [102] for mass fluxes ranging from 200 kg/m^2·s to 800 kg/m^2·s. From their investigations, it was also concluded that the heat transfer performance of the herringbone tube was higher than that of the microfin tube.

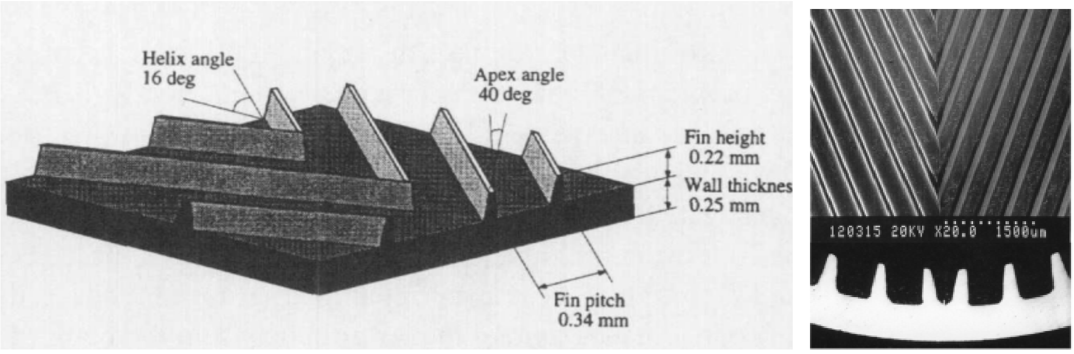

(a) (b)

Fig. 2-10 (a) Schematic [99] and (b) photograph [101] of the herringbone structure.

Enhanced heat transfer (EHT) tubes

The enhanced heat transfer (EHT) tubes typically consists of a hybrid of primary dimples and secondary petal arrays on their internal tube walls. As shown in Fig. 2-11, the dimensions of the dimples are larger than the petal array and has diameter and height of approximately 3.5 mm and 1.1 mm, respectively. On the other hand, the diameter of the petal array is approximately 2.54 mm and has the height of only 0.18 mm. Guo et al. [25] first investigated the condensation and evaporation heat transfer performance of the EHT tube using R22, R32 and R410A refrigerants. Their experiments were performed between the refrigerant mass fluxes of 50 kg/m^2·s and 200 kg/m^2·s. In comparison with the herringbone tubes, the EHT tube showed the best evaporation heat transfer coefficient while its condensation heat transfer coefficients were found to be poorer. A separate investigation on the ETH tube was conducted by Kukulka et al. [103]. They reported that the enhancements in the heat transfer coefficient were 1.3 – 1.95 times that of a smooth tube. In addition to the increased heat transfer area, they also suggested that the higher heat transfer coefficient of the EHT tube was due to (1) the higher turbulence and flow separation produced by the primary dimples and (2) the boundary layer disruption and flow mixing produced by the secondary petal arrays. More recently, Li et al. [104] investigated the condensation performances of three-dimensional EHT tubes. Unlike the EHT tubes tested by Guo et al. [25] and Kukulka et al. [103], the three-dimensional EHT tubes consisted of regularly spaced dimples with periodic grooves. Using R410A and the refrigerant mass fluxes of 60 kg/m^2·s to 260 kg/m^2·s, it was reported that a heat transfer coefficient of up to 2750 W/m^2·K can be achieved with the three-dimensional EHT tubes. They suggested that the grooves enhanced heat transfer by promoting condensate drainage and assisting in the redistributing of the condensate film. Similar investigations on three-dimensional EHT tubes were also reported by Sun et al. [105] and Chen and Li [106] where up to 62% higher heat transfer coefficient as compared to a smooth tube was recorded.

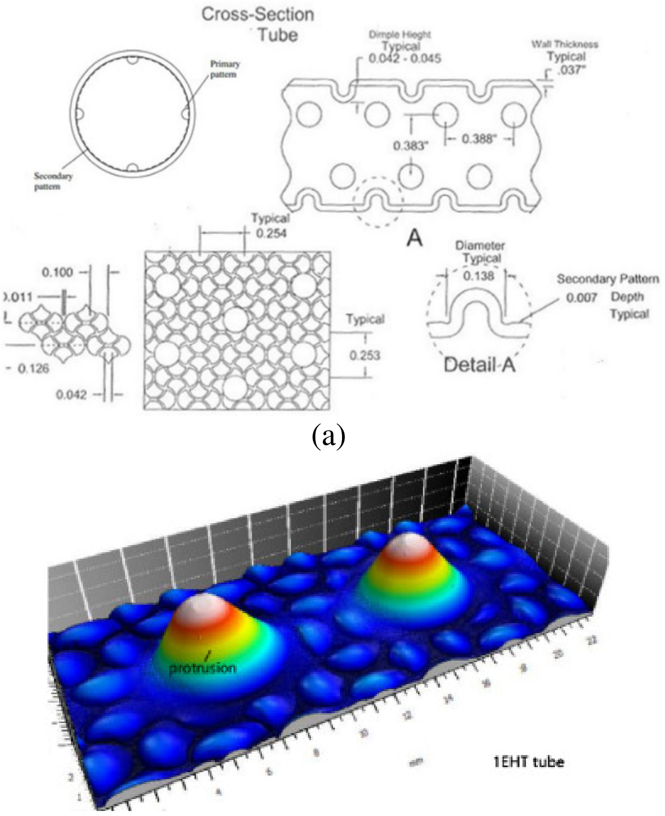

(a)

(b)

Fig. 2-11 (a) Schematic drawings [25] and (b) imaging profile [105] of an EHT tube.

<u>Corrugated and dimple tubes</u>

Corrugated tubes such as those shown in Fig. 2-12 (a) consist of helical-ribs on their internal tube walls. These helical-ribs are expected to increase heat transfer by inducing mixing at the fluid boundary layer and by limiting the boundary layer thickness along the tube wall. Due to these advantages, corrugated tubes have been widely investigated for single phase forced convection heat transfer and significant enhancements in their heat transfer coefficients were reported [107-110]. On the other hand, the condensation heat transfer characteristics of corrugated tubes were reported by Laohalertdecha and Wongwises [111]. They experimentally studied the effects of corrugated pitch on the condensation heat transfer coefficient using R134a as the working fluid. It was determined that the heat transfer coefficient increases with decreasing corrugated pitch. In addition, the corrugated tubes also demonstrated 10 – 50% higher heat transfer coefficients as compared to a smooth tube while their pressure drops were up to 70% higher. Subsequently, Laohalertdecha and Wongwises [112] extended their studies by examining the effects of corrugation depth. They found that noticeable improvements in Nusselt number were achieved with the corrugation depths of 1.25 mm and 1.5 mm. However, when the corrugation depth was only 1 mm, its Nusselt numbers were similar to those of a plain tube.

An image of a dimpled tube is shown in Fig. 2-12 (b). Unlike the EHT tubes, the dimpled tubes consist only of periodic spherical dimples on the tube walls. Aroonrat and Wongwises [23] compared the condensation heat transfer and pressure drop performances of a dimpled tube and plain copper tube using R134a. The dimples have an average diameter of 1.5 mm and depth of 0.75 mm. Their results show that the dimpled tube enhanced the Nusselt number by 1.3 – 1.4 times whereas the two-phase friction factor increased by 2.8 – 4.1 times as compared to the plain tube. The effects of dimpled depth were subsequently investigated by Aroonrat and Wongwises [113] in which they compared the condensation heat transfer performances of three different dimpled tubes with 0.5 mm, 0.75 mm and 1.0 mm dimple depths. From their experimental results, it was revealed that the heat transfer coefficient and frictional pressure drop increase with increasing dimple depth. The highest heat transfer enhancement of 84% and pressure drop penalty of 892% were recorded for the dimpled tube of 1.0 mm dimple depth.

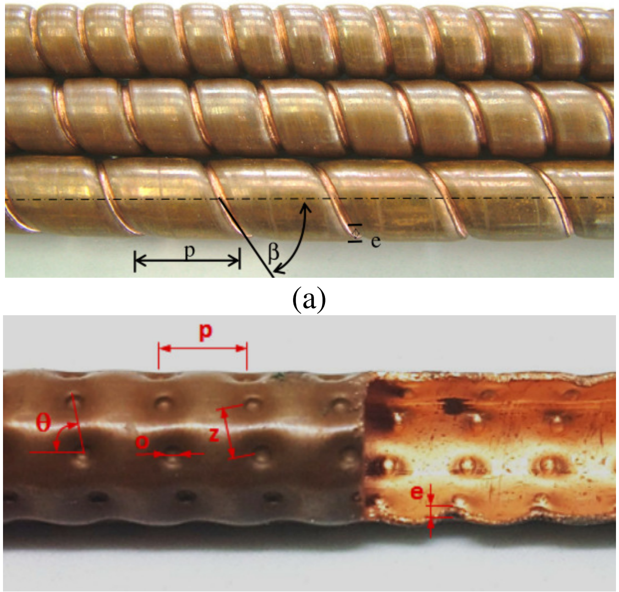

(a)

(b)

Fig. 2-12 (a) Image of corrugated tubes [112] and (b) image of a dimpled tube [113].

2.3 Fabrication of enhanced heat transfer devices by Selective Laser Melting

Selective Laser Melting (SLM) is an additive manufacturing technique suitable for fabricating complex two- or three-dimensional metallic parts. Recent advancements in the SLM technique have resulted in an increasing interest on the use of this technique to develop components with enhanced heat transfer capabilities. For instance, Wong et al. [114] fabricated heat sinks of different complex structures using aluminium 6061 and determine that the elliptical array heat sink offered the highest heat transfer rate per unit pressure drop. On the other hand, Ventola et al. [115] used direct metal laser sintering technique and produced air-cooled heat sinks of different artificial surface roughness for the cooling of electronic components. The artificially created roughness was intended to enhance the forced convection heat transfer performances of the heat sinks in the fully turbulent flow regime and a peak enhancement of 73% as compared to smooth surfaces was obtained. Ho et al. [116] fabricated staggered arrays of the NACA0024 airfoil heat sink with different angles of attack (AOA). It was determined that the heat transfer coefficient increases with increasing AOA. They suggested that the formation of vortices at high AOA was responsible for the enhancements observed. As compared to the conventional cylindrical heat sink, the airfoil heat sink enhanced Nu by up to 34.8%. More recently, a new class of lattice structures which consists of the Rhombi-Octet unit cells was fabricated by Ho and Leong [117] and Ho et al. [118] for enhancing single-phase forced convection heat transfer with air and water as the working fluids. They determined that the new lattice structures produced better heat transfer performances and lower pressure drops as compared to conventional metallic porous foams.

Apart from heat sinks, the additive manufacturing technique has also been employed by Hutter et al. [119] to develop metallic porous foams for tubular reactor application. In comparison to commercially available metal foam inserts, the use of fully sintered metallic porous foams produced convective heat transfer coefficients which are more than two times higher. Subsequently, Ameli et al. [120] attempted to engineer aluminium/ammonia heat pipes of various wicking characteristics using SLM. They demonstrated that the parameters of wick structures such as thickness, porosity, permeability and pore size in different regions of a heat pipe could be adequately controlled by this manufacturing technique. In addition, the entire heat pipe including end cap, wall, wick and fill tube could also be produced in a single process.

The use of the SLM technique to fabricate structures that enhance nucleate boiling heat transfer was first attempted by Ho et al. [121]. They fabricated surfaces with arrays of micro-finned and micro-cavity structures and conducted the pool boiling experiments using FC-72. In comparison to a plain surface, the enhancements in heat transfer coefficient and critical heat flux (CHF) of the SLM fabricated surfaces were found to be 70% and 76%, respectively. Subsequently, lattice structures of different unit cell sizes and heights were developed by Wong and Leong [122] for enhancing nucleate boiling heat transfer. From their experiments, it was determined that the lattice structure of 3 mm unit cell size and 5 mm height has the highest average nucleate boiling heat transfer coefficient of 1.35 W/cm^2 which is 2.81 times that of a plain surface. Three-dimensional pin fin arrays were produced by Wang et al. [123] to explore the heat transfer characteristics of these structures near the Leidenfrost point. They determined that a high fin density allows the droplet integrity to be maintained after impact while a larger fin height also improves the droplet heat transfer. Recently, Zhang et al. [124] reported the use of a 3D thin wall grid structure fabricated from stainless steel to enhance nucleate boiling heat transfer of water and achieved an increase in CHF of up 3.3 times as compared to a plain surface.

The above brief review demonstrates the potential of producing functional heat transfer parts with SLM. This technique also allows intricate geometries with relatively good dimensional accuracies to be fabricated. In addition, parameters of the enhanced structures such as the structure height, pitch, thickness and density can also be systematically varied. This, therefore, enables detailed parametric studies to be conducted and the relevant transport mechanisms to be identified.

2.4 Summary and current research gaps

Based on the above review, it can be seen that the experimental and theoretical investigations on improving natural and forced convection condensation have achieved some successes. However, existing research works are still incomplete and there are areas which still require further investigations. These areas are summarised as follows:

<u>Natural convection condensation</u>

1. Existing investigations have demonstrated that the three-dimensional pin fin structures have better filmwise condensation performance than conventional two-dimensional integral and longitudinal fins. While the two-dimensional fins can promote heat transfer by inducing surface tension force, the three-dimensional pin fins have the added advantage of reducing the condensate retention height. However, likely due to the limitation of current manufacturing techniques, geometries of existing three-dimensional fin structure are limited to rectangular pin. New fin geometries which could possibly take further advantage of surface tension and promote condensate drainage are still not investigated. In order to investigate the natural condensation heat transfer performances of the new pin fins, the fins can be designed using CAD software and the SLM technique be used to fabricate the specimens.
2. Novel pin fin structures such as spine integral-fin [54] and petal-shaped fins [55] were investigated. However, there is a lack of systematic study to investigate the effects of fin height and fin pitch so as to determine the better fin arrangements. A

systematic study can also shed light into the key transport mechanisms influencing the condensation performances of the new structures.

3. Existing theoretical models on natural convection condensation on extended surfaces mainly dealt with two-dimensional fin structures and examples of these models are described in Section 2.1.2. The only model for three-dimensional pin fins was developed by Ali and Briggs [47]. However, this is a semi-empirical model and it was proposed only for pin fins of rectangular geometry. To the best of the author's knowledge, no theoretical model has been developed to predict the condensation heat transfer performances of three-dimensional pin fin structures of other geometries and therefore this would warrant further investigation.

Forced convection condensation

1. Existing enhanced condenser tubes are mainly limited to microfin, herringbone, EHT, corrugated and dimpled tubes. Amongst these structures, the herringbone tube demonstrated the highest enhancement in heat transfer coefficient of up to 336% as compared to a plain tube at mass fluxes higher than 300 $kg/m^2 \cdot s$. At low mass fluxes, enhancements of herringbone and microfin tubes were determined to be between 2 – 3 times that of a smooth tube. The newer enhanced tubes that were recently investigated such as the EHT, corrugated and dimpled tubes were unable to achieve the same degree of enhancement as that of the microfin and herringbone tubes. It is therefore essential to develop new internal structures to further enhance in-tube condensation heat transfer.
2. Three-dimensional pin fin structures have shown potential in enhancing natural convection condensation on external surfaces and these structures can also be

employed to enhance in-tube forced convection condensation. The presence of three-dimensional pin fins on the internal tube wall can promote condensate drainage by surface tension force and induce turbulence on the liquid film. In addition, when the fin height is sufficiently large, it enables the fins to penetrate the vapour core (even under low vapour quality) to further enhance condensation. However, likely be due to the difficulty in fabricating the pin fin structures on the internal tube walls by conventional manufacturing techniques, no work on enhancing in-tube forced convection condensation using pin fin structures has been reported. In this regard, the SLM technique can be explored to produce three-dimensional pin fin structures for enhancing in-tube condensation.

3. The SLM technique can also be employed to fabricate different pin fin tubes where their fin parameters such as circumferential and longitudinal fin pitches are systematically varied. Parametric studies can then be conducted to examine the effects of the fin parameters on the condensation heat transfer coefficient and pressure drop. Through these studies, it is hoped that the key transport mechanisms associated with the pin fin tubes can be identified and a mechanistic model can be developed to characterise their thermal performances.

Chapter 3 – Fabrication and Characterisation of Test Specimens

3.1 SLM fabrication parameters

The SLM 250 HL (SLM Solutions GmbH) facility at the Future of Manufacturing Laboratory 1 of Singapore Centre for 3D Printing (SC3DP) in Nanyang Technological University (NTU), Singapore was employed to fabricate the test specimens in the present investigations. The machine which consists of a Gaussian distributed Yb:YAG laser with a maximum power of 400 W and a laser beam spot size of 80 µm was utilised to melt and fuse the base powder. The laser melting process was carried out in the machine's build chamber where inert argon gas was first used to flush the chamber to attain an oxygen level of less than 0.2% so as to minimise oxidation and combustion of powder. The first layer of powder was distributed evenly on the base-plate by a recoater and the laser beam was directed to melt the powder based on a preprogramed model. Upon completion of the laser melting process for the first layer, the base-plate was then lowered by one-layer thickness of 50 µm and the process was repeated until the parts are fully constructed. In the present investigations, an aluminium alloy (AlSi10Mg) was used as the base powder due to its relatively high thermal conductivity and light weight. The composition of the powder, obtained from Ref. [125], is tabulated in Table 3-1, it can be seen that aluminium makes up more than 87% of the alloy while the trace elements are included to improve the melting and fusion of the powders. In addition, the AlSi10Mg powder is spherical and has a particle size distribution of 20 µm to 63 µm. An image of the powder taken using the scanning electron microscope (SEM) is shown in Fig. 3-1. In this thesis, the specimens used for the heat transfer investigations were fabricated using the laser powers of 200 – 350 W, scanning speeds of 1150 – 1300 mm/s and hatch spacings of 0.08 – 0.17 mm.

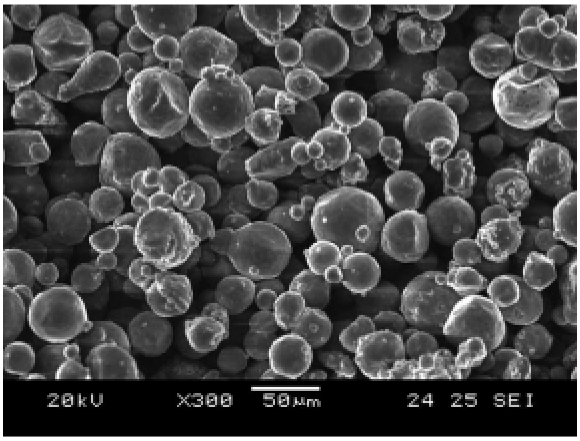

Fig. 3-1 Scanning electron microscope (SEM) image of AlSi10Mg powder.

Table 3-1 Composition of AlSi10Mg alloy [125].

Al	Si	Fe	Cu	Mn	Mg	Ni	Zn	Pb	Sn	Ti
Balance	9.0-11.0	0.55 (max)	0.05 (max)	0.45 (max)	0.2-0.45	0.05 (max)	0.10 (max)	0.05 (max)	0.05 (max)	0.15 (max)

3.2 Two- and three-dimensional fin arrays for natural convection condensation investigations

For the natural convection condensation investigations, 31 surfaces with enhanced structures and a plain surface were fabricated and experiments were conducted to determine their heat transfer characteristics. The enhanced structures can be categorised into two-dimensional longitudinal fin arrays and three-dimensional pin fin arrays. For each enhanced surface, the fin arrays are fabricated onto a 25 mm × 25 mm × 4 mm base plate as an integrated build piece. A summary of the geometrical parameters of all the surfaces investigated is shown in Table 3-2.

The two-dimensional fin arrays include a surface with triangular longitudinal fins, a surface with sinusoidal longitudinal fins and a surface with rectangular longitudinal fins. These specimens are named $T1$, $W1$ and $R1$, respectively. The $T1$ fin has a triangular cross-section with the base width (d_b) of 1.16 mm and the fin height (l) of 1.28 mm whereas the $R1$ fin has a rectangular cross-section with the same base width (d_b) and height (l) as the $T1$ fin. On the other hand, the $W1$ fin has a sinusoidal cross-section with a concave stem (in red) and a convex tip (in blue) as shown in Fig. 3-2. In the concave region of the fin, it can be observed that the fin width decreases and then increases with increasing fin height. On the other hand, in the convex region, the fin width increases and then decreases with increasing fin height. Therefore, there exists a minimum fin width which corresponds to the largest radius of curvature in the concave region and it is denoted as d_s. Similarly, there also exists a maximum fin width in the convex region and it is denoted as d_t in Fig. 3-2. The base width (d_b) and fin height (l) of a $W1$ fin are 1.24 mm and 1.25 mm, respectively. In addition, $T1$, $W1$ and $R1$ also have the same fin pitch (p) of 1.25 mm which is measured from the centre of one fin to the centre of the adjacent fin. The schematic diagrams of the longitudinal fin parameters are shown in Fig. 3-3 and the microscope images of the fin structures taken using an Olympus SZX7 microscope are depicted in Fig. 3-4.

The three-dimensional fin arrays include nine surfaces with conical pin fins (specimens $C1$ – $C9$), nine surfaces with sinusoidal pin fins (specimens $S1$ – $S9$) and 10 surfaces with cylindrical pin fins (specimens $MF1$ – $MF9$ and $L1$). These specimens are summarised in Table 3-2. Out of the 10 cylindrical pin fin specimens, only the pin fins of specimen $L1$ are in the millimetre range scale whereas the pin fins of specimens $MF1$ – $MF9$ fins are in the micrometre size range. The $L1$ specimen has the same d_b,

l and p values as $R1$. On the other hand, all the cylindrical pin fins of $MF1$ – $MF9$ have the same diameter (d_b) of 300 µm but are of different fin pitch (p) and fin height (l). The schematic diagram of a cylindrical pin fin specimen is shown in Fig. 3-5 (a) where p and l of the pin fins are depicted. In this investigation, the p values of the pin fins are 300 µm, 600 µm and 900 µm. On the other hand, similar l values of 300 µm, 600 µm and 900 µm are used for the pin fin arrays. Figure 3-6 shows the microscopic images of specimens $MF7$ and $MF8$.The conical pin fin specimens ($C1$ – $C9$) have the same fin base diameter (d_b) of 1.16 mm but are of different p and l. In this investigation, the fin pitch (p) of 1.25 mm, 1.67 mm and 2.50 mm and the fin height (l) of 1.28 mm, 1.92 mm and 2.56 mm are used. The sinusoidal pin fin specimens ($S1$ – $S9$), on the other hand, have the same fin base diameter (d_b) of 1.24 mm but are of three different fin heights (l) of 1.25 mm, 1.66 mm and 2.49 mm and three different fin pitches (p) of 1.25 mm, 1.67 mm and 2.50 mm. It should be noted that similar values of p are used for both the conical and sinusoidal pin fin specimens. Isometric drawings of the sinusoidal pin fins of different heights are shown in Fig. 3-7. The pin fin with l of 1.66 mm, as shown in Fig. 3-7 (b) has a profile similar to those developed by Wang et al. [43]. It can be seen from this figure that in order to maintain the same fin base diameter (d_b) for all the pin fins, the longer pin fins of Fig. 3-7 (c), with l of 2.49 mm, are elongated in the vertical direction whereas the shorter pin fins of Fig. 3-7 (a), with l of 1.25 mm are shortened in the vertical direction. This resulted in the shorter pin fin having a rounder tip and the longer pin fin having a sharper tip. However, in order to minimise the radii of curvature of the fins at different fin heights, the sinusoidal fins of different heights were designed to have the same d_s, d_t and d_b values depicted in Fig. 3-2.

The microscope images of the *C*1, *L*1 and *S*1 pin fin structures taken using an Olympus SZX7 microscope are shown in Fig. 3-8.

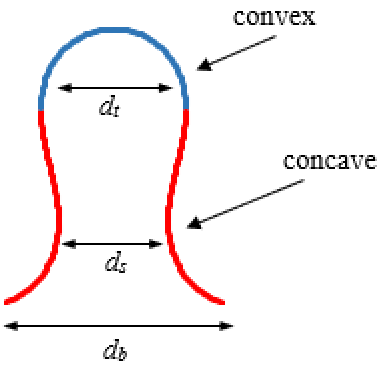

Fig. 3-2 Schematic diagram of a sinusoidal fin.

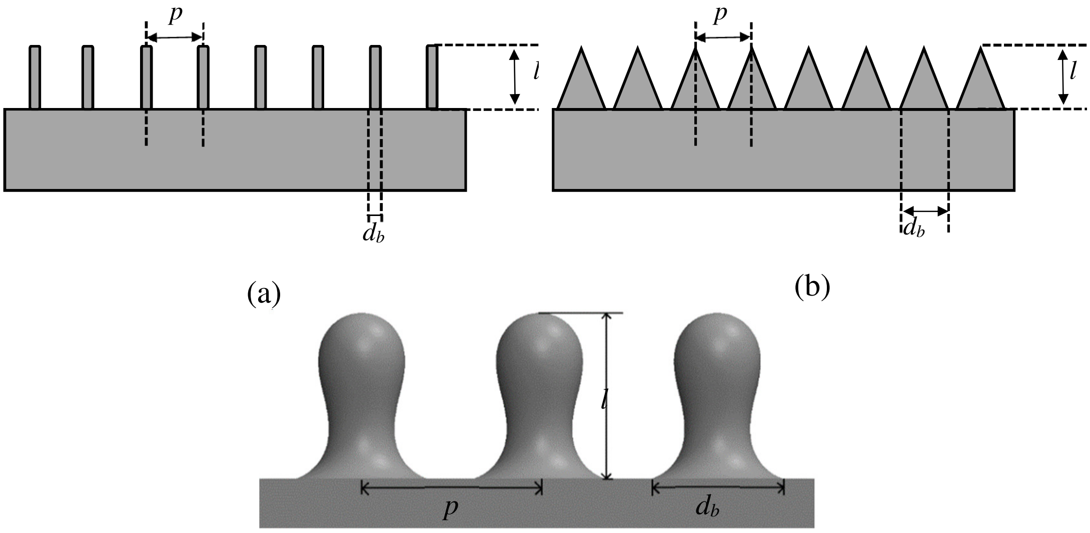

(a)

(b)

(c)

Fig. 3-3 Schematic diagrams of longitudinal fin parameters of (a) *R*1, (b) *T*1 and (c) *W*1 specimens.

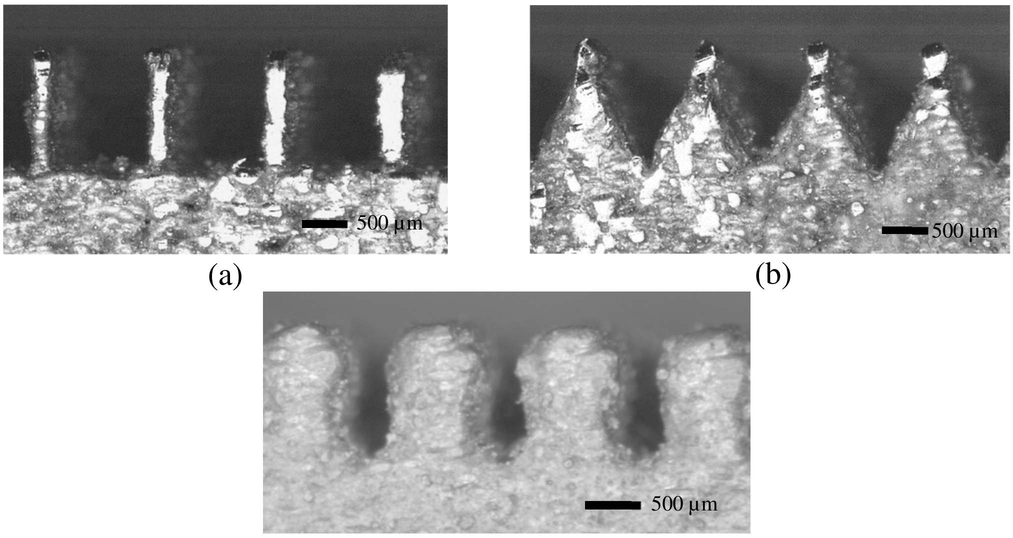

(a) (b)

(c)

Fig. 3-4 Microscope images of (a) *R*1, (b) *T*1 and (c) *W*1 longitudinal fin structures.

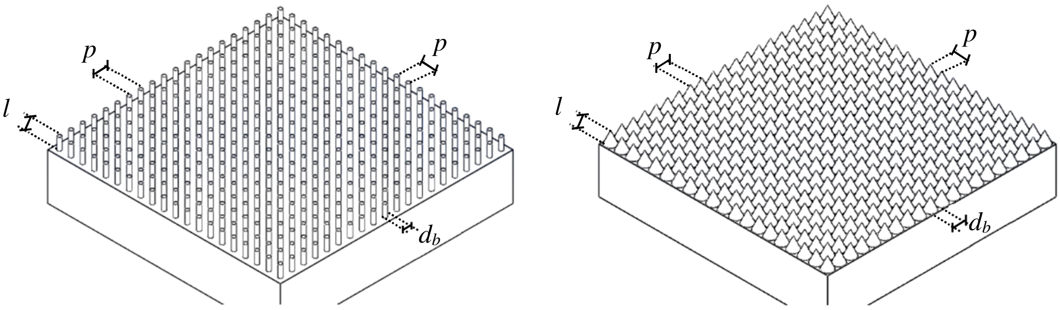

(a) (b)

Fig. 3-5 Schematic diagrams of pin fin parameters of (a) cylindrical pin fin specimens (*MF*1 – *MF*9 and *L*1) and (b) conical pin fin specimens (*C*1 – *C*9).

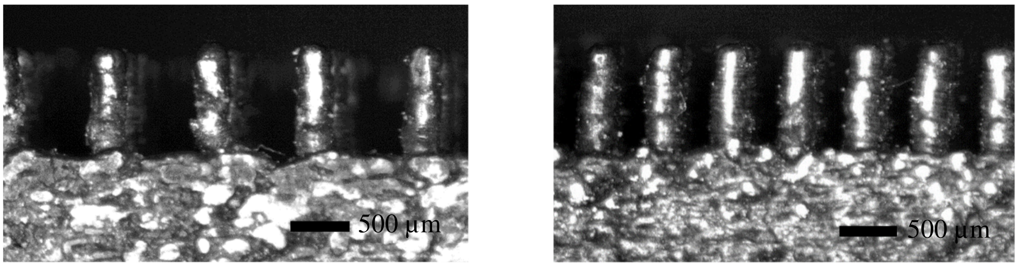

(a) (b)

Fig. 3-6 Microscope images of (a) specimen *MF*7 and (b) specimen *MF*8.

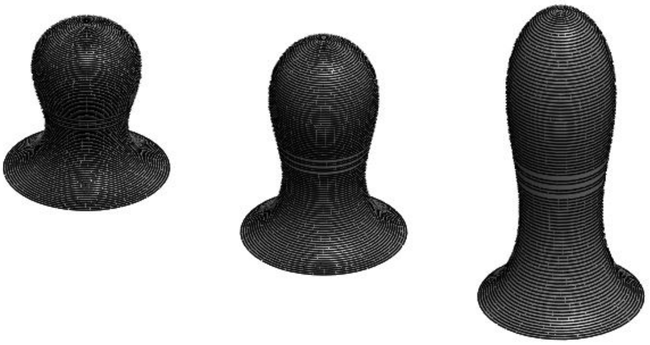

(a) (b) (c)

Fig. 3-7 Three-dimensional drawings of sinusoidal pin fin with (a) $l = 1.25$ mm, (b) $l = 1.66$ mm and (c) $l = 2.49$ mm.

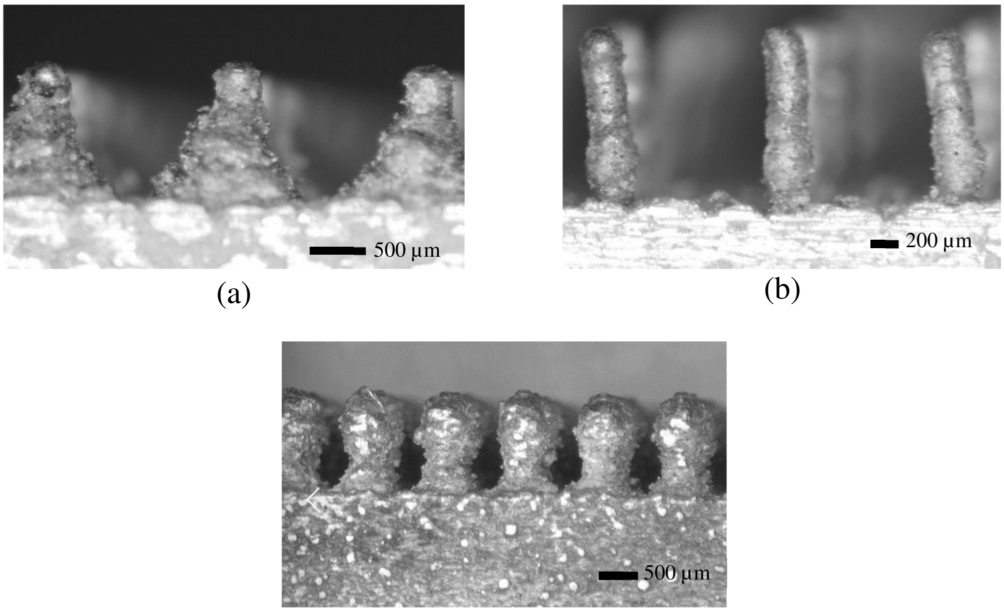

(a) (b)

(c)

Fig. 3-8 Microscope images of (a) *C*1 pin fin, (b) *L*1 pin fin and (c) *S*1 pin fin structures.

The conical pin fins (*C*1 – *C*9) and the triangular longitudinal fins (*T*1) geometries are selected for the investigation as they have large curvatures at their tips. The large curvatures can promote condensate thinning at the fin tip and have the potential of enhancing condensation heat transfer. On the other hand, the sinusoidal fin designs (*S*1

– *S*9 and *W*1) aim to improve condensate drainage from the fin tip to the fin base by taking advantage of surface tension forces induced by the change in curvature of the fin shape. In addition, due to its large convex tip, this fin structure also resulted in a large region where the condensate film is thin and has the potential of increasing the overall heat transfer rate from the surface. The sinusoidal fin design was originally proposed by Wang et al. [43] from their numerical investigation. However, this is the first time such a fin structure has been fabricated and experimentally investigated. In addition, the *MF*1 – *MF*9 designs aim to explore the use of micro-size pin fins to enhance condensation heat transfer. Micro-pin-fins have large surface areas and were found to be effective in enhancing single-phase [126] and boiling [127] heat transfer. However, to the best of the author's knowledge, investigations on the use of cylindrical micro-pin-fins have not been reported. Finally, the conventional millimetre size cylindrical pin fin specimen (*L*1), the rectangular longitudinal fin (*R*1) and a plain AlSi10Mg surface with dimensions of 25 mm × 25 mm × 4 mm were also fabricated. The plain surface served as a control surface for comparison against other enhanced surfaces. Prior to the experiments, it was polished using grit 800, 1200, 2000 and 5000 emery papers so that the top side of the surface had a mirror-like finish. In addition, the area enhancement factors (ε) which denote the ratio of the total heat transfer area (A_t) of a fin surface to the heat transfer area of the plain surface (A_{plain}) are also summarised in Table 3-2. Measurements of the fabricated specimens were performed and the details are reported in Appendix A. It should be noted that the maximum deviation in the design and fabricated dimensions of the fin structures is not more than 8%.

Table 3-2 Geometrical parameters of specimens fabricated for natural convection condensation investigation.

Specimen name	d_b (mm)	l (mm)	p (mm)	A_t (mm^2)	f_d (mm^{-2})	ε	Description
$C1$	1.16	1.28	1.25	1227	0.64	1.96	Conical pin fin
$C2$	1.16	1.28	1.67	963	0.36	1.54	
$C3$	1.16	1.28	2.50	775	0.16	1.24	
$C4$	1.16	1.92	1.25	1664	0.64	2.66	
$C5$	1.16	1.92	1.67	1210	0.36	1.94	
$C6$	1.16	1.92	2.50	885	0.16	1.42	
$C7$	1.16	2.56	1.25	2115	0.64	3.38	
$C8$	1.16	2.56	1.67	1463	0.36	2.34	
$C9$	1.16	2.56	2.50	998	0.16	1.60	
$S1$	1.24	1.25	1.25	1558	0.64	2.49	Sinusoidal pin fin
$S2$	1.24	1.25	1.67	1150	0.36	1.84	
$S3$	1.24	1.25	2.50	858	0.16	1.37	
$S4$	1.24	1.66	1.25	1890	0.64	3.02	
$S5$	1.24	1.66	1.67	1337	0.36	2.14	
$S6$	1.24	1.66	2.50	941	0.16	1.51	
$S7$	1.24	2.49	1.25	2578	0.64	4.12	
$S8$	1.24	2.49	1.67	1724	0.36	2.76	
$S9$	1.24	2.49	2.50	1113	0.16	1.78	
$MF1$	0.3	0.3	0.9	802	1.00	1.28	Cylindrical micro-pin-fin
$MF2$	0.3	0.3	0.6	1100	2.69	1.76	
$MF3$	0.3	0.3	0.3	1677	5.95	2.68	
$MF4$	0.3	0.6	0.9	978	1.00	1.57	
$MF5$	0.3	0.6	0.6	1576	2.69	2.52	
$MF6$	0.3	0.6	0.3	2729	5.95	4.37	
$MF7$	0.3	0.9	0.9	1155	1.00	1.85	
$MF8$	0.3	0.9	0.6	2051	2.69	3.28	
$MF9$	0.3	0.9	0.3	3781	5.95	6.05	
$L1$	0.3	1.28	1.25	1108	0.64	1.77	Cylindrical pin fin
$T1$	1.16	1.28	1.25	1480	-	2.37	Triangular longitudinal fin
$W1$	1.24	1.25	1.25	1696	-	2.71	Sinusoidal longitudinal fin
$R1$	0.3	1.28	1.25	1905	-	3.05	Rectangular longitudinal fin
Plain	-	-	-	625	-	1.00	Plain surface

3.3 Three-dimensional pin fin tubes for forced convection condensation investigations

In order to explore the effects of millimetre size three-dimensional pin fin structures on the forced convection condensation heat transfer in circular tubes, two fin geometries, viz., the conical pin fins and the dome-shape pin fins were tested. These pin fins were fabricated on the internal walls of the condenser tubes with a total of seven condenser tube designs with pin fin structures being fabricated by SLM. Their geometrical parameters are summarised in Table 3-3.

The conical pin fins of the enhanced tubes have the fin base diameter (d_b) of 1.11 mm and fin height of 1.22 mm and are similar in dimensions to the pin fins of specimen $C1$ used for the natural convection condensation investigation. As shown in Table 3-3, five enhanced tubes ($CF1$ – $CF5$) have conical pin fins integrated on their internal tube walls. The conical pin fins are uniformly arranged circumferentially and axially on the inner tube wall. In this investigation, the conical pin fin tubes consist of different circumferential fin pitches (p_c) of 0.262 rad, 0.349 rad and 0.524 rad and longitudinal fin pitches of 1.20 mm and 1.80 mm. The circumferential fin pitch (p_c) is defined as the angular distance between the centre of one fin to the adjacent fin while the longitudinal fin pitch (p_l) is defined by the distance from the centre of one fin to its adjacent fin in the axial direction.

The images and perspective drawings of two condenser tubes with dome-shape pin fins ($PF1$ – $PF2$) are shown in Fig. 3-11 and their geometrical parameters are summarised in Table 3-3. The dome-shape pin fins closely resemble the sinusoidal pin fins used in the natural convection condensation experiments and consist of a convex tip but with a cylindrical stem. The fin base diameter (d_b) is fixed at 2 mm while $PF1$ and $PF2$ have fin lengths (l) of 4.0 mm and 2.5 mm, respectively. The pin fins are integrated onto the internal tube walls in the circumferential and axial directions and are tilted at 45° with respect to the tube central axis. It should be noted that the pin fins are tilted in order to facilitate the SLM fabrication process. This is because the condenser tubes have to be fabricated vertically in the SLM built chamber to obtain good dimensional tolerance and tube roundness. However, this may result in the collapse of the overhanging internal pin fin structures during fabrication, especially when the fins are long and are comprised of large fin tips such as the dome-shape fins. To overcome this issue, the dome-shape fins are tilted at an inclination angle of 45° to prevent excessive overhang.

Due to the size limitation of the SLM built chamber, five tubes of the same design with each having a length of 170 mm, were fabricated. After fabrication, all five tubes were then welded to form the test specimen. In addition, a plain tube (without any internal structure) was fabricated by SLM and a commercial plain aluminium tube that was made from Al-6061 was also prepared and experimentally investigated for comparison. All the condenser tubes have an inner diameter (d_i) of 8.7 mm and an outer diameter (d_o) of 12.7 mm.

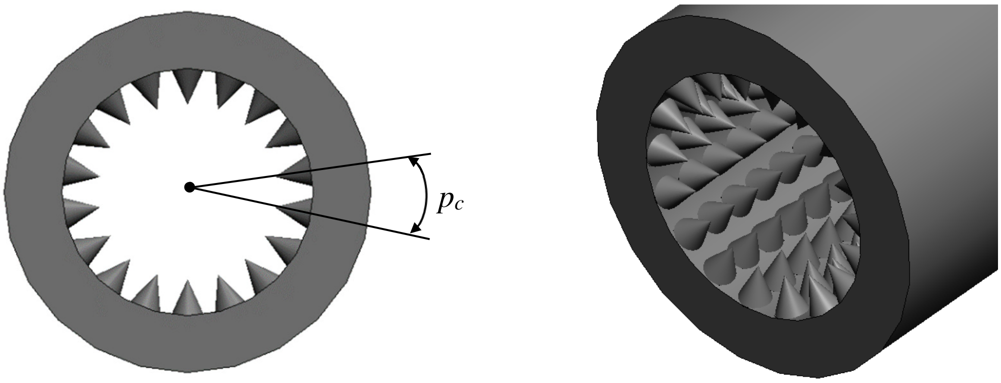

(a) (b)

Fig. 3-9 (a) Cross-sectional view and (b) isometric view of condenser tube with conical pin fins.

(a) (b) (c)

Fig. 3-10 Images of conical pin fin tubes (a) *CF*1, (b) *CF*2 and (c) *CF*3.

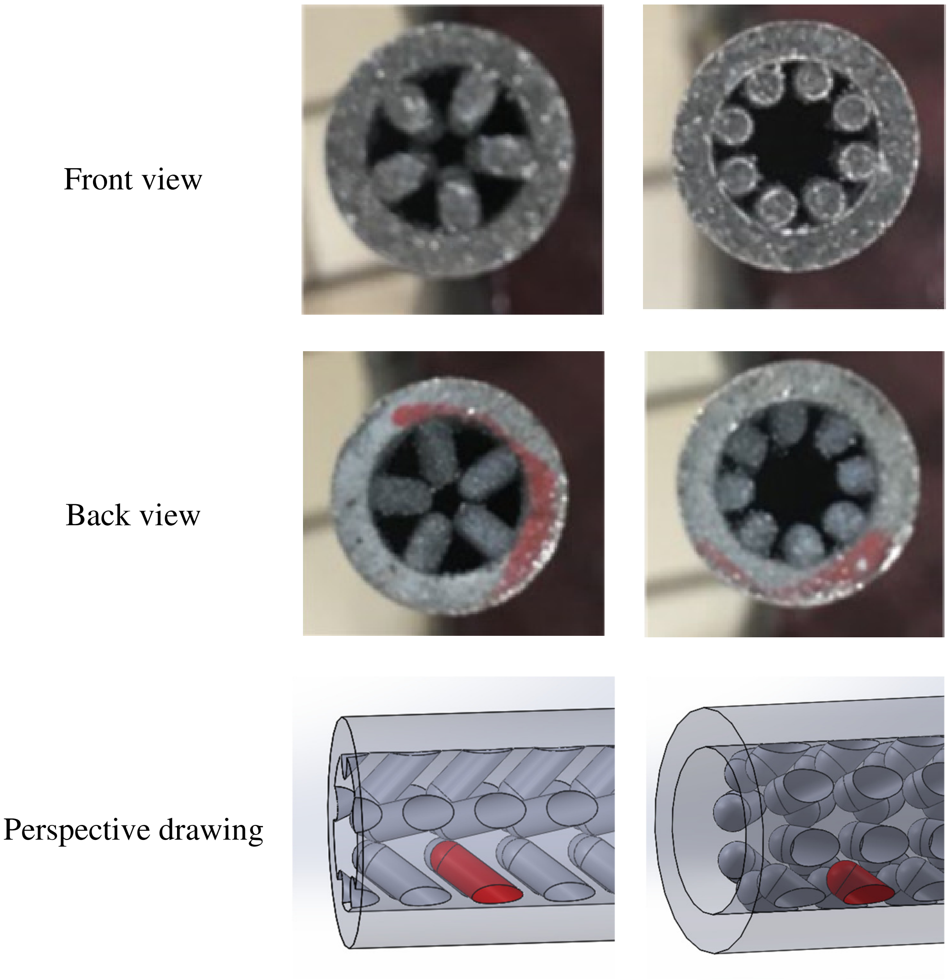

(a) (b)

Fig. 3-11 Front view, back view and perspective drawing of dome-shape pin fin tubes (a) *PF*1 and (b) *PF*2.

Table 3-3 Geometrical parameters of pin fin and plain tubes fabricated for forced convection condensation investigation.

Test specimens	d_o (mm)	d_i (mm)	p_c (rad)	p_l (mm)	d_b (mm)	l (mm)	A_t (mm^2/100 mm)	Description
*CF*1	12.7	8.7	0.262	1.20	1.11	1.22	9917	Conical pin fin
*CF*2	12.7	8.7	0.349	1.20	1.11	1.22	8108	
*CF*3	12.7	8.7	0.524	1.20	1.11	1.22	6300	
*CF*4	12.7	8.7	0.262	1.80	1.11	1.22	7506	
*CF*5	12.7	8.7	0.349	1.80	1.11	1.22	6300	
*PF*1	12.7	8.7	1.257	3.00	2	4.5	5818	Dome-shape pin fin
PF2	12.7	8.7	0.785	3.00	2	2.5	5064	
Plain SLM	12.7	8.7	-	-	-	-	2733	
Commercial Al	12.7	8.7	-	-	-	-	2733	

Chapter 4 – Experimental Setup and Procedures

Two sets of test facilities were designed and developed to investigate both the natural and forced convection condensation of the SLM fabricated specimens. The natural convection condensation experiments were conducted with steam as the working fluid and fundamental studies on the filmwise condensation on external surfaces were carried out. On the other hand, the forced convection condensation experiments on the enhanced and plain tubes were conducted with R134a refrigerant as the working fluid. R134a is a hydrofluorocarbon (HFC) which has insignificant ozone layer depletion potential (ODP) and is non-flammable. Amongst the other HFCs, R134a also has one of the lowest global warming potential (GWP) of 1430 and has been used as the replacement for R12 since the 1990s. It has been widely used in many commercial chillers, refrigerators and automobile air conditioning systems and therefore is selected for the present investigation. In this chapter, details of the components used in each set of test facilities, experimental procedures and data reduction are elaborated.

4.1 Natural convection condensation test facilities

4.1.1 Experimental facilities

The experimental setup for the filmwise condensation investigation is shown schematically in Fig. 4-1. It consists of a vapour loop and a water loop. In the vapour loop, a variable speed gear pump was used to supply water to an evaporator system. The variable speed drive of the gear pump allows the water flow rate into the evaporator system to be controlled. The evaporator system employed in the present investigation is a two-stage evaporator, consisting of a primary stage and a secondary stage. The evaporators were installed with heaters which could supply up to 1.2 kW of heat. Two variable power transformers were connected to the heaters and were used to control the heater output power. The supplied water into the primary stage evaporator was converted into a saturated liquid-vapour mixture and the secondary stage evaporator was used to further convert the saturated liquid-vapour mixture to superheated vapour. By controlling the heater output power, the superheated steam temperature can be varied. After leaving the evaporator, the steam was channelled to the condensation chamber. With the water mass flow rate recorded from the rotameter installed before the evaporator and from the conservation of mass, the vapour velocity entering the condensation chamber can be calculated. Details of the condensation chamber are shown in Fig. 4-2. The test specimen was bonded onto the top surface of the copper block using a thermally conductive paste. Before adhering the specimen, both the back surface of the specimen and top surface of the copper block were smoothened using emery papers of 2000 and 5000 grit sizes to reduce the thermal contact resistance. As the vapour comes into contact with the specimen, chilled water is allowed to circulate through the water channels at the base of the copper block to maintain the specimen top surface at a subcooled temperature (ΔT). Four K-type thermocouples (T_1 to T_4) were positioned at locations along the copper block at 10 mm intervals apart and another K-type thermocouple was embedded within the specimen 1.5 mm below the condensing top surface to measure the specimen temperature (T_s). An image of the natural convection condensation test facility is shown in Appendix B

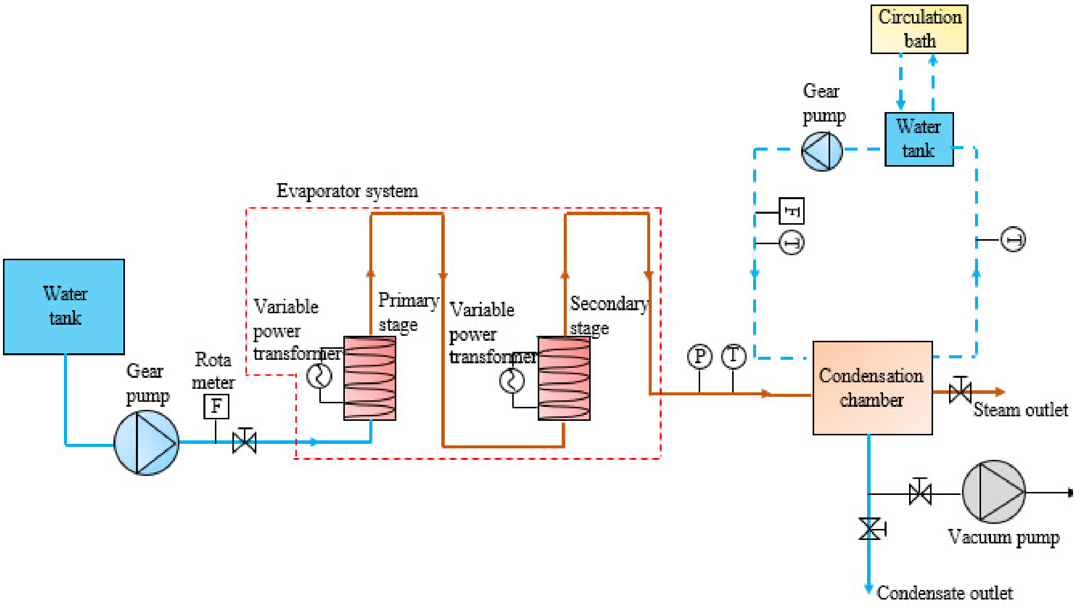

Fig. 4-1 Schematic of experimental setup.

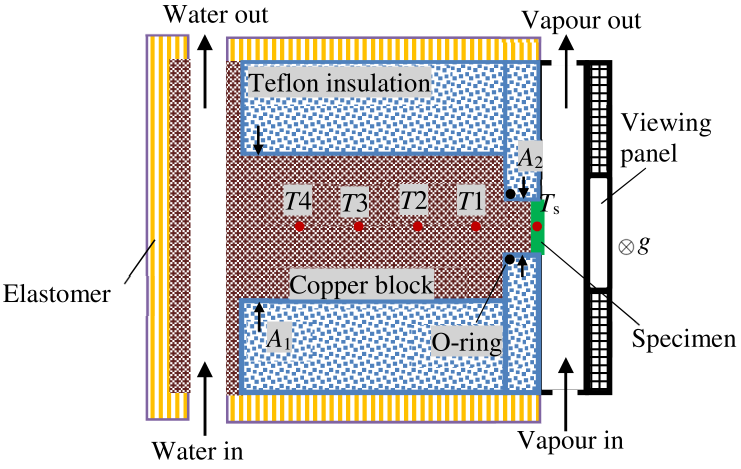

Fig. 4-2 Top view of condensation chamber.

4.1.2 Experimental procedures and data reduction

The experiments were conducted close to ambient pressure and the pressure and temperature of the steam were measured using a manometer and thermocouple installed before the condensation chamber. In addition, the variable power transformer connected to the secondary stage evaporator was used to vary the heater input power to achieve the inlet vapour temperature of 2.0°C above the saturation value to ensure that the inlet vapour is dry. In order to vary the wall subcooling temperature of the specimen (ΔT), a water loop system was used. The water loop system consists of a chiller and a gear pump which allows the chilled water supply flow rate and temperature to the water channels of the copper block to be varied. The chilled water flow rate and temperature were adjusted to vary ΔT. Prior to the start of the experiments, a vacuum pump was first employed to remove any trace of non-condensable gas and thereafter, vapour generated from the evaporator was used to flush the condensation chamber continuously for up to an hour prior to the start of the experiment. The condensation heat flux (q'') was determined using Eq. (4-1) and the wall temperature of the condensing surface (T_w) was computed from Eq. (4-2). In Eqs. (4-1) and (4-2), k_c and k_s denote the thermal conductivities of the copper block and the specimens made of AlSi10Mg, respectively. The $\frac{dT}{dx}$ term is the temperature gradient between T_1 and T_4 and Δy is the distance from T_s to T_w. Finally, using Eq. (4-3) the condensation heat transfer coefficient (h) can be calculated.

$$q'' = -k_c \frac{A_1}{A_2} \frac{dT}{dx} \tag{4-1}$$

$$T_w = T_s + \frac{q'' \Delta y}{k_s} \tag{4-2}$$

$$h = \frac{q''}{T_{sat} - T_w} = \frac{q''}{\Delta T} \tag{4-3}$$

For k_c, a thermal conductivity value of 391 W/m·K for oxygen-free copper was used. However, as a wide range of AlSi10Mg thermal conductivity (k_s) values were reported in the literature [125, 128], a bulk AlSi10Mg specimen was fabricated with the same laser parameters as the test specimens and its thermal conductivity was determined experimentally. Details of the thermal conductivity measurements can be found in Appendix C. From the measurements, k_s was found to be 124 W/m·K. In the present investigation, the rotameter flow rate was fixed at 10 mL/min which translates to a low vapour velocity of 0.6 m/s through the condensation chamber to simulate free-convection condensation. Steady state is deemed to be achieved when the temperature changes (T_1, T_2, T_3, T_4 and T_w) were observed to be within ±0.1°C for more than 5 minute. The temperatures were than acquired using the "Yokogawa MX100" data acquisition unit at the sampling rate of 2 Hz averaged over 1 min. The thermocouples, rotameter and manometer have accuracies of ± 0.1°C, ± 0.5 mL/min and ± 10 Pa, respectively. Using the method by Taylor [129], the uncertainties of q'' and h were determined to be not more than ± 7.2%. The details of the uncertainty analyses can be found in Appendix D.

4.2 Forced convection condensation test facilities

4.2.1 Experimental facilities

Figure 4-3 shows the test facility used in the investigations on forced convection condensation. It consists of a refrigerant circulation system and four water circulation systems. The refrigerant circulation system consists of a refrigerant separator, a gear pump, a Coriolis mass flow meter, an evaporator, a test section, and two post condensers. The gear pump was used to circulate the subcooled R134a in the separator through the Coriolis mass flow meter to measure the refrigerant mass flow rate. This Coriolis mass flow meter has a nominal flow rate range of 0 to 20 kg/min and a relative accuracy of ± 0.1%. The subcooled refrigerant was subsequently heated by the evaporator to achieve the required vapour quality at the evaporator outlet. Thereafter, the refrigerant liquid-vapour mixture was channelled into the test section where convective condensation in the circular tubes occurs. After leaving the test section, two post condensers were employed to further condense the refrigerant to a subcooled temperature. Finally, the refrigerant was circulated back to the separator. Three K-type thermocouples, calibrated to an accuracy of ± 0.1°C, were installed in the refrigerant system to measure the refrigerant inlet and outlet temperatures of the evaporator and the test section. Three pressure sensors with a range of 0 to 20 bar and an accuracy of ± 0.05% were used to measure the refrigerant pressure at the evaporator inlet, the test section inlet and the test section outlet. The four water circulation systems supplied water to the evaporator, test section and the two post condensers. The evaporator and test section are double pipe heat exchangers with refrigerant flowing through the internal tube and water flowing through the tube annulus. Details of the test section are shown in Fig. 4-4. Each test specimen was enclosed by a larger copper pipe of outer diameter 19 mm and thickness 1.2 mm to form a counter-flow double pipe heat exchanger. Cold water flows through the copper pipe. The effective length of the condenser tubes which are enclosed by the copper pipe was fixed at 670 mm. Four K-type thermocouples, calibrated to an accuracy of ± 0.1°C, were installed at the evaporator and test section inlets and outlets. The water flow rate was measured by two turbine wheel flow meters with a nominal flow range of 0.4 to 5.0 L/min and an accuracy of ± 0.5%. After leaving the test section, the refrigerant was channelled into two heat exchangers, which served as the post condensers, to further condense the liquid-vapour refrigerant to subcooled liquid. One of the post condensers is a plate type heat exchanger with a constant heat load and the other post condenser consists of a coil of copper tube inserted into a chilled water tank. By controlling the water inlet temperature and flow rate of the water circulation systems, different experimental conditions can be achieved. An image of the forced convection condensation test facility is shown in Appendix B

4.2.2 Experimental procedures and data reduction

In order to determine the inlet vapour quality (x_{in}) and outlet vapour quality (x_{out}) of the refrigerant at the test section, the enthalpy of the refrigerant at the evaporator inlet ($H_{ref,in}$) was first obtained using the temperature and pressure measured at the evaporator inlet. In the evaporator, heat is transferred from the hot water to the refrigerant. Therefore, the heat gained by the refrigerant in the evaporator can be calculated using Eq. (4-4), where m_h, $T_{h,in}$ and $T_{h,out}$ are the mass flow rate, inlet and outlet temperatures of the hot water, respectively. Due to the heat gain, the refrigerant changes phase from subcooled liquid to two-phase mixture and the vapour inlet quality at the test section (x_{in}) can be calculated using Eq. (4-5), where H_{sat}, h_{fg} and $\dot{m}_{ref}$ are the refrigerant saturation liquid enthalpy, latent heat of vaporisation and refrigerant mass flow rate, respectively. Using the same principle, the vapour outlet quality at the test section (x_{out}) can be determined by performing an energy balance at the test section as shown in Eqs. (4-6) and (4-7) where m_c, $T_{c,in}$, $T_{c,out}$ are the cold water mass flow rate, inlet temperature and outlet temperature at the test section. Using x_{in} and x_{out}, the average vapour quality (x_{ave}) of the refrigerant in the test section can be determined by Eq. (4-8).

$$Q_{evp} = c_{p,h} m_h \left(T_{h,in} - T_{h,out}\right) \tag{4-4}$$

$$x_{in} = \frac{\frac{Q_{evp}}{\dot{m}_{ref}} - \left(H_{sat} - H_{ref,in}\right)}{h_{fg}} \tag{4-5}$$

$$Q_{test} = c_{p,c} m_c \left(T_{c,out} - T_{c,in}\right) \tag{4-6}$$

$$x_{out} = x_{in} - \frac{Q_{test}}{\dot{m}_{ref} h_{fg}} \tag{4-7}$$

$$x_{ave} = \frac{x_{in} + x_{out}}{2} \tag{4-8}$$

The condensation heat transfer coefficients of the test specimen (h_{ref}) were computed by the log-mean-temperature difference (*LMTD*) approach. Energy balance is first performed on the test section using Eqs. (4-9) and (4-10), where $T_{ref,in}$ and $T_{ref,out}$ are the refrigerant temperatures at the test section inlet and outlet, and *UA* is the product of the overall heat transfer coefficient and heat transfer area. Using Eq. (4-6), the Q_{test} values of Eq. (4-10) can be computed. On the other hand, *UA* consists of the cold water-side (h_c) and refrigerant-side (h_{ref}) heat transfer coefficients and can be expressed as Eq. (4-11).

In order to determine h_c, the internal tube was first supplied with hot water and the external tube with cold water to perform single-phase heat transfer tests. Therefore, Eq. (4-11) is replaced by Eq. (4-12) where h_h is the internal single-phase heat transfer coefficient and can be predicted by the Gnielinski correlation [130] of Eq. (4-13) for $3000 < \mathrm{Re} < 5 \times 10^6$ and $0.5 < \mathrm{Pr} < 2000$. The Fanning friction factor is determined from the Petukhov equation of Eq. (4-14) [131] and is valid for $3000 < \mathrm{Re} < 5 \times 10^6$. For the commercial aluminium tube, a relative roughness of 2.8×10^{-5} is used whereas for the plain SLM tube the relative roughness was measured to be 8.4×10^{-4} [121]. During the single-phase heat transfer tests, the Reynolds number inside the tube was held constant at 4490. By performing tests over a range of cold water flow rates, the cold water-side heat transfer coefficient (h_c) of the plain SLM and commercial aluminium tubes were obtained as Eqs. (4-15) and (4-16) where u_c is the mean velocity of the cold water.

$$LMTD = \frac{(T_{ref,out} - T_{c,in}) - (T_{ref,in} - T_{c,out})}{ln\left[\frac{(T_{ref,out} - T_{c,in})}{(T_{ref,in} - T_{c,out})}\right]} \tag{4-9}$$

$$UA = \frac{Q_{test}}{LMTD} \tag{4-10}$$

$$\frac{1}{UA} = \frac{1}{h_{ref}A_{ref}} + \frac{\ln(d_o/d_i)}{2\pi L_{pipe}k_{pipe}} + \frac{1}{h_c A_c} \tag{4-11}$$

$$\frac{1}{UA} = \frac{1}{h_h A_h} + \frac{\ln(d_o/d_i)}{2\pi L_{pipe}k_{pipe}} + \frac{1}{h_c A_c} \tag{4-12}$$

$$\frac{h_h d_i}{k_f} = \frac{(f/8)(\mathrm{Re}-1000)\mathrm{Pr}}{1+12.75(f/8)^{1/2}(\mathrm{Pr}^{2/3}-1)} \tag{4-13}$$

$$f = (0.790\ \mathrm{lnRe} - 1.64)^{-2} \tag{4-14}$$

$$h_c = 3030 \cdot {u_c}^{0.3811},\ \mathrm{W/m^2 \cdot K} \qquad \text{(Commercial Al tubes)} \tag{4-15}$$

$$h_c = 5056 \cdot {u_c}^{0.5026},\ \mathrm{W/m^2 \cdot K} \qquad \text{(SLM fabricated tubes)} \tag{4-16}$$

In this investigation, experiments were conducted at the R134a saturation pressure (P_{sat}) of 13.4 bar which is measured at the inlet of the test section, the refrigerant mass flow rate (m_{ref}) ranging from 50 kg/m^2·s to 200 kg/m^2·s and the average vapour quality (x_{ave}) between 0.2 and 0.8. Steady state condition is deemed to be reached when the temperature and pressure fluctuations were observed to be within ±0.1°C and ±0.03 bar, respectively for more than 10 minutes. The temperature, pressure and flow rates were than acquired using the "Yokogawa MX100" data acquisition unit at the sampling rate of 2 Hz averaged over 1 minute. Using the method described by Taylor [129], the maximum uncertainties of x_{in}, x_{out}, h_{ref} and ΔP were determined and found to be not more than ±2%, ±3%, ±15% and 22%, respectively. Details of the uncertainty analyses can be found in Appendix E. It should be noted that the uncertainty of pressure drop (ΔP) of ±22% is the maximum relative uncertainty. This corresponds to the lowest measured ΔP of 0.06 bar. As the measured ΔP value increases with vapour quality and mass flux, the uncertainty of ΔP reduces. For instance, for specimen *CF*1 at m_{ref} of 200 kg/m·s and x_{ave} of 0.76, the measured ΔP value is 0.17 bar, this corresponds to a relative uncertainty of only ±8.7%.

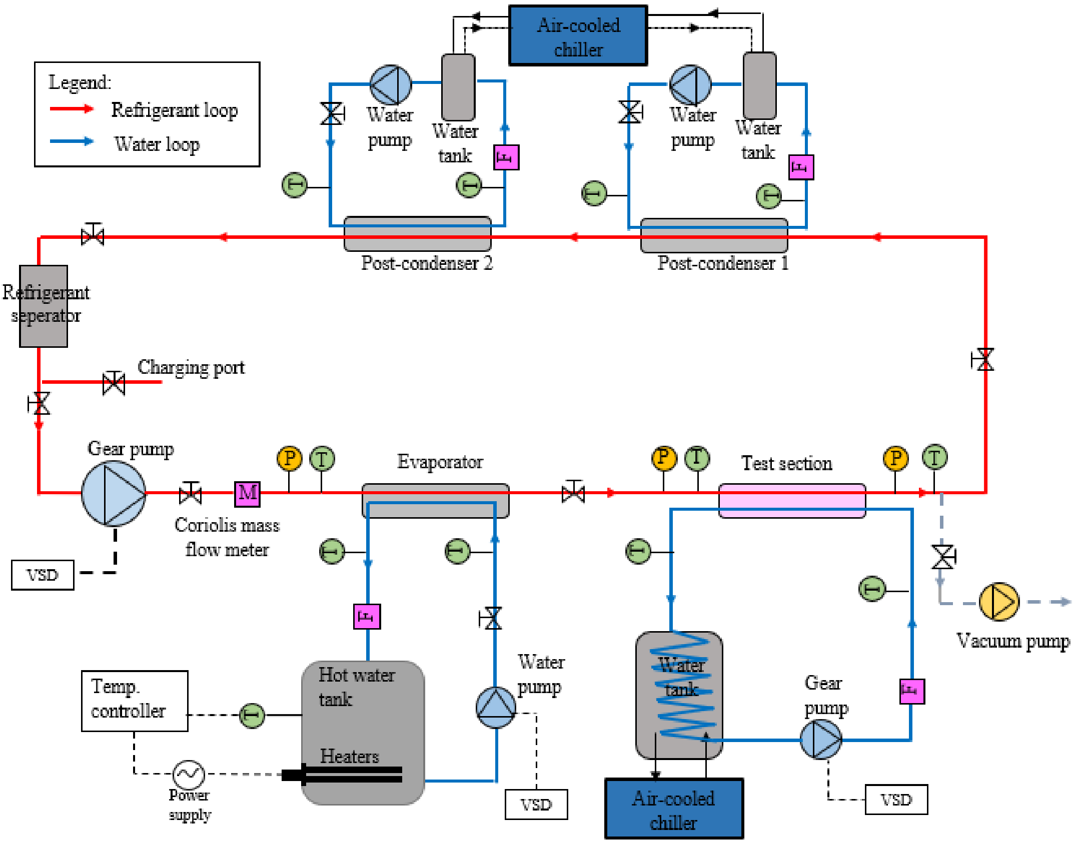

Fig. 4-3 Schematic of experimental facility.

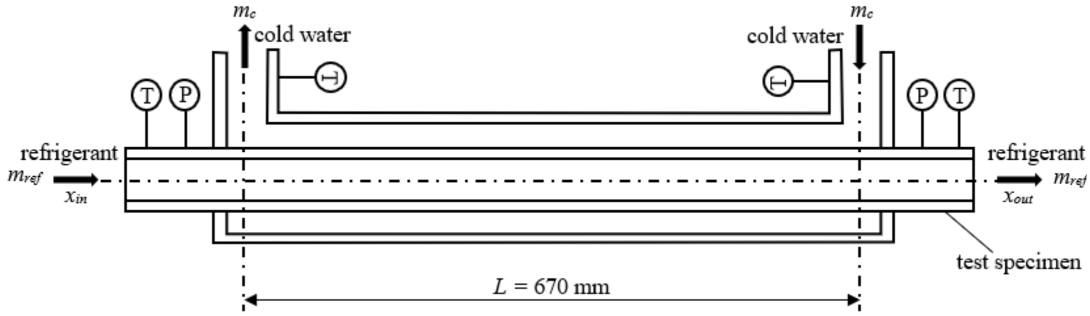

Fig. 4-4 Schematic of test section.

Chapter 5 - Natural Convection Condensation on Two and Three-dimensional Fin Arrays Produced by Selective Laser Melting

5.1 Validation of experimental results

A plain SLM specimen was first tested to validate the accuracy of the data obtained from the test facility of Fig. 4-1. Figure 5-1 shows the typical temperatures recorded from thermocouples T_1 to T_4 along the copper block. It can be seen that the temperatures vary linearly with the axial location (x) and, therefore, the one-dimensional heat conduction assumption used to compute the condensation heat flux as shown in Eq. (4-1) is valid. A model for predicting filmwise condensation heat transfer from a plain vertical flat plate surrounded by stagnant saturated vapour was proposed by Nusselt [27] and is shown in Eq. (2-3). This model considers the condensate flow to be laminar and driven only by gravity. In the present investigation, the vapour velocity was maintained at a low value of 0.6 m/s so as to minimise the convection effect due to the flowing vapour. Figure 5-2 compares the condensation heat flux of the plain AlSi10Mg surface obtained from the experiments (q''_{exp}) and the values of q''_{Nu} predicted by Eq. (2-3). For the range of ΔT tested, it can be seen that the experimental results lie within ±15% of the theoretical model. It should be noted that the Nusselt model considers only the effects of momentum diffusion and gravity driven flow. The other effects such as the formation of waves on the liquid film [29] and the retardation of liquid film due to the interfacial shear stress between the condensate and the stagnant vapour [33, 34] may have contributed to the observed deviation. On the other hand, even though the vapour was slightly superheated by 2°C in this experiment, due to the high latent heat of vaporization (h_{fg}) of steam, the additional sensible heat produced by the superheated steam had negligible effect on the q''_{exp} values [28]. In all, the comparison of q''_{exp} and q''_{Nu} indicates relatively good accuracy of the experimental setup.

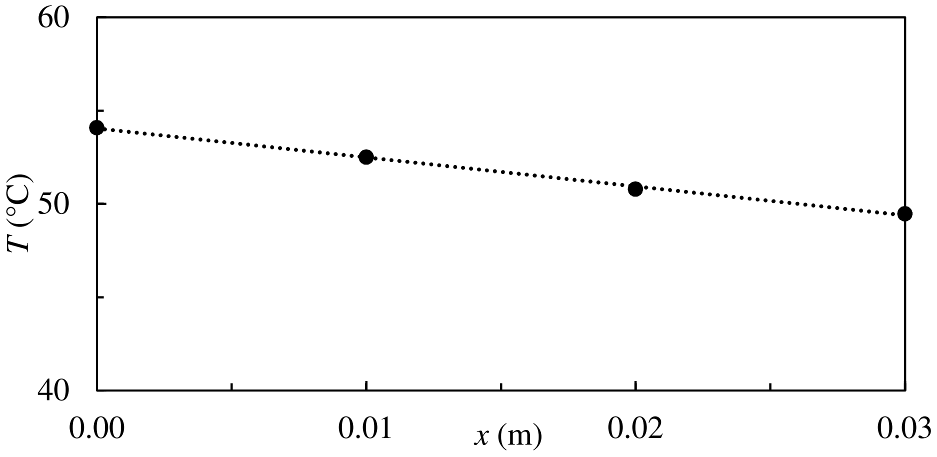

Fig. 5-1 Plot of temperatures measured from thermocouples T_1 to T_4 against x-direction for plain SLM surface at $\Delta T = 10.3$°C.

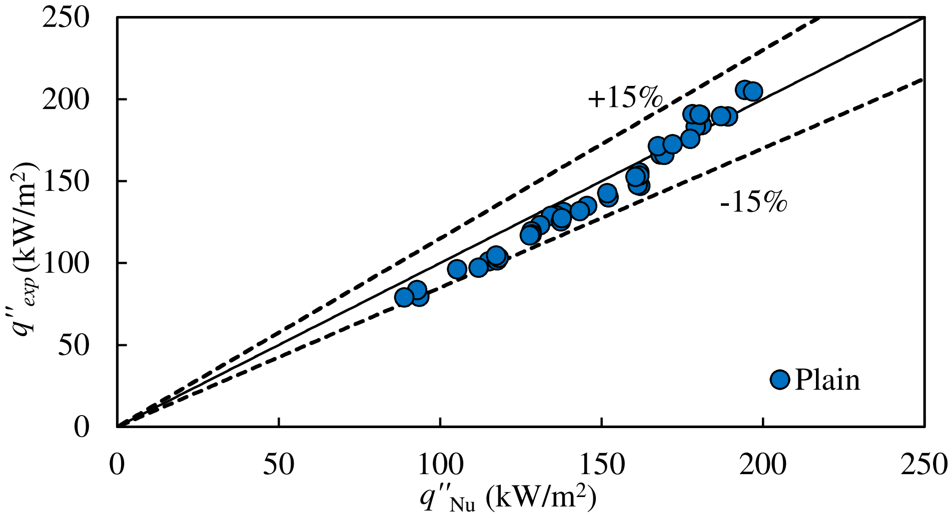

Fig. 5-2 Comparison of experimental result and theoretical model of Eq. (2-3) for plain surface.

5.2 Comparison of two and three-dimensional fins

It can be seen from Table 3-2 that specimens $C1$ and $T1$ have the same d_b of 1.16 mm, l of 1.28 mm and p of 1.25 mm and the triangular planes of their fins also have the same dimensions. Similar comparisons can also be made (1) between the sinusoidal pin fins of $S1$ and the sinusoidal longitudinal fins of $W1$ and (2) between the cylindrical pin fins of $L1$ and the longitudinal fins of $R1$. In this section, each of these three-dimensional pin fin arrays is compared against their equivalent two-dimensional longitudinal fin array to evaluate their condensation heat transfer performances.

Figure 5-3 shows the condensation heat flux (q'') and heat transfer coefficient (h) of the $L1$ and $R1$ specimens. It can be seen that $L1$ and $R1$ have higher q'' and h as compared to the plain surface. For instance, at ΔT of 10°C, the enhancements in h were 50% for $R1$ and 89% for $L1$ as compared to the plain surface. On the other hand, Fig. 5-4 shows the q'' and h values of the $C1$ and $T1$ specimens and comparisons were made against the plain surface. Similarly, due to the presence of the enhanced structures, larger q'' and h values were recorded for the $C1$ and $T1$ specimens as compared to the plain surface. At ΔT of 10°C, for example, the enhancements in h for were 126% and 70% for $C1$ and $T1$, respectively. A comparison of the q'' and h values of the sinusoidal pin fin specimen ($S1$) and the equivalent two-dimensional longitudinal fin specimen ($W1$) is shown in Fig. 5-5. Using the similar ΔT of 10°C for comparison, it can be seen that the enhancements in h as compared to the plain surface for $S1$ and $W1$ are 102% and 87%, respectively.

The above comparison only evaluates the heat transfer coefficient of the specimens at the reference ΔT of 10°C. In order to characterise the enhancements in the heat transfer coefficients of the specimens over the range of ΔT tested, Eq. (5-1) which denotes the thermal enhancement factor (η) was used. In this equation, q''_{enh} is the condensation heat flux of the enhanced surface and q''_{plain} is the condensation heat flux of the plain surface. As the experimental results for the plain surface are in good agreement with the Nusselt theory, Eq. (2-3) was used to estimate q''_{plain}. On the other hand, q''_{enh} for each of the enhanced surface was determined by curve-fitting the experimental data using a power function of Eq. (5-2). The curve-fitting was performed by the non-linear regression method from which the values a and b of Eq. (5-2) were determined. In Eq. (5-1), $\Delta T_{1,\mathrm{enh}}$ and $\Delta T_{2,\mathrm{enh}}$ are the lower and upper limits of the wall subcooled temperatures of the enhanced surfaces whereas $\Delta T_{1,\mathrm{plain}}$ and $\Delta T_{2,\mathrm{plain}}$ are the lower and upper limits of the wall subcooled temperatures of the plain surface. In order to standardise the computation of η, the values of $\Delta T_{1,\mathrm{enh}} = \Delta T_{1,\mathrm{plain}} = 3°\mathrm{C}$ and $\Delta T_{2,\mathrm{enh}} = \Delta T_{2,\mathrm{plain}} = 13°\mathrm{C}$ were used. The values of a, b and η for the various surfaces are shown in Table 5-1.

From Table 5-1, it can be seen that the pin fin structures (*L*1, *C*1 and *S*1) exhibit higher η values than the equivalent longitudinal fin structures (*R*1, *T*1 and *W*1). For instance, *L*1 has a η value of 1.60 whereas its equivalent longitudinal fin surface (*R*1) has a η value of only 1.37. In addition, the conical pin fin specimen (*C*1) also shows significantly higher η value of 2.02 as compared to its equivalent longitudinal fin surface *(T*1) which has an η value of only 1.36. Despite having larger η values, it can also be seen from Table 3-2 that the pin fin specimens have smaller heat transfer areas (A_t) than the equivalent longitudinal fin specimens. For example, *L*1 has 30% smaller A_t as compared to *R*1 but has 17% larger η values and *C*1 has 17% smaller A_t as compared to *T*1 but has 50% larger η values. In addition, it can also be computed from

Table 5-1 that $S1$ has 9% smaller A_t and 2% larger η value as compared to $W1$. Among the three pin fin specimens, the sinusoidal pin fin specimen ($S1$) exhibits the smallest difference in η value as compared to its equivalent longitudinal fin surface ($W1$).

$$\eta = \frac{\int_{\Delta T_{1,enh}}^{\Delta T_{2,enh}} q''_{enh} dT/(\Delta T_{2,enh}-\Delta T_{1,enh})}{\int_{\Delta T_{1,plain}}^{\Delta T_{2,plain}} q''_{plain} dT/(\Delta T_{2,plain}-\Delta T_{1,plain})} \tag{5-1}$$

$$q''_{enh} = a\Delta T^{b} \tag{5-2}$$

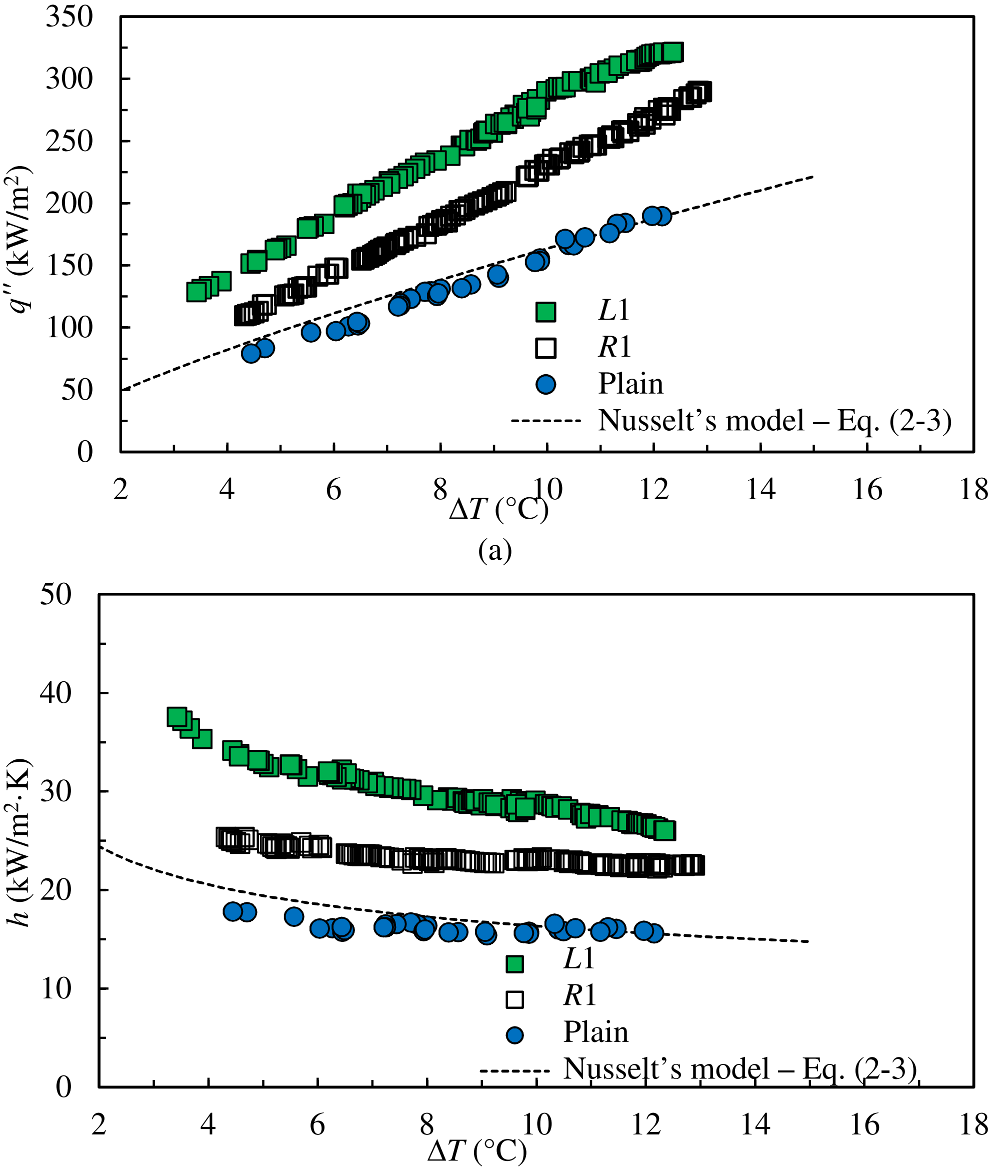

(a)

(b)

Fig. 5-3 Comparison of (a) q'' and (b) h at different ΔT for $L1$ and $R1$ specimens.

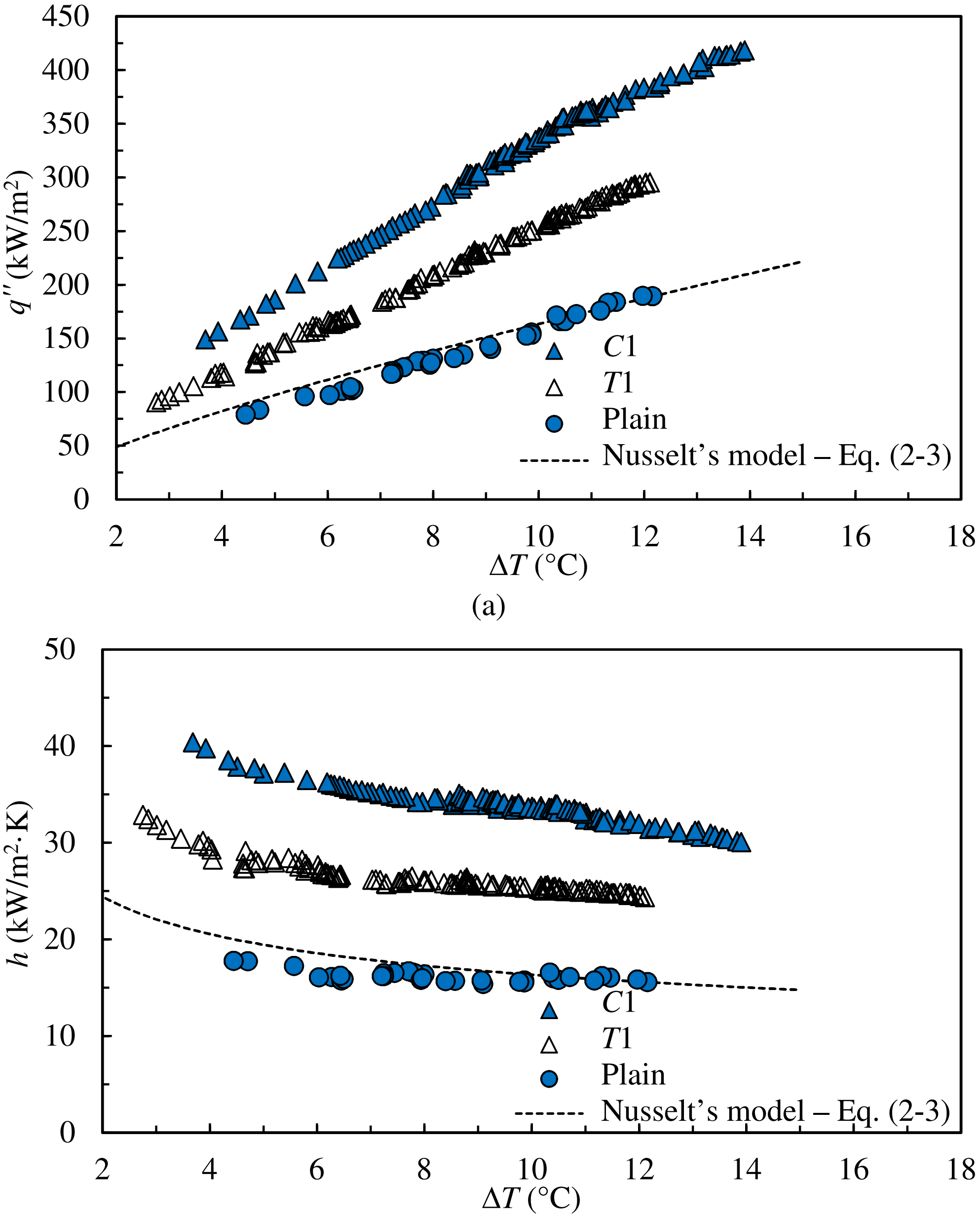

(a)

(b)

Fig. 5-4 Comparison of (a) q'' and (b) h at different ΔT for $C1$ and $T1$ specimens.

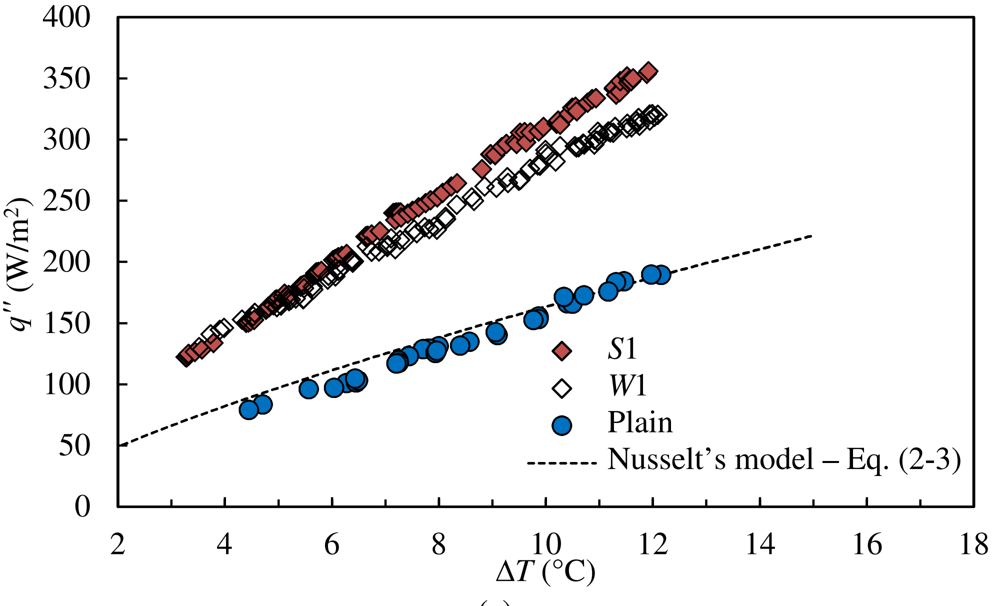

(a)

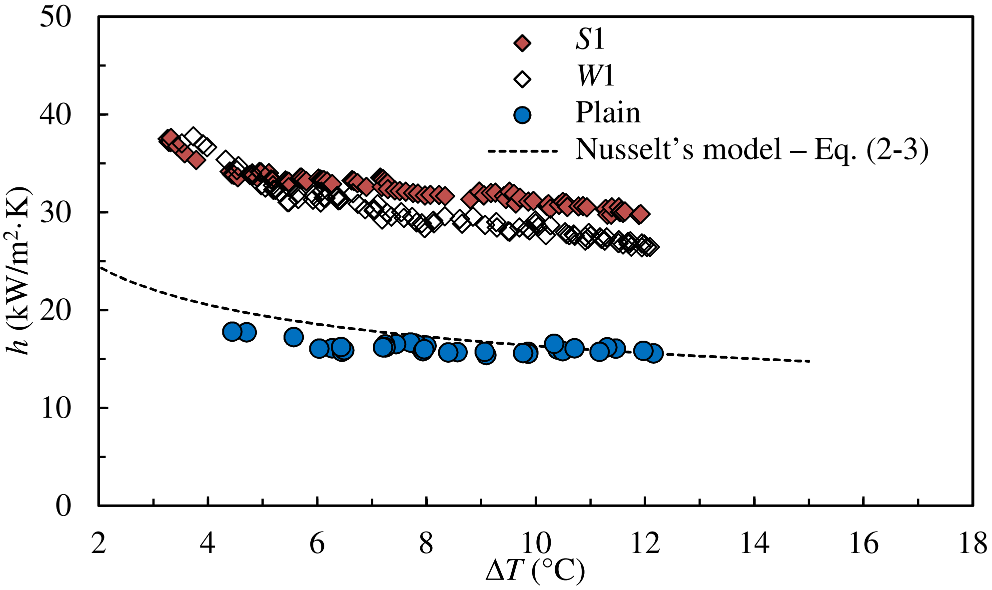

(b)

Fig. 5-5 Comparison of (a) q'' and (b) h at different ΔT for $S1$ and $W1$ specimens.

The above results suggest that apart from the heat transfer area, other factors may have also resulted in the better heat transfer performances of the pin fin surfaces. Based on the review performed in Section 2.1.3, the condensate retention heights on the enhanced surfaces may have significant effect on their heat transfer characteristics. Therefore, after each condensation experiment, the average static condensate retention heights (H_{ave}) of the specimens were measured. A method similar to that reported by Ali and Briggs [49] was used to measure the H_{ave} of the enhanced structures. A fine spray was used to produce small water droplets. The spray was controlled to ensure low velocity droplets were produced and a uniform liquid film was formed on the specimen surfaces. For each surface, images were taken over 30 second duration to verify that H_{ave} remained the same. Figure 5-6 shows the liquid retention on $R1$, $T1$ and $W1$ (front view) and $L1$, $C1$ and $S1$ (side view). Due to the difficulty in visualising the retention height of the $R1$ specimen, a small amount of red dye was used. For the other specimens, no dye was added. In addition, a red line is used to demarcate the waterline on the $S1$ specimen to facilitate the visualisation of the condensate retention height on this specimen. The H_{ave} values of the specimens are shown in Table 5-1.

It can be seen from Fig. 5-6 that the conical and cylindrical pin fin structures resulted in the reduction in H_{ave} as compared to the equivalent longitudinal fins. The $L1$ specimen has 15% lower H_{ave} than $R1$ and the $C1$ specimen has 19% lower H_{ave} than $T1$. Therefore, it can be concluded that the reduction in condensate retention height has contributed to the enhanced condensation of the conical and cylindrical pin fin structures. The sinusoidal pin fin, on the other hand, exhibits a different condensate retention characteristic as compared to the conical and cylindrical pin fin. From Fig. 5-6 (f), it can be seen that $S1$ has two distinct flooding regions (*viz.*, Region I and Region II). In Region I, the fins are completely flooded and it is at the lower portion of the specimens. As the thick liquid film covers the entire fin, there is negligible heat transfer in this region. In Region II, a thick layer of liquid film is trapped between the concave stems of the fins and the thickness of the liquid film in this region reduces towards the upper portion of the specimen. Even though the fin stems are blanketed by a layer of liquid, the tip of the fin can be seen to protrude out of the liquid layer. Similarly, as shown in Fig. 5-6 (e), a completely flooded region (Region I) and a thick liquid film region (Region II) can also be observed on specimen $W1$. Region I of specimen $W1$ can be measured from Fig. 5-6 (e) and it was found to be slightly lower than that of $S1$. This comparison indicates that, for the sinusoidal geometry, the use of three-dimensional pin fin does not reduce the condensate retention height. As the condensate retention heights of $S1$ and $W1$ are similar, this also resulted in the small difference in their η values of 2%. Finally, it should be noted that in Table 5-1, H_{ave} of the $S1$ and $W1$ represents only the region where the fins are completely flooded.

Table 5-1 Constants a and b of Eq. (5-2), thermal enhancement factors (η) and condensate retention height ratios of $L1$, $C1$, $S1$, $R1$, $T1$ and $W1$ specimens.

Specimen name	a	b	η	H_{ave}/H	Description
$C1$	51.503	0.8109	2.02	0.17	Conical pin fin
$S1$	37.135	0.8946	1.74	0.23	Sinusoidal pin fin
$L1$	50.068	0.7494	1.60	0.41	Cylindrical pin fin
$T1$	36.545	0.8398	1.36	0.21	Triangular longitudinal fin
$W1$	49.947	0.7481	1.71	0.21	Sinusoidal longitudinal fin
$R1$	28.836	0.8991	1.37	0.48	Rectangular longitudinal fin

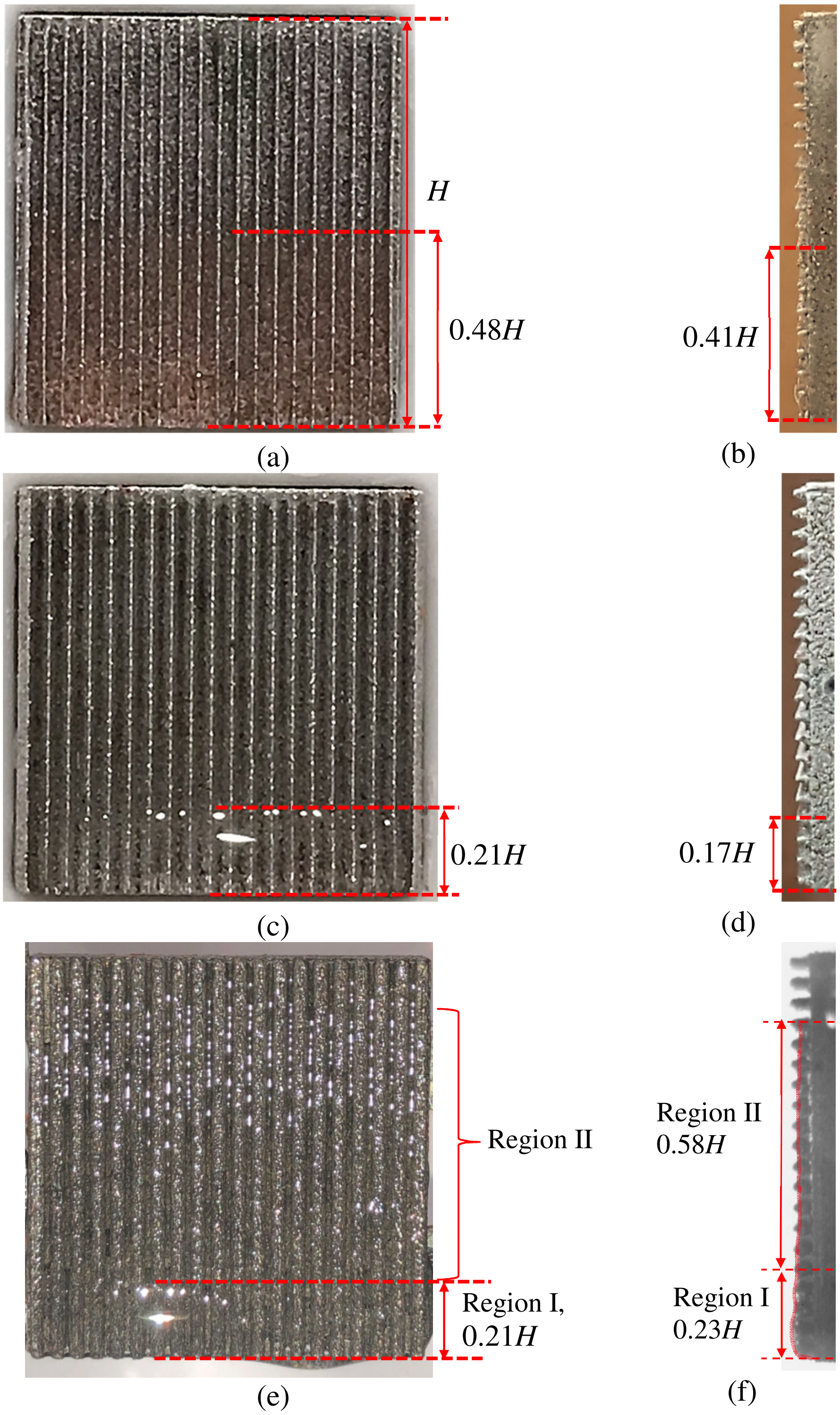

Fig. 5-6 Image of liquid retention height on (a) *R*1 – front view, (b) *L*1 – side view, (c) *T*1 – front view, (d) *C*1 – side view, (e) *W*1 – front view and (f) *S*1 – side view.

By comparing the η and H_{ave} values of specimens $C1$ and $T1$, it can be observed that $C1$ has 50% higher η as compared to $T1$ and this enhancement in η is significantly larger than the reduction in H_{ave} of just 19%. This comparison suggests that, apart from the condensate retention height, other mechanisms may also have contributed to the specimen's enhanced performances. As mentioned in Section 2.1.2, the presence of finned structures produced additional surface tension forces which drained the condensate film from the fin tip to the fin base. This produces a thin layer of condensate film near the fin tip. The change in pressure induced by surface tension ($\frac{\partial P}{\partial S}$) can be described by the Young-Laplace equation [132] and shown as Eq. (5-3). In this equation, R_i and R_{ii} are the radii of curvature in their principal directions and the s-direction is along the liquid-vapour interface from the fin tip to the fin base. As shown in Fig. 5-7, for a longitudinal triangular fin, $R_{ii} = \infty$ and Eq. (5-3) is reduced to $\frac{\partial P}{\partial s} = \frac{\partial}{\partial s}(\frac{\sigma}{R_i})$. On the other hand, as a conical pin fin resulted in the variation of curvatures in their principal directions, the two terms on the right-hand side of Eq. (5-3) are maintained. This additional variation of curvature of the pin fin could have resulted in larger induced pressure which enhanced the draining of condensate to the fin base, reducing the film thickness near the fin tip and promoted heat transfer. By comparing the η and H_{ave} values of specimens $L1$ and $R1$ and specimens $S1$ and $W1$, similar conclusions can be drawn for the other fin geometries.

$$\frac{\partial P}{\partial s} = \sigma \frac{\partial}{\partial s}\left(\frac{1}{R_i} + \frac{1}{R_{ii}}\right) \tag{5-3}$$

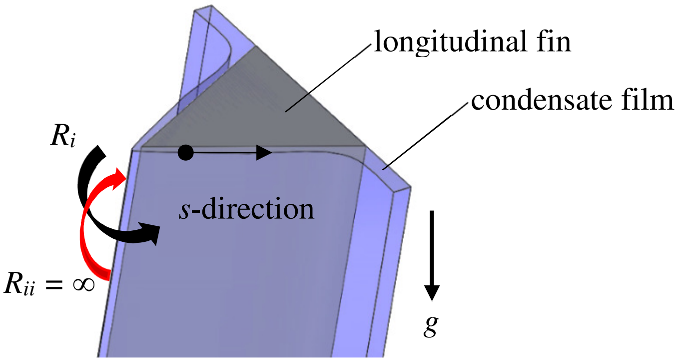

Fig. 5-7 Liquid film on triangular longitudinal fin.

5.3 Effects of fin geometry

Figure 5-8 (a) and (b) compares the q'' and h values of the $C1$, $L1$ and $S1$ specimens, respectively. These specimens are pin fins of the same fin pitch (p) and similar fin height (l) but of different fin geometries. It can be seen from the figure that the pin fin structures significantly improve the q'' and h values as compared to the plain surface. Specimen $C1$ exhibits the highest performance followed by $S1$ and $L1$. From Table 5-1, it can be seen that $R1$ has the highest liquid retention height among the pin fin specimens, where the liquid fully covers the whole fin. This high retention height explains the poorer heat transfer performance of $R1$ as compared to $C1$ and $S1$. On the other hand, even though $S1$ has slightly higher retention height as compared to $C1$ and has a large portion of its surface covered by a thick layer of liquid film (denoted by Region II in Fig. 5-6 (f)), the η values of $C1$ and $S1$ do not deviate significantly and it can be computed that the η value of $C1$ is only 12% higher than that of $S1$. The $S1$ fins were designed with a large convex fin tip and a concave fin stem where the curvature changes continuously along the fin surface. This resulted in the drainage of condensate to the fin base and producing a thick liquid film in Region II. However, since the liquid film is thin at the fin tip and the heat transfer area at the fin tip is large, this resulted in significantly high transfer rate from the fin tip. This, therefore, explains the high heat transfer performance of the *S*1 specimen. For specimen *C*1, it can be seen from Fig. 5-7 (d) that it has the lowest retention height and the liquid film on the remaining portion of the specimen surface is also significantly thinner. This low condensate retention height of the conical pin fin and the surface tension effect induced by its three-dimensional structure are the main factors contributing to the specimen's heat transfer enhancements.

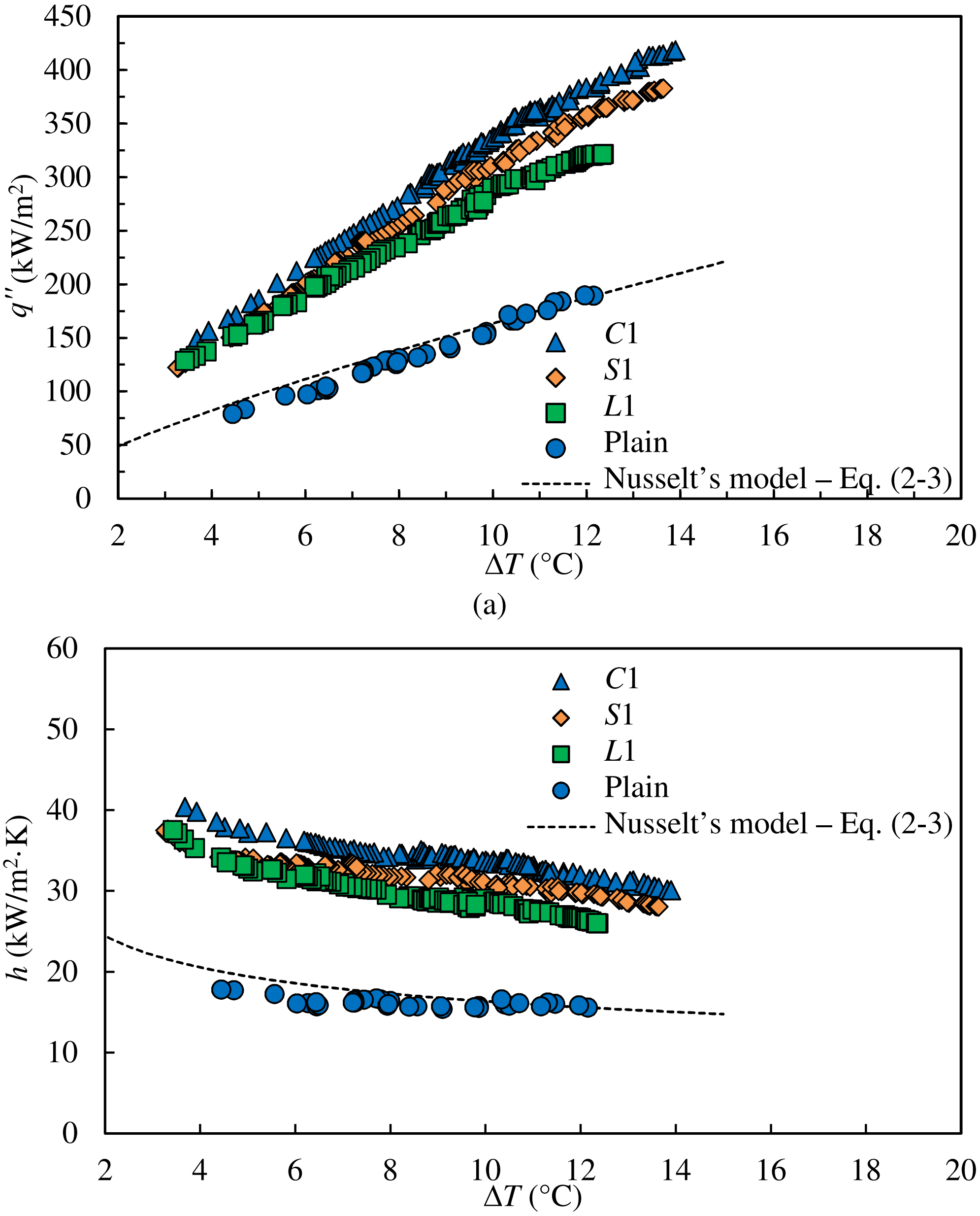

(a)

(b)

Fig. 5-8 Comparison of (a) q'' and (b) h at different ΔT for $C1$, $S1$, $L1$ and plain specimens.

5.4 Effects of fin height and fin pitch

As shown in Section 5.2, significant heat transfer enhancements can be achieved with three-dimensional pin fin structures as compared to two-dimensional longitudinal fins. To explore the possibility of further increasing the heat transfer performances and to have a better understanding of the condensation heat transfer mechanisms associated with the pin fin arrays, the effects of fin pitch and height were investigated and the results are presented in this section. The pin fin specimens can be classified into three different geometries and they are conical, sinusoidal and cylindrical micro pin fins. For each geometry, nine specimens with pin fin arrays of different fin height and fin pitch were produced and investigated.

5.4.1 Conical pin fins

The experimental results of q'' and h of specimens $C1$ – $C9$ at various ΔT are shown in Figs. 5-9 and 5-10, respectively. In Fig. 5-9, three graphs of q'' versus ΔT are presented whereas Fig. 5-10 shows the variation of h at different ΔT values. In order to evaluate the effects of fin pitch, the specimens of the same fin height (l) but different fin pitches (p) are plotted on the same graph and comparisons are also made against the plain surface. From these figures, it can be seen that for the specimens with the same fin height (l), q'' and h initially increase as p increases from 1.25 mm to 1.67 mm. However, with the further increase in p from 1.67 mm to 2.50 mm, reductions in the q'' and h values are recorded. For instance, specimens $C1$, $C2$ and $C3$ have the same fin height (l) of 1.28 mm. At ΔT of 10°C, specimen $C1$ (with p = 1.25 mm) has the q'' value of approximately 366 kW/m^2 whereas specimen $C2$ (with the higher p of 1.67 mm) exhibited higher q'' of 397 kW/m^2. On the other hand, specimen $C3$ (with the highest p of 2.50 mm) demonstrated the lowest q'' of 292 kW/m^2 among the three specimens.

In order to determine the thermal performances of specimens $C1$ – $C9$ over the range of ΔT tested, their thermal enhancement factors (η) were calculated using the method described in Section 5.2. The η values and a and b values of Eq. (5-2) for the conical pin fin specimens are shown in Table 5-2. In addition, the static condensate retention heights (H_{ave}) of each conical pin fin specimen were also measured and images of the liquid retained on specimens are shown Fig. 5-11. It can be seen from Fig. 5-11 that the condensate retention height generally reduces with increasing p, except for specimens $C2$ and $C3$ where $C2$ show slightly lower H_{ave} than $C3$. On the other hand, from Table 3-2, it can also be noticed that the area enhancement factor (ε) of the specimens with the same fin height (l) also decreases with increasing fin pitch (p). Taking specimens $C1$ and $C2$ for example, due to the larger fin pitch of $C2$, its ε value is approximately 21% smaller than $C1$. However, from Fig. 5-11, it can be computed that the condensate retention height (H_{ave}) of $C2$ is approximately 41% lower than $C1$. Therefore, even though the heat transfer area of $C2$ is lower than $C1$, the lower condensate retention height of $C2$ may have reduced the thermal barrier across the pin fins and resulted in higher heat transfer coefficients as compared to $C1$. On the other hand, even though H_{ave} of $C3$ is also lower than $C1$, the fin spacing of $C3$ may be too sparse to produce a higher heat transfer rate than $C1$. Finally, it can be concluded from the experimental results that, for the specimens of the same fin height, the fin pitch (p) of 1.67 mm resulted the highest heat transfer coefficients as compared to other fin pitches. In addition, among all the conical pin fin specimens tested, $C2$ exhibits the best heat transfer performance with the highest η value of 2.46.

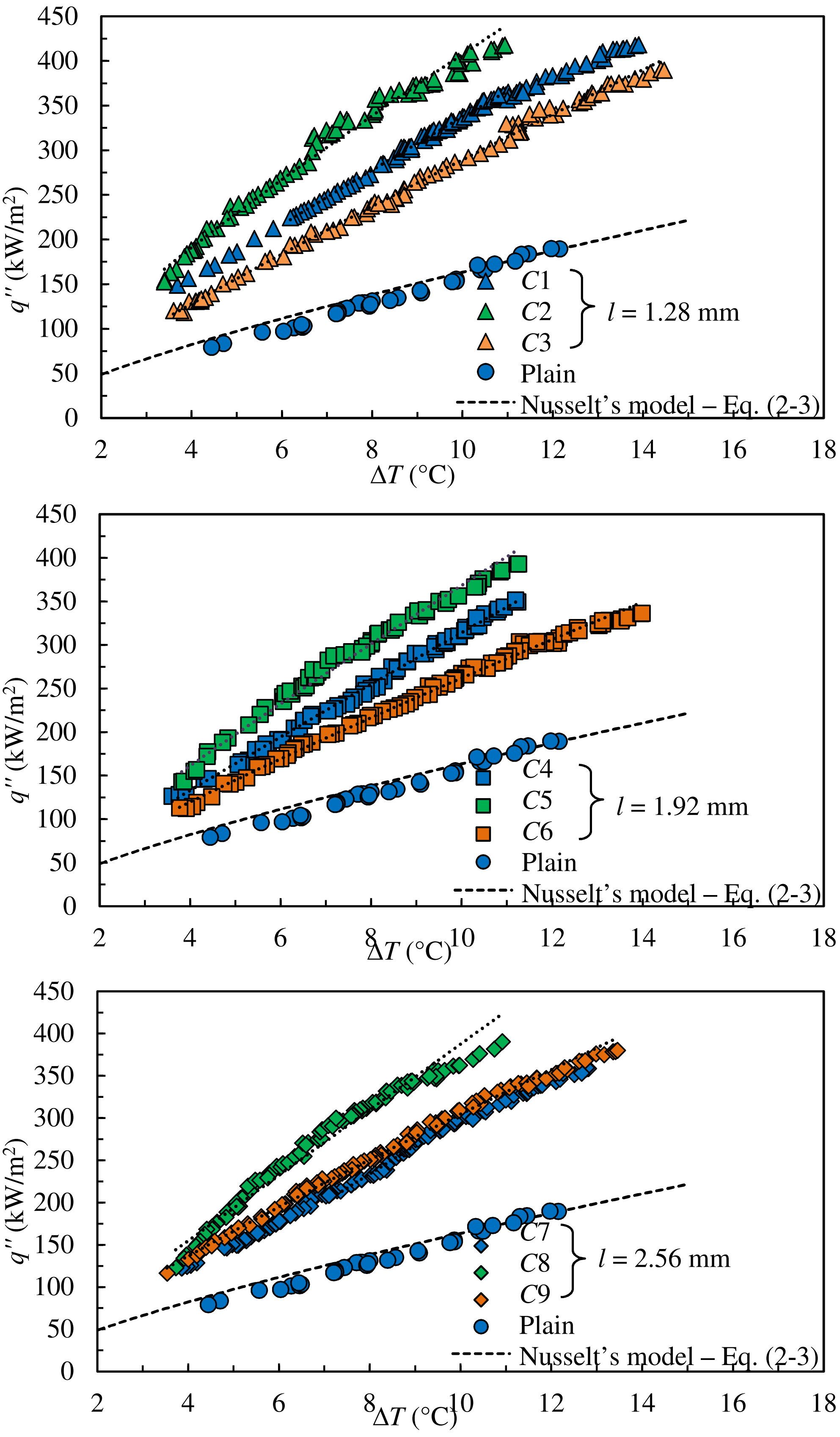

Fig. 5-9 Effects of conical pin fin pitch on q'' at different ΔT.

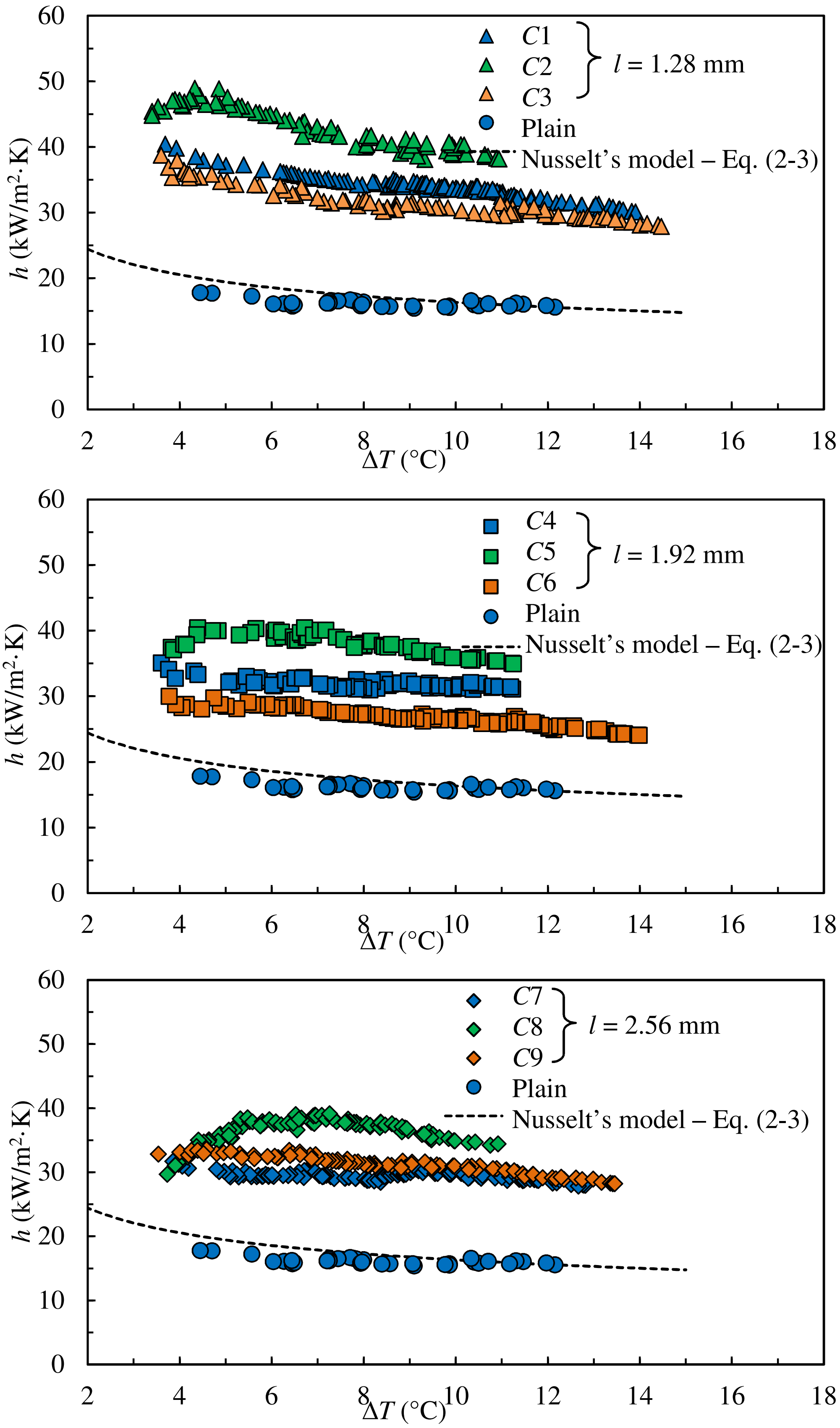

Fig. 5-10 Effects of conical pin fin pitch on h at different ΔT.

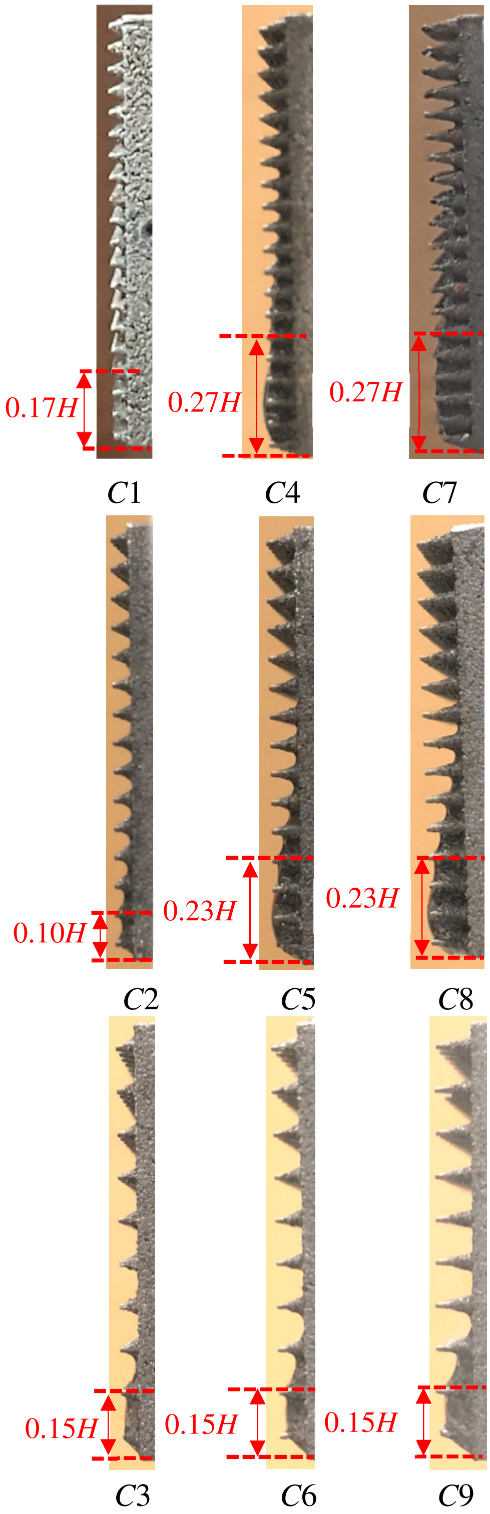

Fig. 5-11 Condensate retention heights for conical pin fin specimens (C1 – C9) of different fin pitches and fin heights.

Table 5-2 Constants *a* and *b* of Eq. (5-2), thermal enhancement factors (η) and condensate retention height ratios of *C*1 – *C*9 specimens.

Specimen name	*a*	*b*	η	H_{ave}/H	Description
*C*1	51.503	0.8109	2.02	0.17	Conical pin fin
*C*2	60.620	0.8274	2.46	0.10	
*C*3	37.285	0.8897	1.73	0.15	
*C*4	36.140	0.9392	1.86	0.27	
*C*5	46.214	0.9015	2.19	0.23	
*C*6	36.589	0.8549	1.57	0.15	
*C*7	32.558	0.953	1.73	0.27	
*C*8	38.557	1.002	2.27	0.23	
*C*9	40.650	0.8747	1.82	0.15	

Figure 5-12 (a) and (b) shows a comparison of the q'' and *h* of the *C*1, *C*4 and *C*7 specimens, respectively. These three specimens are conical pin fin arrays of the same fin pitch (*p*) and but with different fin heights (*l*). It can be seen from this figure that the heat transfer performances of the specimens decrease with increasing fin height with *C*1 and *C*7 showing the highest and lowest *h* values, respectively. As depicted in Fig. 5-11, *C*1 has the lowest condensate retention height of 0.17*H* whereas *C*4 and *C*7 has the same retention height of 0.27*H*. Despite having short fins, the lower condensate retention height of *C*1 as compared to *C*4 and *C*7 is a factor that has contributed to higher heat transfer coefficients of *C*1.

As compared to *C*1, *C*7 has a reduction in η of 14% and an increase in condensate retention height of 59%. In addition, due to the larger fin height, *C*7 also has 72% higher ε value as compared to *C*1. Despite having a larger percentage increase in ε as compared to the percentage increase in condensate retention height, the heat transfer performance of *C*7 is still poorer than that of *C*1. This could be due to larger fin height of *C*7 which have resulted in a larger temperature difference between the fin base and the fin tip. The larger temperature difference thus led to a poorer fin efficiency of *C*7 as compared to *C*1 and thereby reducing its overall heat transfer performance.

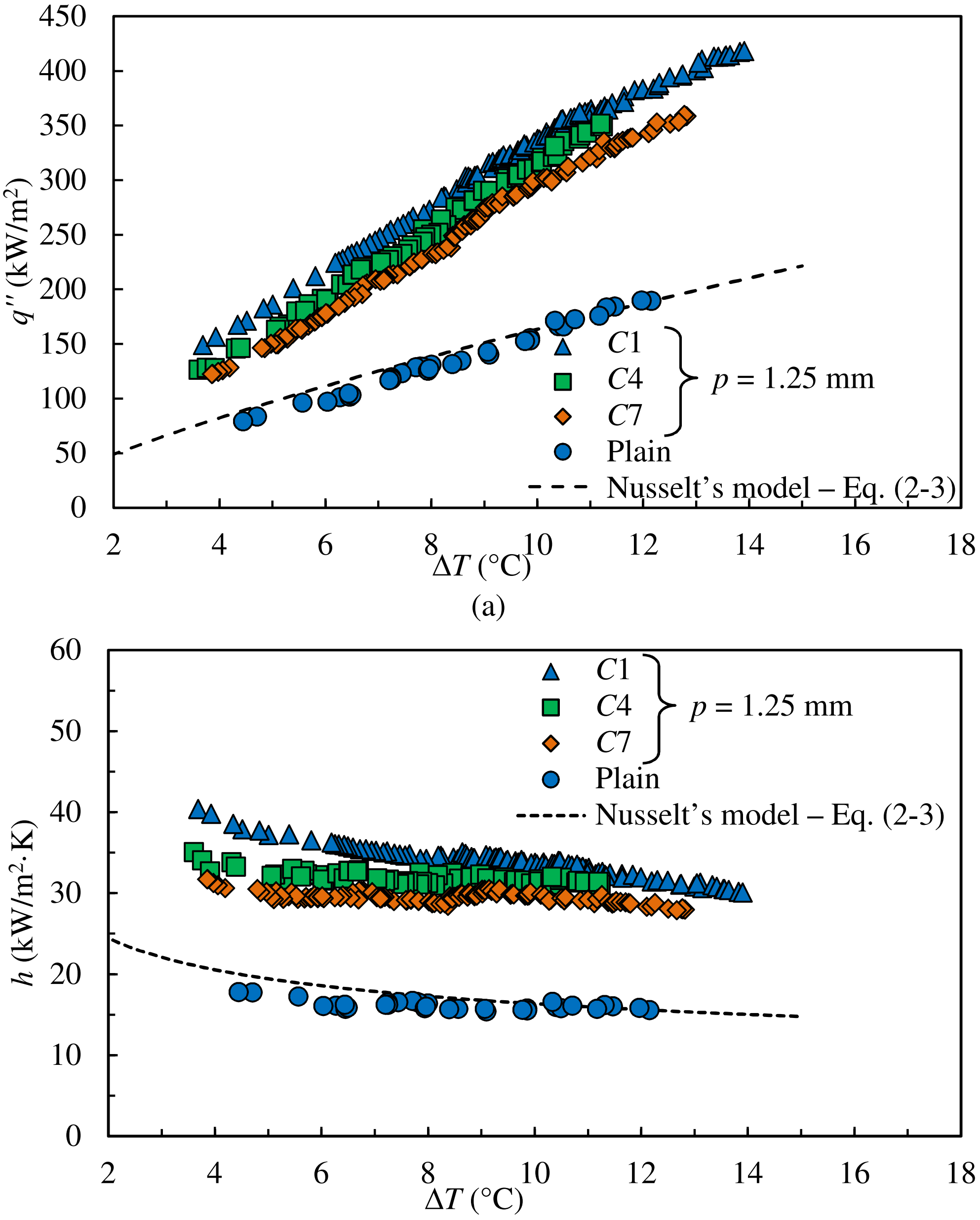

(a)

(b)

Fig. 5-12 Effects of conical pin fin height on (a) q'' and (b) h at different ΔT.

5.4.2 Sinusoidal pin fins

The experimental results of q'' and h for specimens $S1$ – $S9$ at various ΔT are shown in Figs. 5-13 and 5-14, respectively. Sinusoidal pin fin surfaces of the same fin height (l) but different fin pitches (p) are plotted in each graph. From Figs. 5-13 and 5-14, it can be seen that at l = 1.25 mm and l = 1.66 mm, specimens with p = 1.25 mm and p = 1.67 mm show higher q'' and h values than the specimens with p = 2.50 mm. On the other hand, at l = 2.49 mm, the specimen with p = 2.50 mm resulted in lower q'' and h values as compared to other two specimens with smaller p values.

The thermal enhancement factors (η) of the sinusoidal pin fin surfaces were also computed based on the method described in Section 5.2 and their values are shown in Table 5-3. In addition, their condensate retention heights were also measured and images of the liquid retained on specimens $S1$ – $S9$ are shown in Fig. 5-15. From Fig. 5-15, it can be seen that two distinct flooding regions can also be identified for all the sinusoidal pin fin surfaces. As explain in Section 5.1, in Region I the fins are completely flooded whereas in Region II a thick layer of liquid film covers only the stems of the fins. In addition, at the same l value, the condensate retention height also increases with decreasing p. This trend is similarly observed for the conical pin fins. For instance, at l = 1.25 mm, the number of fins unflooded (i.e., outside Regions I and II) for $S1$, $S2$ and $S3$ are 80, 120 and 70, respectively. Even though the number of unflooded fins of $S1$ is smaller than those of $S2$, its heat transfer performance is similar to S2. As shown in Fig. 5-15, $S1$ has a large number of fins in Region II as compared to $S2$, where the fin tip protrudes out of the thick liquid layer. An illustration of the condensate film thickness of one sinusoidal fin with the fin shape similar to $S4$ that was numerically determined by Wang et al. [43] is shown in Fig. 5-16, where δ is the condensate film thickness and S^* is the dimensionless fin length. In Ref. [48], Wang et al. defined S^* as the ratio of the s-coordinate along the fluted surface to the crest-to-trough distance on the fluted surface (D), viz. $S^* = s/D$. It can be seen from the figure that the change in curvature of the fin structure induces surface tension forces and produces a thin film region along the fin tip. Due to the thin liquid film, heat transfer occurs mainly at the fin tip. For Specimen $S1$, even though the fin stems in Region II are flooded, the fin tip which protrude out of the thick liquid film may have contributed significantly to the overall heat transfer rate of the specimens and thereby maintaining the high η values. On the other hand, the lower η value of $S3$ as compared to $S1$ and $S2$ could be due to its low fin density which resulted in a low heat transfer area.

For specimens with larger fin height (l) such as those of $S7$, $S8$ and $S9$, the low fin efficiency may have resulted in significantly lower heat flux from the fin tip and resulting in negligible heat transfer rate from Region II. Therefore, the heat transfer rates from $S7$, $S8$ and $S9$, are largely dependent on the unflooded region. Since $S7$ has the smallest unflooded area of 506 mm^2 as compared to the unflooded areas of $S8$ and $S9$ of 919 mm^2 and 763 mm^2, respectively, its η value is also the smallest.

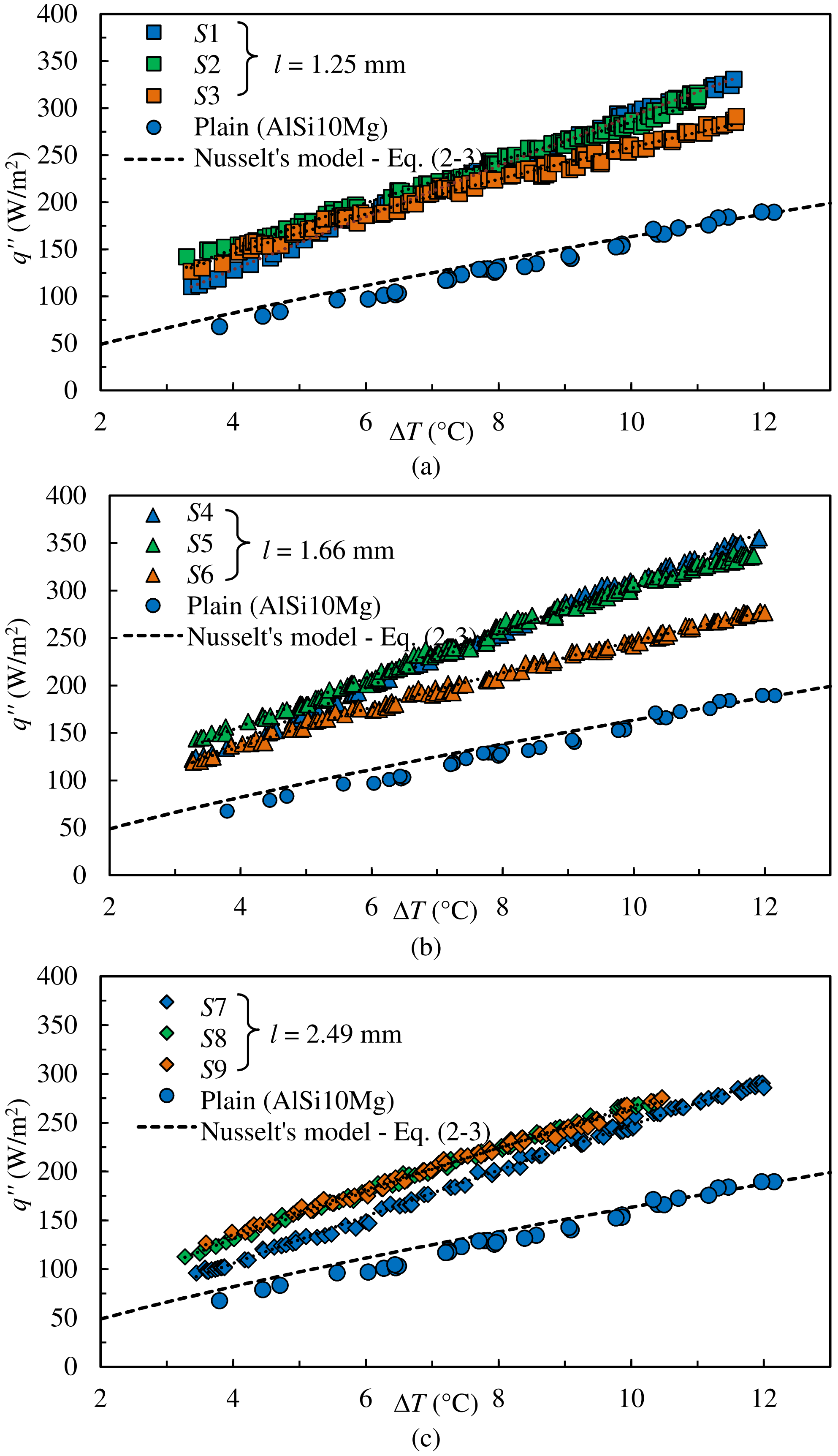

Fig. 5-13 Effects of sinusoidal pin fin pitch on q'' at different ΔT.

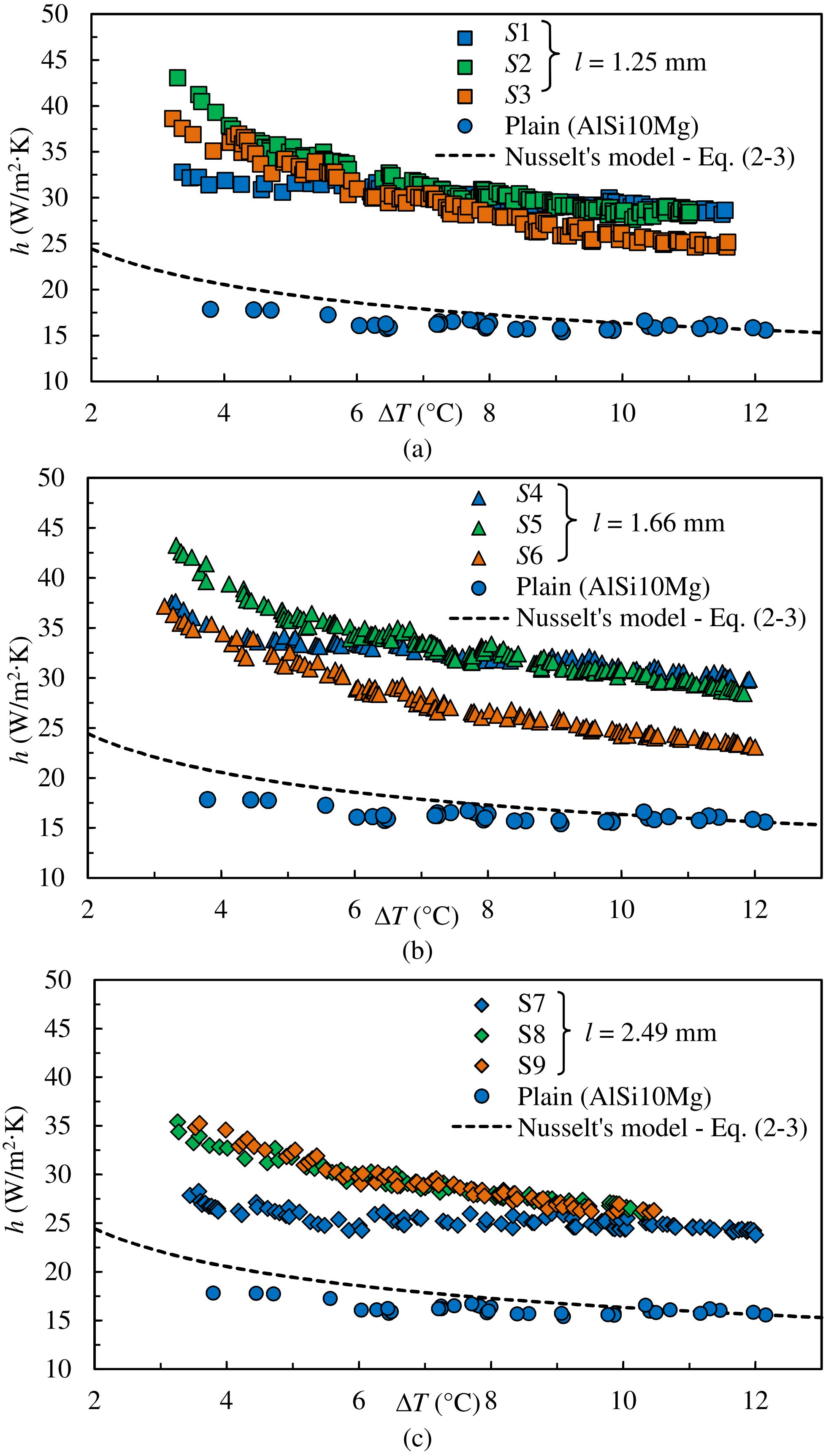

(a)

(b)

(c)

Fig. 5-14 Effects of sinusoidal pin fin pitch on h at different ΔT.

Table 5-3 Constants *a* and *b* of Eq. (5-2), thermal enhancement factors (η) and condensate retention height ratios of *S*1 – *S*9 specimens.

Specimen name	*a*	*b*	η	H_{ave}/H	Description
*S*1	37.135	0.8946	1.74	0.23	Sinusoidal pin fin
*S*2	56.861	0.6996	1.76	0.17	
*S*3	60.640	0.6297	1.62	0.15	
*S*4	43.181	0.8558	1.86	0.23	
*S*5	58.036	0.7174	1.86	0.17	
*S*6	55.075	0.6509	1.54	0.15	
*S*7	29.418	0.9249	1.47	0.23	
*S*8	44.869	0.7736	1.62	0.17	
*S*9	49.530	0.7253	1.62	0.15	

Figure 5-17 shows the plots of q'' and *h* of specimens *S*1, *S*4 and *S*7 at various ΔT. These specimens have the same fin pitch (*p*) of 1.25 mm but different fin heights and therefore allow the effects of fin height (*l*) on q'' and *h* to be analysed by plotting the specimens of the same fin pitch (*p*) but different fin heights (*l*). It can be observed from this figure that increasing *l* from 1.25 mm (Specimen *S*1) to 1.66 mm (Specimen *S*4) also increases the q'' and *h* values, with *S*4 exhibiting better heat transfer performance than *S*1. However, further increasing *l* from 1.66 mm (Specimen *S*4) to 2.50 mm (Specimen *S*7) resulted in the reduction in q'' and *h*, *viz.*, the heat transfer performance of *S*7 is poorer than both *S*1 and *S*4. This above trend is similarly observed for the conical pin fin as depicted in Fig. 5-12.

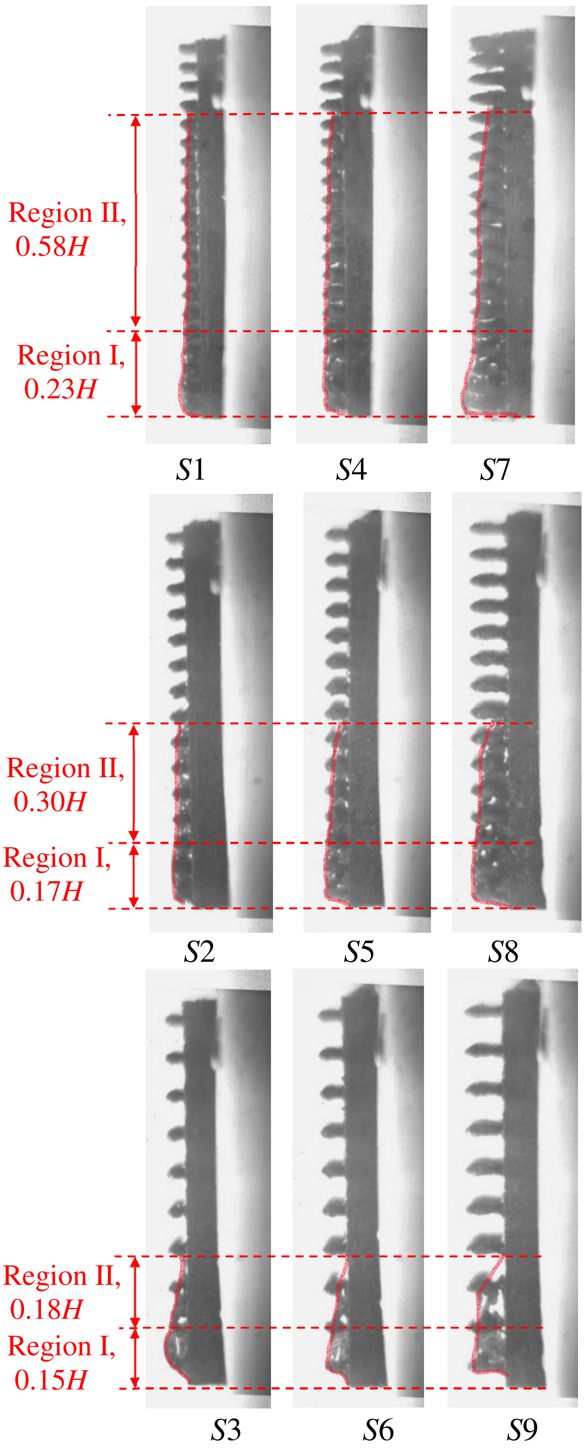

Fig. 5-15 Condensate retention heights for sinusoidal pin fin specimens (*S*1 -*S*9) of different fin pitches and fin heights.

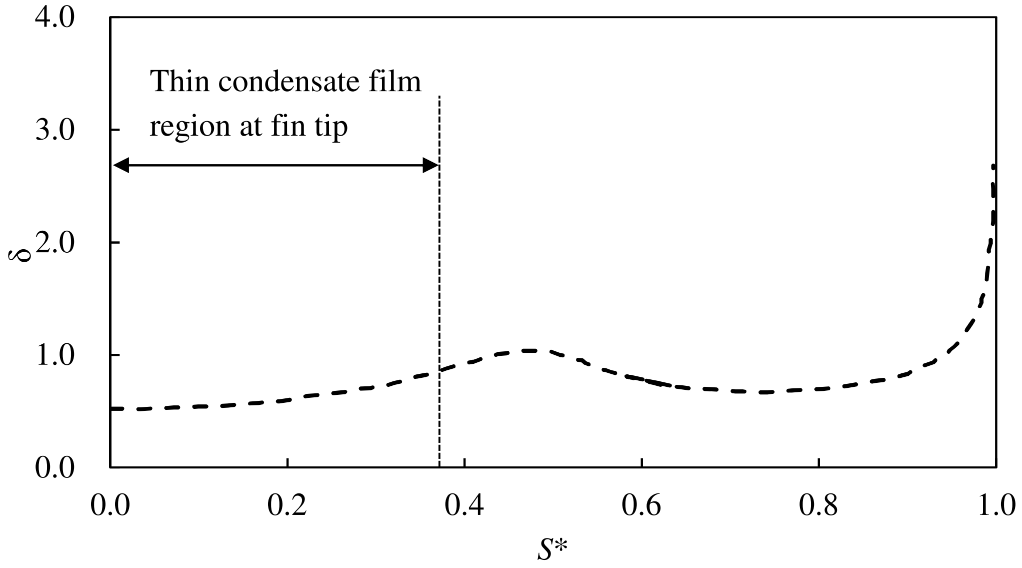

Fig. 5-16 Condensate film thickness of sinusoidal fin reproduced from Ref. [43].

From the condensate retention height images of Fig. 5-15, it can be seen that the increase in fin height has no effect on H_{ave}. For instance, at p = 1.25 mm, specimens *S*1, *S*4 and *S*7 have the same H_{ave}/H ratio of 0.23 for Region I and H_{ave}/H ratio of 0.58 for Region II. This resulted in the same number of unflooded fins (80 fins) for the three specimens. However, as the *S*4 fins are longer than *S*1 fins, *S*4 has a larger unflooded area as compared to *S*1. Therefore, this accounts for the higher heat transfer performance of *S*4. However, even though *S*7 has the largest unflooded area as compared to Specimens *S*1 and *S*4, its heat transfer performance is the poorest. This could be due to the larger fin height of S7, the temperature difference between the fin base and the fin tip is also larger resulting in its poorer fin efficiency as compared to *S*1 and *S*4. Since condensation occurs mainly near the fin tip where the condensate film is thin, a small temperature difference between the fin tip wall and the surrounding vapour may have resulted in the poor heat transfer performance of *S*7.

Finally, it should be noted that the maximum η value of 1.86 was achieved with specimens *S*4 and *S*5 whereas *S*7 showed the lowest η value of 1.47.

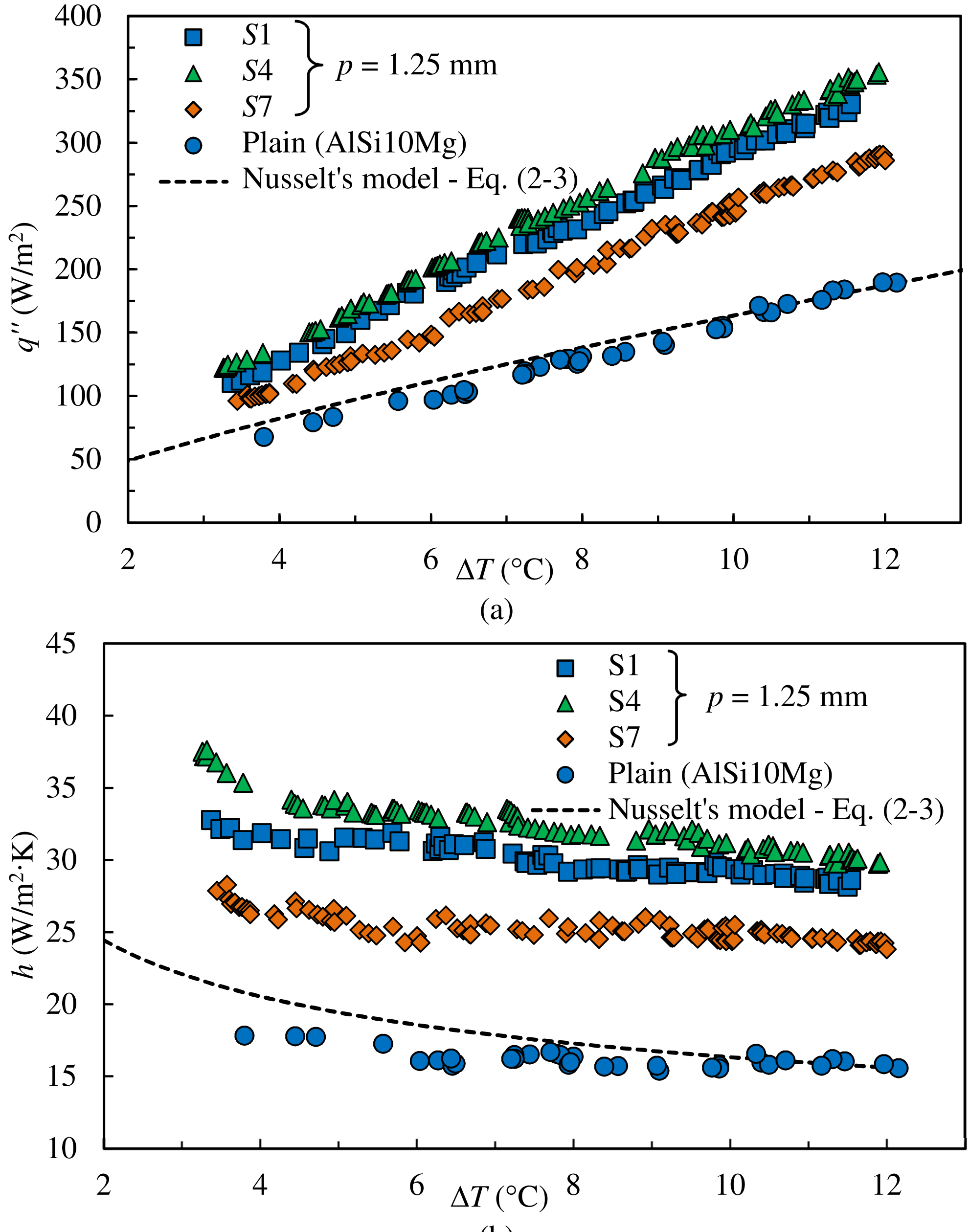

(a)

(b)

Fig. 5-17 Effects of sinusoidal pin fin height on (a) q'' and (b) h at different ΔT.

5.4.3 Micro-pin-fins

In this section, the thermal performances of the micro-pin-fin specimens ($MF1 – MF9$) are compared and evaluated. This micro-pin-fins have the same geometry of a cylinder and the same fin diameter (d_b) of 0.3 mm. However, the specimens have different fin heights (l) and fin pitches (p). Figure 5-18 compares the q'' values of $MF1 – MF9$ whereas their h values are depicted in Fig. 5-19. In these figures, the specimens of the same fin height (l) but different fin pitches (p) are plotted on the same graph. Taking $MF1$, $MF2$ and $MF3$ as an example, these specimens have the same fin height of l = 300 µm but have different fin pitches (p), i.e., $MF1$, $MF2$ and $MF3$ have p values of 0.9 mm, 0.6 mm and 0.3 mm, respectively. From Fig. 5-18, it can be seen that the reduction in p resulted in the increase in q''. In addition, the reduction in p from 0.9 mm to 0.6 mm also produced a more significant increase in q'' as compared to the reduction in p from 0.6 mm to 0.3 mm. For instance, at ΔT of approximately 10°C, the increments in q'' for $MF1$, $MF2$ and $MF3$ are 16.7%, 38.2% and 47.2%, respectively as compared to the plain surface. By comparing the percentage enhancements of these three surfaces, it can be observed that the reduction in p from 0.9 mm to 0.6 mm resulted in the increment in q'' of 18.4%. This increment in q'' is more significant than the reduction in p from 0.6 mm to 0.3 mm which only shows a marginal increment in q'' of 6.6%. As shown in Fig. 5-18, a similar trend is also recorded for $MF4$, $MF5$ and $MF6$. The change in fin pitch has shown to have significant influence on the condensate retention height on the fin arrays. Unfortunately, due to the small fin dimensions of the micro-pin-fin specimens, clear images of the liquid retained on these specimens cannot be obtained. However, based on the results obtained for the conical and sinusoidal pin fins in Sections 5.4.1 and 5.4.2, it can be deduced that the small increase in q'' when p reduces from 0.6 mm to 0.3 mm (such as those of $MF3$ and $MF6$) could likely be due to the significant increment in the condensate retention height. A large retention height resulted in a large portion of the fin flank being covered by the condensate and therefore reduces the available heat transfer area.

On the other hand, for specimens $MF7$, $MF8$ and $MF9$, the reduction in p resulted in a linear increment in q''. For example, at ΔT of approximately 10°C, the enhancements of q'' for $MF7$, $MF8$ and $MF9$ are 46.7%, 62.8% and 83.0%, respectively as compared to the plain surface. By comparing the percentage enhancements of these three surfaces, it is determined that the reduction in p from 0.9 mm to 0.6 mm and the reduction in p from 0.6 mm to 0.3 mm resulted in a similar increment in q'' of approximately 12%. This different trend of $MF7$ – $MF9$ as compared to those of $MF1$ – $MF6$ is likely due to the larger fin height (0.9 mm) of specimens $MF7$ – $MF9$. A larger fin height enables a portion of the fins to protrude out of the condensate film, especially in the region where the condensate film is thick. This maintains a similar percentage increment in q'' when p is reduced from 0.9 mm to 0.3 mm.

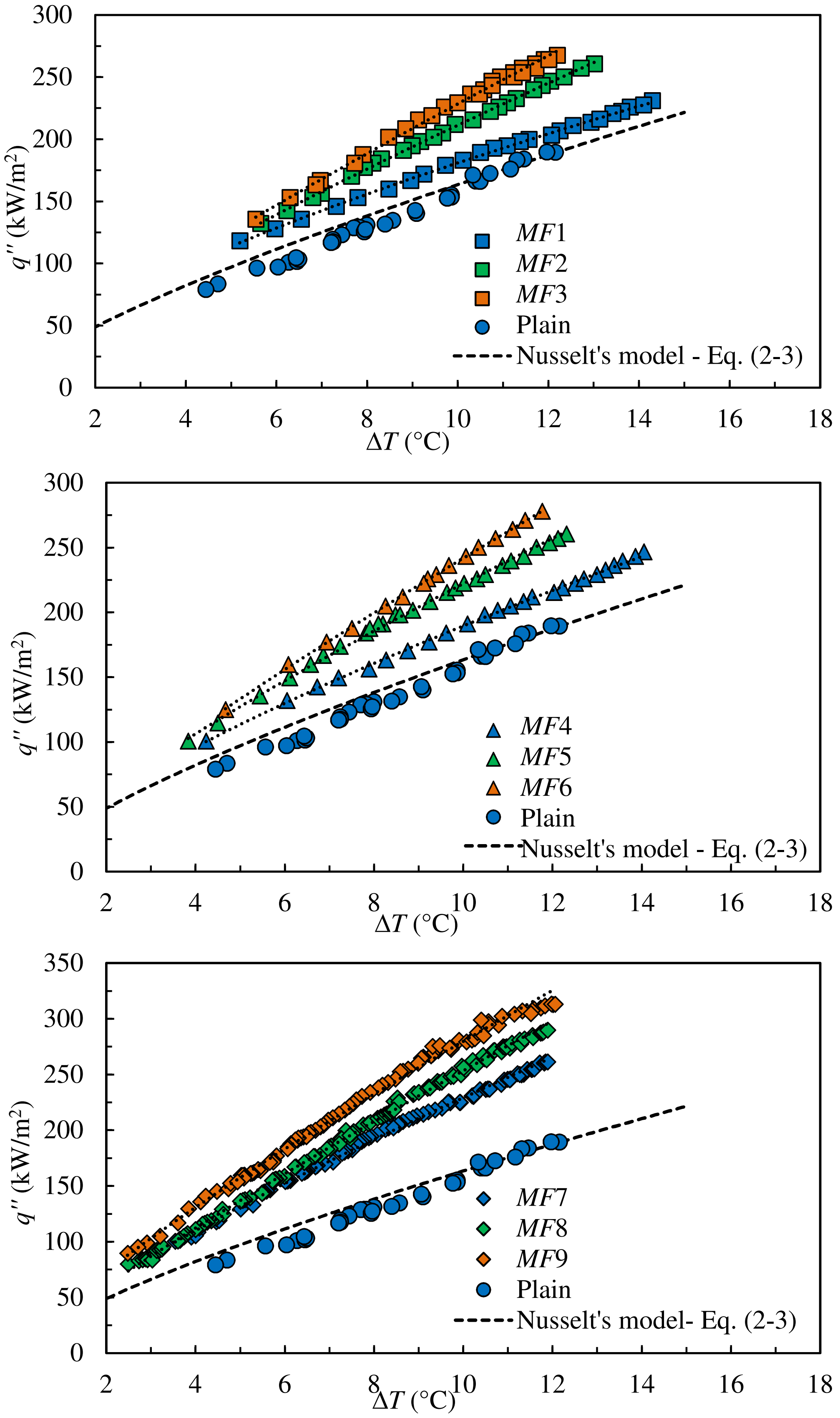

Fig. 5-18 Effects of cylindrical micro-pin-fin height on q'' at different ΔT.

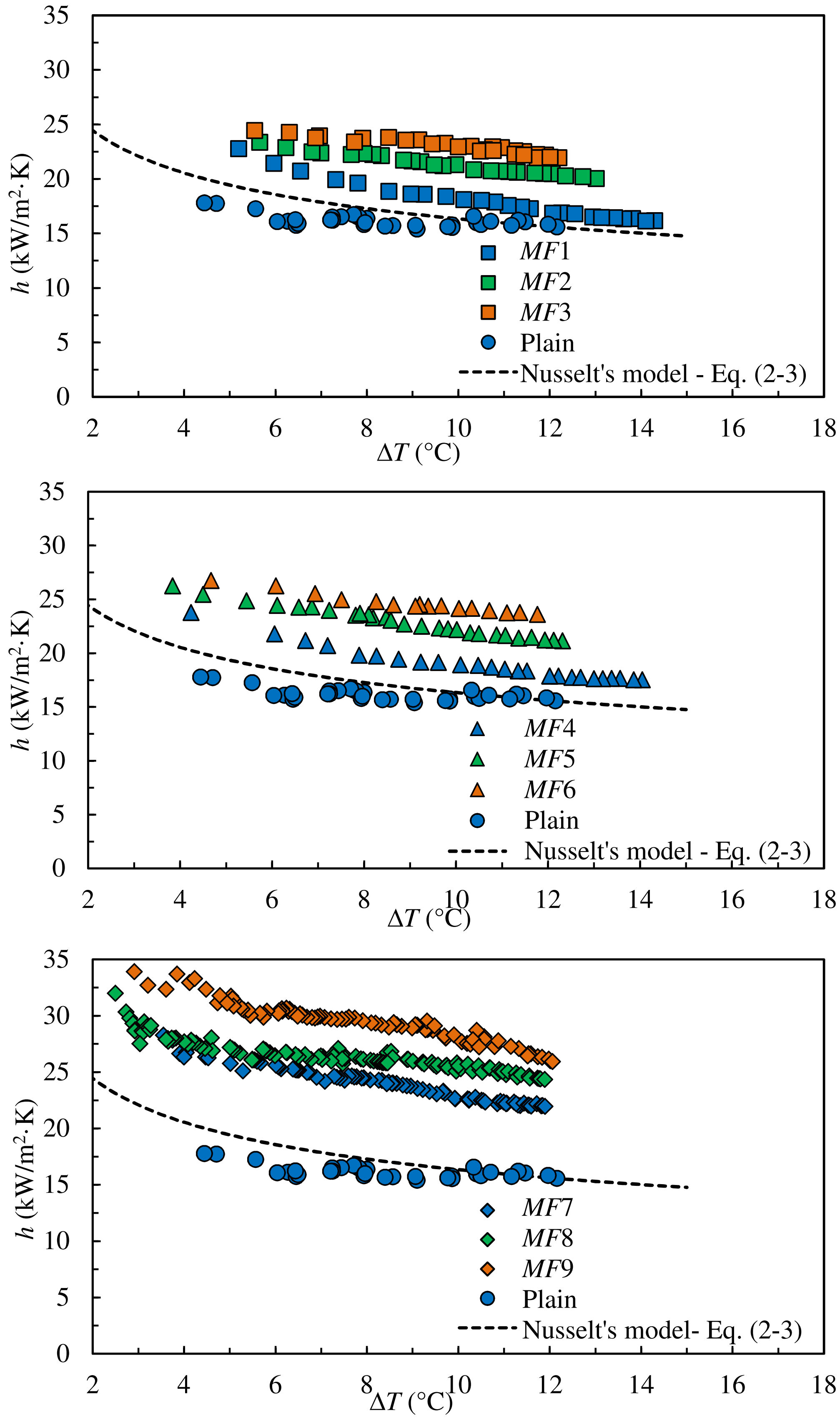

Fig. 5-19 Effects of cylindrical micro-pin-fin height on q'' at different ΔT.

A comparison of the experimental results of specimens *MF*1, *MF*4 and *MF*7 is shown in Fig. 5-20. These surfaces have the same fin pitch (p) of 0.9 mm but are of different fin heights (l). The fin heights of *MF*1, *MF*4 and *MF*7 are 0.3 mm, 0.6 mm and 0.9 mm, respectively. It is observed from Fig. 5-20 that the effects of increasing l from 0.3 mm to 0.6 mm only resulted in a small increment in q'' and h. However, with further increment in l from 0.6 mm to 0.9 mm, more significant enhancements in q'' and h are recorded. For example, at ΔT of approximately 10°C, the increase in l from 0.3 mm (*MF*1) to 0.6 mm (*MF*4) only contributed to an increase in q'' of 11.7%. On the other hand, increasing l from 0.6 mm (*MF*4) to 0.9 mm (*MF*7) produced a larger increase in q'' of 20.9%.

From the above, it can be observed that the increase in l for the micro-pin-fin surfaces resulted in a different effect as those observed for the conical and sinusoidal pin fin surfaces of millimetre sizes. For the conical and sinusoidal pin fins, as shown in Figs. 5-12 and 5-17, the increase in l generally resulted in a poorer heat transfer performance. However, for the micro-pin-fins, the q'' and h values increase with increasing l. It is likely that, for pin fins in the micrometre length scale, a larger effective heat transfer area can be achieved with larger l. This is because when the fin height is large ($l = 0.9$ mm), a large portion of the fin flank will protrude out of the condensate film. On the other hand, with smaller fin heights ($l \leq 600$ μm), a large portion of the fins are flooded which limits their heat transfer rate.

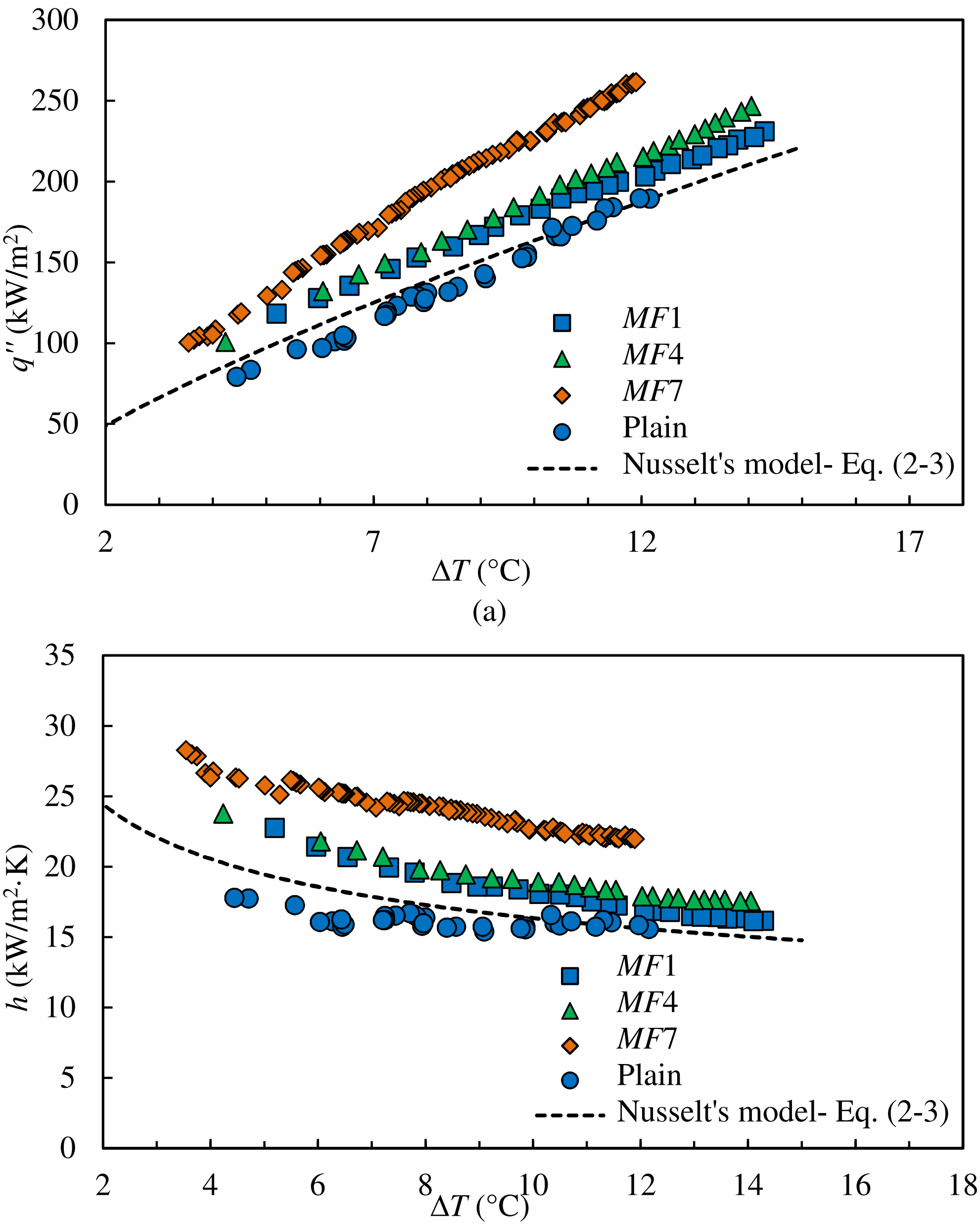

(a)

(b)

Fig. 5-20 Effects of cylindrical micro-pin-fin height on (a) q'' and (b) h at different ΔT.

Table 5-4 Constants *a* and *b* of Eq. (5-2), thermal enhancement factors (η) and condensate retention height ratios of *MF*1 – *MF*9 specimens.

Specimen name	*a*	*b*	η
*MF*1	38.757	0.6691	1.11
*MF*2	32.278	0.8158	1.29
*MF*3	31.352	0.8624	1.40
*MF*4	34.477	0.7402	1.16
*MF*5	34.897	0.8037	1.36
*MF*6	33.421	0.8595	1.48
*MF*7	36.964	0.7923	1.40
*MF*8	32.972	0.8858	1.56
*MF*9	41.411	0.8297	1.72

Finally, using the method described in Section 5.2, the thermal enhancement factors (η) of *MF*1 – *MF*9 were also computed and their values are shown in Table 5-4. It can be seen that, for the micro-pin-fin surfaces, the highest η value of 1.72 is achieved by the specimen *MF*9 which has the largest *l* and smallest *p* values.

5.4.4 Fin analysis

In this section, a fin analysis is performed to evaluate the average heat transfer coefficients (h_t) of the pin fin specimens where the h_t values of each specimen were computed by Eq. (5-4). In this equation, q'' is the condensation heat flux which is based on the specimen base area (A_2) of 25 mm × 25 mm, the fin efficiency (η_{fin}), the wetted area of the fin (A_{fin}), the unfinned area (A_b) and the total number of fins (n). This method of evaluating the heat performances of extended surfaces considers the total heat transfer area (A_t) and the fin efficiency (η_{fin}) of the specimens and has been employed by Xie et al. [133] and Hansen and Webb [134]. In order to determine η_{fin}, the three-dimensional heat conduction equation of Eq. (5-5) was solved numerically to obtain the temperature profile of each pin fin geometry.

An example of a sinusoidal fin structure which represents the computational domain is shown in Fig. 5-21 for illustration. A constant wall temperature at the fin base and a constant heat flux at the surface of the fin structure as shown in Eqs. (5-6) and (5-7) were prescribed. The simulations were performed using "Comsol Multiphysics" software where Eq. (5-5) was solved using the finite element method subjected to the boundary conditions of Eqs. (5-6) and (5-7). An unstructured grid system of different mesh elements was used. Mesh independence tests were conducted and the results were obtained with approximately 38,000 mesh elements. For each fin, the computations were performed over a range of h_t values and at each h_t value, η_{fin} was determined from Eq. (5-8) where A_0 is the area of the fin base. The simulations were performed for a conical pin fin of l = 1.28 mm, 1.92 mm and 2.56 mm, sinusoidal pin fin of l = 1.25 mm, 1.66 mm and 2.49 mm and micro-pin-fins of l = 0.3 mm, 0.6 mm and 0.9 mm. The computed η_{fin} values of the conical, sinusoidal and micro-pin-fins at different fin heights (l) are shown in Fig. 5-22. It can be seen that η_{fin} decreases with increasing h_t and l. Using the computed η_{fin} values and the correlated values of q'' as shown in Tables 5-2, 5-3 and 5-4 for the various specimens, the values of h_t were determined through an iterative approach for ΔT between 3°C and 13°C.

$$q''A_2 = h_t A_b (T_{sat} - T_w) + \sum_{i=1}^{n} \eta_{fin} h_t A_{fin} (T_{sat} - T_w) \tag{5-4}$$

$$\nabla \cdot (k_s \nabla T) = 0 \tag{5-5}$$

Boundary conditions:

$$T(r, \theta, 0) = T_w \tag{5-6}$$

$$-\mathbf{n}\cdot(-k_s \nabla T) = h_t(T_{sat} - T(R, \theta, z)) \tag{5-7}$$

Fin efficiency:

$$\eta_{fin} = \frac{Q_b}{Q_{max}} = \frac{-k_s A_0 \frac{\partial T}{\partial z}_{(r,\theta,0)}}{h_t A_{fin}(T_{sat} - T_w)} \tag{5-8}$$

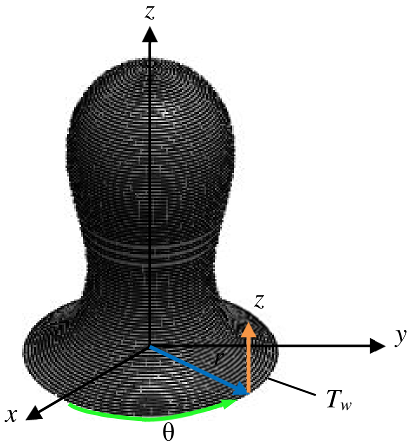

Fig. 5-21 Schematic diagram showing the coordinate system of a sinusoidal pin fin.

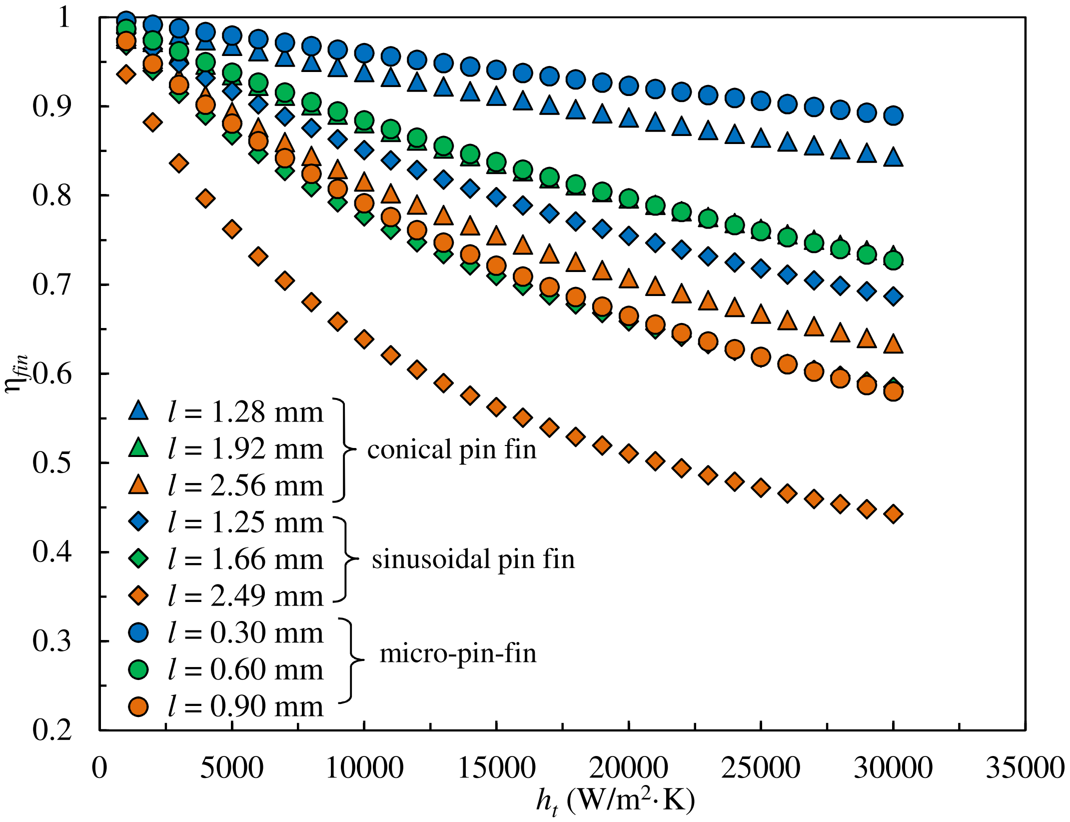

Fig. 5-22 Fin efficiency (η_{fin}) of a conical, sinusoidal and micro-pin-fins at different fin heights (l) and average heat transfer coefficients (h_t).

The average heat transfer coefficients (h_t) of the conical pin fin, sinusoidal fin pin and micro-pin-fin specimens are shown in Figs. 5-23 (a), (b) and (c), respectively. As depicted in Fig. 5-23 (b), for the sinusoidal pin fin specimens, three distinct regions of h_t values can be categorised based on the specimens' fin pitch (p) and their h_t values increase with increasing p. This comparison suggests that if the specimens were to have the same total heat transfer area (A_t), specimens with higher p will dissipate higher heat transfer rates than those with lower p. As shown in Fig. 5-15, the condensate retention height decreases with increasing p which resulted in a larger region of unflooded area. This, in turn, increases the available heat transfer area and increases h_t. The trend of higher h_t values with increasing p can similarly be observed in Fig. 5-23 (c) for the micro-pin-fin specimens. This, therefore, suggests that the increase in p similarly resulted in the reduction in the condensate retention height for the micro-pin-fin arrays. In addition, for specimens with the same p, the shortest fin height (l) exhibited the highest h_t values. As explained in Sections 5.4.1 – 5.4.3, the poorer h_t values of the longer pin fin specimens is due to the significantly lower fin efficiency and this can be further confirmed by the η_{fin} plot of Fig. 5-22. For instance, at h_t of 20000 W/m^2·K, the η_{fin} value of the sinusoidal pin fin with $l = 1.25$ mm is 0.75 and the micro-pin-fin with $l = 0.30$ mm is 0.92. However, for the sinusoidal fin with $l = 2.49$ mm and the micro-pin-fin with $l = 0.90$ mm, the η_{fin} value decreases to only 0.5 and 0.66, respectively.

On the other hand, unlike the sinusoidal and micro-pin-fin specimens, the increase in p of the conical pin fin does not result in a monotonic increase in h_t. For instance, it can be seen from Fig. 5-23 (a) that even though $C2$ has a p value of 1.67 mm, it exhibited significantly large h_t values than $C3$ whose p value is 2.50 mm. This differing trend of the conical pin fin from those of the sinusoidal and micro-pin-fin is likely because the condensate retention heights of the conical pin fin specimens do not increase linearly with increasing p. As can be seen from Fig. 5-11, even though the fin pitch of $C2$ is smaller than $C3$, its condensate retention height is also smaller. This resulted in significantly large number of unflooded fins and increase the available heat transfer area of $C2$ as compared to $C3$.

Finally, the h_t values of the plain surface are also plotted in Fig. 5-23 for comparison. It should be noted that for the plain surface, its h_t values are the same as its h values. It can be seen that for the conical pin fin specimens, only the h_t values of $C1$, $C2$, $C3$, *C*5, *C*6, *C*8 and *C*9 are above those of the plain surface whereas for the sinusoidal pin fin specimens, only the h_t values of *S*2, *S*3, *S*5, *S*6 and *S*9 lie above those of the plain surface. On the other hand, the h_t values of all the micro-pin-fin surfaces are found to be lower than those of the plain surface. The heat transfer performances of the enhanced and plain surfaces are affected mainly by the condensate film characteristics. For the plain surface, the condensate film flow is driven by gravity. On the other hand, for the pin fin arrays, surface tension forces drive the condensate film from the fin tip to the fin base and produce a thin film region near the fin tip which enhances heat transfer. The condensate accumulated at fin base is then removed by gravity. On the other hand, the flooding of the fin structures due to excessive retention of the condensate reduces the heat transfer performances of the surfaces. Therefore, this analysis suggests that for those specimens with h_t values higher than the plain surface, their heat transfer enhancements due to the surface tension forces significantly outweigh the degradation in heat transfer due to condensate retention. This resulted in higher h_t values as compared to that of a plain surface where the condensate flow is driven solely by gravity.

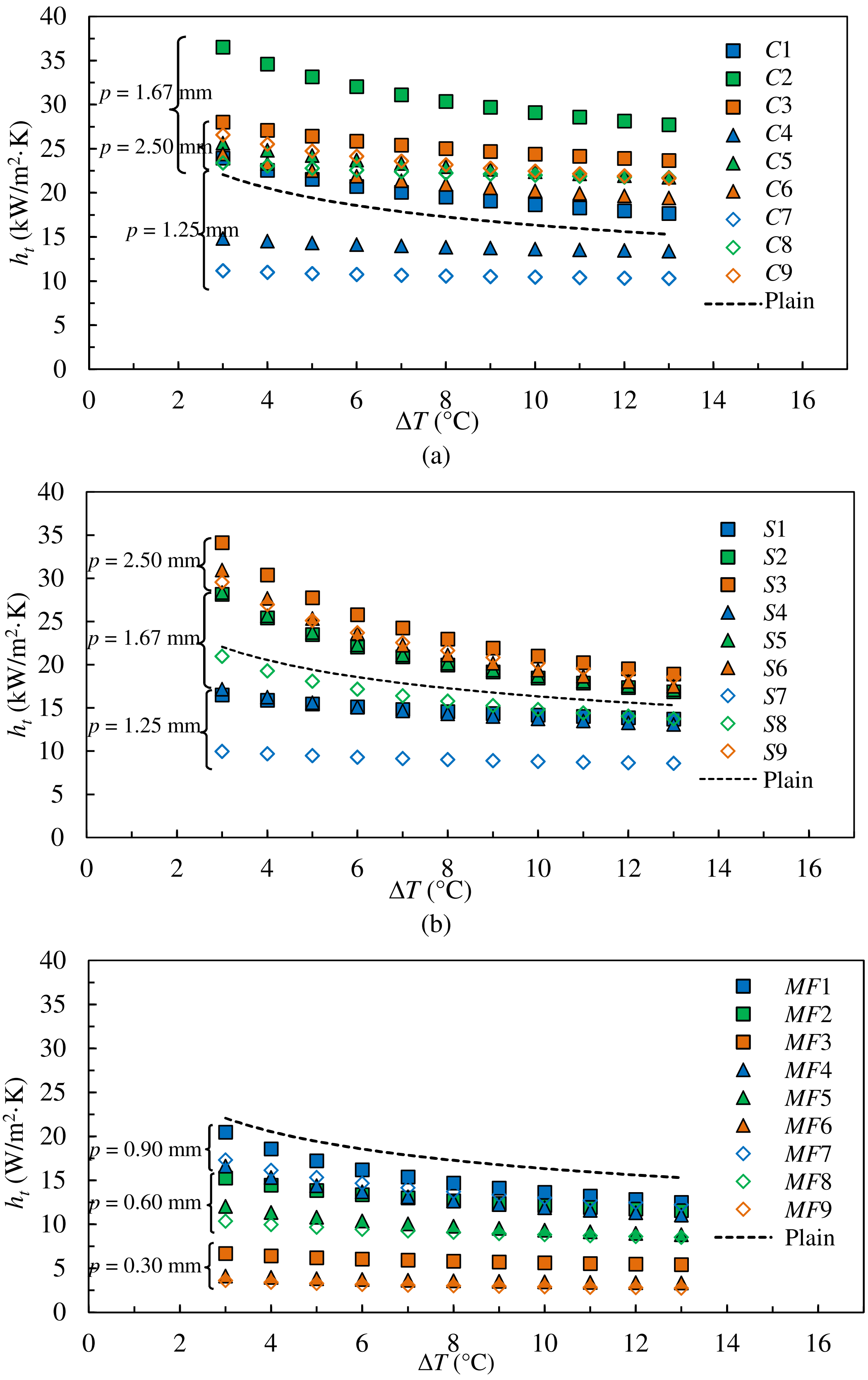

(a)

(b)

(C)

Fig. 5-23 Average heat transfer coefficients (h_t) of (a) conical pin fin, (b) sinusoidal pin fin and (c) micro-pin-fin specimens at various ΔT.

5.5 Performance evaluation

Figure 5-24 shows the thermal enhancement factor-to-area enhancement factor ratio (η/ε) of all the pin fin specimens. This ratio denotes the improvement in heat transfer coefficient per unit increase in the heat transfer area as compared to a plain surface. Since the thermal performances of the specimens are strongly influenced by the fin height (l) and fin pitch (p) of the pin fin array, η/ε is plotted against p/l in Fig. 5-24. It should be noted that η/ε values > 1 indicate that a unit area increment in the pin fin surface is more efficient in condensation heat transfer as compared to the unit area increment in the plain surface. As shown in Fig. 5-24, η/ε of all the pin fin surfaces increases with increasing p/l. In addition, η/ε > 1 was achieved with sinusoidal pin fin specimens *S*3 and *S*6 and conical pin fin specimens *C*1, *C*2, *C*3, *C*5, *C*6 and *C*9. Likely due to the larger surface tension forces induced at the fin tip and low condensate retention height, it can be seen that the conical pin fins achieved larger η/ε values as compared to the sinusoidal and micro-pin fin arrays. On the other hand, even though the sinusoidal pin fin geometry was shown to induce large surface tension forces at the fin tip, the thick condensate layer retained on the structures limits its heat transfer performance. Lastly, due to its fin geometry, it is expected that the micro-pin-fin structure has lower surface tension force and higher condensate retention as compared to the conical and sinusoidal structures. This resulted in the low η/ ε values recorded. Based on the above analysis, it can be concluded that among the three geometries investigated, the conical pin fin structure, which takes advantage of the surface tension effect and reduced condensate flooding, is the best geometry for enhancing natural convection condensation heat transfer.

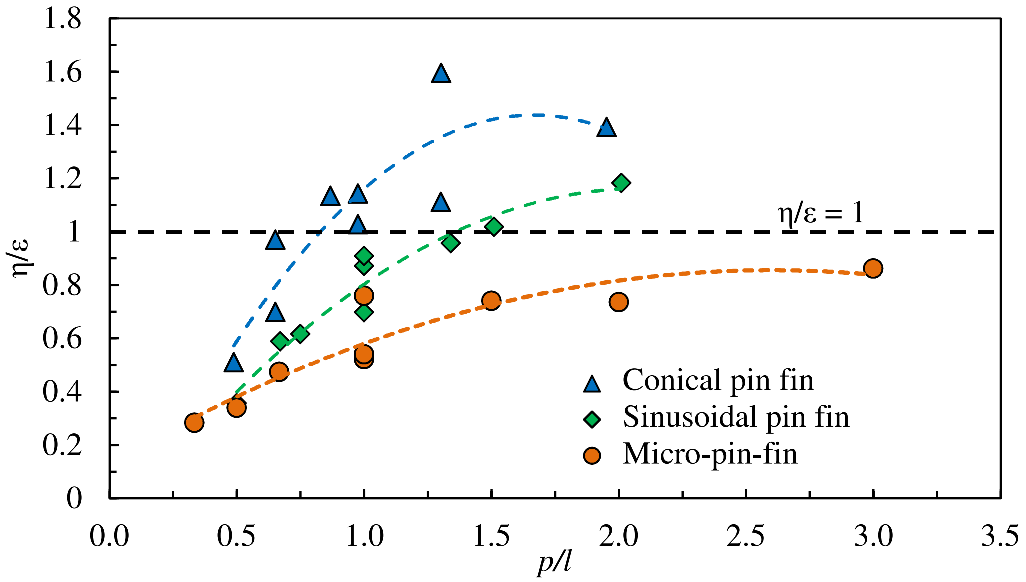

Fig. 5-24 Comparison of η/ε against *p*/*l* of conical pin fin, sinusoidal pin fin and micro-pin-fin structures.

The use of extended surfaces to enhance external condensation of steam on vertical plates has been widely investigated. For instance, Qi et al. [41, 136] conducted experimental and theoretical studies on two-dimensional trapezoidal and involuted grooves whereas theoretical predictions of condensation on two-dimensional triangular grooves with and without drainage strips were reported by Maschmann and Ma [135]. In order to evaluate the thermal performances of the SLM fabricated pin fin structures, a comparison of the q'' values between specimen *C*2 and the enhanced surfaces reported in Refs. [41, 135, 136] at various ΔT is shown in Fig. 5-25. Specimen *C*2 is selected for the comparison as it exhibits the highest heat transfer coefficients (h and h_t) and thermal enhancement factor (η) among all the specimens investigated. It should be noted that the q'' values reported by Maschmann and Ma [135] were for ΔT of 0°C – 3°C. For comparison against other enhanced surfaces, their results were extrapolated to ΔT of 15°C and presented in Fig. 5-25. On the other hand, the condensation heat fluxes of the enhanced surfaces (q_t'') presented by Qi et al. [41, 136]

were based on the total heat transfer area of the grooved surfaces. For comparison against other enhanced surfaces, the grooved areas of the enhanced surfaces in Refs. [41, 136] were estimated and their q_t'' values were converted to the condensation heat fluxes based on the specimen base area (q'') and presented in Fig. 5-25. It can be seen from the figure that, for Δ*T* higher than 6°C, the q'' values of specimen *C*2 are higher than all the other enhanced surfaces. On the other hand, at lower Δ*T*, the q'' values of specimen *C*2 approach those values of the grooved surface reported by Maschmann and Ma [135]. The better heat transfer performance of *C*2 as compared to Refs. [41, 135, 136] could likely be due to the larger surface tension forces induced by the conical geometry of the *C*2 fin. This is because the *C*2 fin is a three-dimensional structure which induces surface tension forces in two principal directions as compared to only one principal direction for the two-dimensional grooved surface.

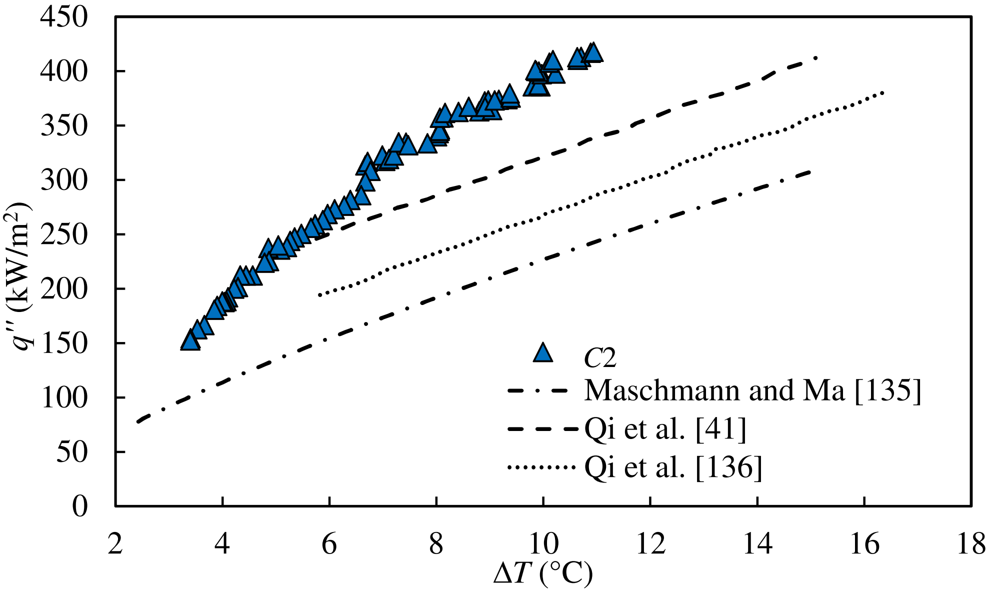

Fig. 5-25 Comparison of the best performing pin fin specimen, *C*2, against existing literature on condensation on vertical plates with fin structures.

The use of surface coating techniques, which allow surfaces of different hydrophobicities to be produced, has also been employed to enhance condensation on vertical surfaces. Peng et al. [137], for example, produced hydrophobic-hydrophilic hybrid surfaces using the self-assembling process. On the other hand, Lu et al. [138] fabricated a superhydrophobic surface by synthesising Si nanowires onto a substrate surface. Huang and Leu [139] and Ma et al. [140] also produce surfaces of different hydrophobicities using other surface coating techniques. A comparison of the experimental results of specimen $C2$ and the coated surfaces reported in Refs. [137 - 140] is shown in Fig. 5-26. It should be noted that dropwise condensation was observed on the surfaces reported in Refs. [138 - 140] whereas a combination of dropwise and filmwise condensation was reported by Peng et al. [137]. From Fig. 5-26, it can be seen that the q'' values of $C2$ are higher than those reported in Refs. [138 - 140]. It is commonly known that dropwise condensation produces a higher heat transfer rate as compared to filmwise condensation and surface coating techniques are often required to increase the hydrophobicity of the surface to promote dropwise condensation. However, sustaining long-term dropwise condensation is difficult. There is also a high tendency of the coatings to degrade and peel over time. Since $C2$ has higher q'' values than those achieved by dropwise condensation, it can be employed for long-term use when the need for such high heat fluxes arises. However, to achieve the q'' values as high as those of Ref. [137], further improvements in the pin fin design are required.

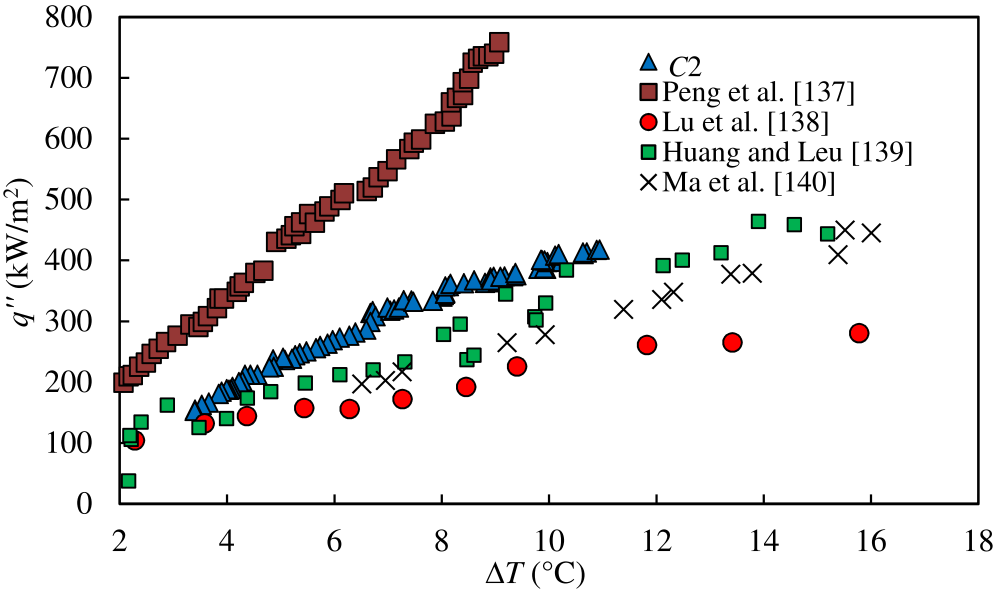

Fig. 5-26 Comparison of the best performing pin fin specimen, *C*2, against existing literature on condensation on vertical plates with coated surfaces.

5.6 Summary

In this chapter, the natural convection condensation of steam on two and three-dimensional fin arrays fabricated by SLM was experimentally investigated in a condensation chamber. Longitudinal fins of triangular, sinusoidal and rectangular geometries and pin fins with conical, sinusoidal and cylindrical geometries were studied. The effects of fin geometries, fin height and fin pitch were determined. Visualisation studies were also performed to determine the condensate retention heights on these specimens. The main findings are summarised as follows:

1. The three-dimensional pin fins exhibited higher heat transfer coefficients compared to their equivalent two-dimensional longitudinal fins even though the pin fin arrays have smaller heat transfer areas than the equivalent longitudinal fin arrays.

2. Based on the visualisation studies, the higher heat transfer coefficients of the pin fins are mainly due to the reduced condensate retention height. In addition, a comparison of their heat transfer areas and condensate retention heights also suggests that the additional surface tension effects on the pin fins have resulted in the enhanced heat transfer.
3. For the sinusoidal pin fin specimens, the fin height of 1.25 mm and the fin pitch of 1.67 mm showed the highest thermal enhancement factor. On the other hand, for the conical pin fin specimens, the highest thermal enhancement factor was obtained by the fin height of 1.28 mm and fin pitch of 1.67 mm.
4. The conical pin fin specimens demonstrated the highest heat transfer coefficient as compared to all other longitudinal and pin fin geometries investigated and the highest thermal enhancement factor of 2.46 was achieved with the $C2$ specimen.

Chapter 6 – Theoretical Modelling of Filmwise Condensation on Three-dimensional Pin Fins

In this section, a theoretical model for filmwise condensation on a three-dimensional conical pin fin is developed. This model considers the effects of surface tension and gravitational forces on the liquid film. An orthogonal curvilinear coordinate system which fits the surface geometry of the pin fin is employed and the liquid film equations are solved. The effects of various mechanisms on the liquid film characteristics were elucidated and the heat fluxes predicted by the theoretical model are compared against the experimental results.

6.1 Derivation of liquid film equation

The geometry of the conical pin fin in Cartesian coordinates (x, y, z) is shown in Fig. 6-1 (a) where y is in the direction of gravity. For the ease of the analysis, a parabolic coordinate system (ζ, ξ, θ), as shown in Fig. 6-1 (b), is proposed to fit the geometry of the pin fin structure. In this orthogonal curvilinear coordinate system, ζ represents the pin fin or liquid film surface and ξ is perpendicular to the surfaces. By revolving the ζ-ξ plane about the z-axis, a three-dimensional parabolic system is obtained. The coordinates of the Cartesian system can be related to the parabolic system by Eqs. (6-1) – (6-3). In addition, using Eqs. (6-4) – (6-6), the Lamé coefficients (or scale factors) of the parabolic coordinate system are defined.

$$x = \xi\zeta\cos\theta \tag{6-1}$$

$$y = \xi\zeta\sin\theta \tag{6-2}$$

$$z = \frac{1}{2}(\zeta^2 - \xi^2) \tag{6-3}$$

$$h_\xi = \sqrt{\left(\frac{\partial x}{\partial \xi}\right)^2 + \left(\frac{\partial y}{\partial \xi}\right)^2 + \left(\frac{\partial z}{\partial \xi}\right)^2} = \sqrt{\zeta^2 + \xi^2} \tag{6-4}$$

$$h_\zeta = \sqrt{\left(\frac{\partial x}{\partial \zeta}\right)^2 + \left(\frac{\partial y}{\partial \zeta}\right)^2 + \left(\frac{\partial z}{\partial \zeta}\right)^2} = \sqrt{\zeta^2 + \xi^2} \tag{6-5}$$

$$h_\theta = \sqrt{\left(\frac{\partial x}{\partial \theta}\right)^2 + \left(\frac{\partial y}{\partial \theta}\right)^2 + \left(\frac{\partial z}{\partial \theta}\right)^2} = \zeta\xi \tag{6-6}$$

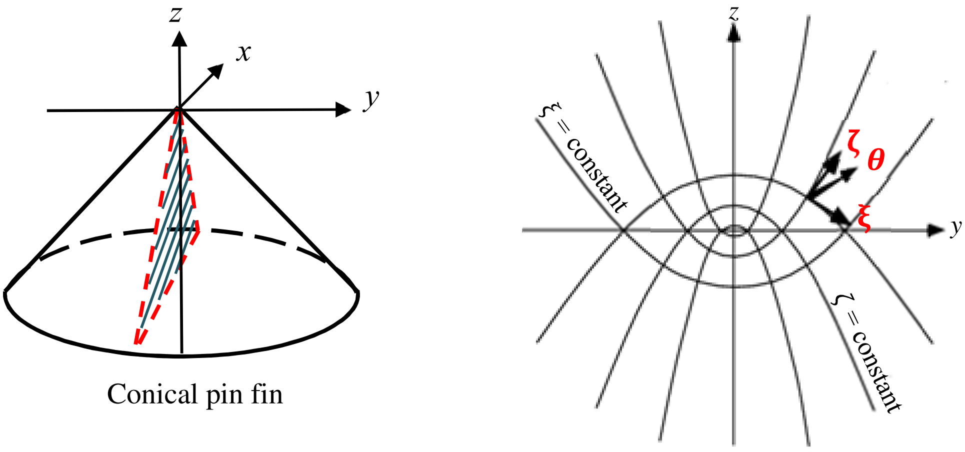

(a) (b)

Fig. 6-1 (a) Geometry and Cartesian coordinate system and (b) parabolic coordinate system of a conical pin fin.

In the present model, the following assumptions are made:

1. The heat transfer occurs under steady state condition.
2. The vapour which surrounds the pin fin is saturated and stagnant. No non-condensable gas is present and the vapour pressure and temperature are constant.
3. The pin fin surface is isothermal.
4. The liquid film flows along the ξ- and θ-directions and the flow is laminar. Along the fin, the liquid film is driven by surface tension in the ξ-direction. At the base of the fin, the liquid film is driven by surface tension and gravity in the θ-direction.

5. The inertia term of the momentum equations and the convection term of the energy equation are negligible as compared to the viscous and diffusion terms. Therefore, heat is transferred only by conduction across the liquid film.
6. The boundary layer theory assumptions are adopted where the temperature and velocity variations in the flow direction (ξ- and θ-directions) are significantly smaller than those in the normal direction (ζ -direction).

Using the above assumptions and employing the Lamé coefficients of Eqs. (6-4) – (6-6), the momentum equations in the ξ- and θ-directions can be written as Eqs. (6-7) and (6-8), respectively.

$$\frac{\mu_f}{\xi\zeta\sqrt{\xi^2+\zeta^2}}\frac{\partial}{\partial\zeta}\left[\frac{\xi\zeta}{\xi^2+\zeta^2}\frac{\partial}{\partial\zeta}\left(\sqrt{\xi^2+\zeta^2}u_\xi\right)\right]=\frac{1}{\sqrt{\xi^2+\zeta^2}}\frac{\partial P}{\partial\xi} \tag{6-7}$$

$$\frac{\mu_f}{\xi^2+\zeta^2}\frac{\partial}{\partial\zeta}\left[\frac{1}{\xi\zeta}\frac{\partial}{\partial\zeta}(\xi\zeta u_\theta)\right]=-\rho_f g sin\theta \tag{6-8}$$

At the surface of the fin, $\zeta = s$, where s is a constant, the no slip boundary condition is applied. On the other hand, at the liquid-vapour interface, $\zeta = s + \delta$, where δ is the liquid film thickness, the liquid film experiences no shear stress. Therefore, the boundary conditions of the momentum equations can be written as

$$\text{At } \zeta = s, u_\xi = u_\theta = 0 \tag{6-9}$$

$$\text{At } \zeta = s+\delta_n, \frac{\partial u_\xi}{\partial\xi}=\frac{\partial u_\theta}{\partial\theta}=0 \tag{6-10}$$

Using the continuity equation and employing Leibniz’s rule, the condensation mass flux ($\dot{m}$) can be written in the integral form as shown in Eq. (6-11). In addition, by assuming that the increase in the mass flux is due to the heat flux transferred across the liquid film, Eq. (6-12) can be obtained.

$$\dot{m} = \rho_f \frac{1}{\sqrt{\xi^2+s^2}} \frac{\partial}{\partial \xi} \int_s^{s+\delta_n} u_\xi \sqrt{\xi^2+s^2} d\zeta + \rho_f \frac{\sqrt{\xi^2+s^2}}{\xi s} \frac{\partial}{\partial \theta} \int_s^{s+\delta_n} u_\theta \, d\zeta \tag{6-11}$$

$$\dot{m} = \frac{k_f}{h_{fg}\sqrt{\xi^2+s^2}} \frac{\Delta T}{\delta_n} \tag{6-12}$$

Performing integration on Eqs. (6-7) and (6-8) with respect to ζ and subjected to boundary conditions of Eqs. (6-9) and (6-10), the expressions for u_ξ and u_θ can be obtained. Thereafter, the expressions of u_ξ and u_θ are substituted into Eq. (6-11) which is then combined with Eq. (6-12) to obtain an expression for the liquid film thickness (δ_n) as Eq. (6-13).

$$\frac{\partial}{\partial \xi}\left[(\xi^2+s^2)\frac{\partial P}{\partial \xi}\left(\frac{-\delta_n^3}{3}\right)\right] + \frac{(\xi^2+s^2)^2}{\xi s}\frac{\partial}{\partial \theta}\left[\left(\frac{\delta_n^3}{3}\right)\left(\rho_f g \sin\theta\right)\right] = \frac{\Delta T}{\rho_f h_{fg}} \frac{k_f \mu_f}{\delta_n} \tag{6-13}$$

In Eq. (6-13), P denotes the induced pressure due to the effect of surface tension (σ) and curvature of the liquid film in the ξ-direction (K_ξ) which can be determined from

$$P = -\sigma K_\xi \tag{6-14}$$

Following the approach of Toponogov [141], the curvature of the liquid film (K_ξ) is defined as Eq. (6-15), where $\vec{\psi}$ denotes the parametric equations (in vector form) of an arbitrary curve in the parabolic coordinate system and can be written as Eq. (6-16). Using Eqs. (6-15) and (6-16) and further assuming δ_n^2 to be much smaller than s^2, an expression for K_ξ as shown in Eq. (6-17) is obtained.

$$K_\xi = \frac{\left\| \frac{\partial \vec{\psi}}{\partial \xi} \times \frac{\partial^2 \vec{\psi}}{\partial \xi^2} \right\|}{\left\| \frac{\partial \vec{\psi}}{\partial \xi} \right\|^3} \tag{6-15}$$

$$\vec{\psi} = \xi(s+\delta_n)\cos\theta, \xi(s+\delta_n)\sin\theta, \frac{1}{2}[(s+\delta_n)^2 - \xi^2)] \tag{6-16}$$

$$K_\xi = \sigma \frac{(\xi^2+s^2)\frac{\partial^2 \delta_n}{\partial \xi^2}+\xi\frac{\partial \delta_n}{\partial \xi}-(s+\delta_n)}{(\xi^2+s^2)^{3/2}} \tag{6-17}$$

Substituting Eqs. (6-14) and (6-17) into Eq. (6-13), the equation to solve for the liquid film thickness is obtained as Eq. (6-18). This is a two-dimensional partial differential equation which is fourth-order in the ξ-direction and first order in θ-direction. A schematic diagram of the conical pin fins is shown in Fig. 6-2. Equation (6-18) applies to Region I where the surface tension force in the ξ-direction is dominant. At the fin tip, where ξ = 0, a film thickness (δ_0) is prescribed and by symmetry, $\frac{\partial \delta_n}{\partial \xi}$ = 0. Similarly, at the top of the fin flank where θ = 0, a symmetry condition of the liquid film also exists, thus giving $\frac{\partial \delta_n}{\partial \theta}$ = 0. Near the base of the fin structure where the condensate accumulates, the liquid interface takes the form of a circular arc. Therefore, the curvature in Region II is a constant in the ξ-direction and the liquid is drained in the θ-direction. The end of Region I occurs at ξ = ξ_l where a finite film thickness δ_l exists. By geometry, the gradient of the film thickness, $\frac{\partial \delta_n}{\partial \xi}$, at ξ = ξ_l can be equated to the gradient of the circular arc, where α and β are the tangent lines to the fin and liquid film surfaces, respectively. The boundary conditions described above are depicted as Eqs. (6-19) – (6-21).

$$\frac{\partial}{\partial \xi}\left[(\xi^2+s^2)\frac{\sigma}{3}\delta_n^3\frac{\partial}{\partial \xi}\left\{\frac{(\xi^2+s^2)\frac{\partial^2 \delta_n}{\partial \xi^2}+\xi\frac{\partial \delta_n}{\partial \xi}-(s+\delta_n)}{(\xi^2+s^2)^{3/2}}\right\}\right]+\frac{(\xi^2+s^2)^2}{\xi s}\frac{\partial}{\partial \theta}\left[\left(\frac{\delta_n^3}{3}\right)\left(\rho_f g \sin\theta\right)\right]=\frac{\Delta T k_f \mu_f}{\rho_f h_{fg}\delta} \tag{6-18}$$

$$\text{At } \xi = 0, \delta_n = \delta_0, \frac{\partial \delta_n}{\partial \xi} = 0 \tag{6-19}$$

$$\text{At } \xi = \xi_l, \delta_n = \delta_l, \frac{\partial \delta_n}{\partial \xi} = \frac{\xi \tan(\beta+\alpha)-(s+\delta_l)}{\xi+(s+\delta_l)\tan(\beta+\alpha)} \tag{6-20}$$

$$\text{At } \theta = 0, \frac{\partial \delta_n}{\partial \theta} = 0 \tag{6-21}$$

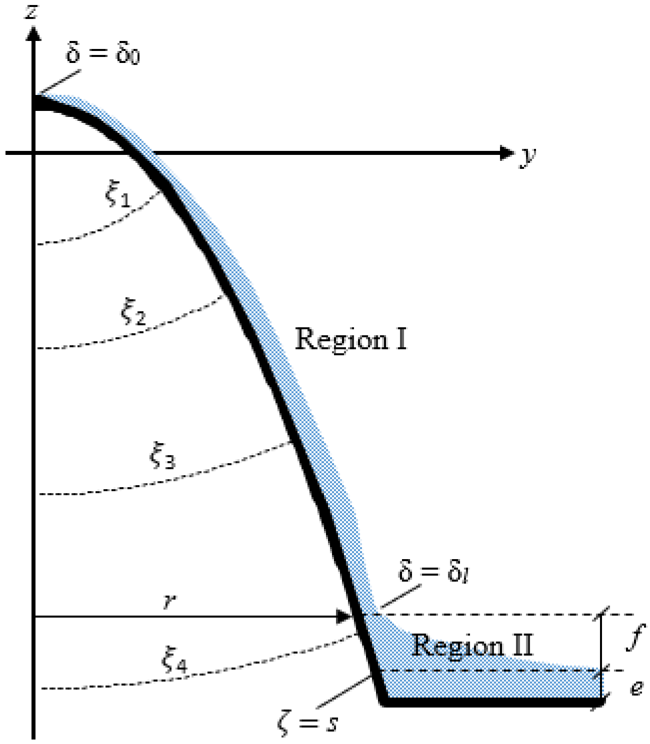

Fig. 6-2 Schematic of liquid film on conical pin fin – side view.

Since the liquid film in Region II has a constant radius with respect to ξ, surface tension has no effect on the liquid film in the ξ-direction and it is drained along the circumference of the pin fin, *viz*., in the θ-direction. As shown in Fig. 6-3, the liquid film flows in the θ-direction and is driven by gravity. In addition, as the curvature of the liquid film also changes as it flows in this direction, the surface tension, K_θ, is induced. Using the method proposed by Krupiczka [37] and following the same procedures above, the variation of the liquid film thickness in the θ-direction due to the combined effects of gravity and surface tension is given by

$$A(\delta^*)^{1/4}\frac{d^2\delta^*}{d\theta^2}+\frac{3}{4}\sin\theta\frac{d\delta^*}{d\theta}+\delta^*\cos\theta-1=0 \tag{6-22}$$

In Eq. (6-22), δ^* is the dimensionless liquid film thickness and is given by Eq. (6-23), where r is the radius of the pin fin at a ξ location. On the other hand, A is related to the

Weber number (We), r and the thermophysical properties of the liquid film as shown in Eqs. (6-24) and (6-25). It should be noted that the relationship between δ_n of Eq. (6-18) and δ of Eq. (6-23) can be approximated through the relation of their respective coordinate systems.

$$\delta^* = \frac{\delta^4}{3r\Delta T k_f \mu_f / \rho_f^2 g h_{fg}} \tag{6-23}$$

$$A = \frac{1}{4}\frac{\mathrm{We}}{r^{3/4}}\left(\frac{3\Delta T k_f \mu_f}{\rho_f^2 g h_{fg}}\right)^{1/4} \tag{6-24}$$

$$\mathrm{We} = \frac{\sigma}{\rho_f g r^2} \tag{6-25}$$

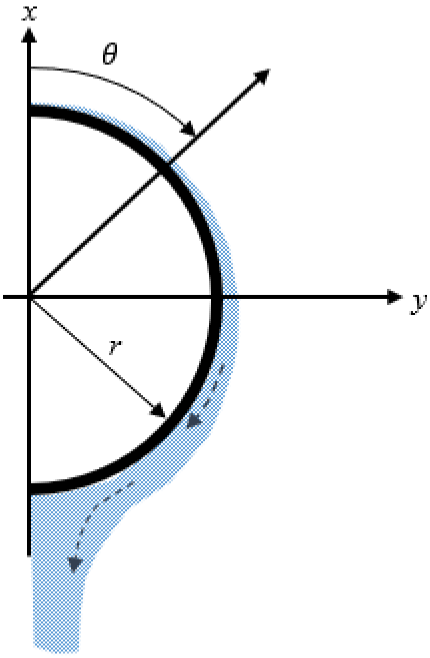

Fig. 6-3 Schematic of liquid film on conical pin fin – top view.

Equation (6-22) represents an initial value problem where two conditions at $\theta = 0$ must be satisfied. By geometrical symmetry, the first boundary condition is obtained as Eq. (6-26).

$$\text{At } \theta = 0, \frac{d^2\delta^*}{d\theta^2} = \frac{d^2\delta}{d\theta^2} = 0 \tag{6-26}$$

On the other hand, the second boundary condition pertains to the value of the liquid film thickness at $\theta = 0$ where the effect of surface tension is negligible. The liquid film thickness can then be obtained by setting A of Eq. (6-22) to zero, thus, yielding Eq. (6-27). The solution to Eq. (6-27) is obtained analytically and is expressed as Eq. (6-28) which is of the same form developed by Nusselt [27]. Finally, by employing L'Hôpital's rule on Eq. (6-28), the limiting value of δ^* when θ approaches zero is determined as Eq. (6-29).

$$\frac{3}{4}\sin\theta\frac{d\delta^*}{d\theta} + \delta^*\cos\theta - 1 = 0 \tag{6-27}$$

$$\delta^* = \frac{1}{\sin^{3/4}\theta}\left(\frac{4}{3}\int_0^\theta \sin^{1/3}\theta d\theta\right) \tag{6-28}$$

$$\text{At } \theta = 0, \delta^* = 1 \tag{6-29}$$

At the end of Region I, the liquid film thickness is determined by solving Eq. (6-22) numerically using the second-order Runge-Kutta method subjected to the boundary conditions of Eqs. (6-26) and (6-29). On the other hand, at the fin tip, r tends to zero and the surface tension in the ξ-direction is negligible. Therefore, the values of the liquid film thickness at the fin tip can be determined by solving Eq. (6-22) using a small value of r. A series of computations was performed using different r values ranging from 0.0001 mm to 1 mm and it was determined that for $r \leq 10^{-6}$ m, no significant change in the results was observed. Therefore, the r value of 10^{-6} m was used.

With the boundary conditions of Eqs. (6-19) – (6-21) fully defined, the liquid film equation of Eq. (6-18) is solved numerically using the finite difference method. The central difference scheme with second-order accuracy is employed to discretise Eq. (6-18) and the 'ghost' point approximation [142] is used to solve the boundary nodes. Since Eq. (6-18) is a non-linear differential equation, an external iterative loop is set up using the Newton-Raphson method with the initial guess values of δ_n. The Jacobian matrix is then solved using the Gaussian elimination solver as the internal iterative loop to compute the new δ_n values. For each interior node, the computation is repeated until the convergence criterion of $\left|(\delta_{n,i} - \delta_{n,i,new})/\delta_{n,i}\right| < 10^{-6}$ is achieved. The computation procedure is summarised in Fig. 6-4 and the calculations were performed using the MATLAB software.

In the next section, the theoretical model developed above is employed to investigate the liquid film characteristics on the conical pin fin and the dimensions of specimen $C1$ are used for the case study. Using the base diameter (d_b) and height (l) of $C1$ fins, the s value of the fin structure in the orthogonal coordinate system was determined. On the other hand, e (shown in Fig. 6-2) is obtained by normalising the condensate retention height over the fin array and was calculated to be approximately 7.2% of the fin height. These values were used for the numerical computation.

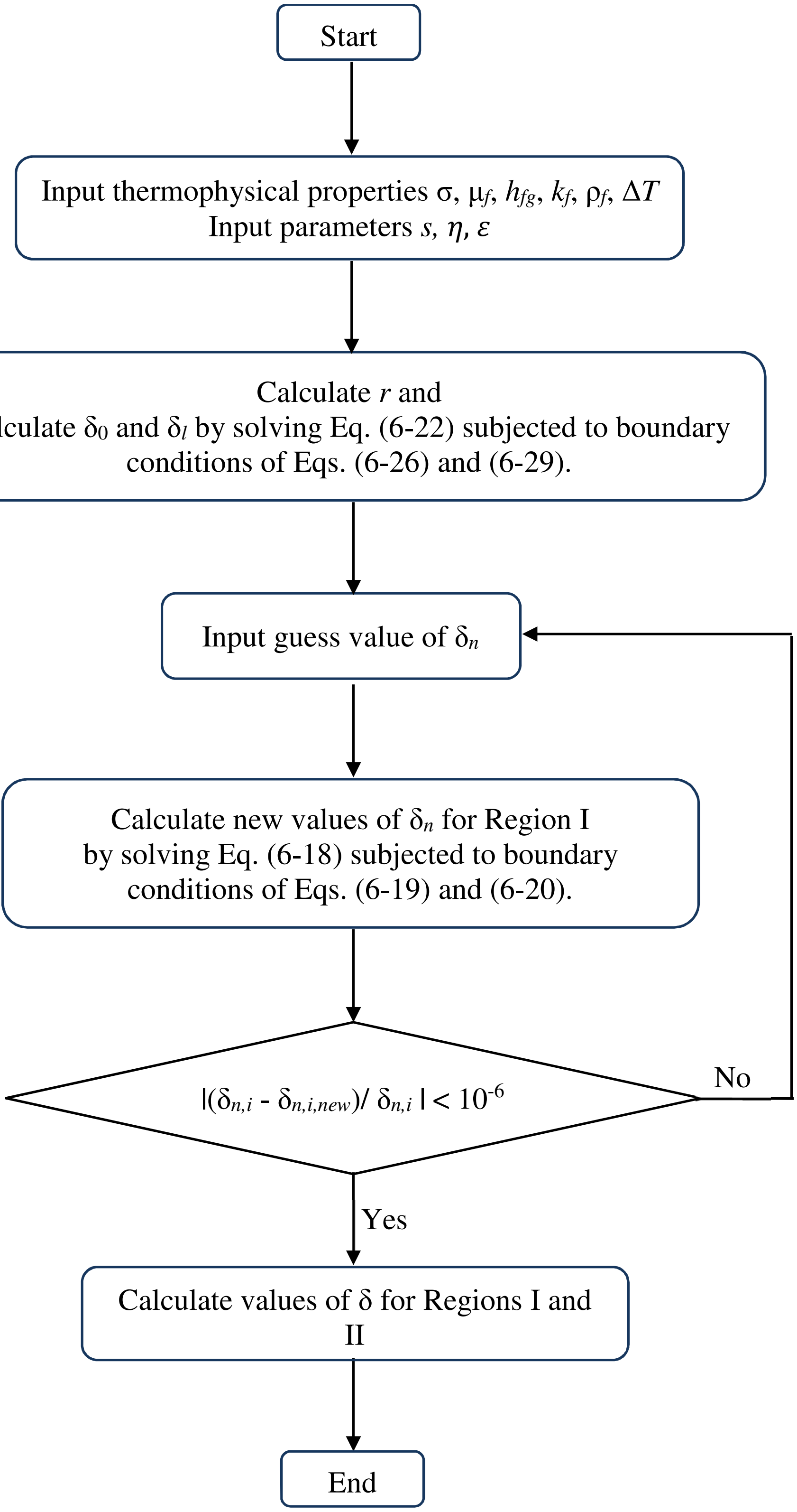

Fig. 6-4 Computation procedure.

6.2 Results and discussions

Figure 6-5 shows the variation of the liquid film thickness (δ) with respect to θ and evaluated at $\Delta T = 5$°C and $\xi = \xi_l$. At this ξ_l value, r corresponds to 0.53 mm. In this figure, the effect of surface tension on the liquid film is compared. The liquid film thickness with the effect of surface tension in the θ-direction is obtained by solving Eq. (6-22) and the liquid film thickness without surface tension is obtained from Nusselt's solution of Eq. (6-28). It can be seen that a thin film region exists near the top of the fin ($0° \leq \theta \leq 40°$), with δ ranging from approximately 0.05 mm to 0.06 mm. In this region, there is a gradual change in the liquid film curvature and therefore, surface tension has no noticeable effect. As the condensate flows circumferentially downstream, there is a steep increment in the film thickness and this resulted in a significant influence of the surface tension force. As can be seen in Fig. 6-5, the liquid film thickness for θ more than 100° is several times smaller as compared to the liquid film thickness when surface tension force is considered. This substantially improves the local heat transfer coefficients near the bottom region of the fin.

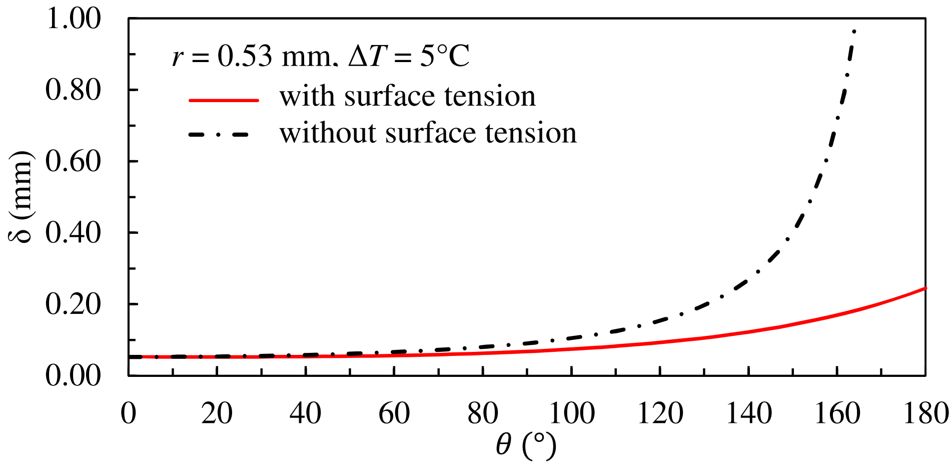

Fig. 6-5 Effects of surface tension on liquid film thickness (δ) at $\xi = \xi_l$, $r = 0.53$ mm and at $\Delta T = 5$°C

Figure 6-6 shows the variation of the liquid film thickness (δ) along the vertical fin distance (ξ-direction) at $\theta = 0°$ and $\Delta T = 5°C$ but with different r values. It should be noted that the fin tip is located $\xi = 0$. As mentioned in Section 6-1, the different δ values at the fin tip are obtained by solving Eq. (6-22) with small values of r ranging from 0.0001 mm and 1 mm. It can be seen from the figure that the change in δ at the fin tip resulted in different liquid film characteristics. For all the δ curves, a distinct thin film region can be identified near the fin tip and thereafter, the liquid film thickness increases significantly along the flank of the fin. In addition, the reduction in the fin tip radius (r) not only reduces the δ at the fin tip but also along the fin flank. For example, with the change in r from 1 mm to 0.1 mm, which corresponds to the change in δ at the fin tip ($\delta_{fin\ tip}$) from 0.0109 mm to 0.00616 mm, a significant reduction in δ is observed between the fin tip and the upper portion of the fin flank where z ranges from 0 to 1.0 mm. However, with the subsequently reduction in r, the corresponding change in δ becomes less significant and no noticeable change in δ can be observed with $r \leq 0.001$ mm. In addition, near the fin base where ξ is between 1 mm and 1.4 mm, another thin film region is observed. This thin film region is similarly reported in Refs. [39, 40] and is due to the presence the liquid pool accumulated at the fin base. This liquid pool is shown as Region II of Fig. (6-2) and it takes the form of a concave shape. As a result of the concave shape, a large change in curvature of the liquid film near the fin base is induced and this produces a thinning effect on the liquid film in this region.

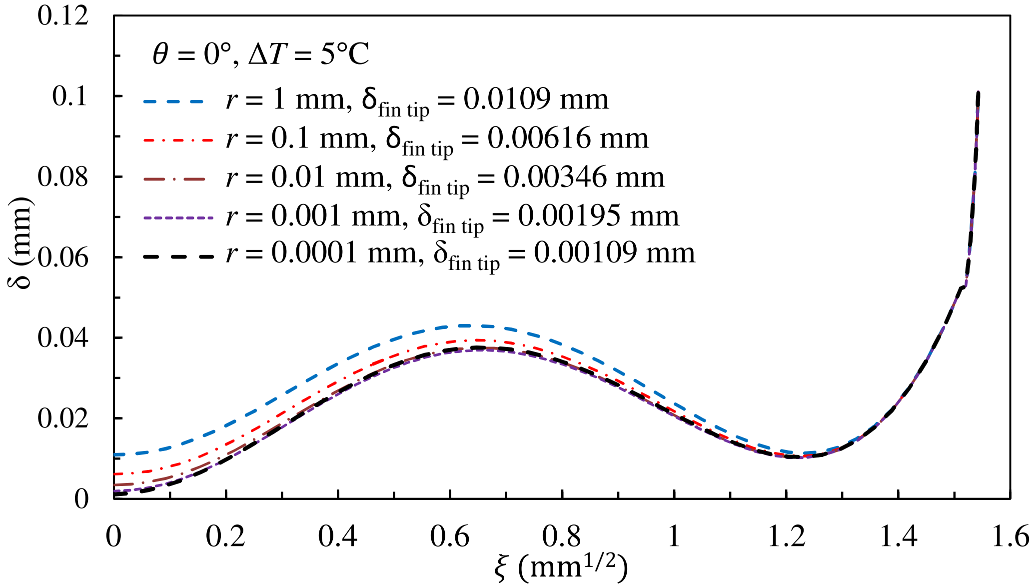

Fig. 6-6 Effects of fin tip radius (r) on liquid film thickness (δ) along ξ-direction at θ = 0° and ΔT = 5°C.

At a constant θ and ΔT, the local condensation heat transfer coefficient (h_l) can be obtained by Eq. (6-30) and the length-averaged heat transfer coefficient ($h_{ave,}$) with respect to ξ can be calculated from Eq. (6-31). The computed results of $h_{ave,}$ at different $\delta_{fin\ tip}$ values are shown in Fig. 6-7. It can be clearly seen from this figure that the effects of $\delta_{fin\ tip}$ on $h_{ave,\mathrm{z}}$ are only significant when the $\delta_{fin\ tip}$ values are large and the effects of $\delta_{fin\ tip}$ diminish when $\delta_{fin\ tip}$ approaches 0.002 mm. As shown in Fig. 6-6, this value of $\delta_{fin\ tip}$ corresponds to the fin tip radius (r) of 0.001 mm. Finally, from Figs. 6-6 and 6-7, it can also be concluded that a small fin tip radius significantly enhances the heat transfer performance of the pin fin.

$$h_l = \frac{k_f}{\sqrt{\xi^2+s^2}\delta_n} \tag{6-30}$$

$$h_{ave,\xi} = \frac{1}{\xi_l}\int_0^{\xi_l} h_l d\xi \tag{6-31}$$

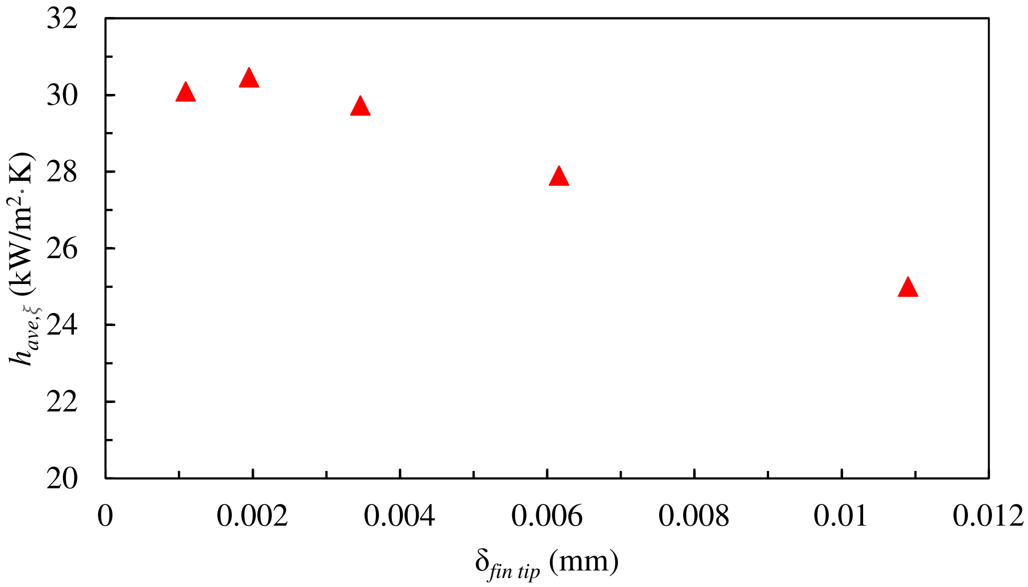

Fig. 6-7 Effects of fin tip liquid film thickness on average heat transfer coefficient ($h_{ave,}$) at $\theta = 0°$ and $\Delta T = 5°C$.

Figure 6-8 shows the liquid film thickness along the ξ-direction at different θ values and with ΔT maintained at 5°C. It can be seen that due to the large surface tension force induced at the fin tip, the liquid film thickness (δ) in this region is significantly small for all θ values. At the same ξ location, on the other hand, the increase in θ from 0° to 60° also produces no noticeable effect on δ and the liquid film profile remains relatively unchanged. However, as θ increases beyond 90°, the liquid film thickens substantially along the fin flank and fin base. For instance, at $\xi = 1.2$ mm$^{1/2}$ and $\theta =$ 90°, the δ is approximately 0.025 mm. However, with the increase in θ to 120°, δ is found to increase to 0.047 mm and is almost two times thicker. As the liquid film thickness is inversely proportional to the local heat transfer coefficient, it is expected that the heat transferred from the bottom section of the fin flank, where $\theta > 90°$, is low. On the other hand, significantly higher heat fluxes can be achieved near the fin tip and along the fin flank and fin base for θ between 0° and 60°.

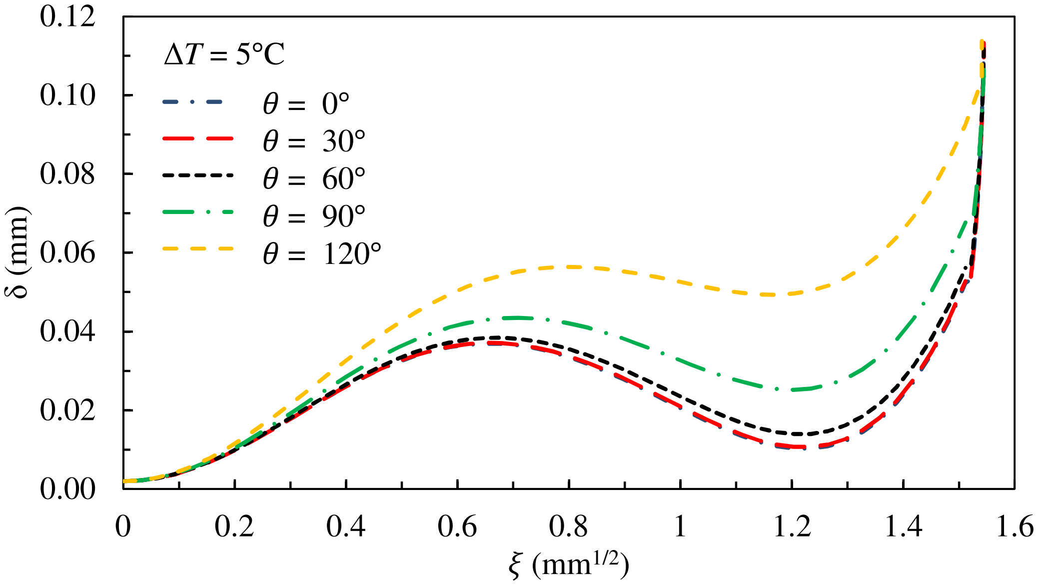

Fig. 6-8 Comparison of liquid film thickness (δ) at $\Delta T = 5$°C and at different θ values.

Figure 6-9 depicts the effects of fin wall temperature on the liquid film characteristics. For the results presented in this figure, the simulation was performed with ΔT ranging from 3°C to 15°C while maintaining value of θ at 0°. As shown in the figure, a consistent increase in the liquid film thickness with increasing ΔT can be observed. This result is expected as the increase in ΔT give raise to the increase in condensate mass flux. As the driving force due to surface tension is unable to keep up with the increase in mass flux, this resulted in the corresponding increase in δ. However, it is also interesting to note that due to the large surface tension effect at the fin tip, a thin liquid film is maintained in this region even at high ΔT and the increase in δ mainly occurs near the fin base.

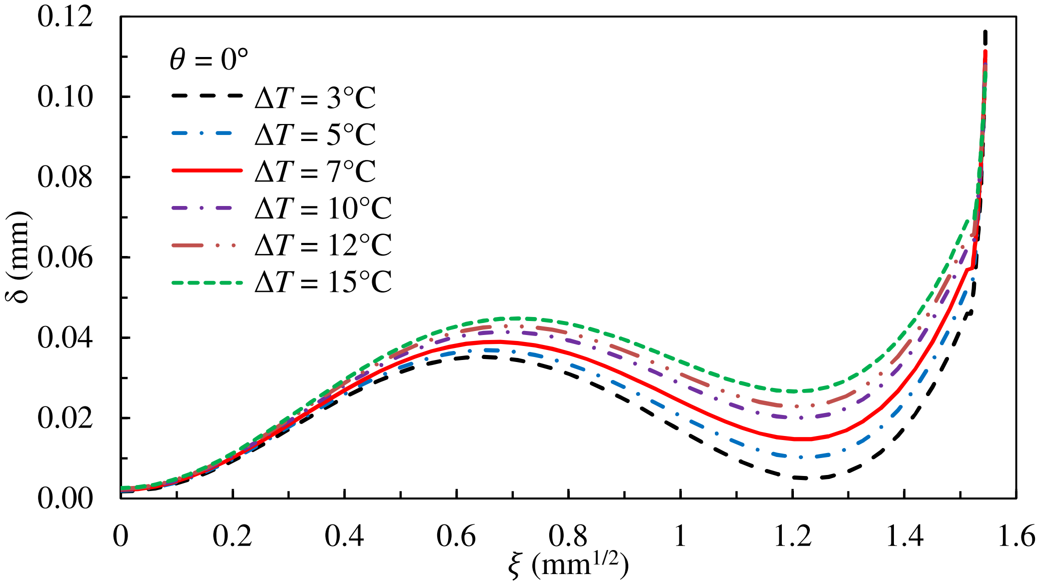

Fig. 6-9 Comparison of liquid film thickness (δ) at $\theta = 0°$ and at different ΔT values.

The theoretical condensation heat flux for specimen $C1$ can be estimated from the local heat transfer coefficient (h_l) using Eq. (6-32), where the first integral term on the right hand side of the equation gives the average heat transfer coefficient in Region I and the second term is that of Region II. In addition, ξ_l and ξ_f are the end points of Regions I and II, respectively, A_w is the total heat transfer area of Regions I and II and A_b is base area of the specimen.

$$q'' = \frac{A_w}{A_b}\left\{\frac{1}{2\pi}\int_0^{2\pi}\frac{1}{\xi_l}\int_0^{\xi_l} h_l d\xi d\theta + \frac{1}{2\pi}\int_0^{2\pi}\frac{1}{\xi_f - \xi_l}\int_{\xi_l}^{\xi_f} h_l d\xi d\theta\right\}\Delta T \qquad (6\text{-}32)$$

At a constant ΔT, the liquid film thickness was determined at each ξ and θ locations and the results were numerically integrated by Eq. (6-32). Based on this approach, the simulation was performed over a range of ΔT values. The results obtained from the theoretical model are plotted in Fig. 6-10 and a comparison is made against the experimental q'' values of specimen $C1$. At low ΔT of between 3°C and 7°C, it can be seen that reasonably close agreement between the theoretical model and experimental results are obtained, with deviations of up to 7.3%. However, with further increase in ΔT, the deviation between the experimental and theoretical results increases. For instance, at ΔT of 12°C, the difference between the q'' value predicted by the theoretical model and that obtained from the experiment is approximately 13.4%. The discrepancy between the theoretical prediction and the experimental results at high ΔT could be due to the high surface roughness of the specimen. As the surfaces of the fins are rough, at higher ΔT when condensate flow rate is higher, it is likely that the rough surface may induce wave formation on the falling liquid film. Wave formation has been reported by several investigators [29, 143] and was shown to enhanced condensation heat transfer. Therefore, this mechanism may have resulted in the higher q'' values as compared to the theoretical predictions.

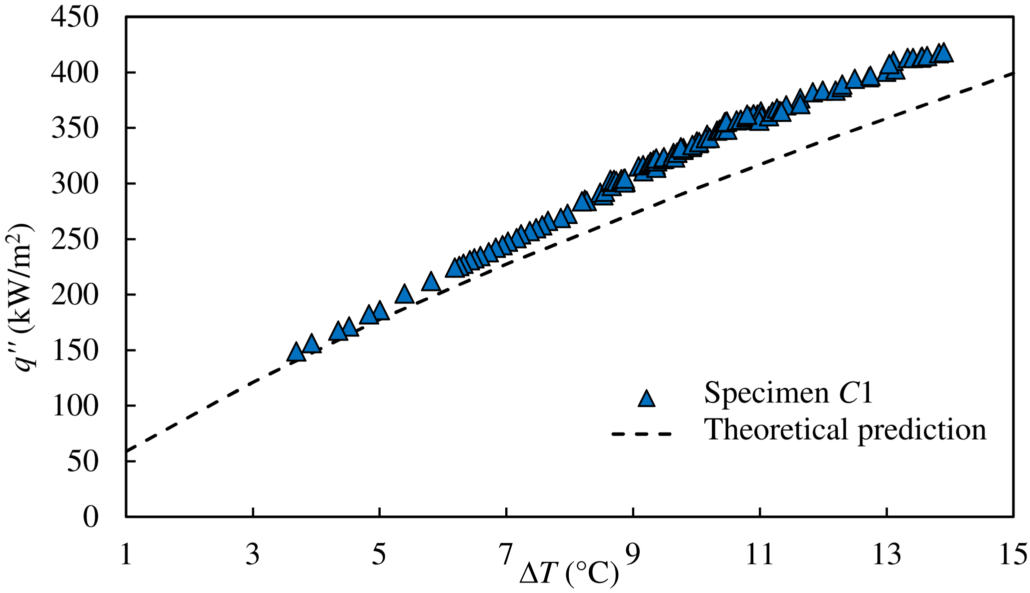

Fig. 6-10 Comparison of experimental and predicted heat fluxes of specimen $C1$.

Chapter 7 – Forced Convection Condensation in Three-dimensional Pin Fin Tubes Produced by Selective Laser Melting

This chapter presents the experimental results of forced convection condensation of R134a refrigerant inside plain and enhanced tubes. The enhanced tubes were fabricated by SLM and their geometrical dimensions are shown in Table 3-3. The experiments were conducted at the saturation pressure (P_{sat}) of 13.4 bar, the refrigerant mass fluxes (m_{ref}) of 50 kg/m^2·s to 200 kg/m^2·s and the average vapour qualities (x_{ave}) of 0.2 to 0.8. The effects of circumferential fin height and pitch of the conical pin fin tubes are examined and comparisons are made other enhanced tubes. Based on the experimental results obtained, a semi-empirical model is developed to predict the heat transfer coefficients of the conical pin fin tubes.

7.1 Validation of experimental results

The flow regime map for two-phase flow in a smooth tube developed by Taitel and Dukler [144] is shown in Fig. 7-1. This flow regime map relates the dimensionless vapour velocity (J_G) with the Martinelli parameter (X_{tt}) and demarcates the flow into four main regions. The expression for J_G is given in Eq. (7-1) whereas X_{tt} is defined in Eq. (2-38). Using the thermophysical properties of R134a at P_{sat} of 13.4 bar, m_{ref} between 50 kg/m^2·s and 200 kg/m^2·s and x_{ave} between 0.2 and 0.8, the flow regimes during the condensation experiments in the commercial Al tube can be determined.

$$J_G = \frac{Gx}{\sqrt{g d_i \rho_g (\rho_l - \rho_g)}} \tag{7-1}$$

As shown in Fig. 7-1, for m_{ref} between 100 kg/m^2·s and 200 kg/m^2·s, the refrigerant is mainly in the annular flow regime. On the other hand, when m_{ref} is at 50 kg/m^2·s, a stratified-wavy flow exists in the tube.

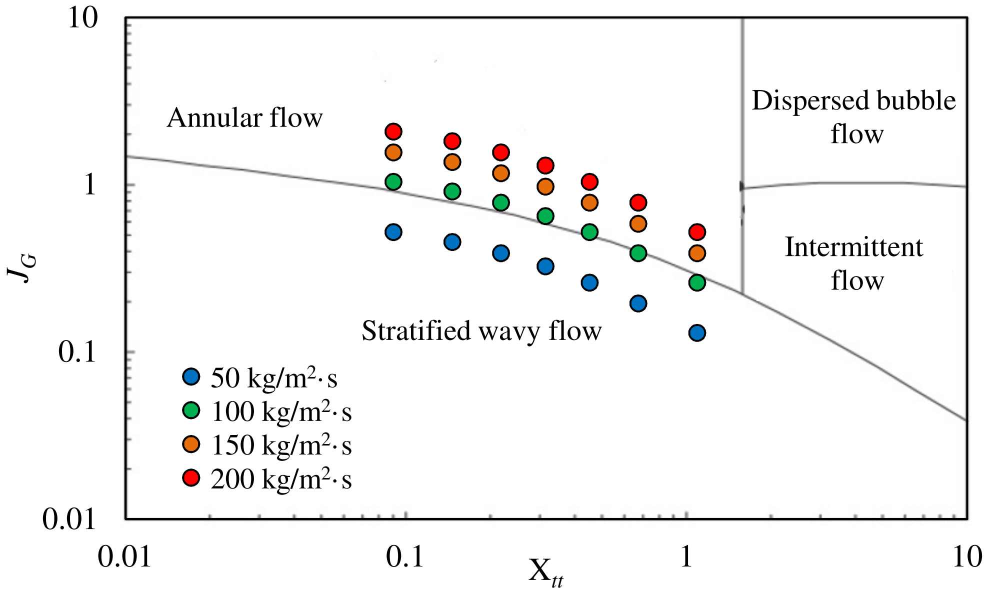

Fig. 7-1 Flow regimes of two-phase flow in a plain tube at P_{sat} = 13.4 bar, m_{ref} from 50 to 200 kg/m^2·s and x_{ave} from 0.2 to 0.8.

In order to determine the accuracy of the test facility, the experimental condensation heat transfer coefficients (h_{ref}) of R134a in the commercial Al tube are compared against existing correlations. For the m_{ref} ranging from 100 kg/m^2·s to 200 kg/m^2·s, the experimental results are compared against the correlations of Shah [79], Cavallini and Zecchin [82] and Dobson and Chato [83] as shown in Eqs. (2-45), (2-47) and (2-48), respectively. These correlations were developed for the annular flow regime. On the other hand, for m_{ref} = 50 kg/m^2·s, the correlation of Jaster and Kosky [75], which was developed for stratified-wavy flow, is used for the comparison.

Figure 7-2 shows the comparison of the experimental values of the commercial Al tube against the h_{ref} values predicted by the correlations of Jaster and Kosky [75], Shah [79], Cavallini and Zecchin [82] and Dobson and Chato [83]. In this figure, the abscissa of each point corresponds to an experimental h_{ref} value obtained from the present investigation whereas the ordinate corresponds to a h_{ref} value predicted by one of the correlations of Refs. [75, 79, 82, 83]. When the point falls on the 45° line, a complete agreement between the experimental and predicted h_{ref} values is obtained. It can be seen that at low h_{ref}, the correlations slightly underestimate the experimental values whereas at higher h_{ref} the correlations predict higher h_{ref} values as compared to the experimental results. Shah [79] compared his correlation against the experimental data obtained from the literature and determined that the h_{ref} values predicted by his correlation were within an accuracy of ± 30%. On the other hand, Cavallini and Zecchin [82] showed that the mean deviation between their correlation and experimental data with different refrigerants was 30%. A similar conclusion was also obtained by Aroonrat and Wongwises [23] where their experimental results for condensation of R134a in a plain tube were found to be within ± 30% of the values predicted by Shah [79] and Dobson and Chato [83]. As shown in Fig. 7-2, since most of the experimental values are within ± 30% of the values predicted by the correlations, this confirms that the equipment and procedures used to obtain the h_{ref} values are reasonably reliable

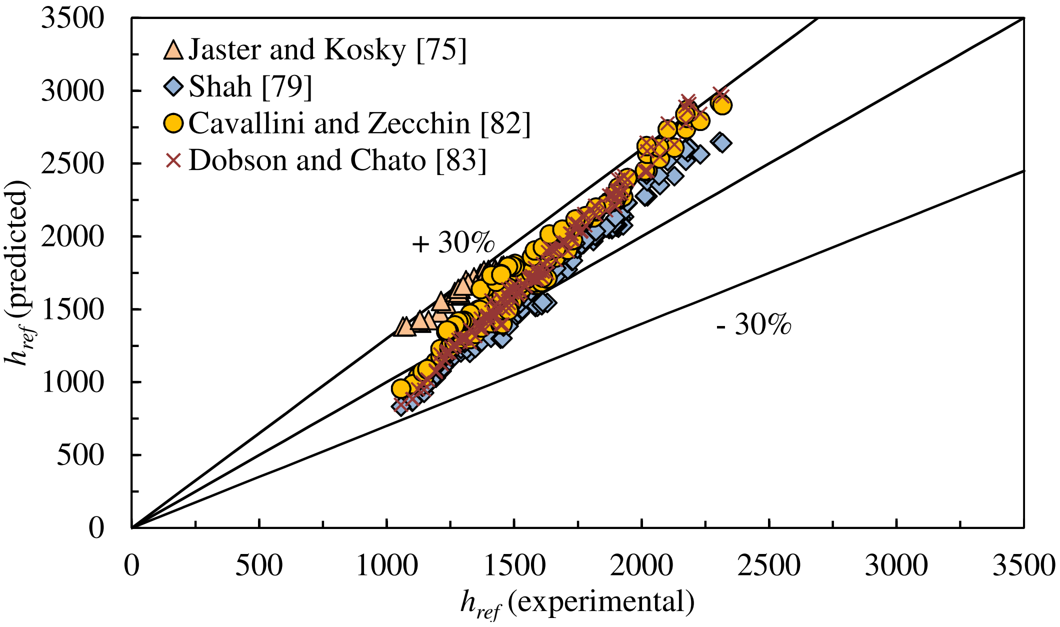

Fig. 7-2 Comparison of experimental h_{ref} of commercial Al tube with existing correlations.

7.2 Effects of vapour quality and mass flux

Figure 7-3 shows the heat transfer coefficients (h_{ref}) of the commercial Al tube, the plain SLM tube and a conical pin fin ($CF2$) tube at different m_{ref} and x_{ave} values. It can be observed that the h_{ref} values of all the tubes increase with increasing vapour quality (x_{ave}). This trend is expected as the increase in vapour quality reduces the thickness of the liquid film which surrounds the internal tube wall and thereby reduces the thermal barrier between the tube wall and the vapour core. In addition, at the same refrigerant mass flux, the increase in vapour quality also resulted in the increase in vapour velocity. The higher vapour velocity, thus, produces a larger shear force which pulls the liquid film in the axial direction and further reduces the liquid film thickness. From Fig. 7-3 it can also be observed that, at the same x_{ave}, the increase in m_{ref} increases the h_{ref} values of the condenser tubes. For the commercial Al and plain SLM tubes, the increase in refrigerant mass flux increases the effects of shear forces acting at the liquid-vapour interface. On the other hand, for the conical pin fin tube (*CF*2), the presence of the fin structure may also induce turbulence on the liquid film which further enhances the heat transfer coefficient.

By comparing the experimental results of the commercial Al tubes, plain SLM and *CF*2 tubes, it can also be seen that at the same x_{ave} and m_{ref} values, the plain SLM tube shows slightly better heat transfer performance than the commercial Al tube whereas significantly higher h_{ref} was achieved with the conical pin fin tube. For example, at m_{ref} = 200 kg/m^2·s and x_{ave} = 0.5, h_{ref} of the plain SLM tube is 23% higher than the commercial Al tube whereas the h_{ref} values of the *CF*2 tube are 1.92 times and 1.56 times of the commercial Al and plain SLM tubes, respectively. The surface roughness of a plain specimen fabricated by SLM was previously measured and presented in Ref. [121]. Its root-mean-square (rms) roughness was determined to be 7.32 μm and this roughness is significantly higher than a commercial Al surface of just 0.25 μm. Due to the higher surface roughness of the plain SLM tube, the formation of waves on the liquid film may have occurred which increases its h_{ref} values. On the other hand, for the *CF*2 tube, the presence of the conical pin fins increases the available heat transfer surface area. In addition, the fins also induce surface tension force which drains the liquid film from the fin tip towards the tube wall. As illustrated in Fig. 7-4, this surface tension effect produces a thin liquid film region near the fin tip and a thick liquid pool near the tube wall. As the conical pin fins are millimetres in size, their fin tips will protrude out of the thick liquid pool near the tube wall and contact the vapour core which further enhances condensation.

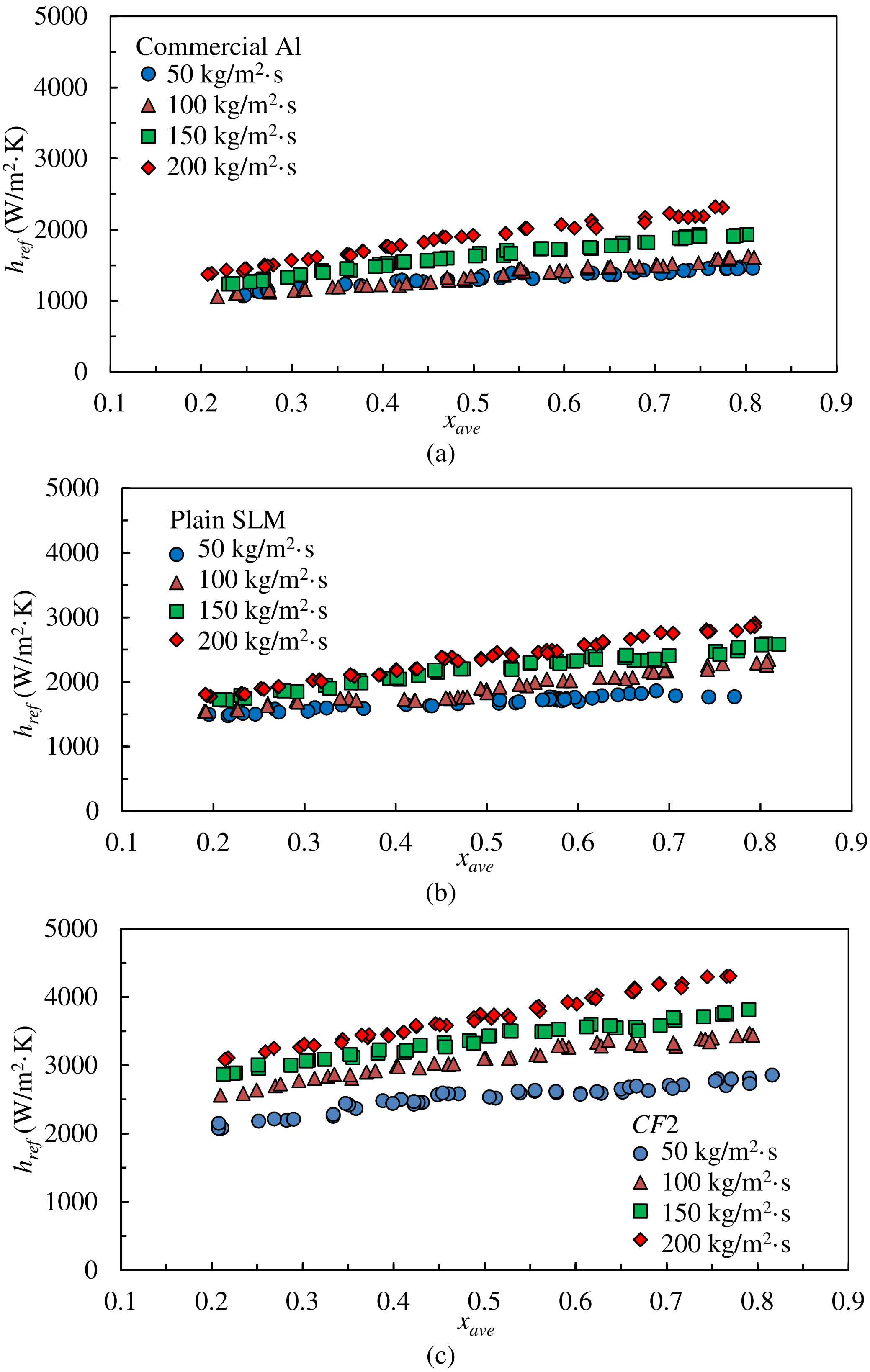

Fig. 7-3 Heat transfer coefficients (h_{ref}) of (a) commercial Al, (b) plain SLM and (c) conical pin fin (*CF*2) tubes at $P_{\text{sat}} = 13.4$ bar, m_{ref} of 50 kg/m^2·s to 200 kg/m^2·s and x_{ave} of 0.2 to 0.8.

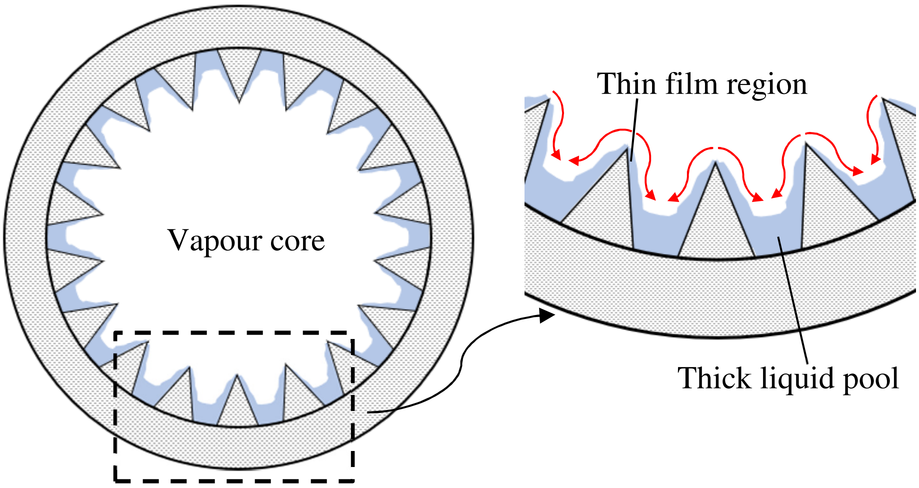

Fig. 7-4 Illustration of the liquid film characteristics on the conical pin fin tube during condensation.

7.3 Effects of circumferential fin pitch

Figure 7-5 shows the experimental results of heat transfer coefficients (h_{ref}) of the conical pin fin tubes *CF*1, *CF*2 and *CF*3. The pin fin arrays of these three enhanced tubes have the same longitudinal pin pitch (p_l) of 1.20 mm but are of different circumferential fin pitch (p_c), with *CF*1 having the smallest p_c and *CF*3 the largest p_c. Due to the small p_c value which corresponds to a high fin density and heat transfer area, the h_{ref} values of *CF*1 are consistently higher than those of *CF*3. For *CF*2, on the other hand, even though its h_{ref} values are similar to those of *CF*3 at low refrigerant mass flux (m_{ref}) of 50 kg/m^2·s, its h_{ref} values increase more significantly with increasing m_{ref} as compared to *CF*3. At m_{ref} = 200 kg/m^{2}s, the h_{ref} values of *CF*2 are noticeably larger than *CF*3 and similar to those of *CF*1.

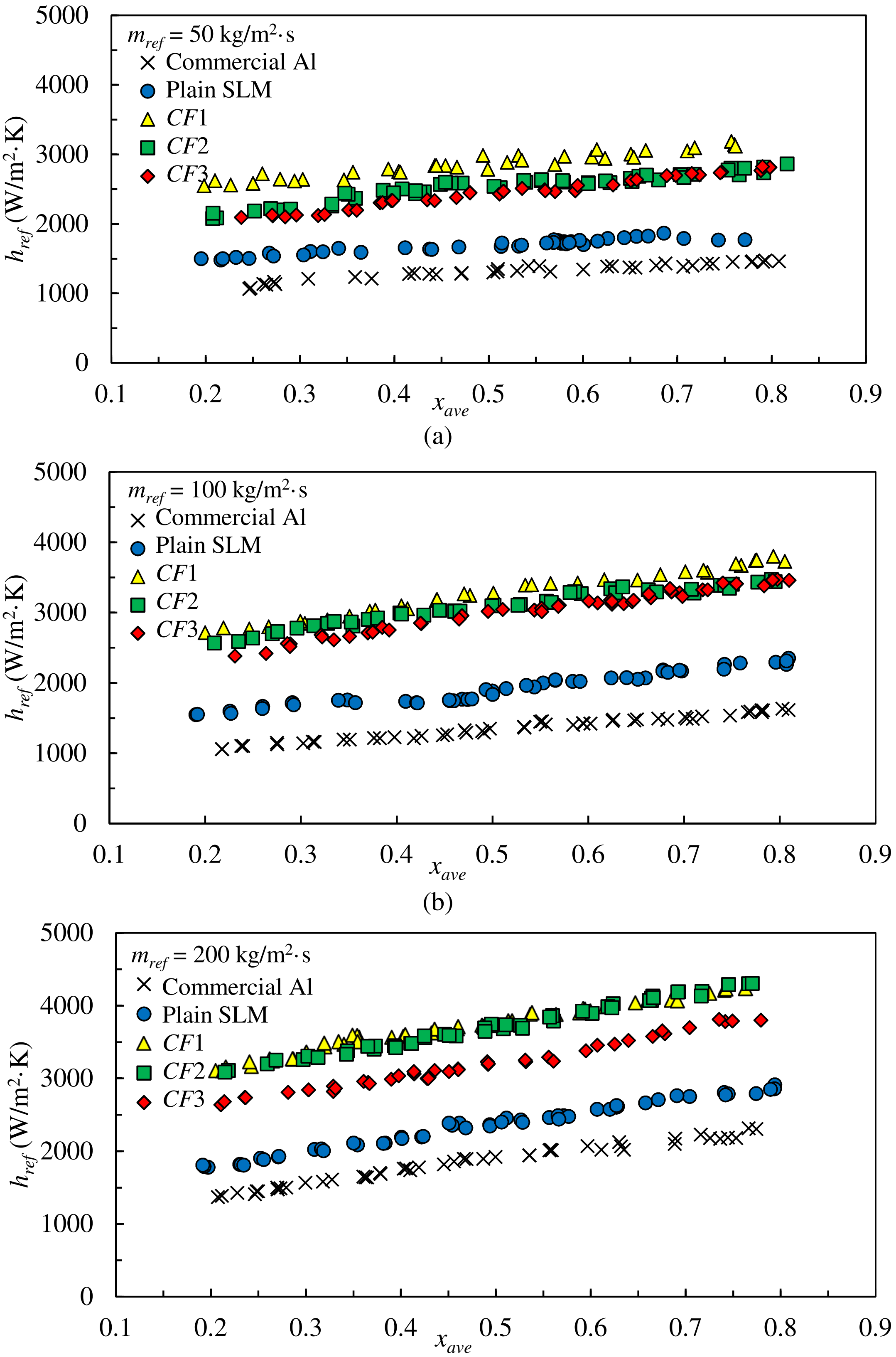

(a)

(b)

(c)

Fig. 7-5 Heat transfer coefficients (h_{ref}) of commercial Al, plain SLM and conical pin fin (*CF*1, *CF*2, *CF*3) tubes at P_{sat} = 13.4 bar, x_{ave} of 0.2 to 0.8 and (a) m_{ref} = 50 kg/m^2·s, (b) m_{ref} = 100 kg/m^2·s and (c) m_{ref} = 200 kg/m^2·s.

For a constant refrigerant mass flux, the average condensation heat transfer coefficient (h_{ave}) over the entire range of vapour quality of a condenser tube can be obtained by Eq. (7-3) where x_1 is the inlet quality and x_2 is the outlet vapour quality. In the present investigation, x_1 and x_2 of Eq. (7-3) were fixed at 0.8 and 0.2, respectively. For each m_{ref}, the h_{ave} of each condenser tube was then determined by numerically integrating its corresponding experimental h_{ref} values of Fig. 7-5. Figure 7-6 (a) shows a comparison of the h_{ave} values of the commercial Al, plain SLM and conical pin fin ($CF1$, $CF2$, $CF3$) tubes ranging from 50 kg/m^2·s to 200 kg/m^2·s. It should be noted that even though the h_{ref} values of the condenser tubes at $m_{ref} = 150$ kg/m^2·s are not presented in Fig. 7-4, experiments were performed at this refrigerant mass flux and their h_{ave} values were computed. It can be seen from Fig. 7-6 (a) that h_{ave} of all the tubes similarly increases with increasing m_{ref} and $CF1$ still exhibits the highest heat transfer performance as compared to the other plain and enhanced tubes. In addition, at low m_{ref}, it can also be observed that h_{ave} of $CF2$ was initially similar to that of $CF3$ but as m_{ref} increases, its h_{ave} values tend toward those of $CF1$. Eventually, at $m_{ref} = 200$ kg/m^2·s, both $CF1$ and $CF2$ have the same h_{ave}.

In order to compare the enhancements in h_{ave} of the conical pin fin and plain SLM tubes against the commercial Al tube, the thermal enhancement factor (η) of Eq. (7-4) was computed and plotted in Fig. 7-6 (b). This factor denotes the ratio of a conical pin fin or plain SLM tube h_{ave} value to the h_{ave} value of the commercial Al tube at the same refrigerant mass flux. From this figure, it can be seen that the η values of the conical pin fin ($CF1$, $CF2$, $CF3$) tubes range from 1.72 to 2.44 whereas those of the SLM tube range from 1.26 to 1.43. The highest η value of 2.44 was achieved by $CF1$ at the m_{ref} of 100 kg/m^2·s. In addition, the η values of the conical pin fin tubes also do not vary monotonically with m_{ref}. The η values of the conical pin fin tubes initially increase with increasing m_{ref} and then peaked at $m_{ref} = 100$ kg/m^2·s. Thereafter, a reduction in η values was observed with further increment in m_{ref}. As shown in Fig. 7-4, the conical pin fins enhanced heat transfer by inducing surface tension forces on the liquid film. On the other hand, the increase in m_{ref} increases the effect of vapour shear force which acts parallel to the tube wall. However, with the presence of the conical pin fins, the interactions between the flowing vapour and the pin fins may have resulted in two possible scenarios. In the first scenario, as illustrated in Fig. 7-7 (a), the local shear stress acts on the liquid pool near the tube wall due to the flowing vapour. As the vapour flows past the pin fins, it may have also pushed the condensate from the upstream side of the pin fin towards the back side of the pin fin and in the process removing some of the condensate from the fin. This phenomenon resulted in a thin film region on the upstream side of the pin fin and the reduction in the overall condensate volume on the pin fin. When m_{ref} increases from 50 kg/m^2·s to 100 kg/m^2·s, this phenomenon may be dominant and therefore explains the increase in η values. In the second scenario, as illustrated in Fig. 7-7 (b), the flowing vapour may be deflected upwards as it approaches the pin fin. This resulted in the vapour flowing in the opposite direction of the liquid film flow due to surface tension force. Under high m_{ref}, the vapour velocity may be sufficiently large to push the liquid film in the upward direction and produce a larger film thickness near the fin tip. The increased film thickness near the fin tip could have resulted in the reduction η when m_{ref} is larger than 100 kg/m^2·s.

$$h_{ave} = \frac{1}{x_1 - x_2} \int_{x_2}^{x_1} h_{ref} \, dx \tag{7-3}$$

$$\eta = \frac{h_{ave,plain\ SLM\ or\ enhanced}}{h_{ave,commercial\ Al}} \tag{7-4}$$

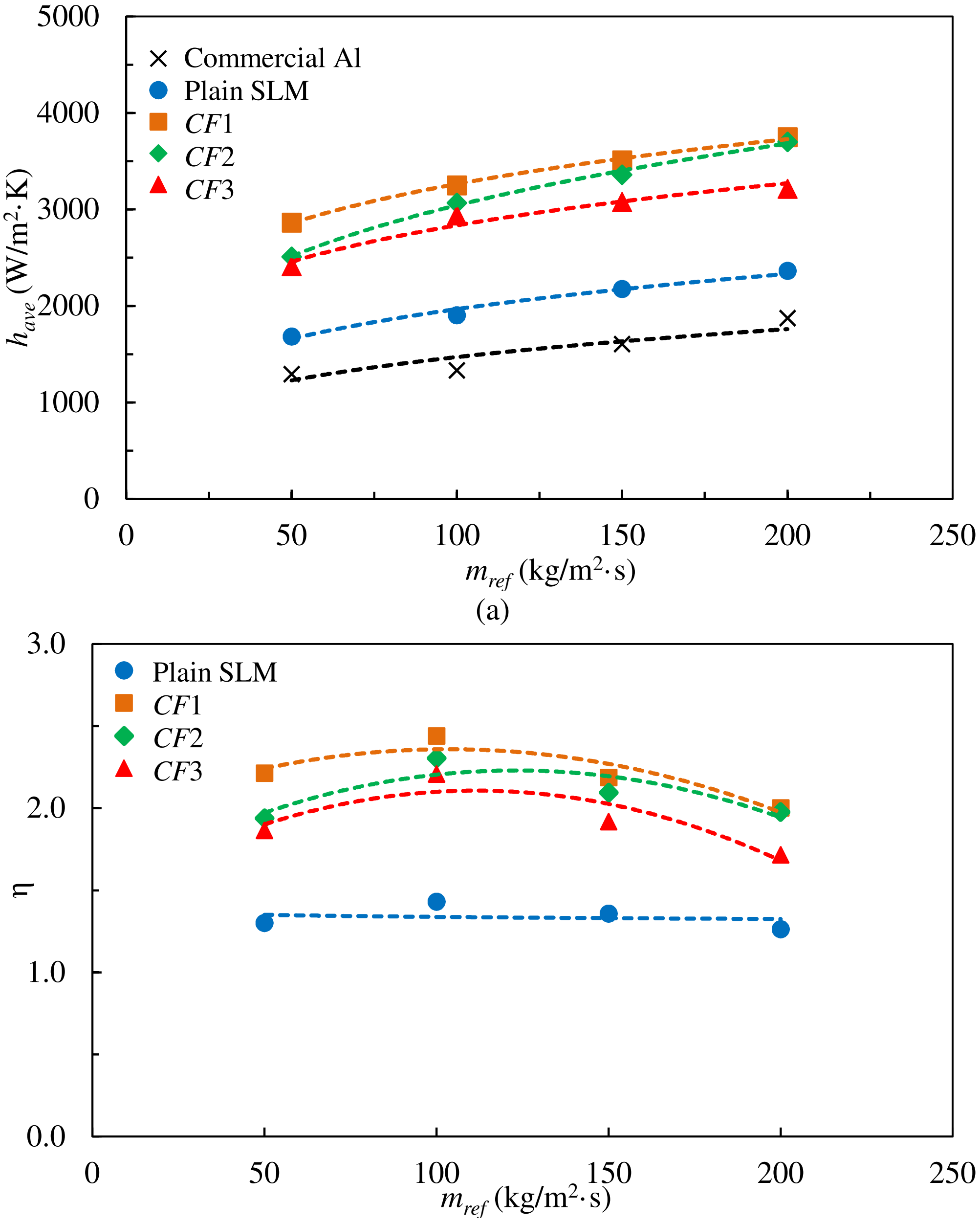

(a)

(b)

Fig. 7-6 Comparison of (a) average condensation heat transfer coefficients (h_{ave}) and (b) thermal enhancement factor (η) of commercial Al, plain SLM and conical pin fin ($CF1$, $CF2$, $CF3$) tubes at P_{sat} = 13.4 bar and m_{ref} ranging from 50 kg/m^2·s to 200 kg/m^2·s.

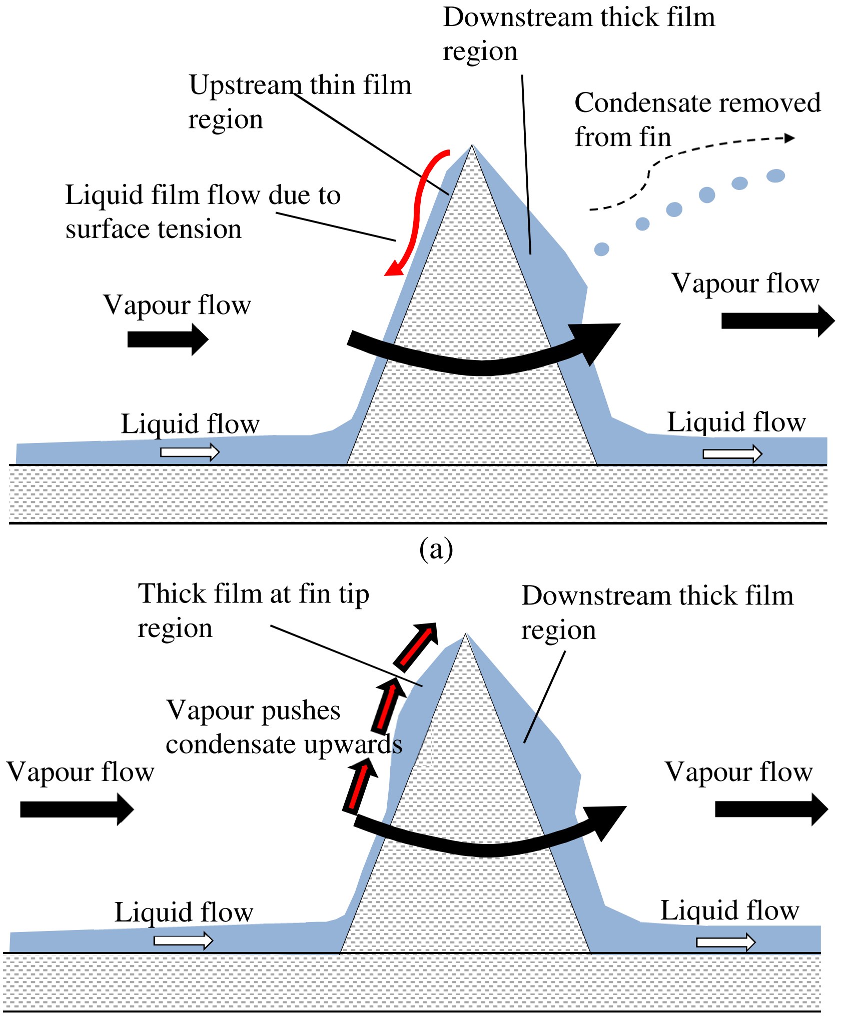

(a)

(b)

Fig. 7-7 Illustration of liquid film characteristics on the conical pin fin at (a) low refrigerant mass flux and (b) at high refrigerant mass flux.

Figure 7-8 (a) depicts the pressure drop (ΔP) across the conical pin fin tubes ($CF1$, $CF2$, $CF3$) at different x_{ave} and m_{ref} values. At the same m_{ref}, the ΔP values of the tubes were found to increase with increasing x_{ave} whereas at the same x_{ave}, increasing m_{ref} resulted in the upward shift of the pressure curves. In addition, by comparing the pressure drops across $CF3$ and $CF2$, it can also be observed that $CF2$ with $p_c = 0.349$ rad has significantly larger ΔP values as compared to $CF3$ with $p_c = 0.534$ rad. On the other hand, even though $CF1$ also has a lower p_c value of 0.262 rad as compared to

*CF*2, its ΔP values are only slightly larger than *CF*2. At a constant mass flux, the average pressure drops (ΔP_{ave}) across the condenser tubes over the entire range of vapour quality tested can be computed by Eq. (7-5) where x_1 and x_2 are the inlet and outlet vapour qualities of 0.2 and 0.8, respectively. The method used to compute h_{ave} is adopted for the ΔP_{ave} calculations whereby the ΔP curve for each enhanced tube at a constant m_{ref} shown in Fig. 7-8 (a) is numerically integrated based on Eq. (7-5). The computed ΔP_{ave} for the mass fluxes of 50 kg/m^2·s to 200 kg/m^2·s for *CF*1, *CF*2 and *CF*3 are shown in Fig. 7-8 (b). From this figure, it can be seen that ΔP_{ave} increases exponentially with increasing m_{ref}. Furthermore, it can also be observed that ΔP_{ave} of *CF*1 and *CF*2 are significantly larger than *CF*3 whereas the ΔP_{ave} values of *CF*1 and *CF*2 only differ slightly. For example, at m_{ref} = 200 kg/m^2·s, ΔP_{ave} of *CF*1 and *CF*2 are 22.4% and 17.8% larger than *CF*3 but at the same mass flux, ΔP_{ave} of *CF*1 is only 4.0% larger than *CF*2.

The reduction in p_c corresponds to the increase in fin density in the flow channel. Due to the increase in circumferential pin fin density, the free flow area for the liquid-vapour mixture reduces and thereby increases the flow resistance. Using the projected area of the flow channel that is perpendicular to the refrigerant flow direction, it was computed that the pin fins of *CF*3, *CF*2 and *CF*1 occupied 13.7%, 20.5% and 27.3% of the free flow area, respectively. Comparing *CF*3 and *CF*2, the reduction of p_c from 0.534 rad to 0.349 rad increases the fin occupied area by 1.5 times. On the other hand, the area occupied by the pin fins of *CF*1 is only 1.3 times larger than that of *CF*2. Since the conical pin fins are millimetre in size, both form and frictional drags may have contributed to the total pressure drop recorded. While the frictional pressure drop increases with increasing wetted surface area, the form drag is directly related to the

$$\Delta P_{ave} = \frac{1}{x_1 - x_2}\int_{x_2}^{x_1} \Delta P dx \tag{7-5}$$

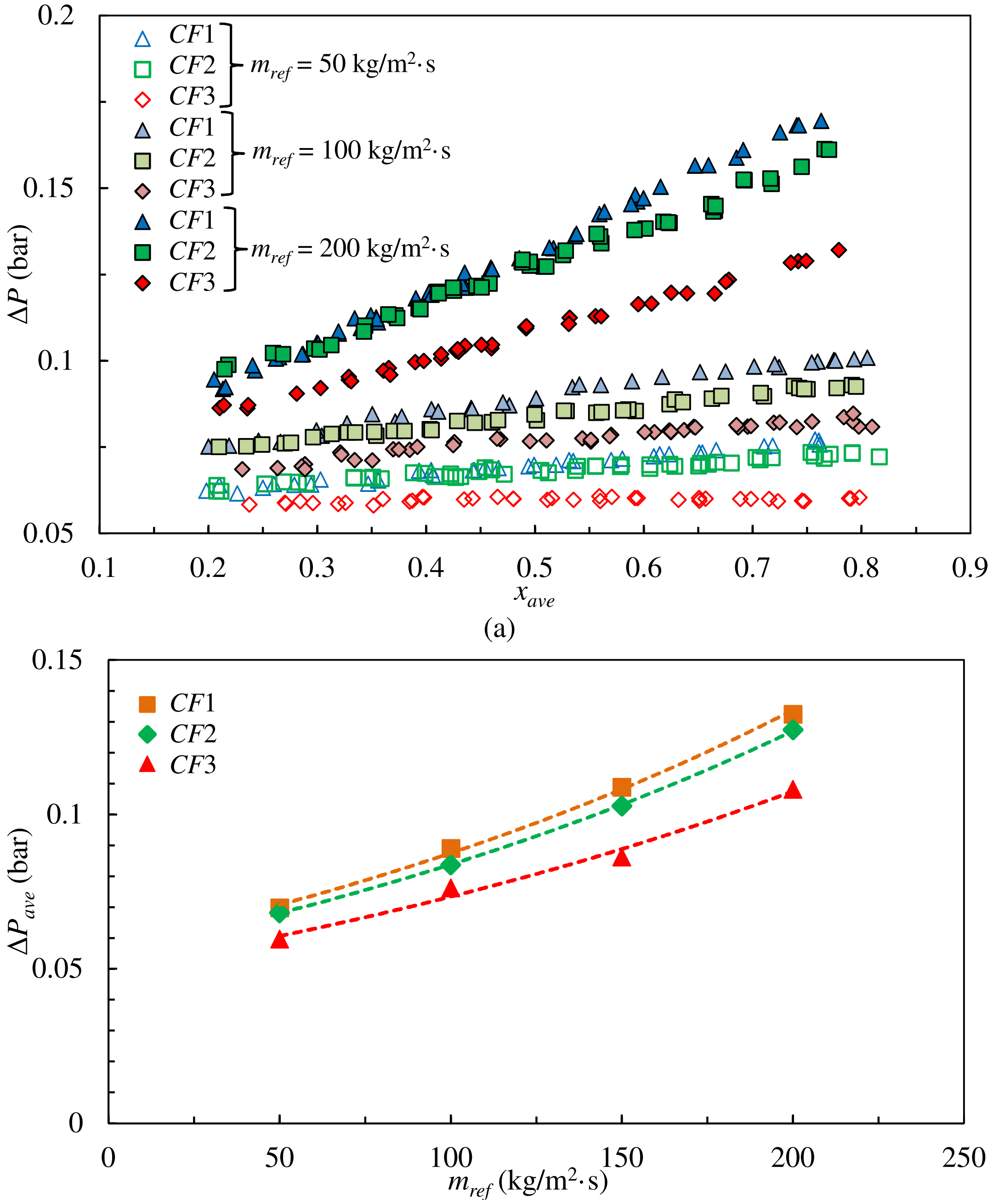

(a)

(b)

Fig. 7-8 (a) Pressure drops (ΔP) and (b) average pressure drops (ΔP_{ave}) of commercial Al, plain SLM and conical pin fin (*CF*1, *CF*2, *CF*3) tubes at $P_{\text{sat}} = 13.4$ bar, m_{ref} of 50 kg/m^2·s to 200 kg/m^2·s and x_{ave} of 0.2 to 0.8.

projected area occupied by the pin fins. Under high vapour velocity, the pressure drop due to form drag is also more dominant than the frictional pressure drop. Since the increment in the fin occupied area between *CF*1 and *CF*2 is smaller than the increment between *CF*2 and *CF*3, the differences in ΔP_{ave} between *CF*1 and *CF*2 due to form drag are therefore expected to be smaller as compared to the differences in ΔP_{ave} between *CF*2 and *CF*3.

7.4 Effects of longitudinal fin pitch

Figure 7-9 shows the experimental h_{ref} values of four conical pin fin tubes at various x_{ave} and m_{ref}. Among these tubes, *CF*1 and *CF*4 have the same circumferential fin pitch (p_c) of 0.262 rad. However, their longitudinal fin pitch (p_l) are different, with *CF*1 having a p_l value of 1.20 mm and *CF*4 with a p_l value of 1.80 mm. Similarly, *CF*2 and *CF*5 also have the same p_c of 0.349 rad but are of different p_l of 1.20 mm and 1.80 mm, respectively.

By comparing *CF*1 and *CF*4, it can be observed that for $p_c = 0.262$ rad, the increase in p_l from 1.20 mm to 1.80 mm resulted in the reduction in the heat transfer coefficients. The h_{ref} values of *CF*4 is also poorer than those of *CF*1 for all x_{ave} and m_{ref} values tested. For instance, at $m_{ref} = 50$ kg/m^2·s and $x_{ave} = 0.75$, a h_{ref} value of 3142 W/m^2·K was obtained for *CF*1. However, the h_{ref} value of *CF*4 at the same m_{ref} and x_{ave} was found to be only 2303 W/m^2·K and is about 36% lower than *CF*1. On the other hand, by comparing *CF*2 and *CF*5 which have the same p_c value of 0.349 rad but different p_l, a different trend from those of *CF*1 and *CF*4 is observed. Even though *CF*5 has a larger p_l which corresponds to a smaller fin density, it has similar h_{ref} values as *CF*2 at low refrigerant mass flux of 50 kg/m^2·s. In addition, it was also found that the increase in m_{ref} has resulted in a higher increment in h_{ref} values of $CF5$ as compared to those of $CF2$ and the h_{ref} values of $CF5$ eventually surpasses those of $CF2$ when m_{ref} is above 100 kg/m^2·s. At the m_{ref} of 200 kg/m^2·s and x_{ave} of 0.8, $CF5$ achieved the highest h_{ref} value of 4915 W/m^2·K. This value also corresponds to highest h_{ref} among all the five conical pin fin tubes.

The average heat transfer coefficients (h_{ave}) and thermal enhancement factors (η) of $CF4$ and $CF5$ were computed by Eqs. (7-3) and (7-4) and plotted in Figs. 7-10 (a) and (b), respectively. In addition, the h_{ave} and η values of $CF1$, $CF2$ and the plain tubes were also plotted in these figures for comparison. From Fig. 7-10 (a), it can be seen that the gradients of the curves for the conical pin fin tubes with p_l = 1.80 mm ($CF4$ and $CF5$) are noticeably steeper than the conical pin fin tubes with p_l = 1.20 mm ($CF1$ and $CF2$). The steeper gradients indicate larger increases in h_{ave} of the $CF4$ and $CF5$ tubes as compared to $CF1$ and $CF2$ with the increase in m_{ref}.

At the same x_{ave}, the increase in m_{ref} increases the vapour velocity. This resulted in a higher shear stress at the liquid-vapour interface which pulls the condensate in the axial direction and reduces the liquid film thickness near the tube wall. However, the presence of fin also imposed additional resistance to the liquid film flow and therefore prevented the thinning of the liquid film by the vapour shear force. As a higher p_l ($CF4$ and $CF5$) corresponds to the reduction in the longitudinal fin density, this resulted in a lower resistance to the vapour shear force as compared to the tubes with smaller p_l ($CF1$ and $CF2$). This, therefore, explains the steeper gradients of $CF4$ and $CF5$ curves in Fig. 7-10 (a).

Finally, from Fig. 7-10 (b), it can be concluded that *CF*5 exhibits the best heat transfer performance as compared to the other conical pin fin tubes for $m_{ref} \geq 100$ kg/m^2·s. In addition, the highest η value of 2.44 is also achieved by *CF*5 at the m_{ref} of 100 kg/m^2·s.

Figures 7-11 (a) and (b) show the pressure drops (ΔP) across *CF*4 and *CF*5, respectively. The ΔP values were measured with m_{ref} ranging from 50 kg/m^2·s to 200 kg/m^2·s and x_{ave} from 0.2 to 0.8. In addition, *CF*1 and *CF*2 are also plotted in the figures for comparison. From these figures, it can be seen that the change in the longitudinal fin pitch (p_l) has insignificant effect on ΔP. For instance, at m_{ref} of 200 kg/m^2·s and x_{ave} of 0.61, *CF*1 and *CF*4 which has the same p_c but different p_l exhibit the ΔP values of 0.150 bar and 0.142 bar, respectively. This corresponds to only about 5.3% difference in their ΔP values. Similarly, for *CF*2 and *CF*5, negligible differences in their ΔP values were recorded. For completeness, ΔP_{ave} of *CF*4 and *CF*5 were also computed using Eq. (7-5) and their values are presented in Fig. 7-11 (c).

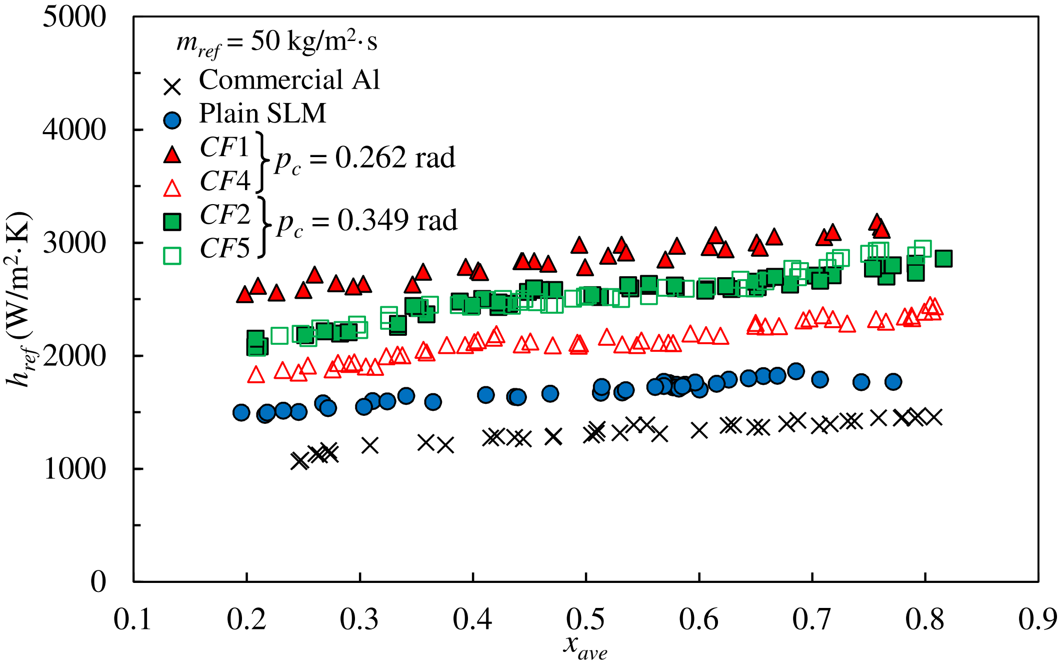

(a)

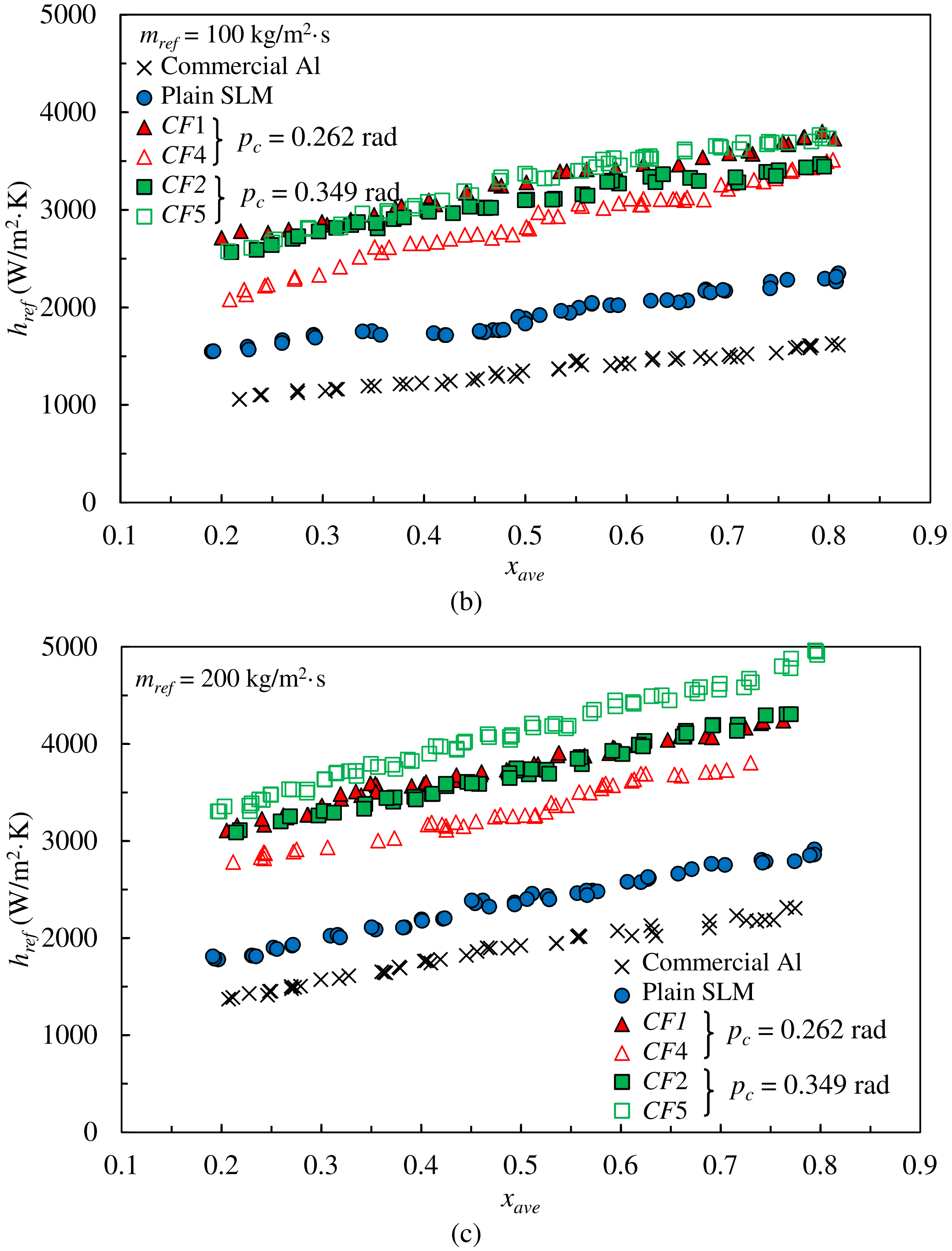

Fig. 7-9 Comparison of heat transfer coefficients (h_{ref}) of conical pin fin tubes with different longitudinal fin pitch (p_l) at P_{sat} = 13.4 bar, x_{ave} of 0.2 to 0.8 and (a) m_{ref} = 50 kg/m²·s, (b) m_{ref} = 100 kg/m²·s and (c) m_{ref} = 200 kg/m²·s.

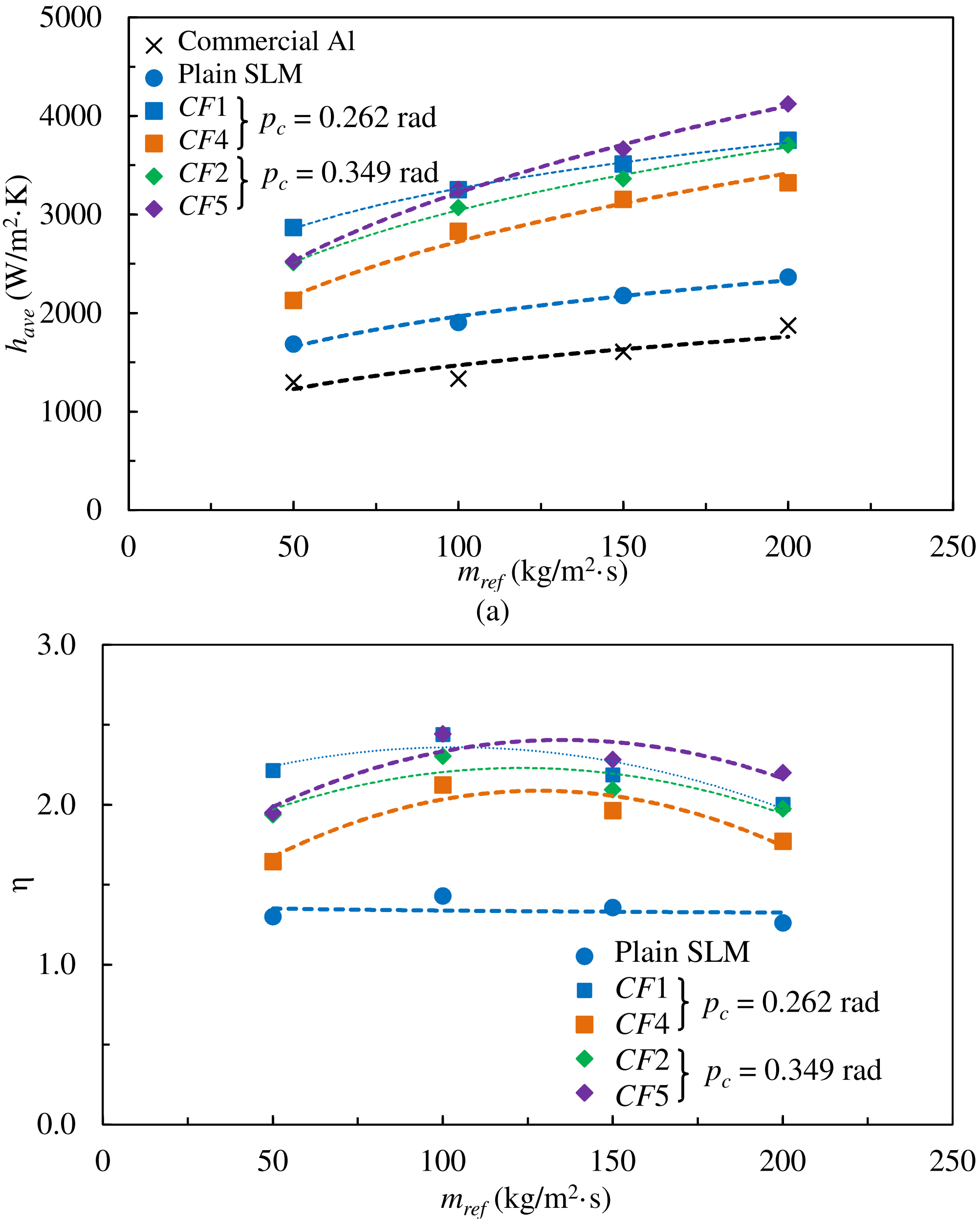

(a)

(b)

Fig. 7-10 Comparison of (a) average condensation heat transfer coefficients (h_{ave}) and (b) thermal enhancement factor (η) of commercial Al, plain SLM and conical pin fin (*CF*1, *CF*2, *CF*4 and *CF*5) tubes at P_{sat} = 13.4 bar and m_{ref} ranging from 50 kg/m^2·s to 200 kg/m^2·s.

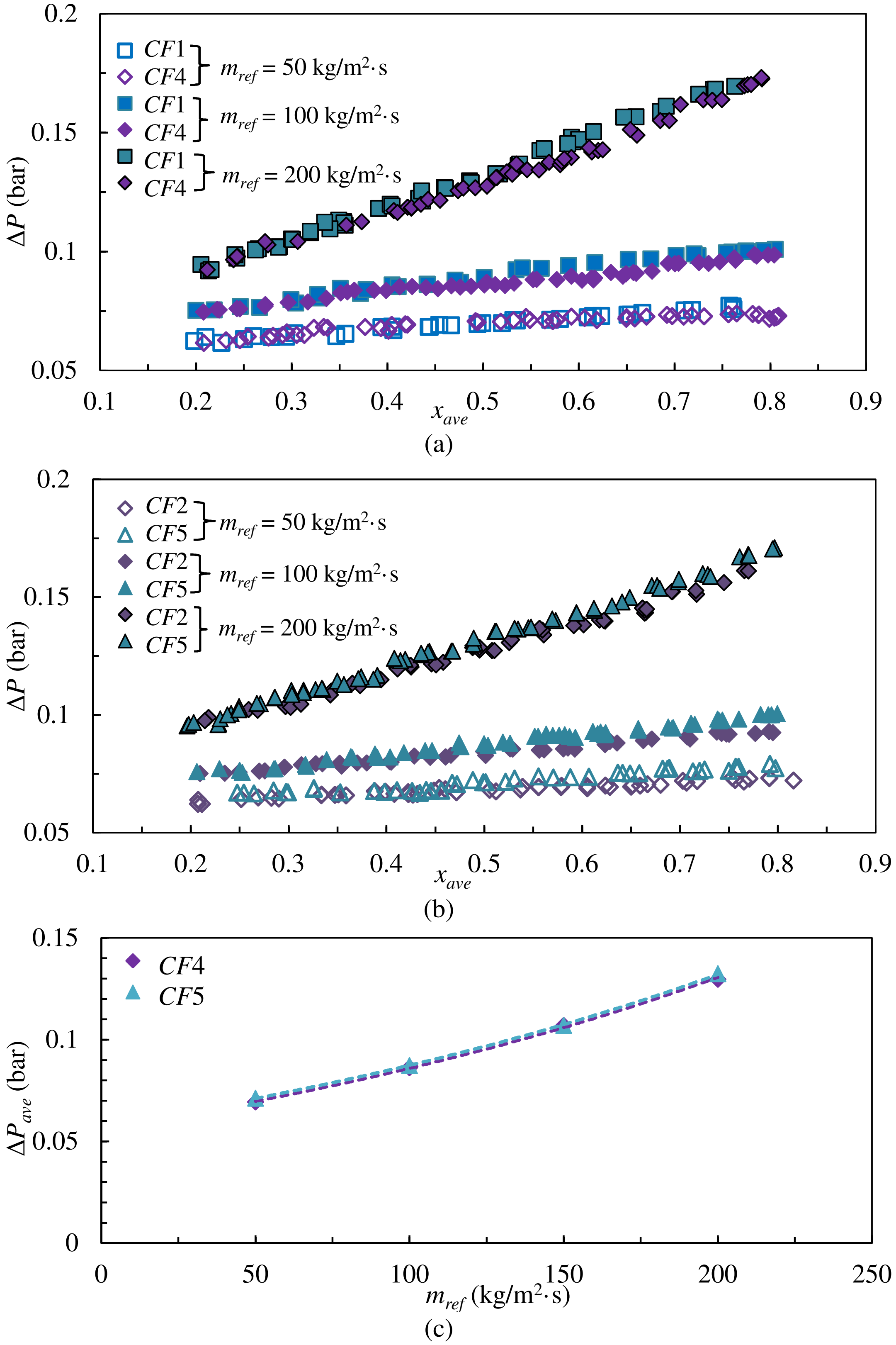

Fig. 7-11 (a) Pressure drop (ΔP) of *CF*4 and comparison against *CF*1, (b) pressure drops (ΔP) of *CF*5 and comparison against *CF*2 and (c) average pressure drop (ΔP_{ave}) of *CF*4 and *CF*5 at P_{sat} = 13.4 bar, m_{ref} of 50 kg/m^2·s to 200 kg/m^2·s and x_{ave} of 0.2 to 0.8.

7.5 Performance evaluation

In addition to the conical pin fin tubes, the two enhanced tubes with dome-shape pin fins ($PF1$ and $PF2$) were also experimental investigated for their heat transfer and pressure drop performances. The $PF1$ and $PF2$ tubes were similarly tested at P_{sat} of 13.4 bar and the R134a refrigerant was condensed from x_{in} of 0.9 to x_{out} of 0.3 to obtain their h_{ave} and P_{ave} values at different refrigerant mass fluxes. As the dome-shape fins are inclined at an angle with respect to the tube central axis, the condensation performance may differ with the tube orientation. In the present investigation, both $PF1$ and $PF2$ were positioned horizontally and oriented such that the refrigerant flow first come into contact with the tip of the fin.

Figure 7-12 shows the results of h_{ave} and ΔP_{ave} of the dome-shape fin pin tubes obtained from the experiments. It can be seen that from Fig. 7-12 (a), that h_{ave} of $PF1$ and $PF2$ differs significantly with $PF2$ exhibiting better thermal performances. The highest h_{ave} value of $PF2$ is 4195 W/m^2·K which is more than 2 times higher than the commercial Al tube and is close to the h_{ave} value of $CF5$. However, from Fig. 7-12 (b), it can also be observed that the ΔP_{ave} values of both $PF1$ and $PF2$ are higher than those of the conical pin fin tubes. For instance, at m_{ref} of approximately 100 kg/m^2·s, the ΔP_{ave} value of $PF1$ is 0.226 bar whereas that of $CF5$ is only 0.087 bar. This ΔP_{ave} value of $PF1$ is approximately 2.6 times higher than that of $CF5$.

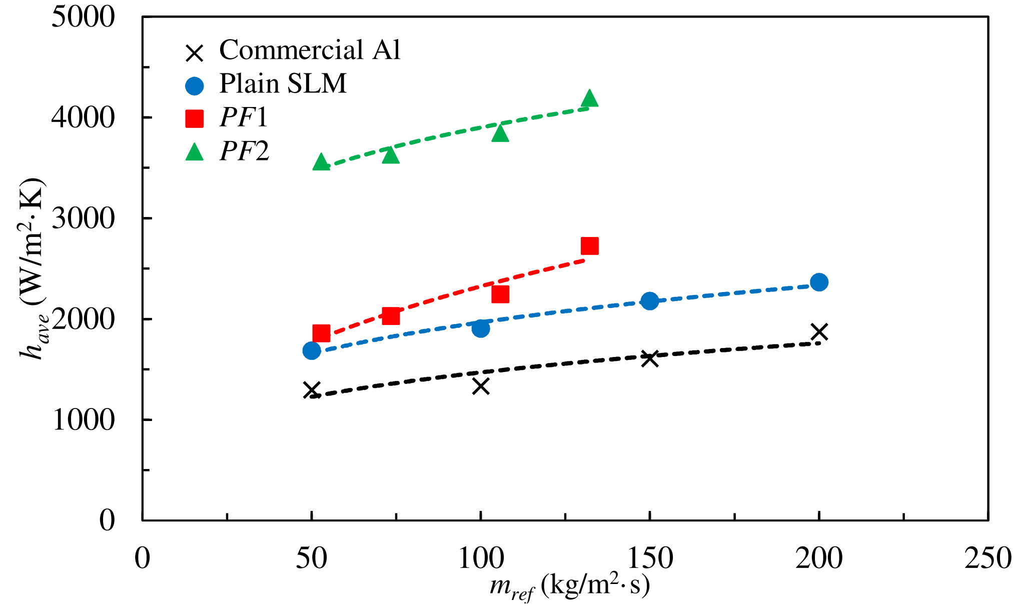

(a)

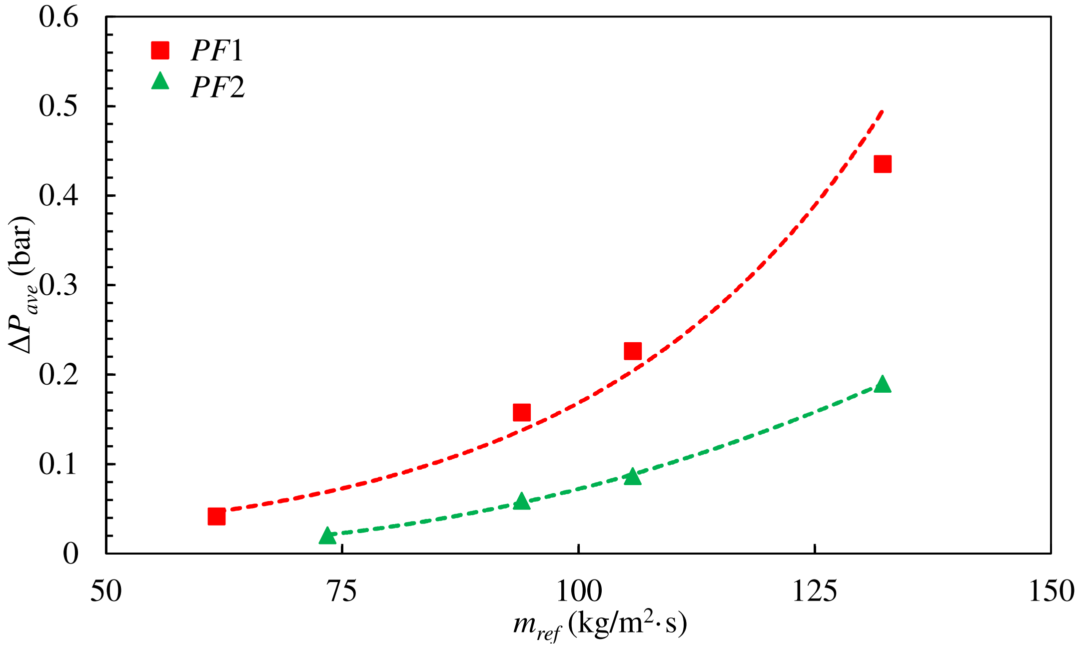

(b)

Fig. 7-12 (a) Average heat transfer coefficients (h_{ave}) and (b) average pressure drops (ΔP_{ave}) of *PF*1 and *PF*2 at P_{sat} = 13.4 bar and m_{ref} of 50 – 150 kg/m^2·s.

From Fig. 3-11, it can be seen that the dome-shape fins have a convex fin tip which is similar to that of the sinusoidal pin fins employed for the natural convection investigation presented in Chapter 5. The improved condensation heat transfer exhibited by $PF1$ and $PF2$ could be due to the enhanced surface tension forces induced at the fin tip. However, as the fins of $PF1$ are significantly longer than $PF2$, the fin efficiency of $PF1$ fins is poor which reduces the heat transfer rate from the fin tip and explain its lower h_{ave} values. In addition, as the size of dome-shape fin is larger than the conical pin fins, this also resulted in much higher flow resistance and pressure drop as compared to the conical pin fin tubes.

In order to evaluate the performances of the conical and dome-shape fin tubes, a performance metric which considers the enhancement in heat transfer and the associated penalty due to higher pressure drop of an enhanced tube as compared to a plain tube is employed. This performance metric, η_1, is defined in Eq. (7-6) where $h_{enh,ave}$ and $h_{slm,ave}$ are the average heat transfer coefficients of an enhanced tube and a plain SLM tube, respectively. $\Delta P_{enh,ave}$ and $\Delta P_{slm,ave}$ are the average pressure drops across the enhanced and plain SLM tubes. For the computation of η_1, the values of the terms on the right-hand side of Eq. (7-6) are evaluated at the refrigerant mass flux (m_{ref}) of 125 kg/m^2·s.

$$\eta_1 = \frac{h_{enh,ave}/h_{slm,ave}}{\Delta P_{enh,ave}/\Delta P_{slm,ave}} \tag{7-6}$$

The computed η_1 values of the conical and dome-shape fin tubes are shown in Fig. 7-13. From this evaluation criterion, it can be seen that $CF3$ has the highest efficiency index of 1.25. In addition, all the conical pin fin tubes also have efficiency indices larger than 1 and are higher than those of the dome-shape fin tubes.

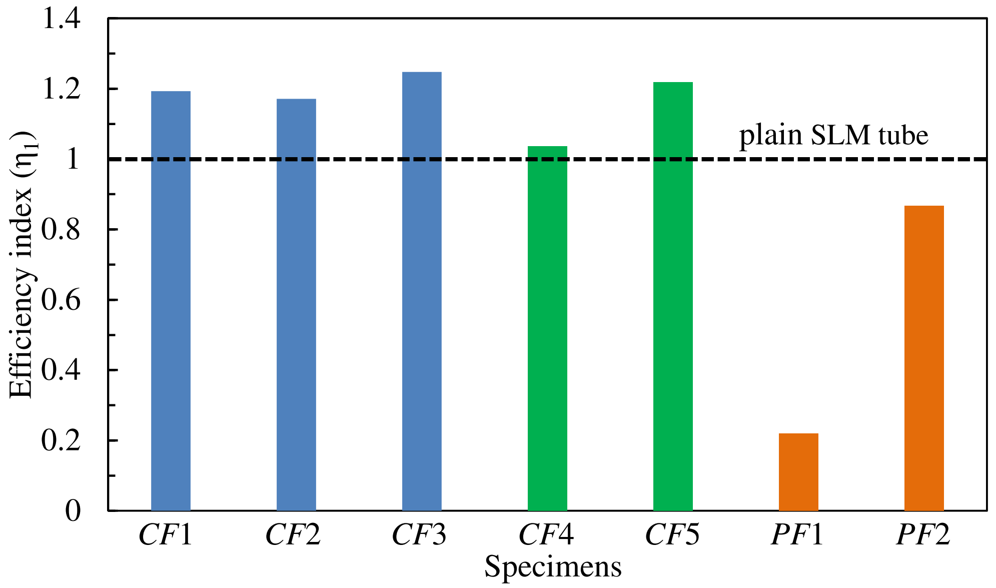

Fig. 7-13 Efficiency indices of conical and dome-shaped pin fin enhanced tubes for $m_{ref} = 125$ kg/m^2·s.

7.6 A semi-empirical model for forced convection heat transfer in three-dimensional pin fin tubes

In the vapour shear dominated flow regime, the local condensation heat transfer coefficient is significantly influenced by diffusion across the liquid film. Hence, the boundary layer approach can be used to develop a predictive model for the conical fin pin tubes. Based on the analysis described in Section 2.2.2, the Nusselt number for condensation heat transfer can be expressed as Eq. (7-7) [85, 86], where $u*$ is the friction velocity as defined in Eq. (7-8) and T^+ is the dimensionless temperature. Based on the two-phase multiplier approach as discussed in Section 2.2.1, the wall shear stress (τ_w) is in turn a function of the liquid phase frictional pressure drop, $(\frac{dP}{dz})_f$, and the two-phase multiplier, ϕ_f^2, as shown in Eq. (7-9). In addition, the liquid phase frictional pressure drop, $(\frac{dP}{dz})_f$, is a function of the liquid-phase friction factor, f_f, given by Eq. (7-10). For liquid flow through a pipe, the Fanning friction factor is given by Eq. (7-11). Substituting Eqs. (7-8) – (7-11) into Eq. (7-7) and introducing constants *r* and *s* to account for the additional frictional pressure drop due to the presence of fins, Nu can be expressed as Eq. (7-12). It should be noted in this equation, the two-phase multiplier, ϕ_f^2, is related to the turbulent-turbulent Martinelli parameter (X_{tt}) as shown in Eqs. (7-13) and (7-14) [67, 68].

$$\mathrm{Nu} = \frac{h_{ref} d_i}{k_f} = \frac{\rho_f C_{p,f} d_i u^*}{k_f T^+} \tag{7-7}$$

$$u^* = \sqrt{\tau_w / \rho_f} \tag{7-8}$$

$$\tau_w = -\left(\frac{dP}{dz}\right)_f \left(\frac{d_i}{4}\right) \phi_f^2 \tag{7-9}$$

$$-\left(\frac{dP}{dz}\right)_f = \frac{2 f_f m_{ref}^2 (1-x)^2}{\rho_f d_i} \tag{7-10}$$

$$f_f = 0.079 \mathrm{Re}_f^{-0.25} \tag{7-11}$$

$$\mathrm{Nu} = \frac{\mathrm{Re}_f^{0.875r} \left(0.079 \phi_f^2 / 2\right)^{s/2} \mathrm{Pr}_f}{T^+} \tag{7-12}$$

$$\phi^2 = 1 + \frac{C_s}{\mathrm{X}_{tt}} + \frac{1}{\mathrm{X}_{tt}^2} \tag{7-13}$$

$$\mathrm{X}_{tt} = \left(\frac{\rho_g}{\rho_f}\right)^{0.5} \left(\frac{\mu_f}{\mu_g}\right)^{0.1} \left(\frac{1-x}{x}\right)^{0.9} \tag{7-14}$$

In order to determine Nu, T^+ of Eq. (7-12) has to be determined. As the dimensionless temperature profile varies with the refrigerant mass flow rate and vapour quality, T^+ is often correlated to the Reynolds number [88 – 90]. To account for the change in both the liquid and vapour phases during the condensation process in the present model, it is proposed that T^+ is related to the equivalent Reynolds number (Re_{eq}) as shown in Eq. (7-15). In this equation, *C* is a constant and is assumed to be related to dimensionless circumferential fin pitch (p_c) to longitudinal fin pitch (p_l) ratio β. Substituting Eq. (7-15) into Eq. (7-12), the expression for Nu is obtained as Eq. (7-17), where m, r and s are constants to be determined and n and C_s are assumed to be functions of β. Using the non-linear regression approximation, Eq. (7-17) is correlated to the experimental results of the conical pin fin tubes ($CF1$ – $CF5$) and m, r and s are found to be 1, -0.2857 and 2, respectively. On the other hand, n and C_s are obtained as Eqs. (7-18) and (7-19), respectively.

$$\frac{1}{T^+} = \mathrm{CRe}_{eq}^{n}\mathrm{Pr}_f = \beta^m \mathrm{Re}_{eq}^{n}\mathrm{Pr}_f \tag{7-15}$$

$$\beta = \frac{\pi d_i p_c}{p_l} \tag{7-16}$$

$$\mathrm{Nu} = \beta^m \mathrm{Re}_{eq}^{n}\left[\mathrm{Re}_f^{0.875r}\left(0.079\phi_f^2/2\right)^{s/2}\right] \tag{7-17}$$

$$n = -0.0133\beta + 0.4046 \tag{7-18}$$

$$C_s = A \cdot \mathrm{X}_{tt}^{1.1059}$$
$$\text{where } A = 2.3594\beta^3 - 52.498\beta^2 + 346.53\beta - 115.31 \tag{7-19}$$

By substituting the values of m, r and s into Eq. (7-17) and after some manipulation, the simplified form of the correlation for Nu is given as

$$\mathrm{Nu} = \mathrm{Re}_{eq}^{n} \cdot \beta \cdot \frac{f_f}{2}\phi^2 \tag{7-20}$$

The Nu values predicted by the correlation were computed by substituting Eqs. (7-11), (7-13), (7-18) and (7-19) into Eq. (7-20). These values are then compared against the experimental results of the conical pin fin tubes ($CF1$ – $CF5$). The comparison of the experimental Nu values and those predicted by the correlation of Eq. (7-20) is depicted in Fig. 7-14. It can be seen that the correlation provides reasonably accurate predictions with most of the experimental data falling within ± 20% of the predicted values. The mean absolute error (*MAE*) which denotes the average normalised difference between the predicted and the experimental Nusselt numbers, defined by Eq. (7-21) is also commonly used to evaluate the accuracy of the heat transfer model. In this equation, M is the number of experimental data whereas Nu_{pred} and Nu_{exp} represent the Nusselt numbers predicted by Eq. (7-20) and the experimental results, respectively. Based on this approach, the new correlation is reasonably accurate with an overall *MAE* of 10.5% for the 891 data.

$$MAE = \frac{1}{M}\sum\frac{|\mathrm{Nu}_{pred}-\mathrm{Nu}_{exp}|}{\mathrm{Nu}_{exp}} \times 100\% \qquad (7\text{-}21)$$

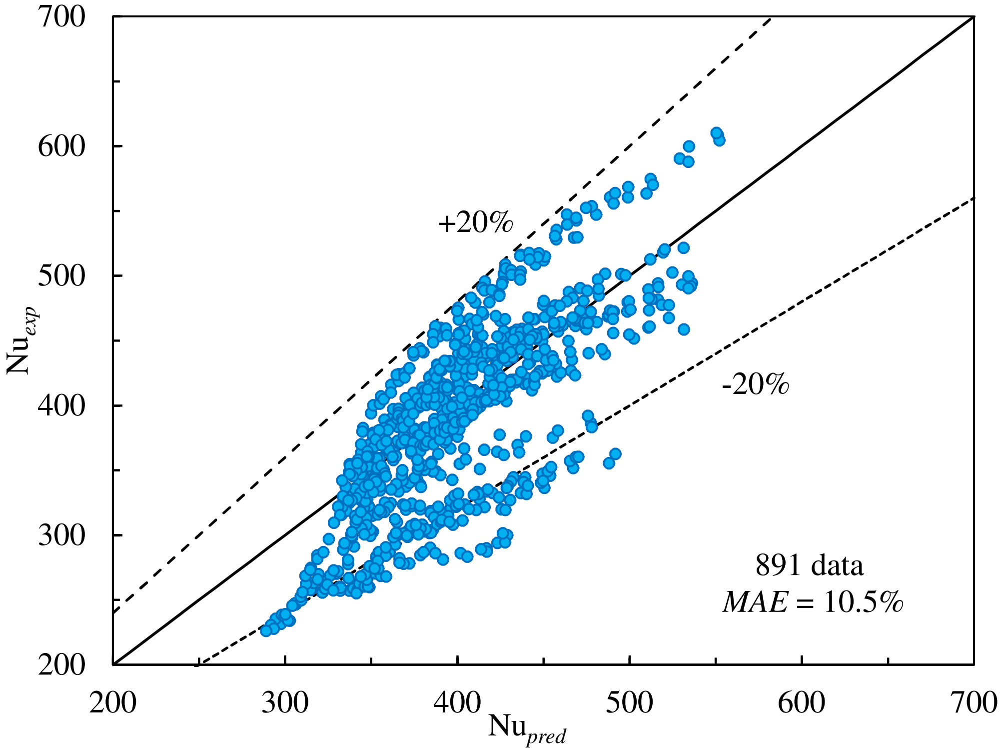

Fig. 7-14 Comparison of Nu predicted by the new correlation of Eq. (7-20) (Nu_{pred}) against the experimental Nu (Nu_{exp}).

7.6 Summary

In this chapter, forced convection condensation of R134a in five enhanced tubes with conical pin fin structures of different circumferential and longitudinal fin pitches was investigated. The results were also compared against two condenser tubes with dome-shape pin fin structures. Condensation of R134a were performed at P_{sat} of 13.4 bar, m_{ref} between 50 kg/m^2·s and 200 kg/m^2·s and x_{ave} ranging from 0.2 and 0.8. The findings can be summarised as follows:

1. The highest h_{ref} value of 4915 W/m^2·K is achieved with the conical pin fin tube of circumferential and longitudinal fin pitches of 0.349 rad and 1.80 mm, respectively and at the m_{ref} of 200 kg/m^2·s and x_{ave} of 0.8. This is more than two times the h_{ref} value of the commercial Al tube at the same m_{ref} and x_{ave}.
2. The reduction in circumferential fin pitch increases the pressure drop across the tube. However, the change in longitudinal fin pitch has insignificant effect on the pressure drop across the enhanced tubes.
3. The drainage of condensate from the fin tip to the fin base by surface tension force and the thinning of condensate film due to vapour shear are suggested as the main contributing factors for the enhanced condensation heat transfer of the conical pin fin tubes.
4. Based on the efficiency index (η_1) proposed, the conical pin fin tubes were evaluated as the better design for forced convection condensation as compared to the dome-shape fins due to their high heat transfer coefficients and lower pressure drop penalties.

5. A semi-empirical model was developed for predicting the Nusselt number of the condensation of R134a in the three-dimensional conical pin fin tubes and reasonably accurate predictions with an overall *MAE* of 10.5% were obtained.

Chapter 8 – Conclusions and Recommendations for Future Work

8.1 Conclusions

In this thesis, natural and forced convection condensation with three-dimensional pin fin structures were investigated. The external natural convection condensation experiments were performed using steam as the working fluid whereas the internal forced convection condensation of R134a in pin fin tubes was investigated. Using selective laser melting (SLM), various novel three-dimensional pin fins were fabricated and their condensation heat transfer performances were characterised. From these investigations, several new findings are obtained. The conclusions drawn from these findings can be summarised as follows:

<u>Natural convection condensation:</u>

1. The three-dimensional pin fin structures were found to exhibit better heat transfer performance than the equivalent two-dimensional fins. This is mainly attributed to the lower condensate retention height and the higher surface tension effects of the three-dimensional fin pins.
2. For the conical and sinusoidal pin fin specimens, visualisation studies show that the condensate retention height (H_{ave}) is mainly affected by the change in fin pitch. While the increase in fin height resulted in slight increment in H_{ave} of the conical pin fins, it has no effect on the sinusoidal pin fins.
3. The highest thermal enhancement factor (η) of 2.46 and average heat transfer coefficient (h_t) is achieved by Specimen *C*2. At the same p/l ratio, the results also

show that the conical pin fin surfaces have the highest heat transfer performance as compared the sinusoidal and micro-pin fin surfaces.

4. The conical pin fin geometry promoted condensate drainage away from the specimen surface, significantly reduced the condensate retention height and thereby enhanced the heat transfer rate. In addition, the three-dimensional geometry of the conical fin also resulted in additional curvature change that reduces the film thickness near the fin tip and promotes heat transfer.
5. A theoretical model which accounts for the effect of surface tension and gravitational forces on the liquid film is developed to evaluate the condensation performance of the conical fins. The modelling results validated the existence of a thin liquid film near the fin tip. In addition, due to the concave trough of the liquid pool, another thin liquid film region is produced near the fin base. With increasing θ, the surface tension force also reduces the film thickness in the circumferential direction. These mechanisms resulted in the significant heat transfer enhancements of the conical pin fins.

Forced convection condensation:

1. The present investigation demonstrated the possibility of fabricating internal tube structures such as the dome-shape and conical pin fins using the SLM technique. These condenser tubes are also fabricated with good integrity and are able to sustain high pressure operation. This is also the first time the SLM technique is used to produce enhanced tubes for improving forced convection condensation with high pressure refrigerant.

2. Specimens *CF*1, *CF*2 and *CF*3 have the same longitudinal fin pitch (p_l) but different circumferential fin pitch (p_c). The h_{ref} values of *CF*1, which has the smallest p_c value, were found to be consistently higher than *CF*3, which has the largest p_c value, for all m_{ref} and x_{ave} tested. On the other hand, at refrigerant high mass fluxes, *CF*2 has demonstrated similar heat transfer performances as *CF*1 even though its p_c value is larger than that of *CF*1.
3. At the circumferential fin pitch (p_c) of 0.262 rad, the increase in p_l from 1.20 mm (*CF*1) to 1.80 mm (*CF*4) resulted in the reduction in h_{ref} and h_{ave} values. However, at the circumferential fin pitch (p_c) of 0.349 rad, the increase in p_l from 1.20 mm (*CF*2) to 1.80 mm (*CF*5) resulted in higher h_{ref} and h_{ave} values when the m_{ref} is more than 100 kg/m^2·s.
4. The reduction in circumferential fin pitch (p_c) from 0.524 rad to 0.349 rad resulted in a more significant increase in pressure drop as compared to the reduction in p_c from 0.349 rad to 0.262 rad. On the other hand, the change in the longitudinal fin pitch (p_l) from 1.20 mm to 1.80 mm has insignificant effect on the pressure drop across the enhanced tubes.
5. An efficiency index (η_1) is proposed to evaluate the thermal-hydraulic performances of the pin fin tubes. Based on this evaluation criterion, all the conical pin fin tubes were found to perform better than the dome-shape fin tubes and *CF*3 achieved the highest η_1 value of 1.25.
6. Based on the boundary layer approach, a semi-empirical model is developed to predict the Nusselt number of the conical pin fin tubes. This model considers the effects of circumferential and longitudinal fin pitches of the condenser tubes and the variation of refrigerant mass fluxes and vapour qualities during the

condensation process. It provides relatively reasonable predictions with most of the experimental data falling within ± 20% of the predicted values with an overall *MAE* of 10.5%.

In this thesis, a comprehensive set of data for natural and forced convection condensation heat transfer coefficients of new three-dimensional pin fin structures is obtained. In addition, a theoretical model for natural convection condensation of steam on conical pin fins and a semi-empirical model which predicts the forced convection condensation heat transfer coefficient of R134a are also developed. It is hoped that these new data and predictive tools would be useful for researchers and engineers in the development of high-performance condensers with three-dimensional pin fin structures.

8.2 Recommendations for future work

1. In this thesis, experiments were performed to investigate the effects of fin height and fin pitch on natural convection condensation heat transfer coefficients of the conical pin fins. The fin pitch values range from 1.25 mm to 2.50 mm and an optimal fin pitch of 1.67 mm, which resulted in the highest heat transfer coefficients, was determined. On the other hand, among the range of fin height tested, the shortest pin fin of 1.28 mm was found to perform better than the taller fins. Even though the reduction in fin height decreases the total surface area of the fin, as shown in Fig. 5-11, it also reduces the liquid retention height which increases the effective heat transfer area. Therefore, conical pin fins with fin heights shorter than 1.28 mm can be investigated to determine the optimal fin height. However, it is recommended that the dimensions of the pin fins be larger

than 0.3 mm in order to obtain good dimensional accuracies of the fabricated parts by SLM.

2. A theoretical model which considers the effects of surface tension and gravitational forces on the liquid film thickness was developed for the conical pin fin and reasonable predictions was obtained. This model assumes the surrounding vapour to be in a quiescent state and therefore applies only for natural convection condensation. On the other hand, for forced convection condensation, the effects of vapour shear on at the liquid-vapour interface can significantly affect the liquid film thickness and the vapour quality also changes along the flow channel. For the prediction of forced convection condensation heat transfer, the existing model can be extended to include the effects of vapour shear force and varying vapour quality. In addition, the model also did not account for the variation in temperature along the fin surface. The temperature variation along the fin surface may affect the liquid film thickness and local heat transfer coefficient. This factor can be included to improve the accuracy of the model.
3. In this thesis, visualisation studies were performed to determine the liquid retention height and its effects on the pin fin arrays under natural convection condensation. For forced convention condensation, experiments have been conducted to characterise the heat transfer performance of the enhanced tubes. To better understand the liquid film and two-phase flow behaviour, flow visualisation can be performed. However, this would require the design of a new test section with visualisation ports which can withstand high operating pressures.
4. The forced convection condensation of enhanced tubes was investigated with the R134a refrigerant. This refrigerant is commonly employed in the air-conditioning

systems. For other applications, such as in the cooling of electronic systems, coolants such as FC-72, a dielectric fluid, is commonly used. Therefore, the condensation performance of 3D printed condenser tubes with other working fluids can be investigated.

5. The present investigation focuses on enhancing forced convection condensation heat transfer of R134a. In order to increase the heat rejection capacity of refrigerant condensers such as the air-cooled condenser, the enhancement of the air-side heat transfer coefficient is also essential. The use of enhanced plate fins such as slit [145] and louvered [146] fins have been shown to improve the air-side heat transfer coefficient of the air-cooled heat exchanger. More recently, additive manufacturing has also been employed to produce manifold-microchannel heat exchangers for air-side heat transfer enhancements [147, 148]. On the other hand, the use of airfoil pin fins [116] and lattice structures [118] have shown the potential of reducing the air-side thermal resistance while maintaining lower pressure drops as compared to conventional heat sink designs. These structures can be further optimised for air cooling and studies can be performed to explore their implementation in an air-cooled condenser.
6. It can be seen from the present investigation that the SLM fabricated parts have high surface roughness. For forced convection condensation, the reduction in frictional pressure drop can be achieved with the reduction in surface roughness of the fin structures. Therefore, post-processing techniques such as shot peening, sandblasting and electrolytic polishing can be explored to improve the surface finish of the SLM fabricated parts.

References

[1] Rose, J.W., Dropwise condensation theory and experiment: A review, *Proceedings of the Institute of Mechanical Engineers, Part A: Journal of Power and Energy*, Vol. 216, pp. 115-128 (2002).

[2] Ahlers, M., Buck-Emden, A., Bart, H.-J., Is dropwise condensation feasible? A review on surface modifications for continuous dropwise condensation and profitability analysis, *Journal of Advanced Research*, Vol. 16, pp. 1-13 (2019).

[3] Del Col, D., Parin, R., Bisetto, A., Bortolin, S., Martucci, A., Film condensation of steam flowing on a hydrophobic surface, *International Journal of Heat and Mass Transfer*, Vol. 107, pp. 307-318 (2017).

[4] Honda, H., Uchima, B., Nozu, S., Torigoe, E., Imai, S., Film condensation of R-113 on staggered bundles of horizontal finned tubes, *Journal of Heat Transfer*, Vol. 114, pp. 442-449 (1992).

[5] Jin, L.W., Leong, K.C., Pranoto, I., Li, H.Y., Chai, J.C., Experimental study of a two-phase thermosyphon with porous graphite foam insert, *Journal of Thermal Science and Engineering Applications*, Vol. 3, pp. 024502-1 – 024502-6 (2011).

[6] Dalkilic, A.S., Wongwises, S., Intensive literature review of condensation inside smooth and enhanced tubes, *International Journal of Heat and Mass Transfer*, Vol. 52, pp. 3409-3426 (2009).

[7] Heat Exchangers Market by Type (Shell & Tube, Plate & Frame, Air Cooled), Application (Chemical, Petrochemical and Oil & Gas, HVACR, Food & Beverage, Power Generation, Pulp & Paper), and Region - Global Forecast to 2023, MarketsandMarkets^{TM}, https://www.marketsandmarkets.com/Market-Reports/heat-exchanger-market-750.html (2017).

[8] Global Market Study on Automotive Condensers: Passenger Cars to Zoom Past LCVs and HCVs in Terms of Revenue Growth During 2017 – 2025, Persistence Market Research, https://www.persistencemarketresearch.com/market-research/automotive-condenser-market.asp (2017).

[9] Yau, K.K., Cooper J.R., Rose, J.W., Effect of fin spacing on the performance of horizontal integral-fin condenser tubes, *Journal of Heat Transfer*, Vol. 107, pp. 377-383 (1985).

[10] Zhu, D., Xu, H., Sun, Y., Qi, B., Numerical heat transfer analysis of laminar film condensation on a vertical fluted tube, *Applied Thermal Engineering*, Vol. 30, pp. 1159-1163 (2010).

[11] Rudy, T.M., Webb, R.L., An analytical model to predict condensate retention on horizontal integral-fin tubes, *Journal of Heat Transfer*, Vol. 107, pp. 361-368 (1985).

[12] Fitzgerald, C.L., Briggs, A., Rose, J.W., Wang, H.S., Effect of vapour velocity on condensate retention between fins during condensation on low-finned tubes, *International Journal of Heat and Mass Transfer*, Vol. 55, pp. 1412-1418 (2012).

[13] Al-Badri, A.R., Gebauer, T., Leipertz, A., Fröba, A.P., Element by element prediction model of condensation heat transfer on a horizontal integral finned tube, *International Journal of Heat and Mass Transfer*, Vol. 62, pp. 463-472 (2013).

[14] Honda, H., Nozu, S., Uchima, B., A generalized prediction method for heat transfer during film condensation on a horizontal low-finned tube, *Japanese Society of Mechanical Engineering (JSME) International Journal*, Vol. 31, pp. 709-717 (1988).

[15] Ali, H.M., Briggs, A., Condensation heat transfer on pin-fin tubes: Effect of thermal conductivity and pin height, *Applied Thermal Engineering*, Vol. 60, pp. 465-471 (2013).

[16] Al-Badri, A.R., Bar, A., Gotterbarm, A., Rausch, M.H., Froba, A.P., The influence of fin structure and fin density on the condensation heat transfer of R134a on single finned tubes and in tube bundles, *International Journal of Heat and Mass Transfer*, Vol. 100, pp. 582-589 (2016).

[17] Briggs, A., Enhanced condensation of R-113 and steam using three-dimensional pin-fin tubes, *Experimental Heat Transfer*, Vol. 16, 61-79 (2003).

[18] Ali, H.M., Briggs, A., Condensation of ethylene glycol on pin-fin tubes: effects of circumferential pin spacing and thickness, *Applied Thermal Engineering*, Vol. 49, pp. 9-13 (2012).

[19] Ali, H.M., Abubaker, M., Effect of circumferential pin thickness on condensate retention as a function of vapor velocity on horizontal pin-fin tubes, *Applied Thermal Engineering*, Vol. 91, pp. 245-251 (2015).

[20] Liebenberg, L., Meyer, J.P., The characterization of flow regimes with power spectral density distributions of pressure fluctuations during condensation in smooth and micro-fin tubes, *Experimental Thermal and Fluid Science*, Vol. 31, pp. 127-140 (2006).

[21] Zhang, J., Zhou, N., Li, W., Luo, Y., Li, S., An experimental study of R410A condensation heat transfer and pressure drops characteristics in microfin and smooth tubes with 5 mm OD, *International Journal of Heat and Mass Transfer*, Vol. 125, pp. 1284-1295 (2018).

[22] Miyara, A., Nonaka, K., Taniguchi, M., Condensation heat transfer and flow pattern inside a herringbone-type micro-fin tube, *International Journal of Refrigeration*, Vol. 23, pp. 141-152 (2000).

[23] Aroonrat, K., Wongwises, S., Experimental study on two-phase condensation heat transfer and pressure drop of R-134a flowing in a dimpled tube, *International Journal of Heat and Mass Transfer*, Vol. 106, pp. 437-448 (2017).

[24] Doretti, L., Zilio, C., Mancin, S., Cavallini, A., Condensation flow patterns inside plain and microfin tubes: A review, *International Journal of Refrigeration*, Vol. 36, pp. 567-587 (2013).

[25] Guo, S.-P., Wu, Z., Li, W., Kukulka, D., Sundén, B., Zhou, X.-P., Wei, J.-J., Simon, T., Condensation and evaporation heat transfer characteristics in horizontal smooth, herringbone and enhanced surface EHT tubes, *International Journal of Heat and Mass Transfer*, Vol. 85, pp. 281-291 (2015).

[26] Loh, L.-E., Chua, C.-K., Yeong, W.-Y., Song, J., Mapar, M., Sing, S.-L., Liu, Z.-H., Zhang, D.-Q., Numerical investigation and an effective modelling on the Selective Laser Melting (SLM) process with aluminium alloy 6061, *International Journal of Heat and Mass Transfer*, Vol. 80, pp. 288-300 (2015).

[27] Nusselt, W., Die Oberflachenkondensation des Wasserdampfes, *VDI-Z.* 60, pp 541-546 and pp. 569-575 (1916) (in German).

[28] Rohsenow, W.M., Heat transfer and temperature distribution in laminar-film condensation, *Journal of Heat Transfer*, Vol. 78, pp.1645-1648 (1956).

[29] Baehr, H.D., Stephan, K., *Heat and Mass Transfer*, 2nd Edition, Springer (2006).

[30] Grimley, L.S., Liquid flow conditions in packed towers, *Transactions of the Institution of Chemical Engineers*, Vol. 23, pp. 228-235 (1945).

[31] Sparrow, E.M., Gregg, J.L., A boundary-layer treatment of laminar-film condensation, *Journal of Heat Transfer*, Vol. 81, pp. 13-18 (1959).

[32] Sparrow, E.M., Gregg, J.L., Laminar condensation heat transfer on a horizontal cylinder, *Journal of Heat Transfer*, Vol. 81, pp. 291-296 (1959).

[33] Chen, M.M., An analytical study of laminar film condensation: Part 1- Flat Plates, *Journal of Heat Transfer*, Vol. 83, pp. 48-54 (1961).

[34] Chen, M.M., An analytical study of laminar film condensation: Part 2- Single and multiple horizontal tubes, *Journal of Heat Transfer*, Vol. 83, pp. 55-60 (1961).

[35] Koh, J.C.Y., An integral treatment of two-phase boundary layer in film condensation, *Journal of Heat Transfer*, Vol. 83, pp. 359-362 (1961).

[36] Koh, J.C.Y., Sparrow, E.M., Hartnett, J.P., The two phase boundary layer in laminar film condensation, *International Journal of Heat and Mass Transfer*, Vol. 2, pp. 69-82 (1961).

[37] Krupiczka, R., Effect of surface tension on laminar film condensation on a horizontal cylinder, *Chemical Engineering and Processing: Process Intensification*, Vol. 19, pp. 199-203 (1985).

[38] Gregorig, R., Hautkondensation an feingewellten Oberflächen bei Berücksichtigung der Oberflächenspannungen, *Zeitschrift für angewandte Mathematik und Physik*, Vol. 5, pp. 36–49 (1954) (in German).

[39] Hirasawa, S., Hijikata, K., Mori, Y., Nakayama, W., Effect of surface tension on condensate motion in laminar film condensation (study of liquid film in a small through), *International Journal of Heat and Mass Transfer*, Vol. 23, pp. 1471-1478 (1980).

[40] Mori, Y., Hijikata, K., Hirasawa, S., Nakayama, W., Optimized performance of condensers with outside condensing surfaces, *Journal of Heat Transfer*, Vol. 103, pp. 96-102 (1981).

[41] Qi, B., Wei, J., Li, X., Enhanced of condensation heat transfer on grooved surfaces: Numerical analysis and experimental study, *Applied Thermal Engineering*, Vol. 115, pp. 1287-1297 (2017).

[42] Honda, H., Nozu, S., A prediction method of heat transfer during film condensation on horizontal low integral-fin tubes, *Journal of Heat Transfer*, Vol. 109, pp. 218-225 (1987).

[43] Wang, X.W., Leong, K.C., Wong, T.N., Numerical analysis of different fluted fins for condensation on a vertical tube, *International Journal of Thermal Sciences*, Vol. 122, pp. 359-370 (2017).

[44] Adamek, T., Webb, R.L., Prediction of film condensation on horizontal integral fin tubes, *International Journal of Heat and Mass Transfer*, Vol. 33, pp. 1721-1735 (1990).

[45] Rose, J.W., An approximate equation for the vapour-side heat-transfer coefficient for condensation on low-finned tubes, *International Journal of Heat and Mass Transfer*, Vol. 37, pp. 865-875 (1994).

[46] Briggs, A., Rose, J.W., Effect of fin efficiency on a model for condensation heat transfer on a horizontal, integral-fin tube, *International Journal of Heat and Mass Transfer*, Vol. 37, pp. 457-463 (1994).

[47] Ali, H.M., Briggs, A., A semi-empirical model for free-convection condensation on horizontal pin-fin tubes, *International Journal of Heat and Mass Transfer*, Vol. 81, pp. 157-166 (2015).

[48] Yau, K.K., Cooper, J.R., Rose, J.W., Horizontal plain and low-finned condenser tubes – Effect of fin spacing and drainage strips on heat transfer and condensate retention, *Journal of Heat Transfer*, Vol. 108, pp. 946-950 (1986).

[49] Honda, H., Nozu, S., Mitsumori, K., Augmentation of condensation on finned tubes by attaching a porous drainage plate, *Proceedings of ASME-JSME Thermal Engineering Joint Conference*, Vol. 3, pp. 289-295 (1983).

[50] Ali, H.M., Briggs, A., An investigation of condensate retention on pin-fin tube, *Applied Thermal Engineering*, Vol. 63, pp. 503-510 (2014).

[51] Ali, H.M., An analytical model for prediction of condensate flooding on horizontal pin-fin tubes, *International Journal of Heat and Mass Transfer*, Vol. 106, pp. 1120-1124 (2017).

[52] Sukhatme, S.P., Jagadish, B.S., Prabhakaran, P., Film condensation on R-11 vapour on single horizontal enhanced condenser tubes, *Journal of Heat Transfer*, Vol. 112, pp. 229-234 (1990).

[53] Cheng, B., Tao, W.Q., Experimental study of R-152a film condensation on a single horizontal smooth tube and enhanced tubes, *Journal of Heat Transfer*, Vol. 116, pp. 266-270 (1994).

[54] Kumar, R., Varma, H.K., Mohanty, B., Agrawal, K.N., Augmentation of heat transfer during filmwise condensation of steam and R-134a over single horizontal finned tubes, *International Journal of Heat and Mass Transfer*, Vol. 45, pp. 201-211 (2002).

[55] Zhang, Z, Li, Q., Fang, X., Gao, X., Condensation heat transfer characteristics of zeotropic refrigerant mixture R407C on single, three-row petal-shaped finned tubes and helically baffled condenser, *Applied Thermal Engineering*, Vol. 39, pp. 63-69 (2012).

[56] Murase, T., Briggs, A., Wang, H.S., Rose, J.W., Condensation on a horizontal wire-wrapped tube, *Journal of Heat Transfer*, Vol. 127, pp. 1207-1213 (2005).

[57] Ali, H.M., Qasim, M.Z., Free convection condensation of steam on horizontal wire wrapped tubes: Effect of wire thermal conductivity, pitch and diameter, *Applied Thermal Engineering*, Vol. 90, pp. 207-214 (2015).

[58] Ali, H.M., Qasim, M.Z., Ali, M., Free convection condensation heat transfer of steam on horizontal square wire wrapped tubes, *International Journal of Heat and Mass Transfer*, Vol. 98, pp. 350-358 (2016).

[59] Ji, W.-T., Zhao, C.-Y., Zhang, D.-C., Li, Z.-Y., He, Y.-L., Tao, W.-Q., Condensation of R134a outside single horizontal titanium, cupronickel (B10 and B30), stainless steel and copper tubes, *International Journal of Heat and Mass Transfer*, Vol. 77, pp. 194-201 (2014).

[60] Zhang, D.-C., Ji, W.-T., Tao, W.-Q., Condensation heat transfer of HFC134a on horizontal low thermal conductivity tubes, *International Communications in Heat and Mass Transfer*, Vol. 34, pp. 917-923 (2007).

[61] Zhao, C.-Y., Ji, W.-T., Jin, P.-H., Zhong, Y.-J., Tao, W.-Q., The influence of surface structure and thermal conductivity of the tube on the condensation heat transfer of R134a and R404A over single horizontal enhanced tubes, *Applied Thermal Engineering*, Vol. 125, pp. 1114-1122 (2017).

[62] Ali, H.M., *Free-Convection Condensation on Single Horizontal Pin-fin Tubes*, Department of Engineering, Queen Mary University of London, Ph.D. Thesis (2011).

[63] Blasius, P.R.H., Das Aehnlichkeitsgesetz bei Reibungsvorgangen in Flüssigkeiten, *Forschungsheft*, Vol. 131, pp. 1-41(1913), in German.

[64] McAdams, W.H., Woods, W.K., Heroman, L.C., Vaporization inside horizontal tubes, II. Benzene-oil mixture, *Transactions of ASME*, Vol. 64, pp. 192-200 (1942).

[65] Cicchitti, A., Lombardi, M., Silvestri, M., Soldaini, G., Zavalluilli, R., Two-phase cooling experiments – pressure drop, heat transfer and burnout measurements, *Energia Nucleare*, Vol. 7, pp. 407-425 (1960).

[66] Zivi, S.M., Estimation of steady-state steam void-fraction by means of the principle of minimum entropy production, *Journal of Heat Transfer*, Vol. 86, pp. 247-252 (1964).

[67] Lockhart, R.W., Martinelli, R.C., Proposed correlation of data for isothermal two-phase, two-component flow in pipes, *Chemical Engineering Progress*, Vol 45, pp. 39-48 (1949).

[68] Chisholm, D., Pressure gradients due to friction during the flow of evaporating two-phase mixtures in smooth tubes and channels, *International Journal of Heat and Mass Transfer*, Vol. 16, pp. 347-358 (1973).

[69] Friedel, L., Improved friction pressure drop correlations for horizontal and vertical two-phase pipe flow, *European Two-phase Group Meeting*, Ispra, Italy, Paper E2 (1979).

[70] Wang, C.C., Chiang, C.S., Lu, D.C., Visual observation of two-phase flow pattern of R-22, R-134a, and R407C in a 6.5-mm smooth tube, *Experimental Thermal and Fluid Science*, Vol. 15, pp. 395-405 (1997).

[71] Collier, J.G., Thome, J.R., *Convective Boiling and Condensation*, 3rd Edition, Oxford Science Publications (2001).

[72] Kim, S.-M., Kim, J., Mudawar, I., Flow condensation in parallel micro-channels – Part 1: Experimental results and assessment of pressure drop correlations, *International Journal of Heat and Mass Transfer*, Vol. 55, pp. 971-983 (2012).

[73] Kim, S.-M., Mudawar, I., Universal approach to predicting two-phase frictional pressure drop for adiabatic and condensing mini/micro-channel flows,

International Journal of Heat and Mass Transfer, Vol. 55, pp. 3246-3261 (2012).

[74] Chato, J.C., Laminar condensation inside horizontal and inclined tubes, *ASHRAE Journal*, Vol. 4, pp. 52-60 (1962).

[75] Jaster, H., Kosky, P.G., Condensation in a mixed flow regime, *International Journal of Heat and Mass Transfer*, Vol. 19, pp. 95-99 (1976).

[76] Rosson, H.F., Meyers, J.A., Point values of condensing film coefficients inside a horizontal tube, *Chemical Engineering Progress Symposium Series*, Vol. 61, pp. 190-199 (1965).

[77] Dobson, M.K*., Heat Transfer and Flow Regimes During Condensation in Horizontal Tubes*, Ph.D. thesis, Department of Mechanical and Industrial Engineering, University of Illinois at Urbana-Champaign (1994).

[78] Dobson, M.K., Chato, J.C., Wattelet, J.P., Gaibel, J.A., Ponchner, M., Kenney, P.J., Shimon, R.L., Villaneuva, T.C., Rhines, N.L., Sweeney, K.A., Allen, D.G., Hershberger, T.T., *Heat Transfer and Flow Regimes During Condensation in Horizontal Tubes*, University of Illinois at Urbana-Champaign, ACRC TR-57 (1994).

[79] Shah, M.M., A general correlation for heat transfer during film condensation inside pipes, *International Journal of Heat and Mass Transfer*, Vol. 22, pp. 547-556 (1979).

[80] Shah, M.M., A new correlation for heat transfer during boiling flow through pipes, *ASHRAE Transactions*, Vol. 82, pp. 66-86 (1976).

[81] Dittus, F.W., Boelter, L.M.K., Heat transfer in automobile radiators of the tubular type, *International Communications in Heat and Mass Transfer*, Vol. 12, pp. 3-22 (1985).

[82] Cavallini, A., Zecchin, R., A dimensionless correlation for heat transfer in forced-convection condensation, *Proceedings of the Fifth International Heat Transfer Conference*, Tokyo, Japan, Vol. 3, pp. 309-313 (1974).

[83] Dobson, M.K., Chato, J.C., Condensation in smooth horizontal tubes, *Journal of Heat Transfer*, Vol. 120, pp. 193-213 (1998).

[84] Akers, W.W., Rosson, H.F., Condensation inside a horizontal tube, *Chemical Engineering Progress Symposium Series*, Vol. 56, pp.145-149 (1960).

[85] Azer, N.Z., Abis, L.V., Soliman, H.M., Local heat transfer coefficients during annular flow condensation, *ASHRAE Transactions*, Vol. 1, pp. 135-143 (1972).

[86] Traviss, D.P., Rohsenow, W.M., Baron, A.B., Forced convection condensation in tubes: a heat transfer correlation for condenser design, *ASHRAE Transactio*ns, Vol. 79, pp. 157-165 (1973).

[87] von Karman, T., The analogy between fluid friction and heat transfer, *Transactions of ASME*, Vol. 61, pp. 705-711 (1939).

[88] Chamra, L.M., Mago, P.J., Tan, M.-O., Kung, C.-C., Modeling of condensation heat transfer of pure refrigerants in micro-fin tubes, *International Journal of Heat and Mass Transfer*, Vol. 48, pp. 1293-1302 (2005).

[89] Wang, W.-W.W., Radcliff, T.D., Christensen, R.N., A condensation heat transfer correlation for millimeter-scale tubing with flow regime transition, *Experimental Thermal and Fluid Science*, Vol. 26, pp. 473-485 (2002).

[90] Kim, S.-M., Mudawar, I., Flow condensation in parallel micro-channels – Part 2: Heat transfer results and correlation technique, *International Journal of Heat and Mass Transfer*, Vol. 55, pp. 984-994 (2012).

[91] Cavallini, A., Censi, G., Del Col, D., Doretti, L., Longo, G.A., Rossetto, L., Zilio, C., Condensation inside and outside smooth and enhanced tubes – a review of recent research, *International Journal of Refrigeration*, Vol. 26, pp. 373-392 (2003).

[92] Han, D., Lee, K.-J., Experimental study on condensation heat transfer enhancement and pressure drop penalty factors in four microfin tubes, *International Journal of Heat and Mass Transfer*, Vol. 48, pp. 3804-3816 (2005).

[93] Sapali, S.N., Patil, P.A., Heat transfer during condensation of HFC-134a and R404A inside of a horizontal smooth and micro-fin tube, *Experimental Thermal and Fluid Science*, Vol. 34, pp. 1131-1141 (2010).

[94] Wu, Z., Sundén, B., Wang, L., Li, W., Convective condensation inside horizontal smooth and microfin tubes, *Journal of Heat Transfer*, Vol. 136, pp. 051504-1-051504-11 (2014).

[95] Li, G., Huang, L., Tao, L., Experimental investigation of refrigerant condensation heat transfer characteristics in the horizontal microfin tubes, *Applied Thermal Engineering*, Vol. 123, pp. 1484-1493 (2017).

[96] Zhang, J., Zhou, N., Li, W., Luo, Y, Li, S., An experimental study of R410A condensation heat transfer and pressure drops characteristics in microfin and smooth tubes with 5 mm OD, *International Journal of Heat and Mass Transfer*, Vol. 125, pp. 1284-1295 (2018).

[97] Cavallini, A., Del Col, D., Doretti, L., Longo, G.A., Rossetto, L., A new computational procedure for heat transfer and pressure drop during refrigerant condensation inside enhanced tubes, *Enhanced Heat Transfer*, Vol. 6, pp. 441-456 (1999).

[98] Cavallini, A., Del Col, D., Mancin, S., Rossetto, L., Condensation of pure and near-azeotropic refrigerants in microfin tubes: A new computational procedure, *International Journal of Refrigeration*, Vol. 32, pp. 162-174 (2009).

[99] Ebisu, T., Torikoshi, K., Experimental study on evaporation and condensation heat transfer enhancement for R407C using herringbone heat transfer tube, *ASHRAE Transactions*, Vol. 2, pp. 1044-1054 (1998).

[100] Oliver, J.A., Liebenberg, L., Thome, J.R., Meyer, J.P., Heat transfer, pressure drop, and flow pattern recognition during condensation inside smooth, helical micro-fin, and herringbone tubes, *International Journal of Refrigeration*, Vol. 30, pp. 609-623 (2007).

[101] Goto, M., Inoue, N., Ishiwatari, N., Condensation and evaporation heat transfer of R410A inside internally grooved horizontal tubes, *International Journal of Refrigeration*, Vol. 24, pp. 628-638 (2001).

[102] Lambrechts, A., Liebenberg, L., Bergles, A., Meyer, J.P., Heat transfer performance during condensation inside horizontal smooth, micro-fin and herringbone tube, *Journal of Heat Transfer*, Vol. 128, pp. 691-700 (2006).

[103] Kukulka, D.J., Smith, R., Li, W., Comparison of tubeside condensation and evaporation characteristics of smooth and enhanced heat transfer 1EHT tubes, *Applied Thermal Engineering*, Vol. 89, pp. 1079-1086 (2015).

[104] Li, W., Chen, J., Zhu, H., Kukulka, D.J., Minkowycz, W.J., Experimental study on condensation and evaporation flow inside horizontal three-dimensional enhanced tubes, *International Communications in Heat and Mass Transfer*, Vol. 80, pp. 30-40 (2017).

[105] Sun, Z.-C., Li, W., Guo, R.-H., He, Y., Kukulka, D.J., Condensation heat transfer in horizontal three-dimensional two-layer two-side enhanced tubes, *International Journal of Heat and Mass Transfer*, Vol. 127, pp. 141-145 (2018).

[106] Chen, J., Li, W., Local convective condensation heat transfer in horizontal double-layer three-dimensional dimpled-grooved tubes, *International Journal of Heat and Mass Transfer*, Vol. 127, pp. 810-820 (2018).

[107] Yang, D., Li, H., Chen, T., Pressure drop, heat transfer and performance of single-phase turbulent flow in spirally corrugated tubes, *Experimental Thermal and Fluid Science*, Vol. 24, pp. 131-138 (2001).

[108] Barba, A., Rainieri, S., Spiga, M., Heat transfer enhancement in a corrugated tube, *International Communications in Heat and Mass Transfer*, Vol. 29, pp. 313-322 (2002).

[109] Rainieri, S., Pagliarini, G., Convective heat transfer to temperature dependent property fluids in the entry region of corrugated tubes, *International Journal of Heat and Mass Transfer*, Vol. 45, pp. 4525-4536 (2002).

[110] Naphon, P., Nuchjapo, M., Kurujareon, J., Tube side heat transfer coefficient and friction factor characteristics of horizontal tubes with helical rib, *Energy Conversion and Management*, Vol. 47, pp. 3031-3044 (2006).

[111] Laohalertdecha, S., Wongwises, S., The effects of corrugation pitch on the condensation heat transfer coefficient and pressure drop of R-134a inside horizontal corrugated tube, *International Journal of Heat and Mass Transfer*, Vol. 53, pp. 2924-2931 (2010).

[112] Laohalertdecha, S., Wongwises, S., Condensation heat transfer and flow characteristics of R-134a flowing through corrugated tubes, *International Journal of Heat and Mass Transfer*, Vol. 54, pp. 2673-2682 (2011).

[113] Aroonrat, K., Wongwises, S., Experimental investigation of condensation heat transfer and pressure drop of R-134a flowing inside dimpled tubes with different dimpled depths, *International Journal of Heat and Mass Transfer*, Vol. 128, pp. 783-793 (2019).

[114] Wong, M., Owen, I., Sutcliffe, C.J., Puri, A., Convective heat transfer and pressure losses across novel heat sinks fabricated by selective laser melting, *International Journal of Heat and Mass Transfer*, Vol. 52, pp. 281-288 (2009).

[115] Ventola, L., Robotti, F., Dialameh, M., Calignano, F., Manfredi, D., Chiavazo, E., Asinari, P., Rough surfaces with enhanced heat transfer of electronic cooling by direct laser sintering*, International Journal of Heat and Mass Transfer*, Vol. 75, pp. 58-74 (2014).

[116] Ho, J.Y., Wong, K.K., Leong, K.C., Wong, T.N., Convective heat transfer performance of airfoil heat sinks fabricated by selective laser melting, *International Journal of Thermal Sciences*, Vol. 114, pp. 213-228 (2017).

[117] Ho, J.Y., Leong, K.C., Cylindrical porous inserts for enhancing the thermal and hydraulic performance of water-cooled cold plates, *Applied Thermal Engineering*, Vol. 121, pp. 863-878 (2017).

[118] Ho, J.Y., Leong, K.C., Wong, T.N., Experimental and numerical investigation of forced convection heat transfer in porous lattice structures produced by selective laser melting, *International Journal of Thermal Sciences*, Vol. 137, pp. 276-287 (2019).

[119] Hutter, C., Buchi, D., Zuber, V., Rudolf von Rohr, P., Heat transfer in metal foams and designed porous media, *Chemical Engineering Science*, Vol. 66, pp. 3806-3814 (2011).

[120] Ameli, M., Agnew, B., Leung, P.S., Ng, B., Sutcliffe, C.J., Singh, J., McGlen, R., A novel method for manufacturing sintered aluminum heat pipes (SAHP*), Applied Thermal Engineering*, Vol. 52, pp. 498-504 (2013).

[121] Ho, J.Y., Wong, K.K., Leong, K.C., Saturated pool boiling of FC-72 from enhanced surfaces produced by selective laser melting, *International Journal of Heat and Mass Transfer*, Vol. 99, pp. 107-121 (2016).

[122] Wong, K.K., Leong, K.C., Saturated pool boiling enhancement using porous lattice structures produced by selective laser melting, *International Journal of Heat and Mass Transfer*, Vol. 121, pp. 46-63 (2018).

[123] Wang, X.W., Ho, J.Y., Leong, K.C., An experimental investigation of single droplet impact cooling on hot enhanced surfaces fabricated by selective laser melting, *International Journal of Heat and Mass Transfer*, Vol. 120, pp. 652-670 (2018).

[124] Zhang, C., Zhang, Li., Xu, H., Li, P., Qian, B., Performance of pool boiling with 3D grid structure manufactured by selective laser melting technique, *International Journal of Heat and Mass Transfer*, Vol. 128, pp. 570-580 (2019).

[125] EOS e-Manufacturing Solutions, *EOS Aluminium AlSi*10*Mg Material Data Sheet*, http://www.eos.info/en, (2014).

[126] Kosar A., Peles, Y., Thermal-hydraulic performance of MEMS-based pin fin heat sink, *Journal of Heat Transfer,* Vol. 128, pp. 121-131 (2006).

[127] Wei, J.J., Honda, H., Effects of fin geometry on boiling heat transfer from silicon chip with micro-pin-fins immersed in FC-72, *International Journal of Heat and Mass Transfer*, Vol. 46, pp. 4059-4070 (2003).

[128] Renishaw plc., *AlSi10Mg-0403 Powder for Additive Manufacturing - Data Sheet*, http://www.renishaw.com/en, (2015).

[129] Taylor, J.R., *An Introduction to Error Analysis*, 2nd Ed., Sausalito: University Science Books, 1997.

[130] Çengel, Y.A., Ghajar, A.J., *Heat and Mass Transfer: Fundamentals and Applications*, 5th Edition (S.I. Units), New York: McGraw-Hill Education, pp. 490-495 (2015).

[131] Petukhov, B.S., Popov, V.N., Theoretical calculation of heat exchanger and friction resistance in turbulent flow in tubes of an incompressible fluid with variable physical properties, *High Temperature*, Vol. 1, pp. 69-83 (1963).

[132] Young, T, An essay on the cohesion of fluids, *Philosophical Transactions of the Royal Society of London*, Vol. 95, pp. 65-87 (1805).

[133] Xie, J.L., Tan, Y.B., Duan, F., Ranjith, K., Wong, T.N., Toh, K.C., Choo, K.F., Chan, P.K., Study of heat transfer enhancement for structured surfaces in spray cooling, *Applied Thermal Engineering*, Vol. 50, pp. 464-473 (2013).

[134] Hansen, L.G., Webb, B.W., Air jet impingement heat transfer from modified surfaces, *International Journal of Heat and Mass Transfer*, Vol. 36, pp. 989-997 (1993).

[135] Maschmann, M.R., Ma, H.B., An investigation of capillary flow effect on condensation heat transfer on a grooved plate, *Heat Transfer Engineering*, Vol. 27, pp. 21-31 (2006).

[136] Qi, B., Song, Z., Li, X., Numerical study on condensation heat transfer of trapezoid grooved surfaces, *Advances in Mechanical Engineering*, Vol. 8, pp. 1-11 (2016).

[137] Peng, B., Ma, X., Lan, Z., Xu, W., Wen, R., Experimental investigation on steam condensation heat transfer enhancement with vertically patterned hydrophobic-hydrophilic hybrid surfaces, *International Journal of Heat and Mass Transfer*, Vol. 83, pp. 27-38 (2015).

[138] Lu, M.-C., Lin, C.-C., Lo, C.-W., Huang, C.-W., Wang, C.-C., Superhydrophobic Si nanowires for enhanced condensation heat transfer, *International Journal of Heat and Mass Transfer*, Vol. 11, pp 614-623 (2017).

[139] Huang, D.-J., Leu, T.-S., Condensation heat transfer enhancement by surface modification on monolithic copper heat sink, *Applied Thermal Engineering*, Vol. 75, pp. 908-917 (2015).

[140] Ma, X.-H., Zhou, X.-D., Lan, Z., Li, Y.-M., Zhang, Y., Condensation heat transfer enhancement in the presence of non-condensable gas using the interfacial effect of dropwise condensation, *International Journal of Heat and Mass Transfer*, Vol. 51, pp. 1728-1737 (2008).

[141] Toponogov, V.A., *Differential Geometry of Curves and Surfaces – A Concise Guide*, Birkhäuser Boston (2006).

[142] Mazumder, S., *Numerical Methods for Partial Differential Equations – Finite Difference and Finite Volume Methods*, Academic Press, Elsevier (2016).

[143] Dukler, A.E., Bergelin, O.P., Characteristics of flow in falling films, *Chemical Engineering Progress*, Vol. 48, 557-563 (1952).

[144] Taitel, Y., Dukler, A.E., A model for predicting flow transitions in horizontal and near horizontal gas-liquid flow, *AIChE Journal*, Vol. 22, pp. 47-55 (1976).

[145] Wang, C.-C., Tao, W.-H., Chang, C.-J., An investigation of the airside performance of the slit fin-and-tube heat exchanger, *International Journal of Refrigeration*, Vol. 22, pp. 595-603 (1999).

[146] Wang, C.-C., Chen, K.-Y., Liaw, J.-S., Tseng, C.-Y., An experimental study of the air-side performance of fin-and-tube heat exchangers having plain, louver, and semi-dimple vortex generator configuration, *International Journal of Heat and Mass Transfer*, Vol. 80, pp. 281-297 (2015).

[147] Arie, M.A., Shooshtari, A.H., Rao, V.V., Dessiatoun, S.V., Ohadi, M.M., Air-side heat transfer enhancement utilizing design optimization and an additive

manufacturing technique, *Journal of Heat Transfer*, Vol. 39, 031901-1-031901-12 (2017).

[148] Arie, M.A., Shooshtari, A.H., Ohadi, M.M., Experimental characterization of an additively manufactured heat exchanger for dry cooling power plants, *Applied Thermal Engineering*, Vol. 129, pp. 187-198 (2018).

Appendix A – Measurements of Fabricated Specimens

Images of the fabricated specimens are taken using the Olympus SZX7 as shown in Fig. A1. In addition, using the images obtained, the physical dimensions of the specimens were also measured. Examples of the measurements taken of the sinusoidal pin fins and the conical pin fins are shown in Figs. A2 and A3. For each fin height (l), fin pitch (p) and fin base diameter (d_b), up to 10 measurements were taken and the maximum deviations between the design and fabricated dimensions were found to be not more than 8%.

Fig. A1 An image of the Olympus SZX7

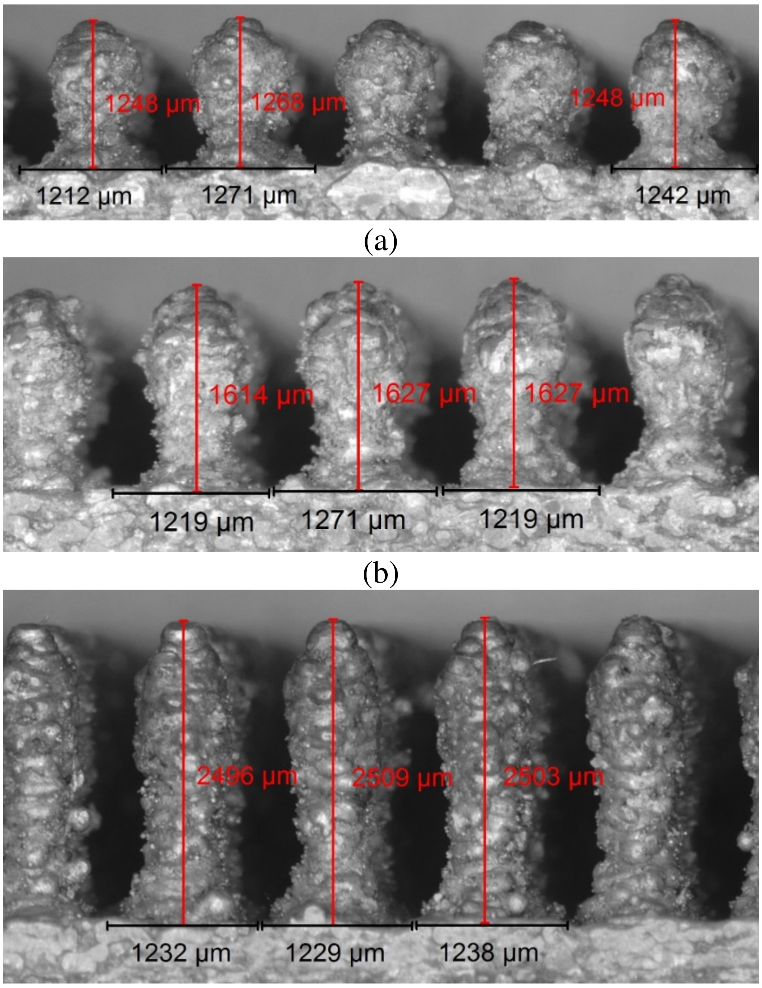

(a)

(b)

(c)

Fig. A2 Microscope images of S1, S4 and S7 specimens.

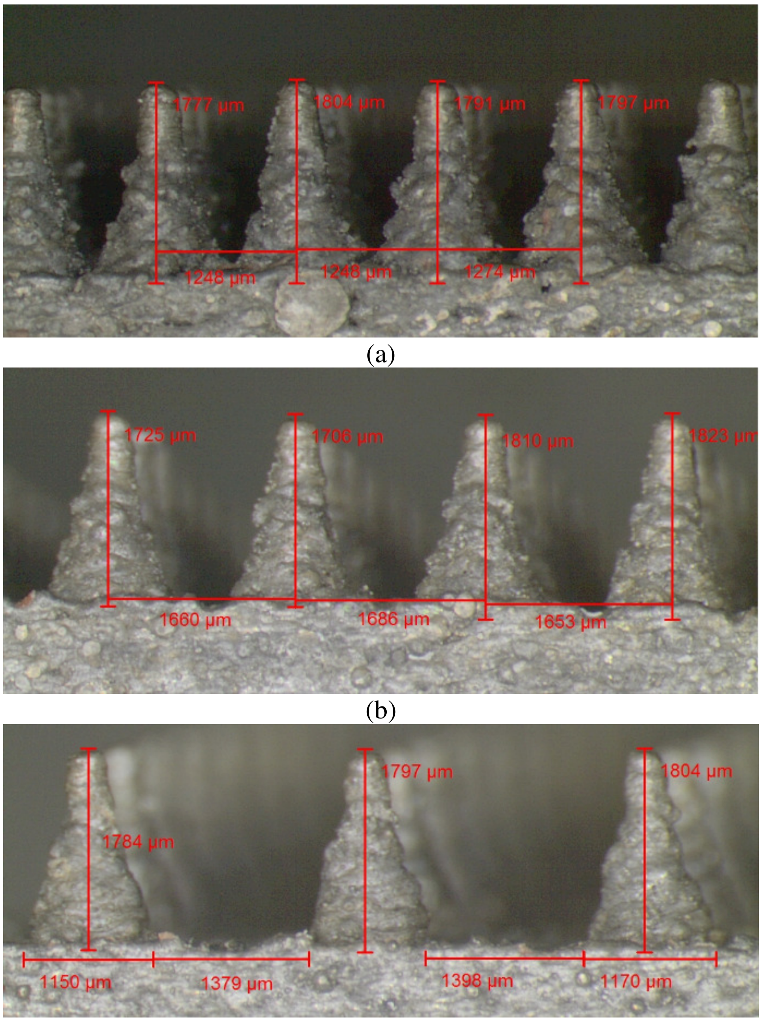

(a)

(b)

(c)

Fig. A3 Microscope images of *C*4, *C*5 and *C*6 specimens.

Appendix B – Experimental Facilities

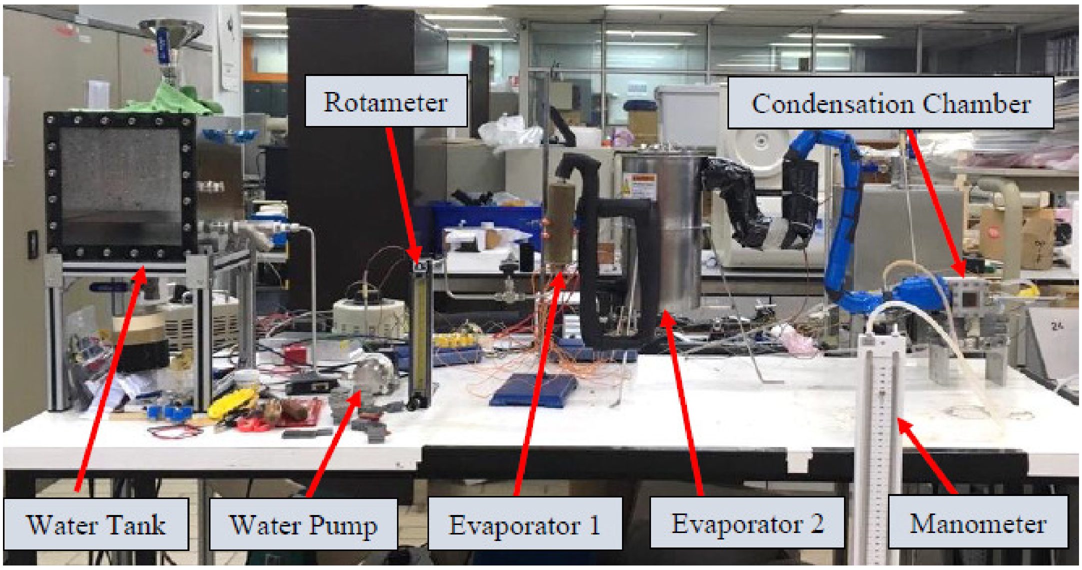

Fig. B1 Image of natural convection condensation test facility.

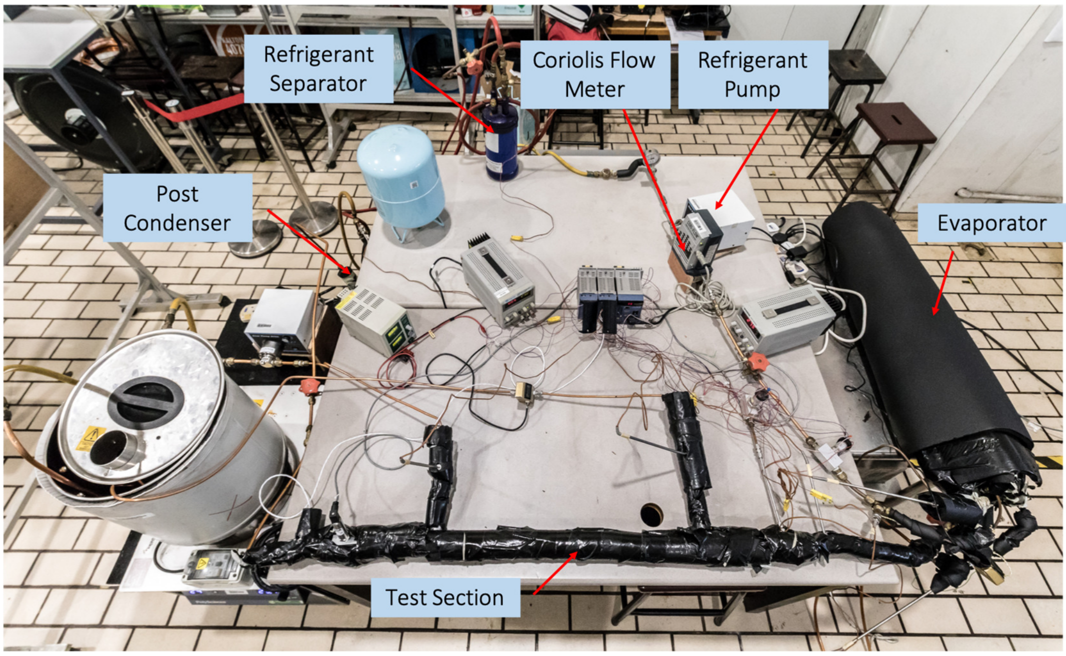

Fig. B2 Image of forced convection condensation test facility.

Appendix C – AlSi10Mg Thermal Conductivity Measurements

Figure C-1 shows a schematic of the experimental setup employed to measure the thermal conductivity of the bulk AlSi10Mg. The bulk AlSi10Mg has dimensions of 33.3 mm × 34.6 mm × 38 mm and was heated at the top by a copper block. The copper block was in turn heated by three cartridge heaters. The cartridge heaters were connected to a variable transformer which allowed the heat rate from the heaters to be controlled. Using an ammeter and a voltmeter, the output heat rates (Q) from the heaters were determined. The bottom surface of the bulk AlSi10Mg was in contact with the heat sink where heat was dissipated. Tap water was used as the cooling medium and was allowed to run through the heat sink flow channels. In order to minimize heat losses, Teflon was used as the insulating material and it enclosed the copper, heaters and the bulk AlSi10Mg. In addition, a layer of elastomer foam (a second layer of insulation) also surrounded the outer surface of the Teflon. Throughout the experiments, six additional thermocouples were installed on the surface of the elastomer foam to estimate the heat loss to the surroundings. Based on the temperatures recorded from these six thermocouples, the heat loss was determined to be less than 2.7%. Using the one-dimensional Fourier's law, the thermal conductivity of the test specimen can be obtained by Eq. (C-1) where the temperature gradient ($\frac{dT}{dx}$) can be determined from thermocouples located at $T1$, $T2$ and $T3$ and A is the cross-sectional area of the bulk AlSi10Mg perpendicular to the heat flow path. Eight thermocouples were installed at location $T1$, six thermocouples at location $T2$ and six thermocouples at location $T3$. The average temperature at each location was used to obtain $\frac{dT}{dx}$.

$$k_s = -\frac{Q/A}{dT/dx} \tag{C-1}$$

Based on the above procedures, the thermal conductivity of the bulk AlSi10Mg (k_s) was found to be 124 W/m·K and the maximum measurement uncertainty was ± 3.2%.

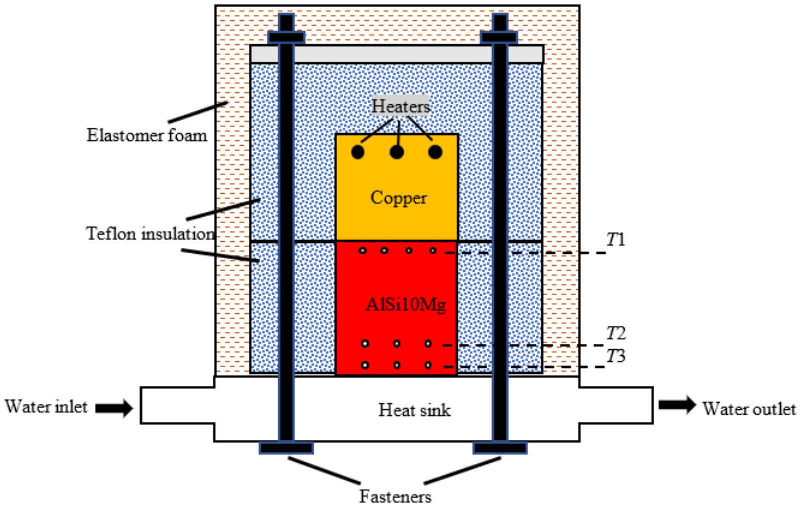

Fig. C-1 Schematic of experimental setup for thermal conductivity measurements.

Appendix D – Uncertainty Analysis of Natural Convection Condensation Heat Flux and Heat Transfer Coefficients

The uncertainties of dependent quantities can be computed by the propagation of error equation of Eq. (D-1) where δR is the total uncertainty and the uncertainty of variable R can be calculated based on the uncertainty of primary measurements of n number of variables x_i.

$$\delta R = \pm\sqrt{\sum_{i=1}^{n}\left(\frac{\partial R}{\partial x_i}\delta x_i\right)^2} \tag{D-1}$$

From Eqs. (4-1) and (4-3), the uncertainties of the heat flux (q'') and heat transfer coefficient (h) can be derived as

$$\frac{\delta q''}{q''} = \sqrt{\left(\frac{\delta T_1}{T_1-T_4}\right)^2 + \left(\frac{\delta T_4}{T_1-T_4}\right)^2} \tag{D-2}$$

$$\frac{\delta h}{h} = \sqrt{\left(\frac{\delta q''}{q''}\right)^2 + \left(\frac{\delta T_{sat}}{T_{sat}-T_W}\right)^2 + + \left(\frac{\delta T_W}{T_{sat}-T_W}\right)^2} \tag{D-3}$$

Based on the accuracies of measuring equipment mentioned in Section 4.1.2, the uncertainty of q'' was determined to be within $\pm 6\%$, while the uncertainty of h was within ±7.2%.

Appendix E - Uncertainty Analysis of Forced Convection Condensation Heat Transfer Coefficients and Vapour Qualities

The uncertainties of dependent quantities can be computed by the propagation of error equation of Eq. (E-1) where δR is the total uncertainty and the uncertainty of variable R can be calculated based on the uncertainty of primary measurements of n number of variables x_i.

$$\delta R = \pm\sqrt{\sum_{i=1}^{n}\left(\frac{\partial R}{\partial x_i}\delta x_i\right)^2} \tag{E-1}$$

From Eqs. (4-4) and (4-11), the inlet vapour quality (x_{in}), outlet vapour quality (x_{out}) and heat transfer coefficient (h_{ref}) can be calculated from Eqs. (E-2) – (E-6) below.

The uncertainty of the heat transfer rate with Q_{test} as an example can be derived as

$$\frac{\delta Q_{test}}{Q_{test}} = \pm\frac{\sqrt{\left(\frac{\partial Q_{test}}{\partial m_c}\delta m_{c,}\right)^2 + \left(\frac{\partial Q_{test}}{\partial T_{c,out}}\delta T_{c,out}\right)^2 + \left(\frac{\partial Q_{test}}{\partial T_{c,in}}\delta T_{c,in}\right)^2}}{Q_{test}} \tag{E-2}$$

The uncertainty of LMTD is

$$\frac{\delta LMTD}{LMTD} = \pm\frac{\delta\sqrt{\left(\frac{\partial LMTD}{\partial T_{ref,out}}\right)^2 + \left(\frac{\partial LMTD}{\partial T_{c,in}}\right)^2 + \left(\frac{\partial LMTD}{\partial T_{ref,in}}\right)^2 + \left(\frac{\partial LMTD}{\partial T_{c,,out}}\right)^2}}{LMTD} \tag{E-3}$$

The uncertainties of the vapour qualities at the inlet and outlet of the test section can be obtained from the following equations

$$\frac{\delta x_{in}}{x_{in}} = \pm \frac{\sqrt{\left(\frac{\partial x_{in}}{\partial Q_{evp}}\delta Q_{evp}\right)^2 + \left(\frac{\partial x_{in}}{\partial m_{ref}}\delta m_{ref}\right)^2}}{x_{in}} \tag{E-4}$$

$$\frac{\delta x_{out}}{x_{out}} = \pm \frac{\sqrt{(\delta x_{in})^2 + \left(\frac{\partial x_{out}}{\partial Q_{test}}\delta Q_{test}\right)^2 + \left(\frac{\partial x_{out}}{\partial m_{ref}}\delta m_{ref}\right)^2}}{x_{out}} \tag{E-5}$$

The uncertainty of h_{ref} can be obtained from

$$\frac{\delta h_{ref}}{h_{ref}} = \pm \frac{\sqrt{\left(\frac{\partial h_{ref}}{\partial Q_{test}}\delta Q_{test}\right)^2 + \left(\frac{\partial h_{ref}}{\partial h_o}\delta h_o\right)^2 + \left(\frac{\partial h_{ref}}{\partial LMTD}\delta LMTD\right)^2}}{h_{ref}} \tag{E-6}$$

Based on the accuracies of measuring equipment mentioned in Section 4.2.2, the uncertainty of x_{in}, x_{out} and h_{ref} were determined to be within ±2%, ±3% and ±15%, respectively.

Appendix F – MATLAB Code for Liquid Film Equations

Liquid film equation in θ-direction:

```
clear all;
clc;
global e
range = linspace(0,3.142,50);
[x,y]=ode45(@rhs_ivp,range,[1 0])
a = y(:,1)*e.^(1/4);
b = x(:,1)*180/3.142;
plot (b,a)

function dy=rhs_ivp(x,y)
global e
sigma = 6.08*10^-2; %water surface tension @95degC in N/m
mu = 0.00315; %water dynamic viscosity @ 95degC in N*s/m2
T = T0; %input wall subcooled temperature
kf = 0.67288; %water thermal conductivity @ 95degC in W/mK
H = 2256.4*10^2; %water latent heat of vaporization @ 1atm in J/kg
rho = 1000; %density of water
r =   r0; %radius of fin at l, input this value based on the
approximated fin tip radius
g = 9.81; %gravitational acceleration
PrK = mu*H/(kf*T);
We = sigma/(rho*g*r^2);
e = 3*(mu/rho)^2*r/(g*PrK);
A1 = (1/4)*We*e^(1/4)/r;
dy = zeros(2,1);
dy(1)=y(2);
dy(2)  = -(3/4)*sin(x)*y(2)/(A1*y(1)^(1/4))-
y(1)*cos(x)/(A1*y(1)^(1/4))+1/(A1*y(1)^(1/4));
```

Liquid film equation in ξ-direction:

```
clear all;
clc;
M = 50;
h(M,:) = 0
theta1 (M,:) = 0;
theta = 3.142*180/180/(M-1)*(1-1)*180/3.142
N = 50;
A = zeros(N);
Q(N,:)=0;
F(N,:)=0;
Q1(N,:)=0;
sigma = 6.08*10^-2; %water surface tension @95degC in N/m
s=s*; %input value for surface of conical fin
mu = 0.00315; %water dynamic viscosity @ 95degC in N*s/m2
T = T0; % input wall subcooled temperature
kf = 0.67288; %water thermal conductivity @ 95degC in W/mK
H = 2256.4*10^2; %water latent heat of vaporization @ 1atm in J/kg
S0 = S*; % input liquid film thickness at fin tip, determined from
first Matlab code
SL = S**; % input liquid film thickness at fin base, determined from
first Matlab code
rho = 1000; %density of water
```

```
L = sqrt(2*(s+SL)^2)/(s+SL)/1000
dx = L/(N-1);
a = (L*tan(0.60045382798736+0.0872664625997165)-
(s+SL))/(L+(s+SL)*tan(0.60045382798736+0.0872664625997165))
%input guess value Q*
for i = 2:N-1
            Q(i) = 1/10000;
end
Q(1) = S0;
Q(N) = SL;
error1 = 1;
while error1 >=0.00001
%input interior nodes
for i = 3:N-2
            d = L/(N-1)*(i-1);
            c = (d^2+s^2);
            A(i,i) = 6/(c^(1/2)*dx^4) + 6*d^2/(c^(5/2)*dx^2)+3*(s^2-
4*d^2)/c^(7/2)+(12*mu*T*kf)/(Q(i)^5*sigma*H*rho);
            A(i,i+1) = -4/(c^(1/2)*dx^4)+2*d/(2*c^(3/2)*dx^3)-
3*d^2/(c^(5/2)*dx^2)+(12*d^3-3*d*s^2)/(2*c^(7/2)*dx);
            A(i,i+2) = 1/(c^(1/2)*dx^4)-d/(2*c^(3/2)*dx^3);
            A(i,i-1) = -4/(c^(1/2)*dx^4)-2*d/(2*c^(3/2)*dx^3)-
3*d^2/(c^(5/2)*dx^2)-(12*d^3-3*d*s^2)/(2*c^(7/2)*dx);
            A(i,i-2) = 1/(c^(1/2)*dx^4)+d/(2*c^(3/2)*dx^3);
            F(i) = -((Q(i-2)-4*Q(i-1)+6*Q(i)-
4*Q(i+1)+Q(i+2))/(c^(1/2)*dx^4)-d*(-Q(i-2)+2*Q(i-1)-
2*Q(i+1)+Q(i+2))/(2*c^(3/2)*dx^3)-3*d^2*(Q(i-1)-
2*Q(i)+Q(i+1))/(c^(5/2)*dx^2)+(12*d^3-3*d*s^2)*(-Q(i-
1)+Q(i+1))/(2*c^(7/2)*dx)+3*(Q(i)+s)*(s^2-4*d^2)/c^(7/2)-
3*mu*T*kf/(Q(i)^4*sigma*H*rho));
end
%boundary nodes @ i = 1
A(1,1) = 1;
F(1) = -(Q(1)-S0);
%boundary nodes @ i = 2
i = 2;
d = L/(N-1)*(i-1);
c = (d^2+s^2);
A(2,1) = -4/(c^(1/2)*dx^4)-2*d/(2*c^(3/2)*dx^3)-
3*d^2/(c^(5/2)*dx^2)-(12*d^3-3*d*s^2)/(2*c^(7/2)*dx);
A(2,2) =
7/(c^(1/2)*dx^4)+d/(2*c^(3/2)*dx^3)+6*d^2/(c^(5/2)*dx^2)+3*(s^2-
4*d^2)/c^(7/2)+12*mu*T*kf/(Q(2)^5*sigma*H*rho);
A(2,3) = -4/(c^(1/2)*dx^4)-2*d/(2*c^(3/2)*dx^3)-
3*d^2/(c^(5/2)*dx^2)+(12*d^3-3*d*s^2)/(2*c^(7/2)*dx);
A(2,4) = 1/(c^(1/2)*dx^4)-d/(2*c^(3/2)*dx^3);
F(2) = -((-4*Q(1)+7*Q(2)-4*Q(3)+Q(4))/(c^(1/2)*dx^4)-d*(-
Q(2)+2*Q(1)-2*Q(3)+Q(4))/(2*c^(3/2)*dx^3)-3*d^2*(Q(1)-
2*Q(2)+Q(3))/(c^(5/2)*dx^2)+(12*dx^3-
3*d*s^2)*(Q(1)+Q(3))/(2*c^(7/2)*dx)+3*(Q(2)+s)*(s^2-4*d^2)/c^(7/2)-
3*mu*T*kf/(Q(2)^4*sigma*H*rho));
%boundary nodes @ i = N
A(N,N) = 1;
F(N) = -(Q(N)-SL);
%boundary nodes @ i = N-1
i=N-1;
d = L/(N-1)*(i-1);
c = (d^2+s^2);
```

```
A(N-1,N) = -4/(c^(1/2)*dx^4)+2*d/(2*c^(3/2)*dx^3)-
3*d^2/(c^(5/2)*dx^2)+(12*d^3-3*d*s^2)/(2*c^(7/2)*dx);
A(N-1,N-1) = 7/(c^(1/2)*dx^4)-
d/(2*c^(3/2)*dx^3)+6*d^2/(c^(5/2)*dx^2)+3*(s^2-
4*d^2)/c^(7/2)+12*mu*T*kf/(Q(N-1)^5*sigma*H*rho);
A(N-1,N-2) = -4/(c^(1/2)*dx^4)-2*d/(2*c^(3/2)*dx^3)-
3*d^2/(c^(5/2)*dx^2)-(12*d^3-3*d*s^2)/(2*c^(7/2)*dx);
A(N-1,N-3) = 1/(c^(1/2)*dx^4)+d/(2*c^(3/2)*dx^3);
F(N-1) = -((Q(N-3)-4*Q(N-2)+7*Q(N-1)-4*Q(N)+2*a*dx)/(c^(1/2)*dx^4)-
d*(-Q(N-3)+2*Q(N-2)-2*Q(N)+Q(N-1)+2*a*dx)/(c^(3/2)*dx^3)-3*d^2*(Q(N-
2)-2*Q(N-1)+Q(N))/(c^(5/2)*dx^2)+(12*d^3-3*d*s^2)*(-Q(N-
2)+Q(N))/(2*c^(7/2)*dx)+3*(Q(N-1)+s)*(s^2-4*d^2)/c^(7/2)-
3*mu*T*kf/(Q(N-1)^4*sigma*H*rho));
%Gaussian elimination
[n,~] = size(A);
z = zeros(n,1);
for i = 1:n-1
    m = A(i+1:n,i)/A(i,i);
    A(i+1:n,:)= A(i+1:n,:) - m*A(i,:);
    F(i+1:n,:)= F(i+1:n,:) - m*F(i,:);
end
z(n,:) = F(n,:)/A(n,n);
for i = n-1:-1:1
    z(i,:) = (F(i,:)-A(i,i+1:n)*z(i+1:n,:))/A(i,i);
end
for i=1:N
Q1(i,:) = Q(i,:) + z(i,:);
error(i,:) = abs((Q1(i)-Q(i))/Q(i))*100;
Q(i,:)= Q1(i,:);
end
error1=max(error);
end

W(N,:)=0;
for i = 1:N
            W(i) = L/(N-1)*(i-1)*1000;
end
plot(W,Q)
```